UNIVERSITAT ROVIRA I VIRGILI

EXPERIMENTAL AND THEORETICAL INVESTIGATION OF PRUSSIAN BLUE-TYPE CATALYSTS FOR ARTIFICIAL PHOTOSYNTHESIS
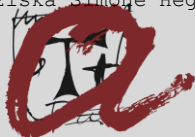
Franziska Simone Hegner

UNIVERSITAT
ROVIRA i VIRGILI

EXPERIMENTAL AND THEORETICAL INVESTIGATION OF PRUSSIAN BLUE-TYPE CATALYSTS FOR ARTIFICIAL PHOTOSYNTHESIS

Franziska Simone Hegner

DOCTORAL THESIS

2018

Franziska Simone Hegner

Experimental and Theoretical Investigation of Prussian Blue-Type Catalysts for Artificial Photosynthesis

DOCTORAL THESIS

Supervised by
**Prof. Núria López Alonso and
Prof. José-Ramón Galán Mascarós**

Institute of Chemical Research of
Catalonia (ICIQ)
and Rovira i Virgili University (URV)

Tarragona
2018

UNIVERSITAT ROVIRA I VIRGILI
EXPERIMENTAL AND THEORETICAL INVESTIGATION OF PRUSSIAN BLUE-TYPE CATALYSTS FOR ARTIFICIAL
PHOTOSYNTHESIS
Franziska Simone Hegner

Institut Català d'Investigació Química
Av. Països Catalans, 16
43007 Tarragona (Spain)

Prof. Núria López Alonso and Prof. José-Ramón Galán Mascarós, group leaders in the Institute of Chemical Research of Catalonia,

WE STATE that the present study, entitled "**Experimental and Theoretical Investigation of Prussian Blue-type Catalysts for Artificial Photosynthesis**", presented by Franziska Simone Hegner for the award of the degree of Doctor in Chemical Science and Technology, has been carried out under our supervision at the Institute of Chemical Research of Catalonia, and that it fulfils all the requirements for the award of the distinction of International Doctor.

Tarragona, 13th November, 2018

Prof. Núria   Prof. José-Ramón
López Alonso   Galán Mascarós

UNIVERSITAT ROVIRA I VIRGILI
EXPERIMENTAL AND THEORETICAL INVESTIGATION OF PRUSSIAN BLUE-TYPE CATALYSTS FOR ARTIFICIAL
PHOTOSYNTHESIS
Franziska Simone Hegner

Sponsors

UNIVERSITAT ROVIRA I VIRGILI
EXPERIMENTAL AND THEORETICAL INVESTIGATION OF PRUSSIAN BLUE-TYPE CATALYSTS FOR ARTIFICIAL
PHOTOSYNTHESIS
Franziska Simone Hegner

Acknowledgements

*"Feeling gratitude and not
expressing it is like wrapping a
present and not giving it."*
– William Arthur Ward

Primer de tot vull donar les gràcies als meus supervisors, na Prof. Núria López i en Prof. José Ramón Galán Mascarós, els quals han fet possible la realització d'aquesta tesi. Gràcies Núria per la teva ajuda i per haver-me guiat durant aquests anys, així com per tot el temps que has dedicat a ensenyar-me i aclarir-me els dubtes. Gràcies JR per oferir-me aquest projecte i donar-me l'oportunitat de descobrir el fascinant món de *Prussian blue*, donant-me el recolzament i la llibertat per ser creativa i desenvolupar les meves pròpies idees. Per vosaltres sempre va ser molt important que aprengués i descobrís, la qual cosa valoro molt.

Me gustaría expresar mi más sincera gratitud al Prof. Sixto Gimenez, quién a veces fue como un tercer jefe para mi ;) Gracias, Sixto, por acogerme en tu grupo, por las charlas tan inspiradoras y por tu ayuda, incluso con esta tesis! También agradezco a Isaac por introducirme en el mundo de la fotoelectroquímica y los misterios de la espectroscopía de impedancia, a Drialys por su ayuda y apoyo, y al resto del grupo que estuvo conmigo.

I would like to thank Prof. James Durrant for giving me the chance to join his group for two months and for exciting my interest in time-resolved spectroscopy. Special thanks go to Ben, who initiated this fruitful collaboration; thanks for all your help, also with this thesis, as well as good moments in and outside the lab. A huge thank you to the rest of the Prussian blue team, Laia, Sasha, and Shababa, for your support and inspiring discussions and meetings. Also to the "peus de gats", Luzi and Carlota, and the other *BANDGAP*–Bright And Noble Durranties Generating Artful Photochemistry!

UNIVERSITAT ROVIRA I VIRGILI
EXPERIMENTAL AND THEORETICAL INVESTIGATION OF PRUSSIAN BLUE-TYPE CATALYSTS FOR ARTIFICIAL
PHOTOSYNTHESIS
Franziska Simone Hegner

*"It is not your fault that
the world is the way that it is,
... but it will be your fault,
if it stays that way!"*

– Die Ärzte

UNIVERSITAT ROVIRA I VIRGILI
EXPERIMENTAL AND THEORETICAL INVESTIGATION OF PRUSSIAN BLUE-TYPE CATALYSTS FOR ARTIFICIAL
PHOTOSYNTHESIS
Franziska Simone Hegner

Prussian Blue
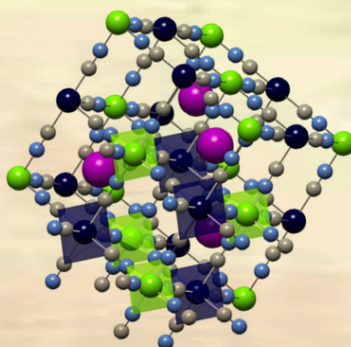
ceci est la couleur de mes rêves

UNIVERSITAT ROVIRA I VIRGILI
EXPERIMENTAL AND THEORETICAL INVESTIGATION OF PRUSSIAN BLUE-TYPE CATALYSTS FOR ARTIFICIAL
PHOTOSYNTHESIS
Franziska Simone Hegner

Contents

List of Publications

Included in this Thesis

- ***Paper I:*** A Database of the Structural and Electronic Properties of Prussian Blue, Prussian White, and Berlin Green Compounds through Density Functional Theory.
  Franziska Simone Hegner, José-Ramón Galán-Mascarós, Núria López
  Inorganic Chemistry, **2016**, *55*, 12851-12862.

- ***Paper II:*** Cobalt Hexacyanoferrate on $BiVO_4$ Photoanodes for Robust Water Splitting.
  Franziska Simone Hegner, Isaac Herraiz-Cardona, Drialys Cardenas-Morcoso, Núria Lopez, José-Ramón Galan-Mascaros, Sixto Gimenez.
  ACS Applied Materials & Interfaces, **2017**, *9*, 37671–37681.

- ***Paper III:*** Level Alignment as Descriptor for Semiconductor/Catalyst Systems in Water Splitting: The Case of Hematite/Cobalt Hexacyanoferrate Photoanodes.
  Franziska Simone Hegner, Drialys Cardenas-Morcoso, Sixto Gimenez, Núria Lopez, José-Ramón Galan-Mascaros.
  ChemSusChem, **2017**, *10*, 4552-4560.

- ***Paper IV:*** Unraveling Charge-Transfer in CoFe-PB Modified $BiVO_4$ Photoanodes.
  Benjamin Moss, Franziska Simone Hegner, Sacha Corby, Shababa Selim, Laia Francàs, Núria López, Sixto Giménez, José-Ramón Galán-Mascarós, James Robert Durrant.
  Submitted, **2018**

Additional publications

- ***Paper V:*** Boosting Photoelectrochemical Water Oxidation of Hematite in Acidic Electrolyte by Surface State Modification.

Peng-Yi Tang, Li-Juan Han, Franziska Simone Hegner, Paul Paciok, Martí Biset-Peiró, Hong-Chu Du, Xian-Kui Wei, Lei Jin, Hai-Bing Xie, Qin Shi, Teresa Andreu, Mónica Lira-Cantú, Marc Heggen, Rafal E. Dunin-Borkowski, Núria López, José Ramón Galán-Mascarós, Joan Ramon Morante, Jordi Arbiol. *Submitted*, **2018**

- ***Paper VI:*** The Nature of Oxygen Vacancies in $BiVO_4$ (001) Surface and Subsurface layers.
  Franziska Simone Hegner, Daniel Forrer, José-Ramón Galán-Mascarós, Núria López, Annabella Selloni.
  In preparation, **2018**

Author contribution

Franziska Simone Hegner performed all calculations of ***Papers I***, ***II***, ***III***, and ***VI*** and nearly all experiments in ***Papers II***, and ***III***. She carried out all the analyses, made the figures, and wrote most of the text.

Paper IV is a shared contribution between Franziska Simone Hegner and Benjamin Moss. In this paper both authors contributed to equal parts in the experiments, analyses, and writing.

Franziska Simone Hegner took part in ***Paper V***. She contributed mainly in revising and discussing the text, as well as performing calculations (unpublished) for overall understanding.

List of Abbreviations

Materials	
PB	Prussian blue (iron(III) hexacyanoferrate(II))
BG	Berlin green (oxidised PB: iron(III) hexacyanoferrite(III))
PW	Prussian white (reduced PB: iron(II) hexacyanoferrate(II))
CoFe-PB	Cobalt iron Prussian blue (Cobalt hexacyanoferrate)
Electronic structure	
DOS	Density of States
E_g	Band gap
E_F	Fermi level
VB	Valence band
VBM	Valence band maximum
CB	Conduction band
CBM	Conduction band minimum
HOMO	Highest occupied molecular orbital
LUMO	Lowest unoccupied molecular orbital
CFSE	Crystal field splitting energy
hs	high-spin
ls	low-spin
is	intermediate-spin
FM	Ferromagnetic
AFM	Antiferromagnetic
Computational	
DFT	Density Functional Theory
KS	Kohn–Sham
VASP	Vienna Ab Initio Simulation Package
PAW	Projector Augmented Wave

PBE	Perdew–Burke–Ernzerhof exchange–correlation functional
PBEsol	PBE revised for solids
HSE	Heyd–Scuseria–Ernzerhof hybrid exchange–correlation functional

(Photo)electrochemistry	
PEC	Photoelectrochemistry
PV	Photovoltaic
CV	Cyclic voltammetry
CA	Chronoamperometry
EIS	Electrochemical impedance spectroscopy
IPCE	Incident photon-to-current conversion efficiency
RHE	Reversible Hydrogen Electrode
SHE	Standard Hydrogen Electrode
NHE	Normal Hydrogen Electrode
OCV / OCP	Open-circuit voltage/potential
TOF	Turnover frequency

Absorption spectroscopy	
UV–Vis	Ultraviolet–Visible
IR	Infrared
SEC	Spectroelectrochemistry
TAS	Transient Absorption Spectroscopy
PIAS	Photo-Induced Absorption Spectroscopy

Characterisation	
SEM	Scanning Electron Microscopy
TEM	Transmission Electron Microscopy
EDX	Energy-Dispersive X-Ray
XPS	X-ray Photoelectron Spectroscopy
ICP-OES	Inductively coupled plasma optical emission spectrometry

Other	
OER	Oxygen Evolution Reaction
HER	Hydrogen Evolution Reaction
FTO	Fluorine-doped tin oxide
DMSO	Dimethyl sulfoxide

Abstract

Artificial photosynthesis, in which high energy compounds such as hydrogen are produced from water by using sunlight, seems to be a very promising solution to the global energy crisis, regarding its huge advantages of sustainability and abundance. Large progress has been made in the development of photoelectrochemical water splitting using Earth-abundant semiconductor materials. Nonetheless, industrial implementation is still hampered by the lack of a stable, efficient, and cost-competitive photoanode for water oxidation catalysis. To overcome these drawbacks and to enhance reaction rates, a co-catalyst can be deposited on such a metal oxide photoanode.

Materials based on Prussian blue, which fulfil all those requirements, have shown high water oxidation activities with exceeding long-term stabilities. Notwithstanding, the detailed catalytic mechanisms remain unclear. In combining experimental methods with theoretical calculations I aimed to elucidate the underlying photophysical mechanisms and its determining factors, such as electronic structure and charge-transfer properties.

In this context, I successfully applied the cobalt iron analogue of Prussian blue (CoFe-PB) onto the light-harvesting semiconductors Fe_2O_3 and $BiVO_4$ in order to increase their performance. Deposition of CoFe-PB largely increased the photocurrent and significantly lowered the onset potential of light-induced water oxidation on $BiVO_4$, while its beneficial influence on Fe_2O_3 remained rather small. In order to understand the effect of CoFe-PB, a wide range of photoelectrochemical methods, including impedance spectroscopy, and time-resolved spectroscopy, including transient and photo-induced absorption spectroscopy, were used. In the case of $BiVO_4$, it was shown to efficiently transfer charges, whereas in the case of Fe_2O_3, it merely shifted the capacitance of surface states.

Various theoretical methods in the framework of DFT were assessed, with respect to their ability to describe the complex electronic and magnetic structure of Prussian blues. A modified hybrid functional with optimised amount of exact exchange was found appropriate to compute the electronic energy levels of all employed

compounds. Their analysis and alignment demonstrated the thermodynamic feasibility of charge-transfer from $BiVO_4$ to CoFe-PB and further to H_2O, in line with the experimental predictions. In CoFe-PB/Fe_2O_3 such a favourable alignment of electronic structures is not given; therefore, charge-transfer via the CoFe-PB catalyst is less likely, which may explain its inferior performance compared to CoFe-PB/$BiVO_4$.

Taken together, the role of CoFe-PB was concluded to be different on both modified photoanodes: it acts as a *true* hole transfer catalyst on $BiVO_4$, whereas it only affects the surface electronic structure on Fe_2O_3.

Chapter 1

Introduction

1.1   Solar fuels – a global challenge

The development of a viable alternative to fossil fuels is one of the greatest challenges science and technology are facing today. Population growth and technological progress lead to a rapid increase of the world's energy demand, which is mainly met by fossil resources, like coal, oil, or natural gas. The consumption of fossil fuels to power the planet and to fulfil the needs of society lies at the origin of a variety of socio-economic, geopolitical, environmental, and health-related issues.

Although there may still be plenty of fossil resources available on Earth, they are unevenly distributed and not always easily accessible.[1,2] Their unequal distribution gives rise to geopolitical instabilities, while their limited accessibility may lead to use of environmentally detrimental extraction methods.[1,2] Moreover, combustion of fossils increases air pollution, often forming smog in highly populated places, which is a risk factor for human health.[3] The major problem, however, is related to the largely enhanced carbon dioxide emissions and their impact on the Earth's atmosphere.[4] Exhaust gases, such as CO_2, resulting from burning fossil fuels are the main contributor to the greenhouse effect. These gases impede the release of heat back into space and cause warming of the Earth's atmosphere.[5] Apart from a rising global temperature, other consequences of climate change involve increased intensities and frequencies of heat waves,[6] heavy rain falls and other extreme weather events,[7] the expansion of dry lands and deserts,[7] and the enhanced melting rate of ice from the Antarctic, Arctic, and Greenland.[8,9] Another detrimental effect of CO_2 emission is its uptake by the oceans, which leads to an oceanic acidification.[10]

Figure 1.1 shows the increase of greenhouse gas emission since 1700, measured in the Mauna Loa observatory by the National

Oceanic and Atmospheric Administration. The Annual Greenhouse Gas Index (AGGI), which is indexed to 1 for the year 1990 (on right ordinate in red), gives a measure of the climate-warming influence of long-lived trace gases and how that influence has changed since the onset of the industrial revolution.[11] Its by far largest contribution comes from CO_2 emissions (light-blue in Figure 1.1a or cyan in Figure 1.1b).[1,4,5,11]
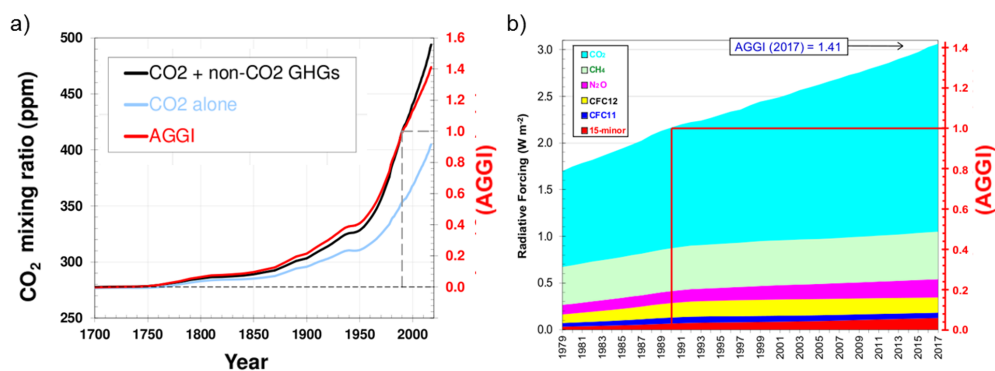
Figure 1.1: a) Changes in the emission of CO_2 and other greenhouse gases, and the corresponding AGGI since the year 1700. b) Radiative forcing, relative to 1750, of all the long-lived greenhouse gases. Adapted from Ref. [11].

With the drastically increasing rate of energy consumption, the amount of accumulated carbon dioxide in the atmosphere is expected to double by 2050.[1,12] Taken together, finding an alternative energy supply, which needs to be clean, sustainable, and secure, is of uttermost importance. Sunlight, which is by far the most abundant energy source, appears to be an obvious choice. Being able to harvest the energy of sunlight would be beneficial in many ways. Apart from being environmentally friendly and non-toxic, it is available everywhere on the planet (even countries on the Northern or Southern hemisphere do get sufficient solar irradiation to compensate their energy needs),[1] which may also facilitate access to power for economically less strong countries.

In order to efficiently utilise intermittent solar power, it has to be harvested and stored. Its capture and its conversion into electricity can be accomplished by photovoltaic (**PV**) devices. Batteries could be used for storing that energy, but their relatively heavy weight poses problems for transportation. Furthermore, state-of-the-art batteries are still an issue for environmental compatibility and safety, as well as availability of raw materials, such as lithium.[13]

A more elegant way to tackle the challenge of storing solar energy is by artificial photosynthesis - *"to fix the solar energy through*

suitable photochemical reactions" as it was described already more than a century ago by Ciamician.[14] The replacement of fossil fuels by *solar fuels*, energy-rich chemicals formed with the aid of sunlight, is the motivation for the work presented in this Thesis.

1.2 Artificial photosynthesis – approaches

Plants use photosynthesis in order to convert water into oxygen and hydrogen, which is further combined with CO_2 to sugars and other carbohydrates. Mimicking this process with a catalytic system is the basic idea of artificial photosynthesis (see Figure 1.2).[15]
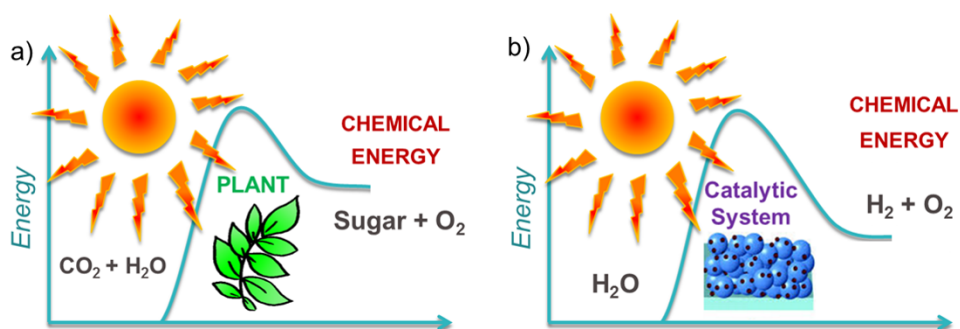
Figure 1.2: Schematic representation of a) plant photosynthesis and b) artificial photosynthesis by a catalytic system.

The first step in natural photosynthesis, which is key to energy storage, is the splitting of water (Equation 1.1):[15–17]

$$H_2O \longrightarrow H_2 + \frac{1}{2}O_2 \qquad (1.1)$$
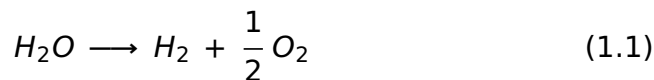
The thermodynamic energy stored in this reaction is 2.46 eV (∼237 kJ/mol) at standard conditions (25 °C, $p(H_2) = 1$ atm).[18] By taking hydrogen as an energy vector in a hydrogen-based economy, one could make use of this energy by burning it in a hydrogen fuel cell, i.e. in the back reaction.[19] Moreover, the produced hydrogen can be supplied as feedstock for other reactions, for example, for the reduction of atmospheric CO_2 to liquid fuels or for ammonia production, which is crucial to sustain the planet.[19]

The overall water splitting reaction can be divided into its reduction and oxidation half-reactions, the Hydrogen Evolution Reaction (**HER**, Equation 1.2) and the Oxygen Evolution Reaction (**OER**, Equation 1.3).

$$2H^+ + 2e^- \rightleftharpoons H_2 \qquad V^o = 0 \ V_{SHE} \qquad (1.2)$$

$$O_2 + 4H^+ + 4e^- \rightleftharpoons 2H_2O \quad V^o = 1.23 \ V_{SHE} \qquad (1.3)$$

The reversible reaction potentials V^o are defined with respect to the Standard Hydrogen Electrode (SHE). By convention, the reference zero is set to the potential of hydrogen reduction in the SHE configuration (Pt electrode in 1 molar acidic solution at standard conditions).[†][18] In order to avoid a later confusion of labels, the redox potential is referred to as V^o instead of the often used E^o, which is also consistent with many reports in the field,[20,21] while the letter "E" remains reserved to energy terms.

Finding a suitable catalytic system that can do both OER (Equation 1.3) and HER (Equation 1.2) with a high efficiency appears to be infeasible. Thus, a straightforward solution is to find and optimise suitable systems for both reactions separately. With its high potential cost of $V^o = 1.23 \ V_{SHE}$ the water oxidation reaction is particularly demanding, not only from a thermodynamic view point, but also from a kinetic aspect, as it requires the transfer of four electrons and four protons. This is why the search for an adequate water oxidation catalyst system is often regarded as being the bottleneck step to implement artificial photosynthesis in an industrial scale.[22,23]

Realising water oxidation catalysis and understanding its underlying mechanisms is also the main focus of my research. There are different ways to put water splitting into practice, which are outlined below.

1.2.1   Electrochemical water splitting

Electricity, generated by a photovoltaic cell, can be used to split water electrochemically. This phenomenon of water electrolysis, that electrical discharge can decompose water into "*combustible air*" and "*life-giving air*", has been first reported by Troostwijk and Diemann in 1789.[24,25] An electrolyser consists of two electrodes, a positively charged anode and a negatively charged cathode, at which the respective oxygen evolution and hydrogen reduction reactions occur, and is schematically presented in Figure 1.3.

[†]Often reaction potentials are given relative to NHE (Normal Hydrogen Electrode) or RHE (Reversible Hydrogen Electrode), which are both similar to the SHE. In the NHE the effective acidic concentration (*normality*) is taken to be 1 N. The potential of the RHE is independent of pH and it is related to the NHE by $V_{RHE} = V_{NHE} + 0.059 \cdot pH$.

From a purely thermodynamic aspect, the required voltage needs to be higher than the voltage difference between the HER and OER redox potentials, that is 1.23 V. Nonetheless, in order to overcome the kinetic barriers for the reactions to occur, a higher potential needs to be applied, which is called the *overpotential η*. High overpotentials are needed for water oxidation, on the order of 0.2–0.4 V for state-of-the art heterogeneous catalysts.[23]
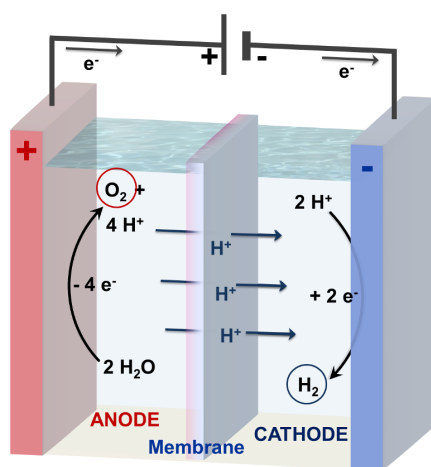
Figure 1.3: Scheme of the working mechanism of electrochemical water splitting in liquid electrolyte (water with dissolved salt): On the positively charged anode (left) water is oxidised to oxygen, on the negatively charged cathode (right) protons are reduced to hydrogen. Here, an ion–exchange membrane separates the two compartments but permits ion diffusion for charge equilibration.

Artificial photosynthesis could therefore be realised by coupling a PV cell to an electrolyser (PV-electrolysis). Although both solar cells and electrolysers are commercially available, a large-scale implementation is still hindered by the fact that it is not economically competitive with the much cheaper fossil fuels.[26] While PV cells are nowadays relatively inexpensive, the electrolyser part suffers from several drawbacks, for instance, low efficiency or corrosion in an alkaline electrolyser, or high cost of materials in a PEM (proton exchange membrane) electrolyser.[23, 27]

1.2.2   Photochemical water splitting

Photoelectrolysis or photochemical water splitting is a more *direct* way of creating solar fuels, as it avoids the coupling of two different devices and entailed energy loss pathways.[28] It can be achieved

by having one photocatalytic system, which is able to harvest light and to transform it directly into chemical bonds, such as shown in Figure 1.4a. Light with an energy high enough to excite an electron from its highest lying electronic states (valence band, **VB**) to its lowest lying excited states (conduction band, **CB**) gets absorbed.[†] The excited electrons can then reduce H_2O or H^+ to H_2 and the *holes* (the missing electrons in the highest electronic state) can oxidise H_2O to O_2. For this, the electron levels must lie above the HER potential and the hole levels below the OER potential.
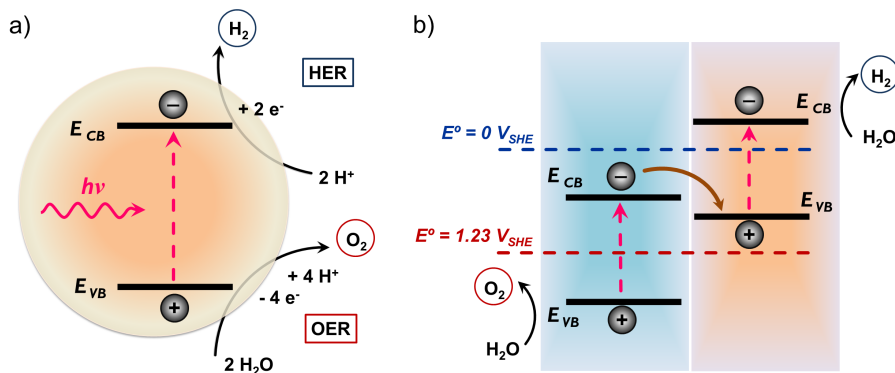
Figure 1.4: Scheme of photocatalysis: a) Incoming light excites an electron from its highest occupied energy level (E_{VB}) to its lowest lying excited state (E_{CB}), leaving a hole in the VB. These photogenerated electrons/holes are then available for HER/OER. b) Two light absorbing semiconductors are connected in a tandem device: After light absorption, the excited electron of the semiconductor with lower lying energy levels (left) fills the hole of the higher lying semiconductor (right).

The first photochemical water splitting was presented in the landmark paper by Fujishima and Honda in 1972, using the inorganic semiconductor TiO_2.[29,30] Nonetheless, the high band gap of TiO_2 and low catalytic efficiencies hinder its practical usage; and ever since there has been a quest to overcome those limitations.[31,32] From an energetic viewpoint, it is unlikely to find a single compound that efficiently absorbs light in the visible region, and is able to do both water oxidation and water reduction.[33] If the band gap is too small, not enough energy gets absorbed to overcome the difference of the HER and OER potentials, which is 1.23 eV plus the respective overpotentials of both half-reactions.[20,34]

A solution to this can be a tandem device, in which two semiconductors with different energy level positions are connected in series, as shown in Figure 1.4b. A semiconductor with a low valence

---

[†]The significance of those energy levels is explained in more detail in Chapter 2 (Section 2.2 about semiconductors).

band (below OER potential) creates holes, which oxidise water. Its excited electrons transfer to the other semiconductor with higher energy levels, which is able to perform HER. This scheme is often referred to as "Z-scheme" named after the shape of the flow diagram of electrons, in analogy to plant photosynthesis.[34]

Nevertheless, also other practical problems, such as corrosion of the photocatalyst in the electrolyte or generating an explosive H_2/O_2 gas mixture, need to be overcome. Another solution, which could circumvent the latter, i.e. mixing of gases, and which I used in this work, is photoelectrochemical water splitting.

1.2.3 Photoelectrochemical water splitting

Both electrochemical and photochemical water splitting can be combined in a photoelectrochemical (**PEC**) cell, such as shown in Figure 1.5. This is only one possible configuration of a PEC device; other structures might be envisaged, as for example found in Refs. [22] and [35]. In the presented two-electrode cell water oxidation takes place at the photoanode, whereas water reduction takes place at the photocathode. Mixing of gases can therefore be avoided, as H_2 and O_2 evolve in separate compartments. Moreover, energy can be supplied externally, for example, by a PV cell, if the energy from light-absorption is insufficient to drive the overall water splitting reaction.
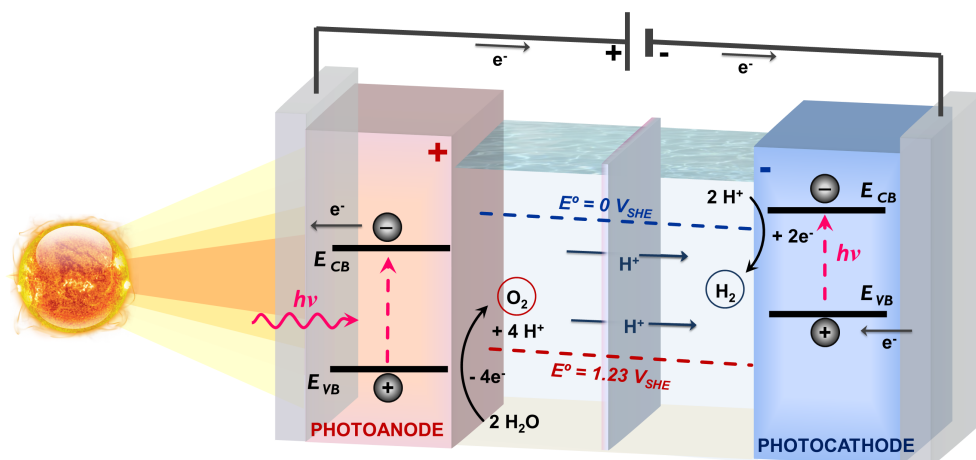
Figure 1.5: Scheme of PEC water splitting: Photoanode (left) with low lying valence band (VB) and photocathode (right) with high lying conduction band (CB), both connected to an electrical circuit. Both absorb light and generate excited electron–hole pairs. Holes in the photoanode oxidise water and electrons flow into the circuit, while in the photocathode electrons from the CB reduce water and holes get filled by electrons from the external circuit.

In my research, I focus on the the photoanode part, i.e. investigation of possible catalytic systems and the underlying physical processes. Finding adequate Earth-abundant photoanode materials, which efficiently catalyse the OER, is still one of the major limitations that prevent an industrial implementation of PEC water splitting.

1.3 Photoanode systems

A suitable photoanode material needs i) to absorb light in the visible region; ii) to have a low lying valence band level E_{VB}, the highest occupied electronic level, which lies below the thermodynamic redox potential for water oxidation (1.23 eV); and iii) to be stable under working conditions.[34] These energetic criteria (i and ii) are the same as was explained for the tandem device (Figure 1.4b) and are further discussed in Chapter 2 along with the properties of (*n*-type) semiconductors.

Figure 1.6 shows the positions of highest occupied (valence band edge) and lowest unoccupied (conduction band edge) electronic levels of different semiconductor photoelectrode materials, compared to water reduction and oxidation potentials.[36] Only those materials with the valence band edge (dark blue) below the OER potential fulfil the *thermodynamic* requirement for an application as photoanode.
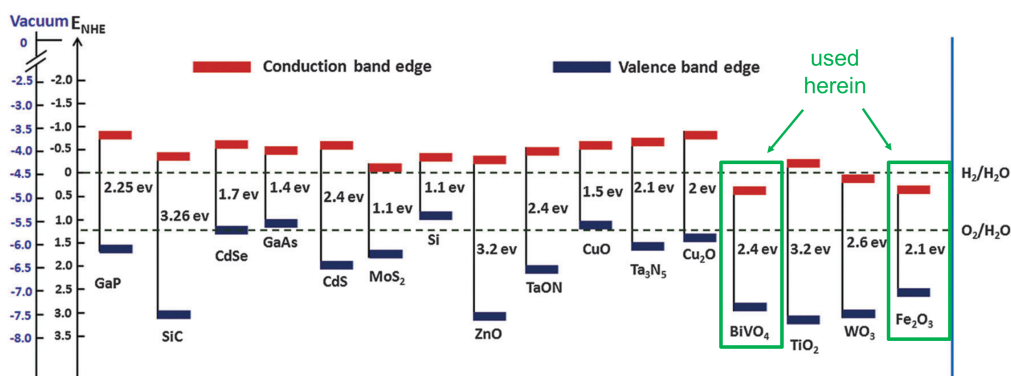
Figure 1.6: Photoelectrode semiconductor materials and their valence (highest occupied) and conduction (lowest unoccupied) band edges in contact with aqueous electrolyte at pH 0, relative to NHE and the absolute vacuum level, and compared to HER (0 V_{NHE}) and OER (1.23 V_{NHE}) potentials. The metal oxides $BiVO_4$ and Fe_2O_3, which are studied in this thesis, are highlighted in green. Adapted from Ref. [36].

Apart from those key prerequisites, an appropriate candidate material has to be inexpensive, non-toxic, and consist of Earth-abundant elements for PEC water splitting to become competitive to fossil fuels.[1,16]

In this context, first-row transition metal oxides with favourably aligned band edge positions show great promise. Generally, they exert a larger resistance towards photo corrosion, compared to many other typical semiconductor materials.[32] Also, their relatively low toxicity and easily scalable synthesis, which is necessary for industrial implementation, make them interesting materials to study.[32,34,37] This is why much attention has been paid to the development and understanding of different *n*-type metal oxide semiconductors, such as TiO_2,[29,30] α-Fe_2O_3,[38–40] WO_3[41] and $BiVO_4$.[42,43] In my research, I have focused on the materials α-Fe_2O_3 and $BiVO_4$ and their combination with a water oxidation co-catalyst, as explained below.

Implementations of these materials in a PEC device is hindered by several factors. Those include limited photon absorption, inefficient separation of photogenerated electron–hole pairs and high recombination rates, poor conduction, and low catalytic efficiency. More mechanistic details are explained in Chapter 2.

Many current research efforts are devoted to overcome these drawbacks, such as i) *doping*, to increase charge carrier concentration and conduction; ii) *nano-/mesostructuring*, to increase the amount of active surface sites and to shorten the travel distance of photogenerated holes to the surface; iii) *passivation* of defect sites, to eliminate centres of carrier recombination; iv) *heterostructure formation* of different light absorbers, to enhance light absorption; v) *catalyst modification*, to accelerate the OER rate; and others.[22,32,36,37] The latter, addition of an electrocatalyst to act as a co-catalyst, is the approach chosen and discussed herein.

1.4 Water oxidation catalysts

Depositing a water oxidation electrocatalyst on the surface of a semiconductor can lead to an overall performance enhancement. This strategy has often shown great success by increasing the rate of oxygen production and/or reducing the required potential for OER to occur, i.e. the *onset potential*.[36,44–55]

Different materials can be envisaged to be successful water oxidation catalysts.[23,56] A useful identification of catalytic activity is given by Trasatti's *volcano* plot analysis, as shown in Figure 1.7.[56,57] An efficient catalyst with optimal binding energies of reaction intermediates lies close to the top of the *volcano*.[58,59] Its intermediates

neither bind too weakly, nor too strongly, allowing for fast and efficient adsorption and desorption, according to the Sabatier principle.[60,61] In order to be practically implemented in a PEC device, the catalyst also needs to have a high surface area, low toxicity, easy processability, and to be cost-effective.[62]
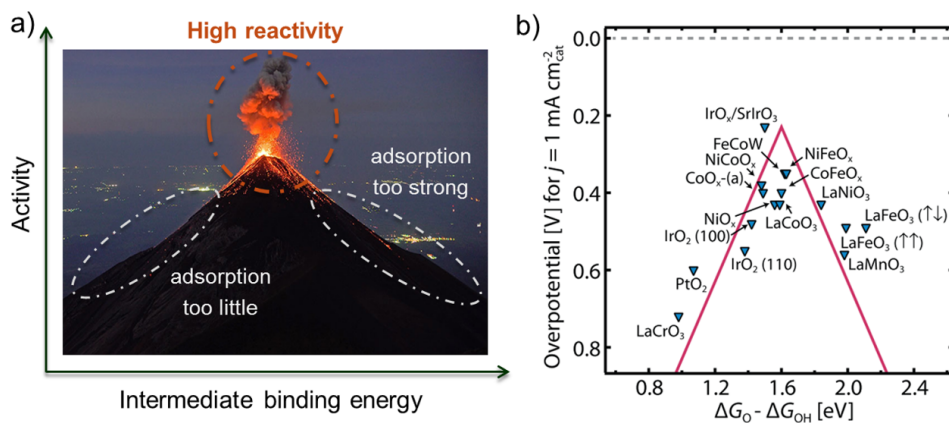
Figure 1.7: Volcano plots: a) General: Reactivity as a function of intermediate binding energy. b) Volcano of metal oxide OER catalysts: The activity, defined by the overpotential, is plotted against the binding energy difference of oxo (ΔG_O) and hydroxo (ΔG_{OH}) intermediates. Taken from Refs. [56] and [61].

1.4.1 Transition metal oxides

Transition metal oxides possessing redox active centres have been known to be effective water oxidation catalysts for many decades.[57,62–64] Those also include most employed metals and alloys, because at anodic water oxidation potentials they form oxidic layers on the surface, which are the actual catalytic phase.[62,65]

Amongst the binary metal oxides, *rutile* type structures show highest water oxidation activities. Due to their ideal intermediate binding energies (lying close to the top of the volcano), RuO_2 followed by IrO_2, are the most efficient.[61,62,66,67] Up to date, IrO_2 still outperforms most water oxidation catalysts in *acidic* medium.[67,68] These catalysts, however, contain rare elements, which prevents their large scale commercialisation.[56] Hence, much research has been focused on the development of Earth-abundant metal oxide catalysts.

Thin film oxides containing first-row transition metals, such as Fe, Co, and Ni, are nowadays state-of the art catalyst for water oxidation in basic medium.[69,70] The reason for their success is their *in situ* formation of an ion-permeable layered oxyhydroxide structure,

which has shown to be crucial to OER activity. Other transition metal oxides like $Ni_yCo_{1-y}O_x$, where transformation to the layered oxyhydroxide is suppressed, are much less effective.[70] Recently, quaternary (FeCoW) oxyhydroxides have reached record performances with less than 0.2 eV overpotential in alkaline media.[71]

Also perovskites, ternary oxides with a ABO_3 stoichiometry, whose water oxidation activity has been known already since the 1980ies,[63,64] have potential for success (see Figure 1.7b).[61,72,73] Through analysis and optimisation of the metal *d*-orbital occupation, a highly efficient composite perovskite material $Ba_{0.5}Sr_{0.5}Co_{0.8}Fe_{0.2}O_{3-\delta}$ was recently found.[72]

Other mixed metal oxides have also shown promising results. Those compounds include spinel-type AB_2O_4 structures[63,74,75] and amorphous mixed metal oxides containing Fe, Co, and Ni,[76,77] among others.

Taken together, excellent water oxidation efficiencies, even higher than that of IrO_2, have been achieved with Earth-abundant (mixed) metal oxides[70–72] in *alkaline* media. Notwithstanding, they lack activity and stability in *acidic* and often also in *neutral* media.[56,78] This is unfavourable for implementing PEC water splitting, as in alkaline media the corresponding hydrogen evolution half-cell reaction is much more demanding.[79,80] Thus, the development of highly active and stable electrocatalysts in acidic and neutral media is still focus of current research activities.[73,81,82]

Cobalt catalysts

The cobalt catalyst CoP_i has attracted recent attention in the field of artificial photosynthesis[16,83] due to its high stability in neutral media and its successful implementation as co-catalyst in PEC devices.[16,44,45,49,50,84–87]

It was found that the catalytically active centres in cobalt phosphate (CoP_i) actually reside on cobalt oxide cores, whereas the phosphate anions (P_i) do not take part in the active catalysis.[88–91] Their role is to stabilise and *self-heal* the catalyst.[88,92] Indeed, a similar catalytic behaviour is obtained for Co_3O_4 in phosphate buffer. Co_3O_4 itself is an excellent catalysts in alkaline media with highest activity at pH 14,[93] but it is stable only at very high pH and dissolves in neutral medium.[94] In a phosphate buffer, however, the dissolved cobalt ions are stabilised and electrodeposited again upon oxidation, which is the process that is termed *self-healing*.[88,95] Experimental[96] and theoretical[97,98] studies suggest that a layered cobalt (oxy)hydroxide, CoO(OH)/CoOOH, is the catalytically active

phase under water oxidation conditions, i.e. at anodic potentials. In this thesis, the general notation CoO_x is used to take into account different oxidic cobalt species that may be involved in the reaction.

CoO_x is undoubtedly the most common water oxidation catalyst that has been combined with semiconductor photoanodes to achieve light-driven water oxidation.[23] However, its catalytic function is highly controversial.[99] While several studies propose that it truly catalyses the water oxidation reaction by accepting and transferring photogenerated holes,[45,86,100] other studies indicate that its influence may be rather of electrostatic nature.[87,101,102] Its effect when forming an interface with a semiconductor is discussed later in the text, and compared to that of cobalt iron Prussian blue, used in this work.

1.4.2   Prussian blue analogues

Another class of materials are Prussian blue (**PB**) type networks, metal hexacyanometallate structures with the general formula $A_{2x}M^a_{(3-x)}[M^b(CN)_6]_2 \cdot nH_2O$,[103] where A is an alkali metal counter cation and M^a and M^b are transition metal centres. Its structural and electronic properties are focus of Chapter 3. Owing to its electronically distinct transition metal centres, the versatile nature of Prussian blue analogues allows for a wide range of applications, amongst them electrocatalytic oxidation and reduction.[104,105] Despite being widely employed as oxidation catalyst of H_2O_2 and organic materials,[105–108] its OER activity was not established until 2013, when the group of Prof. Galán-Mascarós first reported the electrocatalytic water oxidation activity of the cobalt iron analogue (**CoFe-PB**).[103] Since then, several other publications on water oxidation catalysis by Prussian blue analogues from our group and others have followed.[109–115]

Figure 1.8a schematically represents the formation and composition of a highly stable and efficient CoFe-PB electrode, when prepared by a two-step solvothermal–etching method.[110] In here, a dense $Co(OH)_x$ layer on FTO (fluorine-doped tin oxide) is derivatised to cobalt hexacyanoferrate ($A_xCo_y[Fe(CN)_6]_z \cdot nH_2O$, under the magnifying glass in Figure 1.8a). Also other transition metal hexacyanometallates were assessed for their water oxidation activity, but only cobalt hexacyanoferrate (as seen in Figure 1.8b) and cobalt hexacyanocobaltate showed significant oxygen evolution.[109] Indeed, N-coordinated Co with vacant coordination sites are suggested to be the catalytically active centres in the coordination network; a mechanism is proposed in Refs. [110] and [112].
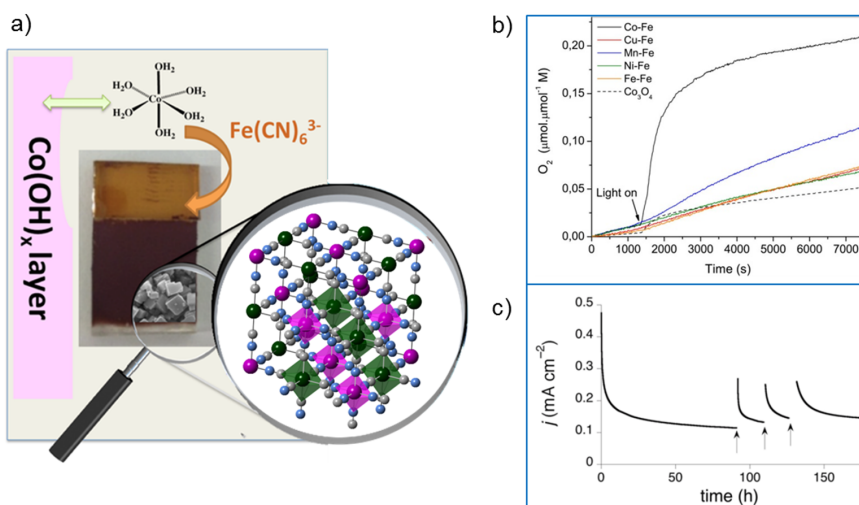
Figure 1.8: Catalytic activity of CoFe-PB: a) Schematic representation of the two-step CoFe-PB preparation by chemical etching of a covalently bound CoO$_x$ film, and magnified image (TEM and ideal atomistic structure) of CoFe-PB (adapted from Ref. [110]). b) Photocatalytic oxygen evolution for a range of metal hexacyanoferrates combined with a photosensitiser (from Ref. [109]). c) Current profile of CoFe-PB during bulk water electrolysis at 1.82 V$_{RHE}$ (from Ref. [103]).

Due to its stabilisation by the hexacyanoferrate group, CoFe-PB remains active in a wide range of pH ($2 \leq pH \leq 13$)[110] with excellent long-term stability (see Figure 1.8c). Hence, while showing comparable performance to CoO$_x$ (and other Earth-abundant metal oxides) in *neutral* media, they largely outperform them in *acidic* media.[23,103,110] In addition, the polymeric structure of CoFe-PB offers several advantages over metal oxides, which are generally associated with molecular-based materials, such as low density, high structural flexibility, facile processability, and large exposure of catalytically active sites. Prussian blue type networks and their interaction with light-absorbing semiconductors are the main focus of my research and are discussed in the following Chapters.

1.4.3   Homogeneous catalysts

So far, I have only considered the implementation of heterogeneous catalytic systems, i.e. solid materials. From an engineering perspective those are clearly beneficial, considering implementation in a real working device. Homogeneous, molecular catalysts are generally more efficient and selective,[116] however they lack stability and are prone to decomposition, particularly under water oxidation reaction conditions.[17,117] There are possible strategies to

combine advantages of homogeneous and heterogeneous systems, such as fixing the homogeneous electrocatalysts on inorganic solid supports. Some successful examples can be found in Ref. [23] and references therein.

1.5 Semiconductor–catalyst interfaces

Commonly used metal oxide photoanodes exhibit relatively slow water oxidation kinetics compared to fast recombination of photogenerated electron–hole pairs at the semiconductor–electrolyte surface.[87,118–122] In order to overcome these drawbacks, a water oxidation co-catalyst can be deposited on the surface; a strategy, which has often led to large performance increase.[36,49,52–54]

Nonetheless, the reasons for the observed photocurrent improvement are often not well understood. An accurate description of the semiconductor–catalyst interface and the interface with the electrolyte, which govern the key processes of water oxidation, is challenging from both experimental and theoretical perspectives.[99,123–126] Most of the employed materials (semiconductor and catalyst) are not perfectly crystalline, and their defects may play a crucial role in the mechanisms. In particular, the structure and growth mechanisms of the electrocatalyst are often not well-defined; it may be an impermeable or porous layer, or grow as separate particles or islands on the semiconductor surface.

Experimental tools to unambiguously characterise the structure and to measure directly interfacial processes are rare.[33,123,126] Also from a theoretical point of view, modelling the semiconductor–catalyst interface is demanding. Not only finding a representative geometric model, but also choosing an adequate theoretical method with sufficient accuracy is not straightforward, and a solution is often hampered by its vast computational cost.[127–131] Moreover, a rigorous determination to assess time-dependent charge-transfer at complex interfaces has yet to be developed.[129] An overview of computational methods to align semiconductor–catalyst–electrolyte interfaces is given in Chapter 4.

1.5.1 Function of the catalyst

In the most simple picture, as in Figure 1.9, the catalyst acts as a *true* charge-transfer catalyst. This means holes transfer from the semiconductor to the catalyst, and from there to H_2O, initiating water oxidation. But also other mechanisms, with which the "catalyst" affects the PEC performance, can be envisaged. These include suppression of recombination by an electrostatic field (i.e.

increasing *band bending*[†]),[132,133] passivation of charge carrier trap defects on the semiconductor surface,[50,124] enhancement of light absorption,[123,134] creation of a surface dipole,[134] or development of a capacitive layer that acts as a hole reservoir.[53]
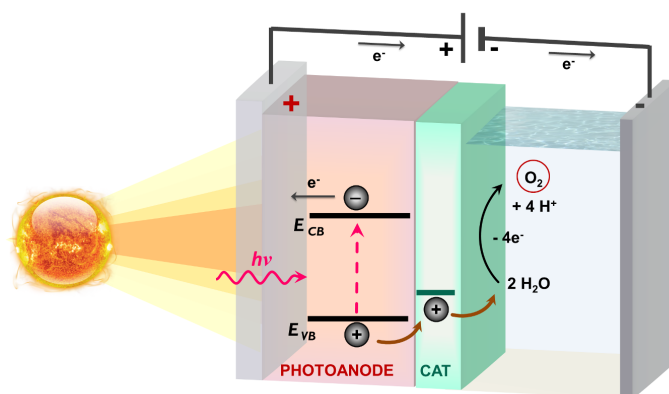
Figure 1.9: Charge-transfer scheme of a photoanode with deposited co-catalyst (cathodic site is neglected for clarity): Electrons are excited from the valence to the conduction band, where they enter the electric circuit. Photogenerated holes transfer to the catalyst, from which they further transfer to H_2O.

Clarifying the underlying mechanisms of performance enhancement upon catalyst deposition is crucial to the development of more efficient functionalised photoanodes. Depending on its role in photo-induced water oxidation, different properties of the catalyst and/or the interface can be optimised and the search of novel catalytic materials can be targeted more effectively.

Literature in this field is often controversial, as it was shown for CoO_x.[45,86,87,99–102] Reasons for this dispute may be based on the ill-defined interface, as well as different measurement methods, which are sensitive to different variables, such as electronic current or optical signals.[100,101]

A screening of different electrocatalyst materials demonstrated that there is a mismatch of performance, when the catalyst is deposited either on a conductive substrate (like FTO) or on a light-absorbing semiconductor anode.[135] For example, IrO_2 showed no activity on W-doped $BiVO_4$ under light, although it was the most active *electrocatalyst* in the study. Also Hajibabaei *et al.* found that of a series of different nickel iron oxides with varying compositions,

---

[†]To establish electronic equilibrium, the electrostatic potential changes when forming an interface, which can be described by *band bending*, explained in Section 2.3.1.

the least electroactive catalyst performs best as a co-catalyst on hematite.[136] Hence, an efficient water oxidation catalyst does not guarantee any catalytic activity when used as co-catalyst for PEC water splitting.

From this consideration follows that the simple assessment of catalytic activity by a linear volcano relation (Figure 1.7), i.e. considering solely the intermediate binding energies as descriptor, does no longer apply for complex heterogeneous semiconductor–catalyst interfaces.[61,65] Additional descriptors may be needed and their applicability, as well as their relative impact on the kinetics and thermodynamics, strongly depend on the system.[58] Therefore an *a priori* evaluation of the system's performance is not possible at the current stage, as it would require a multidimensional volcano-type analysis.

1.5.2   Interface morphology

The detailed structure of the interface, hence catalyst coverage and morphology, is key to its functional properties.[33] Conductive and dense catalysts on top of a semiconductor form a so-called *Schottky junction* with a constant electrostatic barrier,[137,138] which impedes effective hole transfer across the interface.[139–141]

Most active water oxidation catalysts, however, form nonuniform, porous, or layered structures, such as hydrous transition metal oxides or (oxy)hydroxides, including the famous CoO_x/CoP_i[100] and Ni(Fe)OOH catalysts,[70,136] as well as the open Prussian blue networks like CoFe-PB.[103,110] Those ion-permeable and redox active catalysts form so-called *adaptive junctions* at which the electronic charge on the semiconductor surface is compensated by ions from the electrolyte, and thus there is less potential drop at the semiconductor–catalyst interface.[125,139]

This classification of interface types (Schottky or adaptive junctions)[126] is supported by a recent theoretical study by Ping *et al.*[142] In the case of WO_3/IrO_2, a full co-catalyst coverage led to an unfavourable energy level alignment, whereas partial coverage, i.e. permeability, resulted in thermodynamically favourable interfacial charge-transfer.[142]

Another important point to consider is the morphology of the semiconductor anode. In case of a planar and dense semiconductor, electrons in the conduction band travel away from the semiconductor–catalyst or semiconductor–electrolyte interface when applying an electric field. If the semiconductor, however, is mesostructured and electrons travel parallel to the interface with the catalyst, the probability that those electrons recombine

with holes stored in the catalyst is much higher. As thicker the catalyst layer and, hence, the amount of holes stored, as higher the likelihood of recombination, which results in decreasing PEC performance. This effect was indeed observed in hematite and CoO_x.[140,143]

If the semiconductor does not fully cover the underlying conductive FTO, i.e. when the semiconductor film is very thin and/or pin hole defects are present, the deposited catalyst layer comes in direct contact with the substrate. As a result, the holes stored in the catalyst can recombine with electrons from the substrate, similar to an electrical shunt.[140,141]

These morphology-dependent differences in mechanism may also explain the differences observed in the mentioned case of CoO_x, as in the controversial studies both the underlying metal oxide semiconductor and the catalyst were prepared by different methods.[44,100,132]

1.6   Objectives

Artificial photosynthesis, by which the energy of sunlight is stored into chemical bonds, seems the most plausible solution to satisfy the world's energy demand. With my research I want to have an impact on the development of efficient devices for photoelectrochemical water oxidation, needed to make artificial photosynthesis industrially viable.

The general objective of this Doctoral Thesis is to study Prussian blue analogues and their application as water oxidation catalysts by a combination of theoretical and experimental techniques. In particular, I focus on cobalt iron Prussian blue (CoFe-PB) and its role as a co-catalyst on the well-known photoanodes Fe_2O_3 and $BiVO_4$.

The main goals are: i) to identify a robust computational scheme to accurately describe both the electronic structure of Prussian blue and the photoanode systems; ii) to test the applicability and effectiveness of CoFe-PB as water oxidation catalyst on the different metal oxides and to identify an easy synthetic route for its deposition; iii) to study the underlying photochemical and -physical processes on those CoFe-PB modified systems; and iv) to shed light on the reasons for successful implementations of catalyst modified photoanodes with the aim of guiding future investigations on semiconductor–catalyst interfaces. In order to do so, I employed various experimental methods, mainly photoelectrochemistry and (time-dependent) spectroscopy, as well as theoretical calculations in the framework of periodic Density Functional Theory (DFT).

1.7 Thesis outline

- In **Chapter 2**, I explain the background of the computational and experimental methods used, that is DFT and its practical implementations, basics of semiconductor physics and photo-electrochemistry (PEC), as well as electrochemical impedance spectroscopy (EIS) and time-dependent spectroscopy.

- In **Chapter 3**, the applicability of DFT for Prussian blue type structures is assessed; various functionals are tested and evaluated. Moreover, the electronic structures of Prussian blue and its derivatives, in particular the water oxidation catalyst CoFe-PB, and the photoanode materials, hematite and bismuth vanadate, are discussed in detail.

- In **Chapter 4**, the CoFe-PB catalyst is deposited onto Fe_2O_3 and $BiVO_4$ photoanodes. Different synthesis methods are briefly discussed, the semiconductor–catalyst structures are characterised, their photoelectrochemical performance is tested, and its *thermodynamic* feasibility assessed. The mechanisms of photocurrent enhancement are investigated by hole scavenger experiments and EIS. Moreover, the energy level alignment of the interfaces is assessed computationally and discussed in terms of being a possible descriptor for beneficial water oxidation enhancement.

- In **Chapter 5**, time resolved spectroscopy of the well-performing CoFe-PB/$BiVO_4$ interfaces is carried out, namely transient absorption spectroscopy (TAS) and photo-induced absorption spectroscopy (PIAS), in order to determine the hole dynamics of the system. The rates of charge-transfer and water oxidation are estimated and compared to other semiconductor–catalyst interfaces, and their *kinetic* feasibility is discussed.

A part of this work was carried in collaboration with the groups of Prof. Sixto Gimenez (Institute of Advanced Materials, Castellón, Spain)[*] and Prof. James Durrant (Imperial College London, UK)[†], in the context of the A-LEAF project,[144,145] as well as with Prof. Annabella Selloni (Princeton University, USA)[‡].

---

[*]Results from this collaboration are focus of Chapter 4.
[†]Results from this collaboration are focus of Chapter 5.
[‡]Work from this collaboration is still in progress and not included in this thesis.

Chapter 2

Methods and theoretical background

2.1 Theoretical methods

In this Section the main principles from quantum mechanics and condensed matter science are revised, which lie at the basis of the employed computational methods.

2.1.1 Density Functional Theory

The Schrödinger equation

At the basis of electronic structure theory lies the solution of the Schrödinger equation, which, in its time-independent, non-relativistic form, is given by

$$\hat{H}\Psi = E\Psi \qquad (2.1)$$

where $\hat{H}$ is the Hamiltonian and E its associated eigenvalue. The solutions Ψ are a set of particle (electronic and nuclear) wave functions.[146–148] In most cases the Born–Oppenheimer approximation can be assumed,[149] i.e. the heavier and slowly moving nuclei are considered as stationary particles with respect to the electrons, and therefore the electronic Hamiltonian can be written as

$$\hat{H}_{elect} = \hat{T} + \hat{V} = -\frac{h^2}{2m}\underbrace{\sum_{i}^{N}\nabla_i^2}_{kinetic\ energy} + \underbrace{\sum_{I,i}^{M,N}\frac{Z_I\,e}{|\boldsymbol{R_I} - \boldsymbol{r_i}|}}_{e-n\ attraction} + \underbrace{\sum_{i<j}^{N}\frac{e^2}{|\boldsymbol{r_i} - \boldsymbol{r_j}|}}_{e-e\ repulsion} \qquad (2.2)$$

with the kinetic energy operator $\hat{T}$ and the potential energy operator $\hat{V}$, consisting of attractive electron–nuclear and repulsive

electron–electron interactions; N being the number of electrons i with electronic mass m, charge e, and position $\mathbf{r_i}$, M the number of nuclei I with charge Z_I and position $\mathbf{R_I}$.

The solution of the resulting electronic Schrödinger equation,

$$\left[\hat{T} + \hat{V}\right]\Psi_{elect} = E\Psi_{elect} \qquad (2.3)$$

Ψ_{elect}, can be approximated as a *Slater determinant*,[150] the asymmetric product of the individual wave functions ψ_i of all N electrons:

$$\Psi_{elect} = |\psi_1\,\psi_2\ldots\psi_N\rangle \qquad (2.4)$$

Considering three spatial coordinates and the electronic spin, this represents a $4N$ dimensional many-body problem, impossible to solve analytically for $N > 2$. Nonetheless, numerical methods can be used to solve the problem iteratively, in a self-consistent manner, and to find the electronic ground state by relying on the variational principle:[146,147,151]

$$E_0 \leq \langle\Psi|\hat{H}|\Psi\rangle \qquad (2.5)$$

These methods, which are based on computing the electronic wave function, are generally built on the Hartree–Fock (HF) approximation.[151] Although several state-of-the-art post-Hartree–Fock and multi-reference methods, such as coupled cluster and multi-configurational self-consistent field calculations, yield very high chemical accuracy, they are only applicable for small systems, as their computational cost increases exponentially with the number of electrons.[148]

The Kohn–Sham equation

Density Functional Theory (DFT), which does *not* rely on electronic wave functions but electronic density, makes an application to larger systems, especially solids, feasible.[147] Its foundations are the two Hohenberg–Kohn theorems (**HK1** and **HK2**) from 1964:[152]

- **HK1:** *"The external potential $v_{ext}(\mathbf{r})$, and hence the total energy, is a unique functional of the electron density $\rho(\mathbf{r})$."*
  This, in turn, means that the electron density $\rho(\mathbf{r})$ determines energy E, wave function, and all other properties of the system. In its functional form the energy E is expressed as $E[\rho(\mathbf{r})]$.

- **HK2:** *"The ground state energy can be obtained variationally: the density that minimises the total energy is the exact ground state density."*

This is analogous to the variational principle of wave functions.[151] It consequently states that if the true functional form $E[\rho(\mathbf{r})]$ was known, the exact ground state solution of the electronic Schrödinger equation could be obtained.

Together, the Hohenberg–Kohn theorems provided the mathematical basis for the development of the one electron Kohn–Sham (**KS**) equations[153]

$$\hat{H}_{KS}\,\psi_i(\mathbf{r_i}) = \varepsilon_i\,\psi_i(\mathbf{r_i}) \tag{2.6}$$

governed by the Kohn–Sham Hamiltonian $\hat{H}_{KS}$[147,153]

$$\underbrace{-\frac{h^2}{2m}\nabla_i^2}_{kinetic\ energy} + \underbrace{V_{ext}(\mathbf{r})}_{e-n\ attraction} + \underbrace{V_H(\mathbf{r})}_{e-e\ repulsion} + \underbrace{V_{XC}(\mathbf{r})}_{exchange-correlation} \tag{2.7}$$

describing an electron moving in a non-interacting reference system, which experiences an external potential $V_{ext}(\mathbf{r})$, including the electron–nuclei interaction, a Coulomb, or Hartree, potential $V_H(\mathbf{r})$, and the exchange–correlation potential $V_{XC}(\mathbf{r})$.

The Hartree potential

$$V_H(\mathbf{r}) = e^2 \int \frac{\rho(\mathbf{r}')}{|\mathbf{r}-\mathbf{r}'|}d^3\mathbf{r}' \tag{2.8}$$

defines the electrostatic interaction of the electrons.
The exchange–correlation potential

$$V_{XC}(\mathbf{r}) = \frac{\delta E_{XC}(\mathbf{r})}{\delta\rho(\mathbf{r})} \tag{2.9}$$

includes all other inter-electronic interactions, generally speaking, the exchange and correlation contributions. The exact form of the exchange–correlation energy functional $E_{XC}[\rho(\mathbf{r})]$ is basically unknown. Its various description attempts define accuracy and applicability of DFT-based methods, which is discussed in Section 2.1.2.

At a first glance the Kohn–Sham equations (Equations 2.6 and 2.7) seem similar to the electronic Schrödinger equation (Equation 2.3), but with the solutions being independent, single-electron wave functions $\psi_i(\mathbf{r_i})$, which only depend on three spatial coordinates. They are related to the electronic density by:

$$\rho(\mathbf{r}) = \sum_i^N \psi_i^*(\mathbf{r})\psi_i(\mathbf{r_i}) \tag{2.10}$$

Applying the variational principle (Equation 2.5) to the mono-electronic KS-equations (Equation 2.6) and iteratively minimising its energy, this allows for a self-consistent computation of the ground state electron density (and with it all other electronic properties), which only depends on three (four, including the spin) variables to be minimised. Therefore, one can calculate electronic structures of larger systems much more efficiently than with methods based on Hartree–Fock theory.

2.1.2 Exchange–Correlation

One large drawback of DFT is the so-called *self-interaction error*, which results from the fact that the Hartree potential $V_H(\boldsymbol{r})$ (Equation 2.8) defines the interaction of one electron with *all* the electrons, including itself. This unphysical interaction is to some extent corrected in the exchange–correlation potential $V_{XC}(\boldsymbol{r})$ (Equation 2.9), whose mathematical form is unknown. Attempts to describe the exchange–correlation energy functional $E_{XC}[\rho(\boldsymbol{r})]$ with an emphasis on the functionals used in my Thesis are outlined in this Section.

Local Density Approximation (LDA)

In the Local Density Approximation (LDA) the electron density is considered as a homogeneous electron gas. The exchange–correlation energy, which depends only on the electron density $\rho(\boldsymbol{r})$ at the position **r** where it is evaluated, can be described as:[153,154]

$$E_{XC}^{LDA}[\rho(\mathbf{r})] = \int \rho(\boldsymbol{r}) \, \varepsilon_{XC}^{hom}(\rho(\boldsymbol{r})) \, d\mathbf{r} \qquad (2.11)$$

Its extension to spin-polarised systems is termed the Local Spin Density Approximation (LSDA).[155] Although being the most simple description of $E_{XC}(\mathbf{r})$, it usually gives a good description for metallic systems with delocalised electrons, but tends to overestimate binding and cohesive energies.

Generalised Gradient Approximation (GGA)

As the name implies, in the Generalised Gradient Approximation (GGA) not only the density $\rho(\mathbf{r})$ at position **r**, but also its gradient $\vec{\nabla}\rho(\boldsymbol{r})$ is taken into account:[156]

$$E_{XC}^{GGA}[\rho(\mathbf{r})] = \int \rho(\boldsymbol{r}) \, \varepsilon_{XC}(\rho(\boldsymbol{r}), \vec{\nabla}\rho(\boldsymbol{r})) \, d\mathbf{r} \qquad (2.12)$$

Within the GGA a vast range of functionals have been developed,[146] such as PBE (Perdew-Burke-Ernzerhof),[157] PW91 (Perdew-Wang),[158] B88 (Becke),[159] etc. (with names generally composed of the initials of the developers). In principal, one can distinguish between two families, non-empirical (Perdew) functionals and empirical (Becke) functionals, which are obtained by parametrisation of test sets and often used for molecular systems.[148] For periodic calculations of solids, most common are PBE, RPBE (revised PBE),[160] and PBEsol (PBE revised for solids),[161] the latter being the GGA functional of choice in this work as it was especially constructed to improve solid properties like lattice parameters.[161]

Meta-GGA (m-GGA)

The next level of complexity is to introduce also higher-order derivatives in the calculation of the exchange–correlation energy, the meta-GGA:

$$E_{XC}^{mGGA}[\rho(\mathbf{r})] = \int \rho(\mathbf{r})\, \varepsilon_{XC}(\rho(\mathbf{r}), \vec{\nabla}\rho(\mathbf{r}), \vec{\nabla}^2\rho(\mathbf{r}))\, d\mathbf{r} \qquad (2.13)$$

Yet not many practical examples have been presented. Up to now, the increased accuracy of meta-GGAs has often not compensated the largely increased computational cost in the case of solid systems.[162] The recently developed SCAN (Strongly Constrained and Appropriately Normed) functional, however, shows promises for being a successful meta-GGA.[163, 164]

For materials that contain elements with strong electronic correlations, pure local (LDA) or semilocal (GGA, meta-GGA) Density Functional Theory methods are unsuited, due to the *self-interaction error*. It leads to an erroneous over delocalisation of the electrons, especially in systems with localised *d*- and *f*-electrons, thus transitions metals, lanthanides, and actinides.[165] In order to overcome the self-interaction error, corrections to the exchange–correlation energy $E_{XC}[\rho(\mathbf{r})]$ have been made, basically adding a Hubbard U term (DFT+U) or introducing exact exchange (hybrid functionals), and are described in the following.

DFT + U method

The DFT+U method is rooted in the Hubbard model of solid state physics, in which the *Hubbard U* describes the on-site interaction between two electrons on the same atom.[166,167] It was first introduced into the DFT formalism by Animosov and co-workers (LDA+U approach),[168,169] and further simplified by Dudarev, who introduced the effective U parameter $U^{eff} = (U - J)$, combining the on-site Coulomb U and exchange J interaction terms.[170] It is commonly implemented in a rotationally invariant form:

$$E_{DFT+U} = E_{DFT} + \frac{(U-J)}{2} \sum_m^{\sigma} \left(n_m^{\sigma} - (n_m^{\sigma})^2 \right) \qquad (2.14)$$

with the atomic occupation number n_m^{σ} of the mth state (with spin σ), subtracted by a double counting term $(n_m^{\sigma})^2$, thus, avoiding doubly occupying one spin-orbital.[170,171] Conceptually the effective U parameter can be understood as an additional energy penalty, which is applied to partially occupied d and f states. In turn, this means that completely filled or empty d and f states do not "feel" the U, whereas there is an energy cost in partial occupation.

The U parameter can be obtained *ab initio* by linear response theory[172,173] or empirically, through fitting to a known variable, such as band gaps, formation enthalpies, or reaction energies.[174] Its value depends on the chemical environment, and thus lacks in transferability. Nonetheless, DFT+U is the most common method for modelling highly correlated materials. It can give an accurate description of chemical properties, while profiting from the practical efficiency of density functional calculations, compared to the computationally expensive inclusion of Hartree–Fock terms (see below).[174,175]

Hybrid functionals

Another approach to overcome the DFT-inherent self-interaction error is to introduce non-locality in the description of the exchange correlation energy. This means, in practice, that a certain amount of exact exchange from Hartree–Fock theory E_X^{HF} is mixed in to replace that same amount of DFT exchange E_X^{DFT} from pure DFT.[176,177]

$$E_{XC}^{hybrid} = \underbrace{a\, E_X^{HF}}_{\text{exact HF exchange}} + \underbrace{(1-a)\, E_X^{DFT}}_{\text{DFT exchange}} + \underbrace{E_C^{DFT}}_{\text{DFT correlation}} \qquad (2.15)$$

The fraction a of HF exchange usually varies between 0.20–0.25 in most common hybrid functionals, such as B3LYP,[178,179] PBE0,[180]

or HSE.[181] While the former, B3LYP, has been gold-standard in molecular calculations, it fails in accurately describing long-range effects in extended solid systems.[176] Although PBE0, the hybrid version of the non-empirical Perdew-Burke-Ernzerhof (PBE) functional, is more adequate for solids, the computation of its long-range exact exchange, which does *not* scale linearly with system size as in pure DFT, is prone to convergence errors.[180,182] This problem was remedied by Heyd, Scuseria, and Ernzerhof in the range-separated HSE functionals, which are based on PBE0 but screen the long-range exact exchange interaction:

$$E_{XC}^{HSE} = \underbrace{a\,E_X^{HF,SR}(\omega)}_{short-range\ HF\ exchange} + \underbrace{(1-a)\,E_X^{PBE,SR}(\omega)}_{short-range\ PBE\ exchange} +$$
$$\underbrace{E_X^{PBE,LR}(\omega)}_{long-range\ PBE\ exchange} + \underbrace{E_C^{DFT}}_{DFT\ correlation} \tag{2.16}$$

where $a = 25\%$ and ω is governing the extent of short-range interactions, i.e. at which distance the exact exchange will be "cut-off".[181–183] Most frequently employed in solid-state calculations are the functionals HSE03 and HSE06, which only differ in that screening distance, which is 3.33 Å and 5 Å for HSE03 and HSE06, respectively.[183,184]

Introducing exact exchange contributions favour higher spin multiplicities and its commonly employed fraction of 20–25% often leads to a non-physical overstabilisation of those states with high electronic spins.[185–188] Hybrid functionals with less amount of exact exchange, such as B3LYP* ($a = 15\%$), have shown to be more appropriate for molecular complexes,[185] as well as for semiconducting solids containing transition metals.[186,189,190]

In general, hybrid methods are more accurate than the previously described density functionals, but also vastly more computationally expensive, in particular for large periodic structure calculations where they are often practically infeasible. The increase of computational cost by introducing non-local exchange can be one or more orders of magnitude compared to GGA density functionals.[†]

[†] In order to directly compare the computational cost of GGA, GGA+U, and hybrid functionals, a test calculation of the electronic structure of the solid $BiVO_4$ was performed with the functionals PBE, PBE+U (U = 5.5 eV), and HSE03. All other input parameters were kept constant, the accuracy low and no spin-polarisation was introduced. The single-point calculation on a pre-optimised geometry was performed on only one k-point (gamma). The CPU time on 24 processors was *6, 25*, and *370* seconds for PBE, PBE+U, and HSE03, respectively.

2.1.3 Periodic structure calculations

For periodic solid systems, which are studied in this work, plane wave pseudopotential methods are commonly used and are explained in this Section.

Plane wave basis sets

The one-electron Kohn–Sham orbitals $\psi_i(\boldsymbol{r_i})$ (Equation 2.6), which lie at the basis of any DFT calculation, can be defined in different ways. The two main representations are in terms of i) localised atom-centred wave functions, Slater- or Gaussian-type orbitals; or ii) delocalised, extended plane waves.[148] In a crystalline solid the latter, plane wave approach accounts appropriately for the periodic potential experienced by the electrons in the lattice. Applying Bloch's Theorem,[191] the electronic wave function can be expressed in form of a plane wave $e^{i\boldsymbol{k}\cdot\boldsymbol{r}}$ with wave vector k multiplied by a periodic function $u_{n\boldsymbol{k}}(\boldsymbol{r})$ with the same periodicity as the crystalline lattice:[166,191]

$$\psi_{n\boldsymbol{k}}(\boldsymbol{r}) = e^{i\boldsymbol{k}\cdot\boldsymbol{r}}\, u_{n\boldsymbol{k}}(\boldsymbol{r}) \tag{2.17}$$

so that for any lattice vector $\boldsymbol{R}$ follows,

$$\psi_n(\boldsymbol{r} + \boldsymbol{R}) = e^{i\boldsymbol{k}\cdot\boldsymbol{R}}\, \psi_{n\boldsymbol{k}}(\boldsymbol{r}) \tag{2.18}$$

illustrating the translational symmetry of the wave function.

Reciprocal space

Any crystalline solid can be described as a *Bravais* lattice, which expresses its periodicity as an array of infinitely repeated discrete points with lattice vector $\boldsymbol{R}$

$$\boldsymbol{R} = n_1\boldsymbol{\alpha_1} + n_2\boldsymbol{\alpha_2} + n_3\boldsymbol{\alpha_3} \tag{2.19}$$

where n_1, n_2, n_3 are integers and $\boldsymbol{\alpha_1}$, $\boldsymbol{\alpha_2}$, $\boldsymbol{\alpha_3}$ are *direct* primitive vectors that span the lattice in three dimensions.[138,166]
From it, a *reciprocal* lattice with lattice vector $\boldsymbol{k}$ can be created:

$$\boldsymbol{k} = k_1\boldsymbol{b_1} + k_2\boldsymbol{b_2} + k_3\boldsymbol{b_3} \tag{2.20}$$

with *reciprocal* primitive vectors $\boldsymbol{b_1}$, $\boldsymbol{b_2}$, $\boldsymbol{b_3}$, defined as

$$\mathbf{b_1} = 2\pi\frac{\mathbf{a_2} \times \mathbf{a_3}}{\mathbf{a_1} \cdot (\mathbf{a_2} \times \mathbf{a_3})}$$
$$\mathbf{b_2} = 2\pi\frac{\mathbf{a_3} \times \mathbf{a_1}}{\mathbf{a_2} \cdot (\mathbf{a_3} \times \mathbf{a_1})} \qquad (2.21)$$
$$\mathbf{b_3} = 2\pi\frac{\mathbf{a_1} \times \mathbf{a_2}}{\mathbf{a_3} \cdot (\mathbf{a_1} \times \mathbf{a_2})}$$

In reciprocal space, also referred to as *k-space*, the primitive cell, which can be represented by a so-called Wigner–Seitz cell (a geometrical construction of perpendicularly bisecting planes)[192] is defined as the *first Brillouin zone* (**BZ**).[138,166]

A schematic representation of the direct *Bravais* lattice, its reciprocal lattice and BZ in two dimensions is shown in Figure 2.1. The reciprocal lattice is also defined as the set of wave vectors **k** that yield plane waves with the same periodicity as a given *Bravais* lattice,[166] which justifies the use of plane waves as an appropriate basis set. It has to be noted that the wave vector **k** as introduced by Bloch's theorem is *not* proportional to the electronic momentum, although it is often referred to as *crystal momentum*. It can be rather seen as a quantum number characteristic of the translational symmetry of the periodic potential.[166]
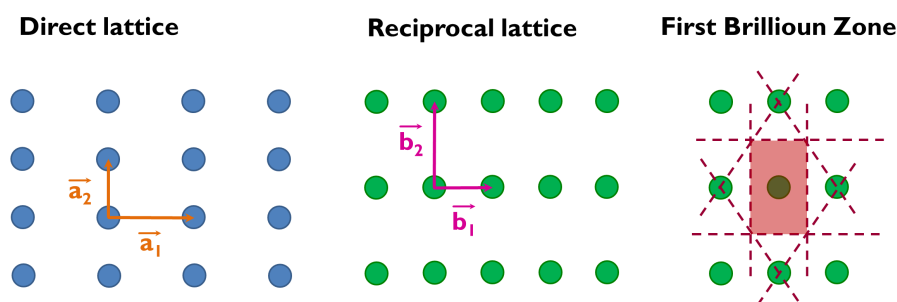
Figure 2.1: Two dimensional representation of the direct *Bravais* lattice, the reciprocal lattice, and the first Brillouin zone obtained by the Wigner–Seitz construction.

In practice, only the eigenvalues of a discrete set of **k** vectors are evaluated; less *k*-points reduce computational cost, but also accuracy.[146] One method of choosing the appropriate k-points in the BZ was developed by Monkhorst and Pack in 1976 and is still widely used in most periodic structure calculations.[193]

Electronic band structure and Density of States

The eigenvalues of **k** give the band structure of a solid, i.e. the electronic energies $\varepsilon_n(\mathbf{k})$ as a function of k. An example of a solid band structure, which is defined by special points in the first Brillouin zone, is shown in Figure 2.2.

According to the Pauli principle, each *band* can be occupied by 2 electrons, giving rise to fully and partially occupied, and empty bands. The number of states per interval of energy $\delta(\varepsilon - \varepsilon(\mathbf{k}))$ is described by the Density of States (**DOS**):[166]

$$DOS(\varepsilon) = \int_{BZ} d\mathbf{k}\, \delta(\varepsilon - \varepsilon(\mathbf{k})) \qquad (2.22)$$
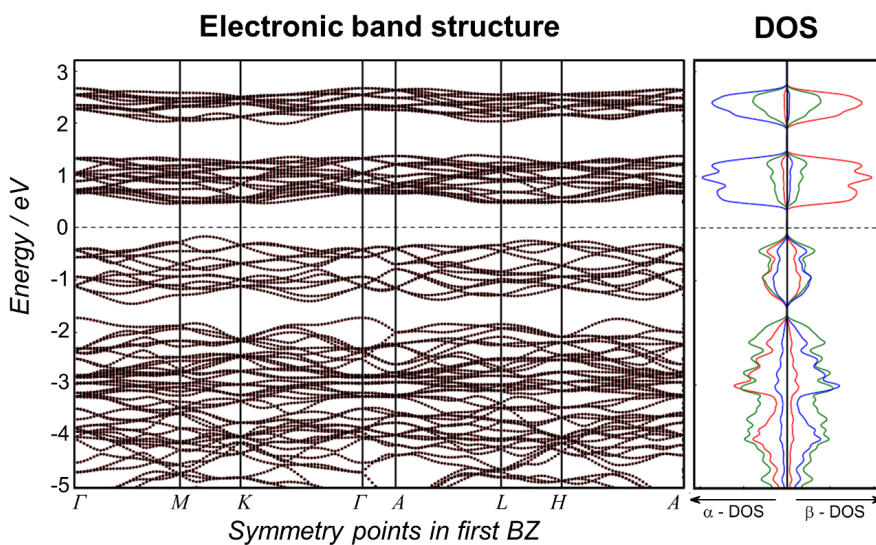
Figure 2.2: Example of a band structure and Density of States (DOS) of hematite (α-Fe$_2$O$_3$), calculated with a PBE functional. Γ, M, K, Γ, A, L, H are special points in the first BZ, defined by the hexagonal crystal symmetry of α-Fe$_2$O$_3$.

Pseudopotentials

In order to account for all electrons in the crystal unit cell, an extremely large set of plane waves would be required, leading to a very high computational cost. In particular, the rapid oscillations close to the atomic nuclei are not easily assessed by plane waves, despite the fact that they are not influenced by the chemical environment and do not contribute to bonding. In the pseudopotential approach, or *frozen core* approximation, the effects of the core

electrons and nuclei are replaced by an effective potential V_{pseudo}, and only the outer valence electrons are considered in the calculation. Those are described by pseudo-orbitals ψ_{pseudo}, which avoid the nodal structure near the nuclei and are therefore also termed as *smooth*. A schematic representation of the pseudopotential and the wave function is shown in Figure 2.3.

A good pseudopotential should be transferable, i.e. applicable to all chemical systems of the same elemental component, and soft, i.e. requiring a small amount of plane waves to represent ψ_{pseudo}. Most common in plane wave codes are optimised norm-conserving (ONCV) pseudopotentials,[194,195] ultrasoft-pseudopotentials (USPPs),[196] and projector-augmented wave (PAW) pseudopotentials,[197,198] all assuming that the valence and core orbital overlap is negligible (*small core* approximation). In this work, only the most recent PAW pseudopotentials are used, as they are efficiently implemented in the employed *VASP*[199,200] code, and comprise a good balance between computational cost and accuracy.[198]
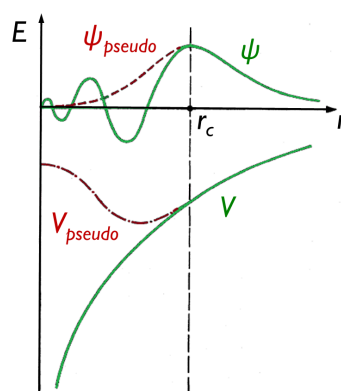
Figure 2.3: Schematic illustration of the pseudopotential V_{pseudo} and pseudo wave function $\psi_{pseudo}(\mathbf{r})$ (red dashed lines) constructed from the corresponding all-electron potential V and wave function $\psi(\mathbf{r})$ (green solid lines). At $\mathbf{r} = \mathbf{r_c}$, the critical radius, the real and pseudised wave functions, and potentials coincide. Adapted from Ref. [201].

Energy cut-off

The infinite sum of plane waves, as given by the Bloch's theorem (Equation 2.17), needs to be truncated by a finite value, which is defined in terms of its kinetic energy solutions and therefore termed the kinetic energy cut-off. A lower energy cut-off implies that less plane waves are used in the solution of Equation 2.17. This reduces the computational effort, but at the expense of accuracy.[201]

2.1.4 Applicability of theoretical methods

Practical considerations

Taken together, the important points to consider for a practical application of periodic structure calculations from Section 2.1.3, are:

- *K-points - sampling of the k-points, the "translational quantum number" in reciprocal space:* As less *k*-points used, as faster the calculation and less accurate the calculation will be. As a rule of thumb, a good compromise between accuracy and efficiency, is to set the number of *k*-points, in direction of lattice vector $\mathbf{a_i}$, multiplied by $\mathbf{a_i}$ (in Å) to be around 30 for metals and around 20 for insulators.[146,193]

- *Pseudopotential:* The use of a pseudopotential $\psi_{pseudo}(\mathbf{r})$ is essential in most implementations as it drastically simplifies electronic structure computations. There are several ways to construct pseudopotentials and a large variety of databases, where they can be found. Care needs to be taken in choosing and testing the appropriate pseudopotential for the used computational method.[194–198]

- *Energy cut-off:* In general the kinetic energy cut-off, which is given by default by the implemented pseudopotential, yields a reasonable accuracy. However, it should be increased (typically by about one third of its default value) when a complete cell-optimisation is carried out. This is due to *Pulay stress*, which arises when changing the basis set by varying the unit cell size.[146,201,202]

- For comparing multiple calculations those parameters, i.e. energy-cutoff, *k*-points, and pseudopotentials, have to be kept *constant*.

Apart from these three points, there are various technical aspects to consider, such as the numerical optimisation algorithms, as described in Ref. [146].

Validity and limits

Within the Born–Oppenheimer approximation, and considering the analytical form of $E_{XC}[\rho(\mathbf{r})]$ was known, Density Functional Theory is accurate, as defined by the Hohenberg–Kohn theorems in Section 2.1.1. Nonetheless, it is a ground state theory and all states other than the true ground state at zero K are by definition no longer

exact and only approximations to the real electronic state. However, keeping this in mind, DFT results can give useful predictions of physically accessible states. As in most theoretical computations, a compromise between efficiency and required accuracy has to be obtained and, hence, the limits of each approach need to be known.

Moreover, the applicability is dependent on the desired property to compute. While one generally obtains correct lattice constants (within the error of about 1%) with local DFT methods, DFT often fails in properly accounting for several electronic properties, especially when many low lying electronic configurations with similar energies co-exist.[146] This is particularly severe in the description of magnetic states, such as high-spin and low-spin configurations of transition metal ions, which is focus of Chapter 3.

Due to its local nature, DFT cannot account properly for dispersion interactions, which result from long-range correlation effects. These attractive dispersion (or *van der Waals*) interactions become crucial when considering adsorption of larger molecules or stacking of layered materials.[146] Nonetheless, in the calculations carried out in this work, they are expected to play only a minor role.

As described in the previous Section, DFT suffers from overdelocalising electrons, which causes an underestimation of the separation of energy bands (see Section 2.1.3) and, therefore, of the fundamental band gap of semiconductors. This issue is extremely important to this work and is further discussed in this Thesis (Chapter 3).

2.1.5 Computational databases

Theoretical modelling of the electronic structure and other key properties is crucial to the development of novel functional materials and catalytic systems. It is evident that openly sharing access to these results leads to faster advances of the scientific community. Computational databases, which allow for fast tracking of desired results, facilitate handling of the increasingly large volumes of data created in numerous research groups worldwide.[203] Further, such databases combined with machine learning tools pave the path for artificial intelligence technologies.[204] The freely-available repository *ioChem-BD*,[205,206] which was recently developed in our group, efficiently manages and stores large volumes of computational chemistry files from different software packages. All my results are openly available on this platform.[207–209]

2.2 Concepts of semiconductor-physics

In this Section the relevant basics of semiconductor physics, the framework of photoelectrochemical water-splitting, are given.

2.2.1 Semiconductors

Semiconductors and insulators are characterised by the presence of an electronic band gap E_g, a region of forbidden energies separating the highest occupied electronic levels, i.e. the valence band (**VB**), from the lowest unoccupied levels, i.e. the conduction band (**CB**) (see Figure 2.4).[†] Hence, in their ground state, all bands are either completely filled or completely empty, which distinguishes them from metals, where at least one band is partially filled.[138,166]

At thermally accessible energies, however, there is a non-zero probability that some electrons will be excited from the valence band into the conduction band, leaving a so-called *hole* in the valence band. The likelihood of excitation across the band gap depends on the size of the gap and is what discriminates a semiconductor from an insulator, which has a much larger band gap, typically larger than 4 eV.[166]
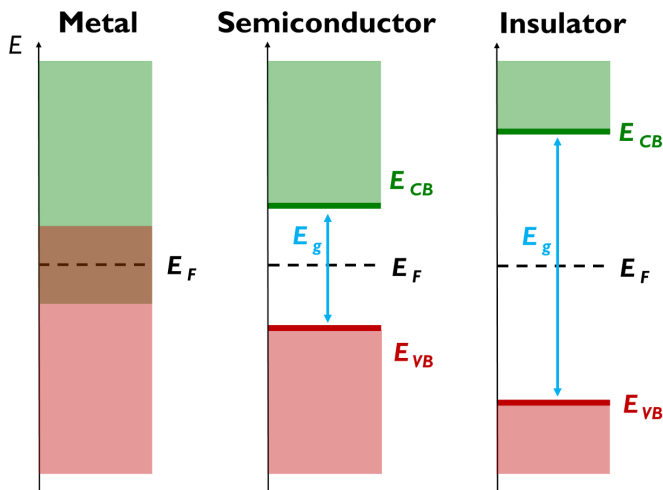
Figure 2.4: Simplified electronic band diagram of a metal, a semiconductor, and an insulator. The energies of the highest occupied electronic level, the valence band, and the lowest unoccupied electronic level, the conduction band, are labelled E_{VB} and E_{CB}, respectively. $E_g = E_{CB} - E_{VB}$ is the band gap and E_F is the Fermi level.

[†]It has to be mentioned that in materials, in which excited electron–hole interactions, i.e. exciton binding energies, become important, a distinction between fundamental and optical band gaps can be made. In semiconductors with a large dielectric constant, however, their difference is negligible.[166]

The underlying physics, used for describing electrons and holes in semiconductor electrodes, can be justified by a semi-classical model.

2.2.2 Semi-classical description of charges

Electron (and hole) motion can be described by the semi-classical model of electron dynamics, in which externally applied fields are treated classically, but the periodic field of the ions is not. In other words, an electron, which moves as a charged particle according to the classical equations of motion in presence of an electrical field, can also be regarded as a wave packet of free electron levels, whose spread is small compared to the considered dimensions.[166] This model allows the description of the absence of an electron, and thus a residual positive charge, as a point-like particle, a *hole*, which produces the same current as a moving electron but with an opposite sign.[166]

Thus, a semiconductor can either conduct electrons in the CB or holes in the VB, out of which the electrons had been excited. The conductivity increases with temperature, in contrast to a metal, whose conductivity decreases with temperature due to thermal lattice vibrations.

2.2.3 Fermi level

For a distribution of energy levels, Fermi-Dirac statistics describes the electron occupation probability $f(E)$ in thermodynamic equilibrium at temperature T:

$$f(E) = \int \frac{1}{1 + exp(\frac{E-E_F}{k_B T})} \tag{2.23}$$

where k_B is the Boltzmann constant and E_F is defining the Fermi energy. At $T = 0$ and $E = E_F$ the electron occupation probability is exactly one half.[20] It corresponds to the electrochemical potential of electrons $\overline{\mu_e}$, or to the negative electrochemical potential of holes $\overline{\mu_p}$, respectively:[210]

$$\overline{\mu_e} = E_F \quad \Longleftrightarrow \quad \overline{\mu_p} = -E_F \tag{2.24}$$

From a computational point of view, however, the Fermi energy of a semiconductor is ill-defined. In most plane wave codes it is obtained by integrating the density of states up to the Fermi level, such that it gives the total number of electrons in the system. In a metal, a system without gap, the Fermi level is simply the highest

occupied electronic state, whereas in a semiconductor its computed value can lie anywhere within the gap and therefore has no physical meaning.[199,200]

2.2.4 Doping

Semiconductors can be classified as being either *intrinsic* or *extrinsic*. An intrinsic (*i*-type) semiconductor is unmodified, i.e. *undoped*, and characterised by its Fermi level lying in the middle of the band gap:

$$E_F = \frac{1}{2}(E_{CB} - E_{VB}) \tag{2.25}$$

Electron donors introduce electrons into the CB (*n*-type doping) and acceptors introduce holes into the VB (*p*-type doping), as shown in Figure 2.5, which leads to a higher *extrinsic* conductivity. Also defects, such as vacant sites, may be considered as dopants, as they generally introduce an excess or lack of electrons.[166]
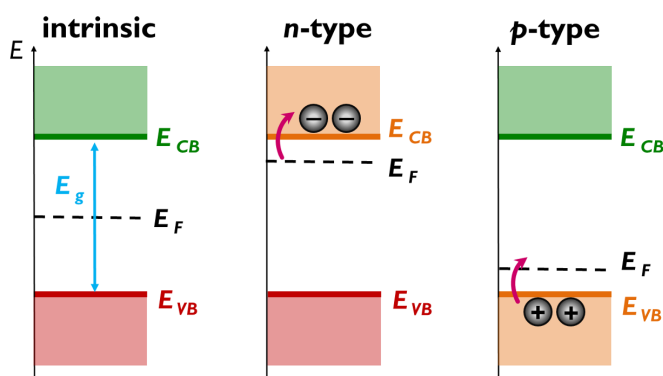
Figure 2.5: Schematic band diagram of an intrinsic and extrinsic semiconductors, both *n*-type and *p*-type doped, showing the position of the Fermi level E_F.

2.2.5 Band gap transitions

As mentioned above, semiconductors are defined by the presence of an energy gap between VB and CB. Yet the position and size of the gap are temperature-dependent and may vary up to 10% due to thermal lattice expansions and phonon vibrations.[166]

If the minimum of the CB and the maximum of the VB lie at the same *k*-point in reciprocal space, the band gap is considered to be *direct*. If this is not the case, and VB maxima and CB minima occur at different points in *k*-space, the band gap is *indirect*.[166] Therefore,

one distinguishes between *direct* and *indirect* semiconductors, as illustrated in Figure 2.6.

Direct semiconductor   **Indirect semiconductor**
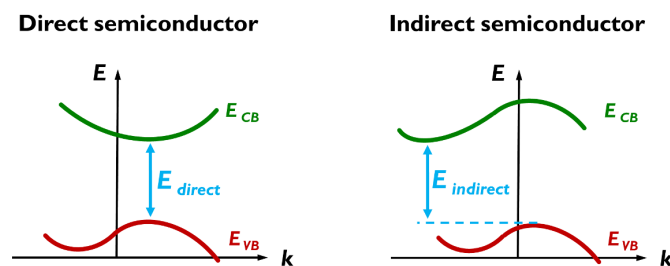
Figure 2.6: Simplified electronic band structure of a *direct* and an *indirect* semiconductor in reciprocal space (*k*-space). If the highest occupied electronic state (in the VB) is directly below the lowest unoccupied state (in the CB) the band gap is direct, if not, the band gap is indirect.

Band gap transitions take place under illumination, if the energy of an incoming photon is larger than the gap. In the case of an indirect semiconductor the photon must couple with a lattice vibration, a phonon, to compensate for the missing *crystal momentum* **k**, due to the principle of momentum conservation.[138,166] Because of involving a third entity, the phonon, indirect transitions are much less likely to occur, and hence show a weaker optical absorption. Therefore, for an application in a photoelectrochemical device, a direct semiconductor is generally favoured. In some cases though, as in the case of the studied $BiVO_4$, where direct and indirect band gap are close in energy, the optical properties can be dominated by the direct transition, even if the fundamental gap is indirect.[211,212] The band gap can be measured by optical absorption spectroscopy. Usually the *Tauc* fitting method is used to obtain the size and nature of the gap (see Appendix A).[213]

2.2.6   Recombination

Once a photon is absorbed and the electron is excited from the VB to the CB, it is subject to *recombination*, either with the hole it has left in the VB, or through a different process. It can be *radiative*, i.e. emitting a photon, or *non-radiative*.[20] Recombination is crucial to the function of a light-absorbing semiconductor and is extensively discussed in the following Chapters.

2.2.7   Quasi-Fermi levels and photovoltage

When irradiating the material with light, one is no longer in thermo-dynamic equilibrium and the definition of the Fermi level as electro-

chemical potential of holes and electrons (Equations 2.23 and 2.24) needs to be modified. As photo-excited electrons and holes relax much more rapidly (in less than picoseconds) with the lattice vibrations, than they recombine, they are in a *quasi*-equilibrium state. Their electrochemical potentials can be described by *quasi*-Fermi levels E_{Fn} and E_{Fp}:[210]

$$\overline{\mu_e} = E_{Fn} \quad \Longleftrightarrow \quad \overline{\mu_p} = -E_{Fp} \tag{2.26}$$

The difference of the *quasi*-Fermi levels is the free energy stored by the electron–hole pair $\overline{\mu_{eh}}$ (the sum of the chemical electron and hole potentials) and is thus the maximum energy that can be extracted from a device (see Figure 2.7). It sets an upper limit to the *photovoltage* V_{photo}, the real observed potential change when illuminating the material.[20]

In an *n*-type semiconductor, the number of electrons is assumed to remain constant upon irradiation as the number of excited electrons is much smaller (by a factor larger than 10^6) than the number of electrons introduced by *n*-type doping. Hence, the electronic Fermi level is not changed $E_F(dark) = E_{Fn}(light)$, and only the hole Fermi level moves, as illustrated in Figure 2.7.[20,214]
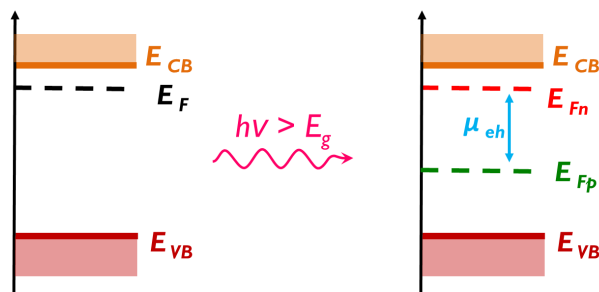
Figure 2.7: Splitting of Fermi levels in an *n*-type semiconductor under irradiation ($h\nu > E_g$). Only the Fermi level of the minority carriers (holes) is strongly affected, while that of the majority carriers (electrons) remains constant.

In the following discussion of *n*-type materials, the constant Fermi level of electrons E_F is assumed, unless otherwise specified.

2.2.8 Surface states

Another important point to consider when discussing reactions on solid surfaces is the presence of *surface states*, electronic states, which are generally located inside the energy gap E_g. Surface states arise from breaking the periodicity of the crystalline lattice. Cleaving a surface leaves under-coordinated atoms with dangling

bonds, which give rise to new electronic states. Some surfaces also undergo reconstruction to lower their energy (and thus form new states). Another origin of surface states at the semiconductor-electrolyte interface can be adsorbed species, forming bonds with the surface atoms.[20] Surface states play a major role in reactions taking place at the surface, nonetheless their catalytic impact and their nature are still under debate.[21,215–217]

2.3 Experimental methods

The main experiments, used in this work, are explained in this Section, along with the theoretical background needed to understand the performed measurements.

2.3.1 Photoelectrochemistry

For the purpose of photoelectrochemical water oxidation n-type semiconductors are used and are therefore the only semiconductor type considered herein. Yet, the same principles can be applied to p-type materials for photoelectrochemical reduction reactions.

Semiconductor–electrolyte interface

When a semiconductor is placed in contact with an electrolyte, it experiences an electrical potential close to the interface, which results in a shift of the Fermi level.[218] The redox level of the electrolyte remains constant, since it is rapidly balanced by the highly mobile ions in solution. Photoanode n-type materials have a Fermi level above the water oxidation potential, hence they transfer electrons to the solution in order to establish electronic equilibrium (see Figures 2.8a and b). This shifts their Fermi level down and causes electronic bands to *bend*. The variation in potential ϕ, the *band bending*, orthogonal to the interface (along x) can be described by the one-dimensional Poisson equation:[219]

$$\frac{d^2\phi}{dx^2} = -\frac{N_d}{\varepsilon_r \varepsilon_0}\left(1 - exp\frac{e\phi}{k_B T}\right)$$

(2.27)

where ε_0 and ε_r are the vacuum and relative electrical permittivity of the material, e the electronic charge, and N_d the density of electrons in the bulk, which is equal to the dopant donor density, since the bulk is electro-neutral. The downward band bending leads to an accumulation of holes and depletion of electrons close to the interface, as shown in Figure 2.8b. Therefore, the region into

which band bending extends is defined as the depletion layer or space–charge layer (**SCL**).[20,138] In analogy to the semiconductor–metal junction, the energy barrier due to the potential drop at the interface is also called *Schottky-barrier*.[137]

Photoelectrochemical water oxidation

Figure 2.8 shows the electronic processes occurring at the *n*-type semiconductor–electrolyte interface under illumination (without external bias).
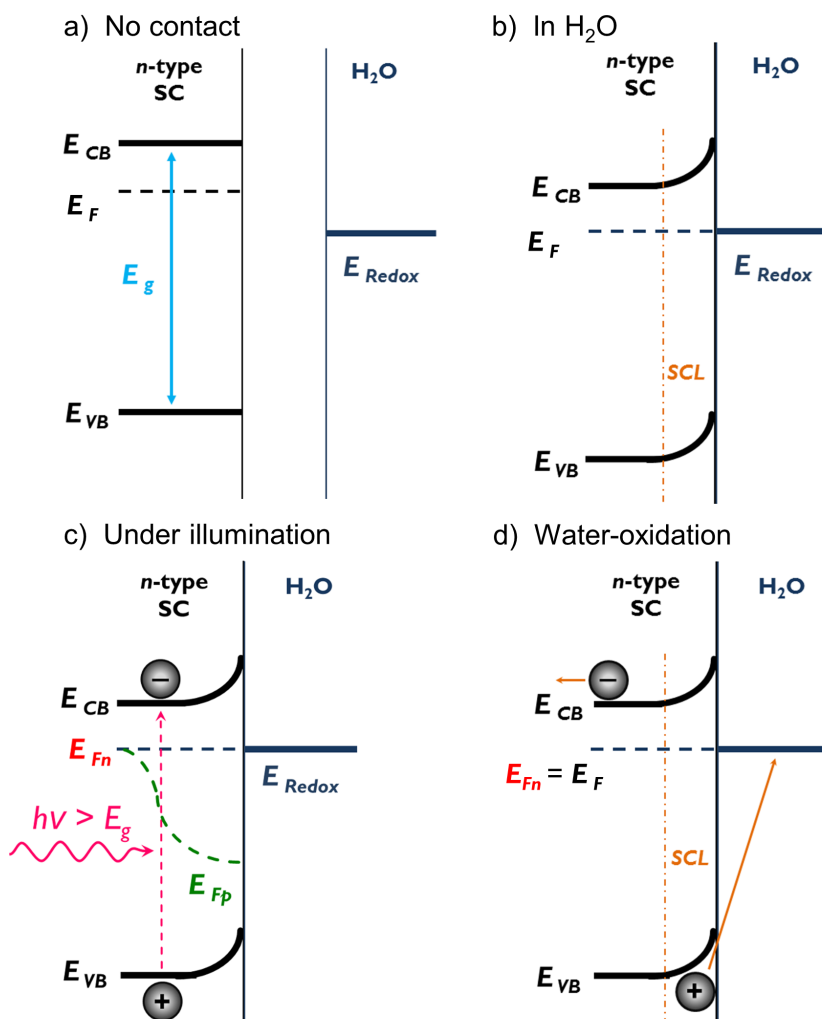
Figure 2.8: Schematic representation of the electronic processes occurring in a) an *n*-type semiconductor (in vacuum), when b) immersing it into an electrolyte and c) irradiating it with light ($E_{photon} > E_g$). d) Holes accumulate in the space–charge layer (SCL), where they can oxidise water, while electrons in the CB move away from the surface.

When a photon gets absorbed and excites an electron–hole pair, the excited electron in the CB experiences a driving force away from the surface due to the potential drop in the SCL (Equation 2.27), while the hole in the VB moves into the opposite direction (Figure 2.8 c). This leads to hole accumulation at the interface. In the absence of surface states, those VB holes at the interface are responsible for water oxidation (Figures 2.8c and d).

Photoelectrochemical measurements

As water-oxidation is a four-electron transfer from solvent water to the semiconductor, it leads to a positive current, which can be measured. The current due to light-excitation is therefore called *photocurrent*. In most photoelectrochemical (**PEC**) measurements, one measures the response of the photoanode (the *n*-type semiconductor to be studied) to an applied voltage. This is done in an electrochemical cell, consisting of the working electrode (WE), a reference electrode (RE), and a counter electrode (CE, usually a platinum wire or mesh). A schematic illustration of such a three-electrode set-up, as well as a picture, is shown in Figure 2.9.[18]
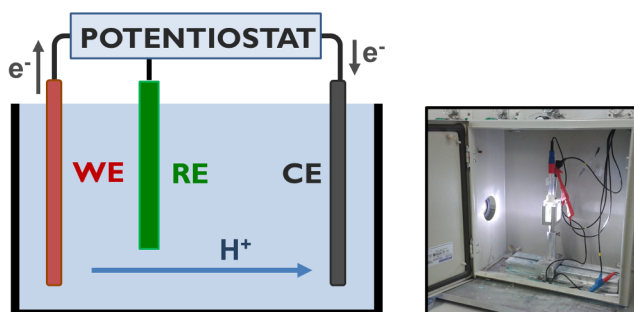
Figure 2.9: Illustration of a photoelectrochemical cell with working (WE), counter (CE), and reference (RE) electrodes. Under a positive potential electrons flow from the WE (anode) to the CE (cathode). The negative charge transport is counterbalanced by protons H^+ (or other cations) from the electrolyte solution. On the right: picture taken from a real PEC set-up.

It is only possible to measure potential differences, not absolute potentials. Hence a reference electrode (RE), like silver chloride (Ag/AgCl), is used to measure the potential difference between WE and RE, which is then usually converted versus SHE or the pH-independent Reversible Hydrogen Electrode (RHE).[220]

The electrode potential V_{red} (or E_{red}) at the working electrode (WE) is given by the Nernst equation (Equation 2.28), which de-

scribes its dependence on electrolyte concentration.[220]

$$V_{red} = V^0 + \frac{RT}{zF} ln \frac{[Ox]}{[Red]}$$ (2.28)

With $[Ox]$ and $[Red]$ being the concentrations of oxidised and reduced species, z the number of transferred electrons, and V^0 the standard redox potential.[†]

Applying an external voltage (V) changes the electrochemical potential, which is defined as the Fermi level (Equation 2.24), and with it the band bending. The variation of the steady-state (photo)current response with applied bias is illustrated in Figure 2.10.
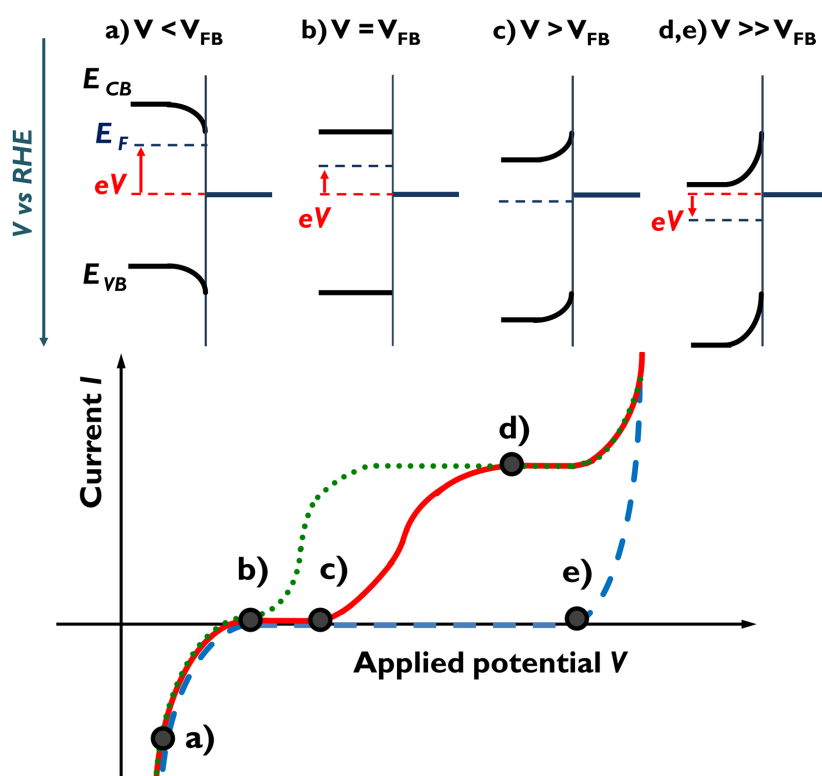
Figure 2.10: Current-to-voltage behaviour in steady-state conditions of an n-type semiconductor electrode in the dark (blue dashed line), under light (red solid line), and in ideal conditions, when no electron–hole recombination is present (green dotted line). a–e) represent the electronic bands at different applied potentials V at the corresponding points along the j–V curve. It is noted that the potential V and energy E are inversely related by $E = eV$, since the electronic charge is negative.

[†]If the electrolyte solution is non-ideal, i.e. the concentration is so high that ions interact with each other, the concentration is replaced by the activity a of the electrolyte species.
Ideal gas constant: $R = 8.31447$ Jmol^{-1}K^{-1}; Faraday constant: $F = 96485$ Cmol^{-1}

Five different scenarios are differentiated here, denoted as a–e in Figure 2.10, which are taking place when increasing the potential (from negative cathodic to positive anodic).

a) at large cathodic potentials ($V < V_{FB}$):
The applied negative bias V pushes the Fermi level so high that it leads to an inversion of the band bending. Under light, the photoholes in the VB experience a driving force away from the surface, while the electrons move to the surface and give a negative current. As the majority carrier concentration is independent of light irradiation, and only depends on the dopant density (N_d), the photocurrent (red and green) and dark current (blue dashed line) coincide.

b) at the flat band potential ($V = V_{FB}$):
The applied potential is such that it compensates the electrostatic potential from the electrolyte and there is no band bending (which is why it is termed *flat band* potential). Since there is no electrostatic driving force, neither from nor to the surface, there is no current.

Under *ideal* conditions (green dotted line), where no recombination takes place, the flat band potential would be equal to the *onset*, at which photocurrent starts to evolve. This is because at any potential higher than the flat band potential, bands bend slightly downward so that holes are driven to the surface where they could oxidise water. In *reality*, however, fast electron–hole recombination limits sufficient hole accumulation and transfer across the interface, causing an anodic shift of the onset potential (red solid line).

c) at the onset potential ($V > V_{FB}$):
At the *onset* of photocurrent, the potential is high enough to overcome the kinetic barrier of electron–hole recombination and water oxidation starts. This means the bands are sufficiently bent to prevent recombination of holes at the surface with electrons from the bulk to favour hole transfer.

d) largely above the flat band potential ($V \gg V_{FB}$):
The photocurrent reaches a plateau when recombination is no longer rate limiting and mass diffusion to the electrode becomes the bottleneck.

e) at the dark onset potential ($V \ggg V_{FB}$):
The potential is high enough so that even dark positive current (blue dashed line) occurs due to extracting holes from the substrate.

In the absence of an externally applied potential, the measured voltage is also referred to as the *open circuit voltage* or *potential (OCV/OCP)*.

As the measured current ($I = q/t$) is an area dependent variable, which defines the electrical charge q passing per time t, it is common to give a current density j rather than I. Usually the photocurrent density $j = I/A$, is given per geometric area A in cm^2. It can also be written as:

$$j_{photo} = j_{absorption}\, \eta_{CS}\, \eta_{CT} \qquad (2.29)$$

Where $j_{absorption}$ is the maximal attainable photocurrent, if all absorbed light was converted into current, and hence depends on the band gap and absorption coefficient, η_{CS} is the efficiency of charge-separation, which is the separation of the excited electron–hole pair and transport to the electrolyte interface, and η_{CT} is the efficiency of charge-transfer at the interface.[221,222] This relationship is important to extract the efficiences of charge-separation and transfer, in order to gain information about the mechanisms taking place in the material.

The main PEC measurements that were conducted in this work are illustrated in Figure 2.11:

- **LSV:** *Linear sweep voltammetry* - An external voltage is applied at a certain scan rate (in *V/s*) in one direction and the resulting current is measured as a function of applied bias and scanning speed. Either an oxidative scan (applying a more positive bias) or a reductive scan (applying a more negative bias) is carried out, oxidising or reducing the electrode (Figure 2.11 a). It is usually performed in order to measure the kinetics of an electrocatalytic reaction.

- **CV:** *Cyclic voltammetry* - In a CV experiment, the applied potential is cycled, i.e. the electrode is alternately reduced and oxidised, usually under static conditions. It therefore gives information about the oxidisability and reducibility of the electrode material, which can be related to the capacitance and the amount of redox active centres.

- **CA:** *Chronoamperometry* - In a CA experiment the potential is kept fix and the *steady-state* current at that potential is measured. This is important to determine the stability of the system and its charge-transfer kinetics.

66

- **IPCE:** *Incident photon-to-current conversion efficiency* - The IPCE describes how many of the incoming photons are converted into electrons, measured as electrical current j_{photo}.[221] The IPCE measurement involves the same three-electrode set-up as described above (Figure 2.9) but a monochromatic light source.
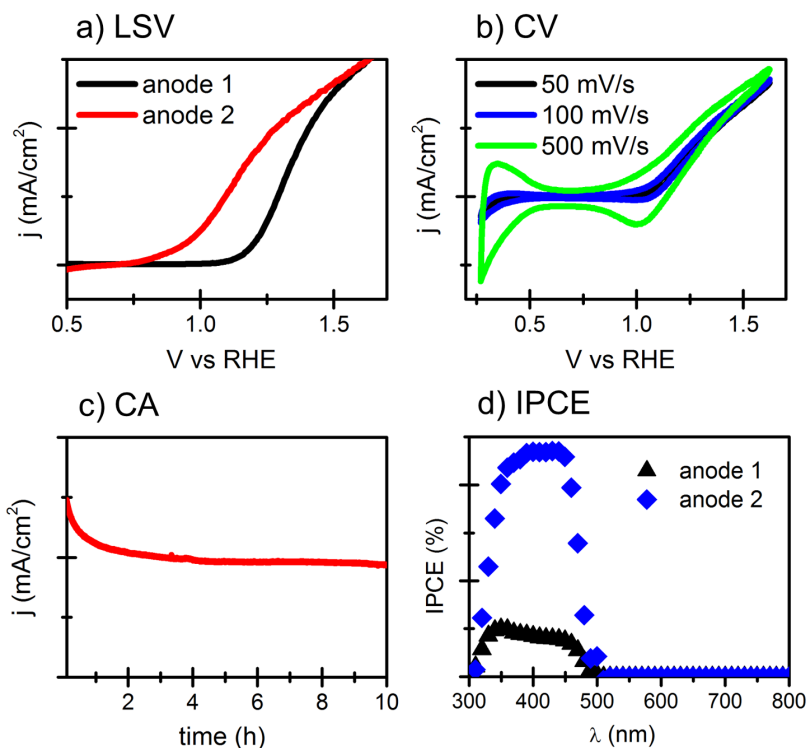
Figure 2.11: Current-to-voltage measurements: a) Linear sweep voltammetry (**LSV**) of two different photoanode systems, b) cyclic voltammetry **CV** of bare hematite at different scanning speeds, c) steady-state chronoamperometry **CA** at constant potential, d) incident-photon-to-current (**IPCE**) measurement of two different photoanode systems.

From the current-to-voltage characteristics alone a distinction between different Faradaic processes that could lead to an observed photocurrent cannot be made. In order to proof that the observed current is due to water oxidation only, a measurement of the evolved oxygen by methods, such as gas chromatography or fluorescence probe sensing, can be done. The Faradaic efficiency

$$FE(\%) = \frac{n_{evolved}(O_2)}{n_{theoretical}(O_2)} \tag{2.30}$$

quantifies how much of the measured current stems from oxygen production.

For a deeper understanding of the underlying electronic processes, different spectroscopic methods were applied in this Thesis, impedance and time-resolved absorption spectroscopy, which are outlined in the following two Sections 2.3.2 and 2.3.3.

2.3.2 Electrochemical impedance spectroscopy

Electrochemical Impedance Spectroscopy (**EIS**) provides a technique for measuring the resistances and capacitances of a PEC device, from which mechanistic information can be extracted. This is done by decoupling the system into an electrical circuit with a set of resistive and capacitive elements, responsible for internal charge-transfer and storage, respectively.[20,21]
It is a frequency-based characterisation method, which measures the response of the electrical system to a small perturbation, in that case to a varying voltage. Other perturbation methods like Intensity Modulated Photocurrent Spectroscopy (IMPS) that are not discussed in this work go along the same line and similar theoretical considerations can be applied.[223,224]

Theoretical description of impedance

The electrical impedance $Z(\omega)$ is a complex transfer function relating potential and current. It can be thought of as the resistance of an *ac* electric current $I(\omega)$ to the applied varying potential $V(\omega)$:

$$Z(\omega) = \frac{V(\omega)}{I(\omega)} = \frac{V^0 + sin(\omega t)}{I^0 + sin(\omega t + \varphi)} \qquad (2.31)$$

With ω being the perturbation frequency, with which the voltage is varied, and I^0 and V^0 being the corresponding *dc* current and voltage, when the voltage is kept constant. The phase φ describes how fast the current responds to the applied voltage.[20]

It is common to represent frequency response data, such as impedance, in so-called *Nyquist* or *Bode* plots as shown in Figure 2.12. The Nyquist plot shows the (negative) imaginary impedance $Z''(\Omega)$ versus its real-valued counterpart $Z'(\Omega)$. The Bode plot shows phase (or gain) response of the system in dependence of the applied frequency ω.[225,226]
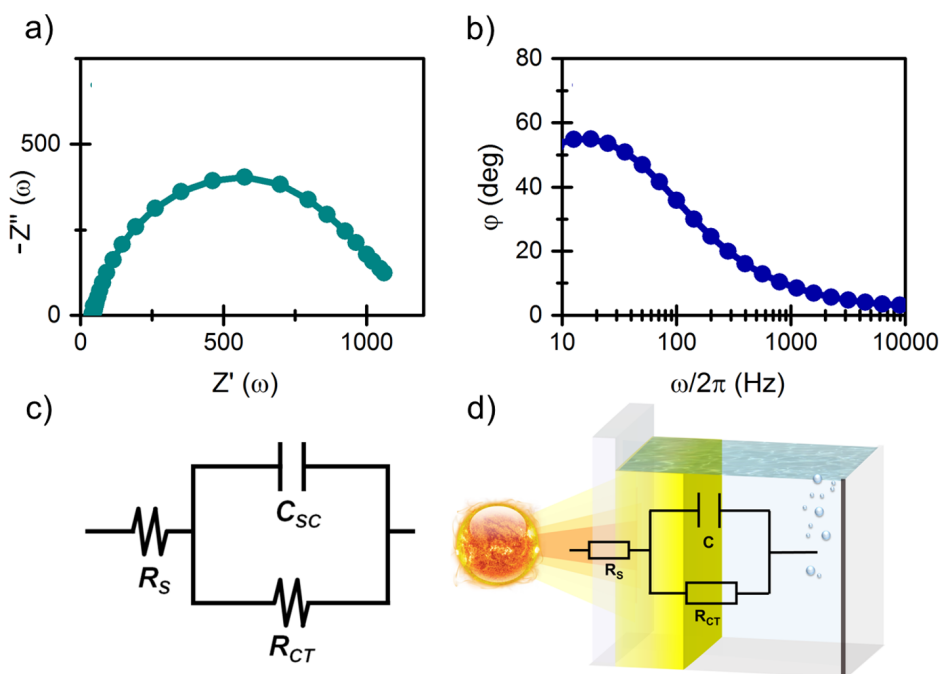
Figure 2.12: a) Nyquist and b) Bode representation of the impedance. c) Equivalent circuit (Randles circuit) obtained from fitting this impedance data and d) correspondence of the equivalent circuit elements to a photoanode system.

Equivalent circuits

The obtained data can be fitted to so-called *equivalent circuits* (**EC**), which represent different classical electrical circuit elements, such as capacitors and resistors (see Figure 2.12 c).[225] This implies a mathematically complex deconvolution of data, which is not described here.[226,227] In practice it can be done by a fitting software, which often is a standard feature coming with the used potentiostat.[226,228] While the resistances are related to the real, frequency independent terms, the capacitances are related to the complex terms of the impedance.

The simplest EC is the Randles circuit represented in Figure 2.12c, which represents only one capacitive and resistive element in parallel, along with a resistance in series.[229] It corresponds to one arc in the Nyquist plot (Fig. 2.12a). The classical electrical circuit can be related to a PEC system as shown in Figure 2.12 d.

Nonetheless, this is a large simplification for a real device, which contains many capacitive and resistive elements, which are explained below.

Resistances

The resistances are associated to different processes of charge transport and transfer. In a PEC device, transport processes generally occur within the electrode materials, in the electrolyte, at the interfaces, as well as at the electrical contacts. Hence one can decouple the system into various resistive elements, corresponding to the different processes.[20] Important to this Thesis are the following resistances:

- *Total resistance* - The total or *dc* resistance is the unperturbed resistance, when no frequency modulation is applied and, thus, corresponds to the real-valued impedance at $\omega = 0$.

$$R_{tot} = Z(0) = \left(\frac{dI^0}{dV^0}\right)^{-1} \tag{2.32}$$

- *Series resistance* - It includes transport through the electrical contact and the electrolyte and is generally constant when using the same experimental set-up.

- *Charge-transfer resistance* - Different interfacial charge-transfer steps, which lead to an electrochemical reaction are defined by the charge-transfer resistance R_{CT}. It can provide information about the kinetics of charge-transfer and therefore water oxidation.

- *Trapping resistance* - In the presence of defects, i.e. trap states, and/or surface states, charges can be trapped into those states, which generally lie inside the band gap. The kinetics of trapping, the population and depopulation of those intragap states, are described by the trapping resistance R_{trap}.

Capacitances

One major strength of EIS as a characterisation tool is that it allows to measure and extract different types of capacitances, which arise from either electric field or carrier density variations.[230] They contain important information about the charge storage properties of the PEC device and are distinguished due to their physical origin:

- *Electrical double-layer capacitance* - The double-layer or Helmholtz capacitance due to the electrochemical double layer at the semiconductor surface is defined by:

$$C_H = \frac{A\varepsilon_r\varepsilon_0}{d} \tag{2.33}$$

Where A is the surface area and d is the thickness of the molecular solvent layer and is on the order of 0.1 nm.[231]
This only holds if the ion concentration in the electrolyte is high enough, so that a plate-like capacitor can be assumed and diffusion can be neglected. Both double-layer and space–charge layer capacitances are dielectric capacitances deriving from the internal electric field produced by charge separation.[230]

• *Space–charge capacitance* - Due to the potential drop and consequent charge accumulation at the semiconductor surface, a capacitance is created in the space–charge layer.[214] It is defined by the *Mott–Schottky* equation[232] (derived from the Poisson equation; Equation 2.27) and is usually given in terms of its inverse square (C_{SC}^{-2}), which is linearly dependent on the applied potential V:

$$\frac{1}{C_{SC}^2} = \frac{2}{e_0 A^2 N_d \varepsilon_r \varepsilon_0}\left(V - V_{FB} - \frac{k_B T}{e_0}\right) \qquad (2.34)$$

It thus basically measures the extent of band bending. From the slope of the Mott–Schottky plot, one can directly obtain the dopant density N_d, and from the intercept with the x-axis the flat band potential V_{FB}.[216]
The value of C_{SC} is usually much lower than C_H (of the order of $10^{-4} - 10^{-5}$ F/cm^2 and thus, if the capacitors are connected in series, C_H can be neglected due to their inverse contributions:

$$\frac{1}{C_{series}} = \frac{1}{C_H} + \frac{1}{C_{SC}} \qquad (2.35)$$

• *Chemical capacitance* - A chemical capacitance arises from storing energy in the form of changing the chemical potential μ_i of the ith species in the material. This species i can be an atom in the structure, which can be reduced or oxidised, or a defect, a *trap* or a *surface state*. The chemical capacitance is thus related to the variation of the Density of States (DOS) (as defined in Equation 2.22 and Figure 2.2) by

$$C_\mu^{(i)} = e^2 \, DOS(\varepsilon_i) = e^2 \, \frac{dN_i}{d\mu_i} \qquad (2.36)$$

where N_i is the number of electronic states of the ith species.

It is therefore related to the redox strength and potential of i; this means that when the variation of electronic states N_i

with applied potential is high, a significant capacitance is observed.[233] It is a local quantity, localised on the ith species. If it is extractable from the EIS experiment, it provides a direct measure of the DOS of i in a certain energy range.

If this chemical capacitance is related to defects in the structure, such as surface states or trap states, it is called *surface state capacitance*, or *trap capacitance*, respectively.[234]

Also other elements, like inductors or Warburg elements,[226] can be obtained by impedance techniques, but are not considered in this work. There are several points to consider when performing an impedance experiment, which are outlined below.

Experimental considerations

- Electrochemical impedance spectroscopy relies on first order perturbation theory. Hence, the amplitude of the frequency perturbation must be low enough for the linear approximation to be valid, but high enough to have a significant system response. Usually a perturbation of 10–20 mV is a reasonable estimate for PEC measurements.

- In order to ensure that the system is relaxed when a perturbation is applied, frequencies ω are scanned from high to low values (around 10^6 to 10^{-2} Hz).

- The range of applied voltages and frequencies to be accessed, as well as the measurement time, is limited by the stability of the PEC system. This is particularly important for metal oxide semiconductors, which are less stable under voltage and irradiation.

- Moreover, diffusion limitations may play a role and need to be excluded from the analysis. Electron diffusion can be seen as a straight line at high frequencies in the Nyquist plot, whereas mass diffusion in the electrolyte solution is often predominant at very low frequencies.

- The Mott–Schottky equation (Equation 2.34), which is often used in the analysis of semiconductor devices, is only valid under the ideal conditions used for its derivation. High dopant concentrations, defects, nanostructuring, or other frequently encountered features of real materials are not described by Equation 2.34 and, thus, obtained values (V_{FB}, N_d) should be carefully checked.

2.3.3   Absorption spectroscopy

Optical spectroscopy allows for a direct measurement of photogenerated charge carriers by probing their respective spectroscopic features and is therefore complimentary to the photoelectrochemical techniques. Moreover, its time evolution can be monitored, giving rise to information about the dynamical processes in the systems such as rates of recombination, charge-transfer, and catalysis.

Spectroelectrochemistry

Spectroelectrochemistry (**SEC**), that is spectroscopy under electrochemical operation, measures the change in absorption when applying a voltage and performing electrocatalysis.[235,236] This in turn allows for the determination of the absorption spectra of oxidised and reduced states, as well as possible reaction intermediates, provided that their respective absorption peaks can be discerned. The experimental set-up is relatively simple; an electrochemical cell (Figure 2.9) is inserted in a common UV-Vis spectrometer, hence enabling the simultaneous measurement of absorption spectra and j–V characteristics. In general, SEC can also be used for obtaining other spectroscopic data, such as vibrational frequencies, light scattering and emission, circular dichroism, etc., when coupling the electrochemical cell to the respective spectrometer, for example to an infrared or Raman spectrometer to monitor vibrational modes. In this work, however, only electronic absorptions are considered.

Figure 2.13 shows two examples of data that can be obtained from SEC.
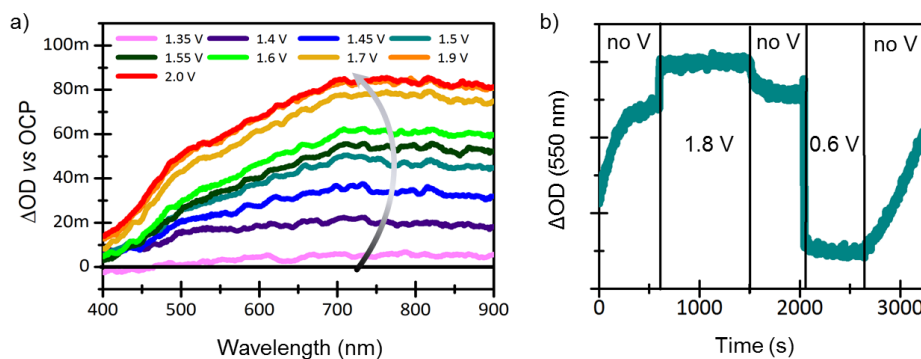
Figure 2.13: a) Absorption spectrum from 400 to 900 nm at increasing potentials (grey arrow) between 1.35 and 2.0 V_{RHE} and b) time-evolution of the 550 nm feature while consecutively applying no potential (open-circuit voltage), 1.8 V_{RHE}, and 0.6 V_{RHE}.

Typically in SEC, steady-state absorption spectra are recorded at different applied potentials, as shown in Figure 2.13a. An absorption increase in the longer wavelength region may be related to oxidising the system (which is discussed in Chapter 5). Figure 2.13b shows another, less common way, in which SEC may be used. By monitoring the monochromatic absorption over time and changing the potential, a time-dependent evolution of the species, to which this absorption belongs, is given.

The measured absorption is generally presented as difference in optical density ΔOD subtracting either the absorption measured at the open-circuit voltage (OCV) or at the water-oxidation onset, i.e. ΔOD vs OCV or ΔOD vs onset, respectively.

Time-resolved spectroscopy

Time-resolved spectroscopy involves transient absorption spectroscopy (**TAS**) and photo-induced absorption spectroscopy (**PIAS**) with an experimental set-up as presented in Figure 2.14.
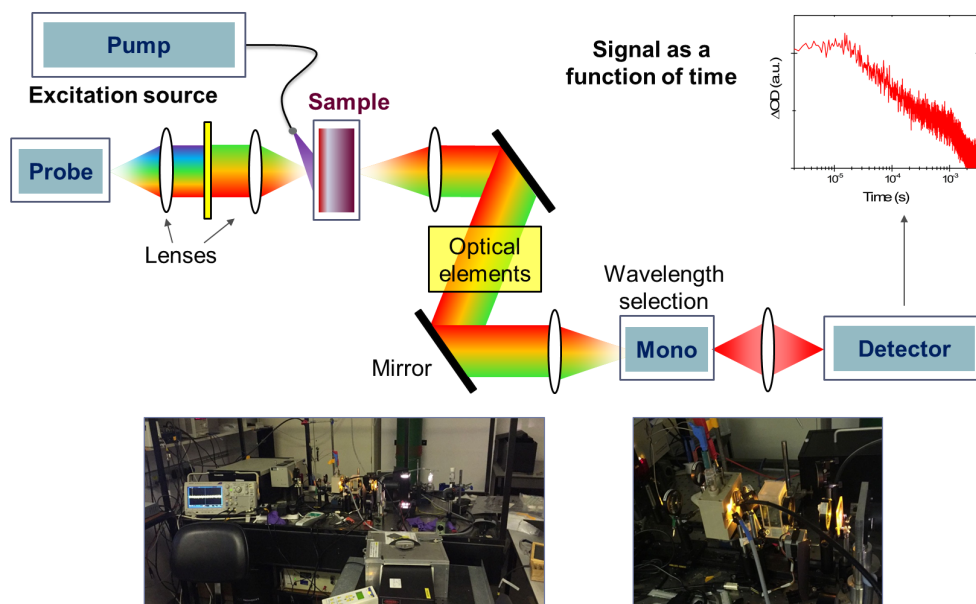
Figure 2.14: Schematic and real set-up of a pump–probe spectroscopy experiment: An excitation source (flash laser (TAS) or LED (PIAS)) excites the sample. Then the probe irradiation, which measures the absorption of the excited state, gets monochromatised and detected as a function of time. On the bottom left, a photographs of the experimental laser set-up is shown, and on the right the sample in an electrochemical cell and irradiated by both pump and probe.

Both TAS and PIAS are pump–probe techniques to characterise photo-induced charge carriers. In a TAS experiment, the excitation source is a short laser pulse, whereas in PIAS, a continuous light LED is used, similar as in the previously described photoelectrochemical measurements, in order to monitor absorption under water oxidation conditions. In the pump excitation the sample gets electronically excited, and this excited state is subsequently probed with a monochromatic beam, detecting the absorption as a function of time. Hence, in contrast to UV-Vis or SEC, which are *ground state* spectroscopic techniques, TAS and PIAS are *excited state* techniques. Generally the absorption of the excited state is given as differential absorption ΔOD with respect to the ground state.

Charge carrier dynamics

Depending on the time-resolution of the experiment, different electronic processes can be monitored. Figure 2.15 shows the relevant electronic processes in a semiconductor photoanode under operation and their typical time scales (neglecting relaxation and charge trapping).[30]
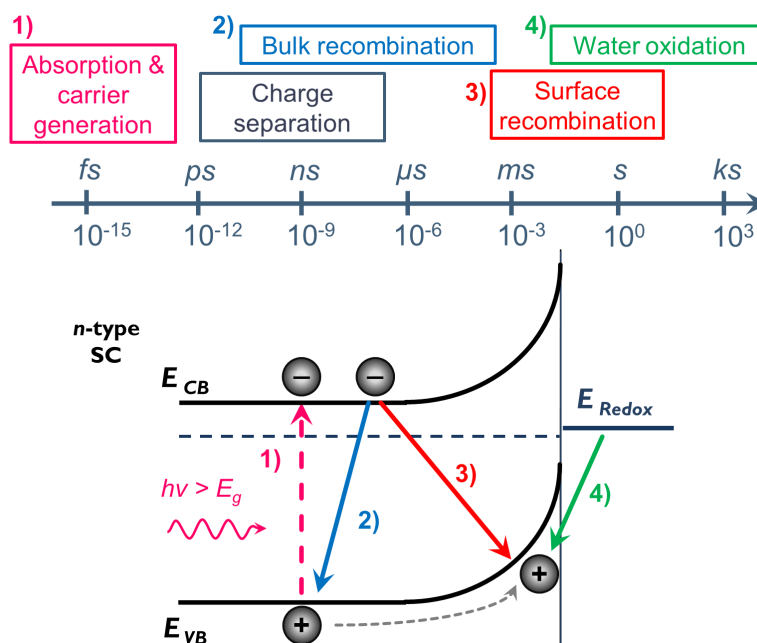
Figure 2.15: Timeline (in seconds) and energy scheme of the occurrence of electronic processes in a typical metal oxide semiconductor after light absorption. Surface recombination is highly dependent on the applied voltage, which determines the degree of band bending. Surface catalysis, i.e. water oxidation, is dependent on the catalytic activity of the system.

Irradiation with supra-band gap energy generates an excited electron–hole pair at fs timescale, which rapidly separates[†] (and relaxes), forming a hole in the VB and an electron in the CB (in the absence of trap states). The hole is then subject to either bulk recombination, or it may travel to the surface. From there it can catalyse water oxidation (on a time scale on the order of milliseconds to seconds, or even longer times for less efficient catalysts) or recombine with electrons in the bulk. The latter, recombination of holes accumulated in the space–charge layer with bulk electrons, is termed *surface*[87,237] or *back*[122,217] (electron–hole) recombination and is strongly dependent on the extend of band bending and applied bias. At sufficiently high bias, surface recombination slows down enough, so that water oxidation becomes a competing process.

Moreover, the decay dynamics are dependent on the excitation intensity. For very high irradiation intensities, ultrafast recombination in the sub-nanosecond time scale, immediately after charge separation, is enhanced due to the high densities of excited electron–hole pairs.[120,238,239] At lower excitation density and under the effect of an applied bias, however, ultrafast recombination gets reduced and bulk recombination on the microsecond to millisecond time scale becomes significant. This is due to increased charge separation, and multiple trapping and detrapping processes, which appear to be a common phenomena in defect-rich metal oxide materials.[120,121,240,241]

The relevant processes this study focuses on, lie in the range of microseconds to seconds. With TAS sub-second relaxation events were monitored, while PIAS was used to study charge carrier dynamics on a time scale of several seconds.

Transient absorption spectroscopy

As the name implies, TAS measures absorption *transients*, i.e. the immediate and fast decaying signal response directly after the excitation pulse. The excitation source is a pulsed flash laser, which is why TAS is sometimes also called flash spectroscopy.

Depending on the probe resolution, processes from attoseconds up to seconds can be detected.[242] In the present case, *slow* TAS was employed, operating at microseconds to seconds, at times where water oxidation may becomes important. At this time scale, the usual processes that take place are trap-mediated bulk recombination, surface recombination and water oxidation. These

---

[†]Exciton formation can be disregarded in the case of a semiconductor with high dielectric constant and relatively large band gap.

processes correspond to the different decay pathways of photo-generated holes, and therefore can be obtained by monitoring the spectral feature of holes created after the excitation pulse.

Figure 2.16 shows such a measured TAS decay at various wavelengths, from which the corresponding TAS spectrum can be generated. From the TAS spectrum at certain times, knowledge about the spectral features of different excited species can be obtained.
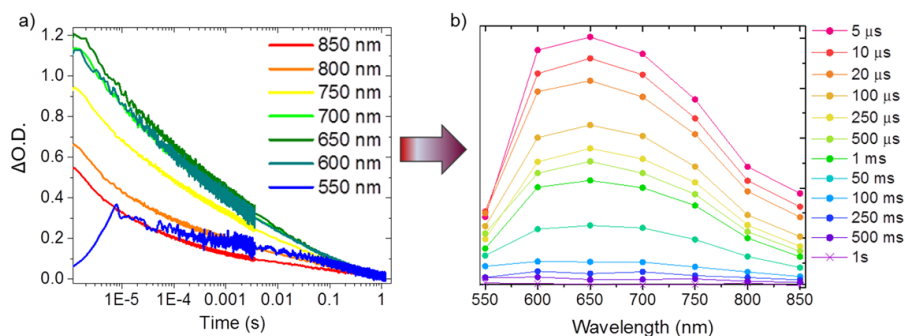
Figure 2.16: Transient absorption signals. a) TAS signal decay at measured at different probe wavelengths. b) TAS spectrum extracted from the TAS decays at different times after the excitation pulse. (Reproduced with permission from B. Moss.)

It was found that in many metal oxides the hole signal can be described by a biphasic decay.[120,122] †

$$\Delta OD = \underbrace{A_{fast}t^{-a}}_{bulk\ rec.} + \underbrace{A_{slow}\,e^{(-\frac{t}{\tau})}}_{surface\ rec.} \tag{2.37}$$

Where A_{fast}, A_{slow}, a, and τ are amplitude and time constants, obtained from signal fitting. The first term corresponds to bulk electron–hole recombination at short times after the excitation (μs–ms). The kinetics of this trap-mediated bulk recombination, can be described by a continuous-time random walk model, leading to a power-law.[122,240,241] The second term, which dominates at longer times, results from both surface recombination and water oxidation, which are in competition with each other. A single exponential term approximates this unimolecular hole decay.[122,241]

---

†Under the assumption that there is enough band bending so that long-lived holes accumulate at the surface, i.e. for a sufficiently high applied bias.

Photo-induced absorption spectroscopy

The PIAS experiment is similar to the TAS experiment (Figure 2.14), but utilises a continuous LED light source to excite the sample, instead of a fast laser flash. Usually the sample is irradiated for several seconds (4–10 s in the present case), in order to emulate *in operando* photoelectrochemical water oxidation conditions. With a time resolution on the order of 0.1 ms, PIAS is able to capture both surface recombination and water oxidation.

Combining PIAS with simultaneous photocurrent measurements allows for correlating the amount of photogenerated holes and their ability to oxidise water. This principle is shown in Figure 2.17.
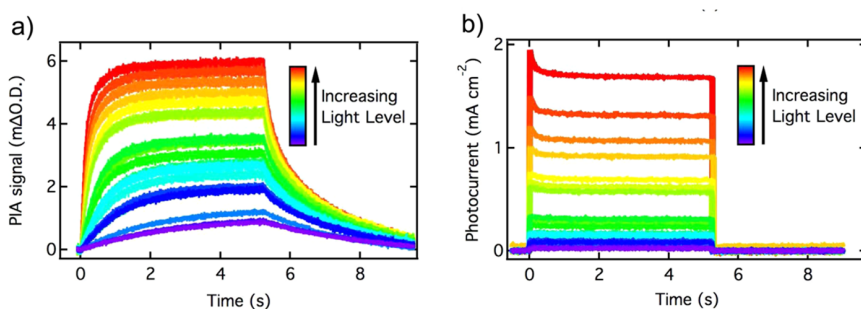
Figure 2.17: a) Photo-induced absorption (monochromatic) at different excitation intensities, switching light on (at 0 s) and off (at 5 s). b) Corresponding photocurrent density, showing that the detected absorption can be related to generation of photocurrent. Adapted from Ref. [243]

If the signal (ΔOD), as shown in Figure 2.17a, corresponds to the signal of photogenerated holes, a linear relation can be established between ΔOD and hole density $[h^+]$, which in turn can be extracted by integrating the photocurrent transients (assuming 100% Faradaic efficiency).

From this knowledge, the rate of photo-induced water oxidation can be determined, as described in Ref. [243]. At high applied bias, recombination is suppressed and all the holes that flow to the surface are assumed to react with H_2O to form O_2. Under steady-state conditions (at 5 s in Figure 2.17), the flux of holes $[h^+]$ towards the surface is equal to the photocurrent.

$$j_{photo} = k_{WO} \cdot [h^+]^\beta \tag{2.38}$$

Where k_{WO} and β are the rate constant and rate order of the reaction, which can be obtained by a logarithmic fit.[243]

Another way of extracting the kinetics of water oxidation is from the decay of the photohole signal, when the light is switched off (after 5 s, in Figure 2.17a). At high applied bias and in the absence of light, the holes accumulated at the surface have no other way to go as to the electrolyte and oxidise water. Therefore their flux can be described as:

$$\frac{d[h^+]}{dt} = -k_{WO} \cdot [h^+]^\beta \tag{2.39}$$

In conclusion, PIAS allows for the extraction of hole dynamics at longer time scales, under steady-state water oxidation conditions, whereas TAS monitors hole dynamics at fast times. In Equations 2.37, 2.38, and 2.39, only charge-transfer from the semiconductor to the electrolyte, i.e. water oxidation, was assumed. In case of a catalyst (or overlayer) deposited on the surface of the semiconductor, charge-transfer to the electrolyte competes with charge-transfer to the catalyst and their relative efficiencies are key to the function of such a semiconductor–catalyst interface.

2.4   Summary of applied methods

As a summary, Table 2.1 lists the main techniques used in this work and points out their respective advantages and applicability. For computational models, the cost scales with the method and the system size; therefore often smaller model structures need to be chosen to represent the system. Such a choice often requires deep chemical/physical knowledge of the material and has to be kept in mind when analysing data. If the employed method is adequate for the system, electronic and geometric structures (in the ground state) can be predicted with high accuracy.

Most photoelectrochemical techniques (apart from EIS) are relatively easy to conduct, and yet give a large amount of information about the system. More detailed kinetic information is obtained with time-resolved spectroscopic techniques, directly probing the dynamics of excited carriers. Such techniques, in particular TAS, require a comparatively expensive laser set-up and handling of the equipment needs specific skills.

Table 2.1: Summary and applicability of the main methods employed in this Thesis.

Approach	Applied techniques	Type of information	Obtained data	Assumed models	Requirements
Density Functional Theory	• Electronic structure calculations – various functionals	• *Thermo–dynamic* – ground state → at zero K	• Geometric parameters • Electronic structure (energies, orbitals, magnetisation)	• Ideal stoichiometry • Perfect crystallinity (no defects)	• Large computer cluster • *generally:* accuracy scales with cost
Photo-electro-chemistry	• Cyclic voltammetry • Chrono-amperometry • IPCE • Impedance spectroscopy	• *Thermo-dynamic & kinetic* – Perturbation response	• Performance • Stability • Charge transport (*resistance*) • Charge storage (*capacitance*)	• Extracted current (back of electrode) = transferred charges • Band bending (flat surfaces)	• Electrochemical cell • Potentiostat • Calibrated light source - *relatively simple set-up and analysis*
Time-resolved spectroscopy	• Transient absorption spectroscopy • Photo-induced absorption spectroscopy	• *Kinetic* – excited state	• Absorption spectra of excited states • Dynamics of charge carriers at short times and under operation	• Spectroscopic features = photogenerated charges • No spectral overlap • Band bending	• Pump-probe laser • Photoelectro-chemical set-up – *expensive set-up* – *complex analysis*

Chapter 3

Electronic structure of catalytic systems

This Chapter focuses on the theoretical aspect of the materials employed forin photoelectrochemical water splitting in this work. These are Prussian blue analogues as water oxidation catalysts and the two photoanode materials, hematite (α-Fe$_2$O$_3$) and bismuth vanadate (*ms*-BiVO$_4$). For the case of Prussian blue, an extended evaluation of various density functionals, and their impact on the geometric and electronic structure, is carried out. It has been published in *Paper I*, along with a complete database of Prussian blue related compounds, its redox forms, and cation intercalation derivatives.

Moreover, the electronic structure of the electrocatalytic cobalt iron analogue of Prussian blue (*CoFe-PB*) is assessed and its unique charge-transfer properties are explained. In the end of this Chapter the light-harvesting metal oxide semiconductors α-Fe$_2$O$_3$ and *ms*-BiVO$_4$ are discussed. Most of the computational results on CoFe-PB, α-Fe$_2$O$_3$, and *ms*-BiVO$_4$ are published in *Papers II* and *III*. All structures can be found on the ioChem-BD database.[207–209]

3.1 Prussian blue-type materials

The versatile class of materials named Prussian blue (**PB**) analogues acquires its name from the parent compound *Prussian blue*, iron-hexacyanoferrate (Fe$_4$[Fe(CN)$_6$]$_3 \cdot n$H$_2$O). These complex compounds are characterised by two octahedrally coordinated transition metal centres, which are linked by cyanide (CN) bridges, binding from both C- and N-site. Having two transition metal centres in different electronic environments (C- or N-coordinated) allows for a variety of mixed oxidation and spin states.[104,105] This

in turn gives rise to many different applications, such as solid-state batteries,[244,245] hydrogen storage,[246] electrochromic devices,[247] magnetic and electric switches,[248–250] room temperature magnets,[251–253] multienzyme mimics,[254] analytical sensors,[105,108] radio waste detection,[255] etc., and also water-oxidation catalysis, which is the focus of this research.[103,109–113]

In the following Section, the electronic structure of Prussian blue and its theoretical simulations are described.

3.1.1 Prussian blue: A mixed-valence compound

The original Prussian blue, also called *Berlin blue*, *Paris blue*, or *Milori blue*, counts as the oldest synthetic compound in the world. Serendipitously discovered in 1706 by the paint maker Diesbach and alchemist Dippel, the dark blue pigment became fashionable in the artist scene and later also as commercial dye, even up to now. One reason for its popularity is that it can be easily prepared by mixing aqueous solutions of hexacyanoferrate, or -ferrite, $[Fe(CN)_6]^{4-/3-}$ and a ferric (Fe^{3+}) or ferrous (Fe^{2+}) salt under mild conditions, i.e. at room temperature and ambient pressure. Moreover, very small nanoparticles of PB, as shown in Figure 3.1a, can be obtained, which makes it widely applicable.[256,257]

As-prepared PB (Figure 3.1b) adopts a non-stoichiometric crystal structure with formula $Fe_4[Fe(CN)_6]_3 \cdot nH_2O$ (n=14–16) and lattice parameters between 10.13 and 10.18 Å. This crystal structure was first proposed by Keggin and Miles[258] and later experimentally evidenced by X-Ray[259,260] and neutron[261] diffraction studies.

Figure 3.1c shows the theoretical regular crystal structure ($KFe[Fe(CN)_6]$) in crystal group $F\overline{4}3m$. In the face-centred cubic (*fcc*) cell, the N-coordinated Fe atoms occupy the corners and face centres, whereas the C-coordinated irons are placed in the middle of the edges (or *vice-versa*).[260,261] Alkali-metal cations are introduced for charge compensation and occupy half of the tetrahedral holes, spanned by either Fe(III)–N or Fe(II)–C. In this case potassium is used, but the effect of other counter cations will be discussed later in this Chapter. Due to "dissolving" K^+ in the PB lattice, $KFe[Fe(CN)_6]$ is often called soluble PB, while $Fe_4[Fe(CN)_6]_3 \cdot nH_2O$ is referred to as insoluble PB.[257,262] These non-systematic labels have, however, nothing in common with the solubility of the compound; both $KFe[Fe(CN)_6]$ and $Fe_4[Fe(CN)_6]_3 \cdot nH_2O$ are highly stable and insoluble in most common solvents.[257]

The iron atoms are octahedrally coordinated by cyanide bridges, which splits their electronic *d*-states into degenerate t_{2g} and e_g levels (Figure 3.1d). Due to the different field strengths of the C-

and N-binding cyanide ligand, the iron atoms experience a different electronic environment and, thus, have a different electronic configuration. They can also be classified as class-II mixed-valence materials.[263] In the ground state, the carbon coordinated Fe adopts a formal oxidation state of +2 (ferrous Fe(II)), while the nitrogen coordinated Fe is in a formal oxidation state of +3 (ferric Fe(III)); therefore, they are denoted as Fe(II)–C and Fe(III)–N.[264]
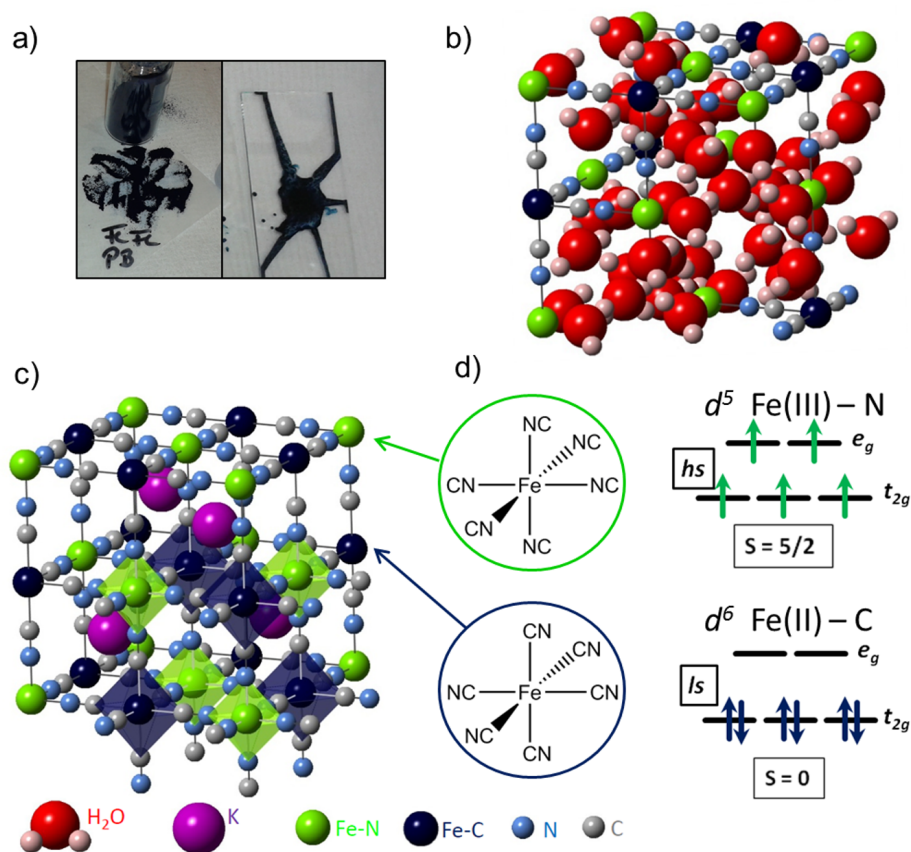
Figure 3.1: a) As-synthesised Prussian blue (in powder form and spin-coated on a glass-plate). b) Crystal structure (from neutron diffraction data)[261] of non-stoichiometric PB ($Fe_4[Fe(CN)_6]_3 \cdot nH_2O$ (n=14–16)). c) Theoretical model of PB ($KFe[Fe(CN)_6]$ with potassium as counter cation) with space group $F\bar{4}3m$. d) Coordination spheres of octahedrally coordinated Fe(II) and Fe(III).

It is noted here that the orbital notations t_{2g} and e_g from molecular point group theory are used, describing the local octahedral symmetry of the metal cyano-complexes. However, a different symmetry may be superimposed by the crystalline lattice and the perfect octahedral symmetry may be broken, leading to a partial loss

of degeneracy. In most cases though, unless otherwise stated, the t_{2g} and e_g description is appropriate and can be used for explaining several effects related to ligand-field splitting.

When binding from its C-site, CN is a strong field ligand and Fe(II)–C adopts a diamagnetic low-spin (ls) configuration, whereas N-binding NC is a weaker ligand of medium strength. Fe(III)–N is therefore in a paramagnetic high-spin (hs) state ($S=5/2$) with 5 unpaired electrons.[252,253,261,265,266] In terms of Bohr magnetons μ_B, that is the intrinsic electronic magnetic moment, the magnetic moment $\mu_{Fe(III)-N}$ is 5 μ_B.[267] The electronic configuration in Fe t_{2g} and e_g states is shown in Figure 3.1, while Figure 3.2 shows a complete molecular orbital diagram, including all the symmetry labels. When applying pressure or electromagnetic field changes, transitions between hs and ls states are possible. Thus, PB can also be classified as a spin-crossover (SCO) compound.
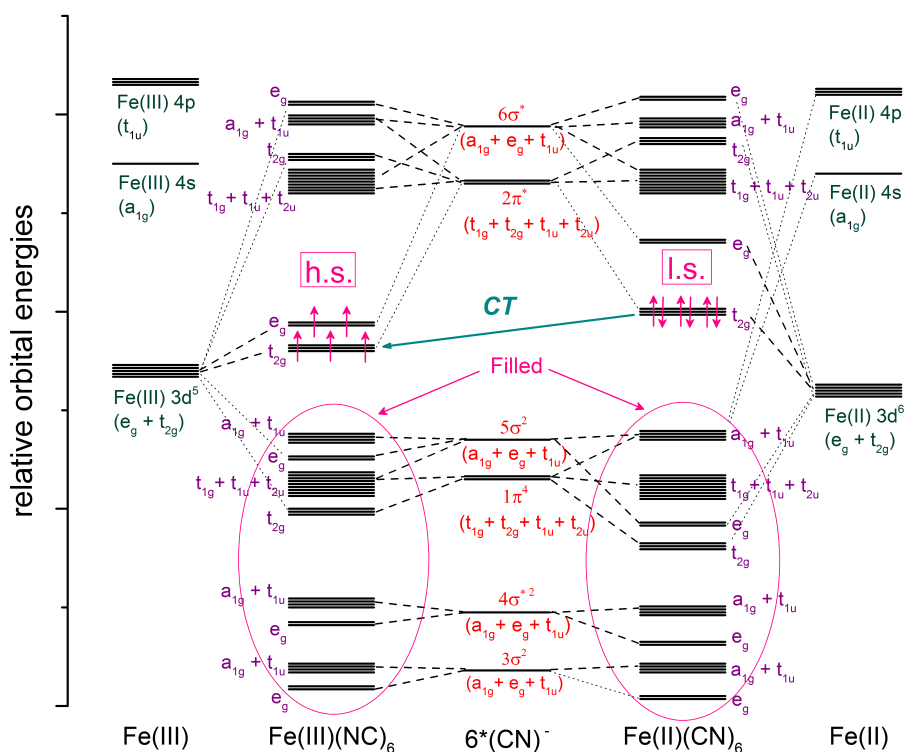
Figure 3.2: Molecular orbital scheme of the octahedrally coordinated Fe(III)(NC)$_6$ and Fe(II)(CN)$_6$, with symmetry labels adapted from molecular point group theory.[268] The charge-transfer from ls-Fe(II)–C to hs-Fe(III)–N band is indicated by a turquoise arrow. Adapted from Ref. [264].

The intense blue colour of PB results from a strong charge-transfer (CT) absorption at 1.75 eV, which is due to intermetallic

electron transfer from ferrous Fe(II)–C to ferric Fe(III)–N.[264] This charge-transfer transition is also illustrated in Figure 3.2.

Below their Curie-temperature of $T_C = 5.6$ K, the Fe(III)–N centres order ferromagnetically.[266,269] The ferromagnetic interaction of the paramagnetic centres can be described by a spin-delocalisation mechanism, in which electronic charge is delocalised throughout the structure via the cyanide π-orbitals.[252,269,270] Apart from the ligand-mediated ferromagnetic interactions, also a direct through-space coupling of the Fe(III)–N magnetic moments cannot be excluded, which is according to calculations of Middlemiss and Wilson the predominant coupling mechanism.[271]

The inverse redox form KFe(II)[Fe(III)(CN)$_6$], in the older literature sometimes referred to as *Turnbull's blue*, is highly unstable. It was believed to consist of ferrous Fe(II) ions and ferricyanide [Fe(III)(CN)$_6$] moieties, which are the most stable oxidation states in aqueous solution. In the solid state, however, it will immediately transform to Prussian blue KFe(III)[Fe(II)(CN)$_6$] by charge-transfer.[272,273]

3.1.2 Calculations of Prussian blue

Modelling the complex electronic structure of Prussian blue by computational simulations still remains a challenge for Density Functional Theory (DFT).[253,271,274–279] Wojdeł *et al.* did pioneering work on the mixed-valent KFe(III)[Fe(II)(CN)$_6$].[274–279] Those studies include the application of mixed ultrasoft pseudopotentials (USPPs)[275] or different Hubbard U parameters on both Fe centres,[274] with which they accurately described the electronic structure of PB, in agreement with experiments. Middlemiss and Wilson applied hybrid functionals with various amounts of exact Hartree-Fock exchange in order to assess the magnetic interactions in PB.[271] They showed that including Hartree–Fock exchange can provide an accurate representation of the key electronic and magnetic interactions. Furthermore, they suggest that an indirect exchange interaction between hs Fe(III)–N centres dominates ferromagnetic couplings in PB.
In this work various functionals on different levels of theory are employed and their applicability is evaluated.

Pure DFT

When applying pure GGA or even meta-GGA, the computational simulation of the ideal KFe(III)[Fe(II)(CN)$_6$] always converges to an overall low-spin (ls-ls) state. In the ls-ls state both Fe centres are in an ls-configuration, which leads to an incompletely filled t_{2g} set of

Fe(III)–N, and thus results in a half-metallic *conducting* ground state. The spin configuration of ls-ls PB is shown in Figure 3.3a. In this ls-ls configuration (Figure 3.3), $\mu_{Fe(III)-N} = 1\ \mu_B$ (one unpaired electron), while the ls d^6 Fe(II)–C has 0 μ_B. This configuration, however, is inconsistent with the experimental results, in which a ferromagnetic hs-ls state with $\mu_{Fe(III)-N} = 5\ \mu_B$, as described above, is observed (Figure 3.3b).[261,266]
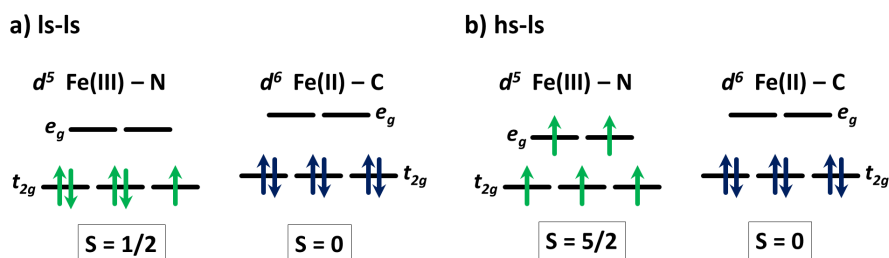
Figure 3.3: Spin configuration of Fe(III)–N and Fe(II)–C in an a) ls-ls state and b) hs-ls state in the limit of complete spin localisation.

Table 3.1 lists the main parameters of the ideal $KFe(III)[Fe(II)(CN)_6]$ structure calculated with the GGA functionals PBE (Perdew-Burke-Ernzerhof),[157,280] PBEsol (PBE revised for solids),[161] RPBE (revPBE),[160] PW91 (Perdew-Wang 1991),[158] AM05 (Armiento and Mattson 2005),[281] and the meta-GGA TPSS (Tao-Perdew-Staroverov-Scuseria),[282] as available in the VASP code.[199,200]

Table 3.1: Lattice constant a, band gap E_g, Bader charges q,[283–285] and magnetisations μ of both Fe centres of the ls-ls Prussian blue, for the GGA functionals PBE,[157,280] PBEsol,[161] RPBE,[160] PW91,[158] AM05,[281] and meta-GGA TPSS.[282] A half-metallic, conducting (*cond.*) state is obtained for each.

Functional	PBE	PBEsol	RPBE	PW91	AM05	TPSS
a, Å	9.897	9.791	9.994	9.897	9.801	9.909
E_g	cond.	cond.	cond.	cond.	cond.	cond.
$q_{Fe(III)-N}$, $|e|$	1.23	1.27	1.33	1.31	1.27	1.32
$q_{Fe(II)-C}$, $|e|$	0.90	0.87	0.91	0.90	0.86	0.94
$\mu_{Fe(III)-N}$, μ_B	0.61	0.61	0.60	0.59	0.61	0.61
$\mu_{Fe(II)-C}$, μ_B	0.38	0.37	0.40	0.38	0.37	0.39

All functionals lead to similar qualitative results for the electronic properties, the charges $q_{Fe(III)-N}$ and $q_{Fe(II)-C}$ and the magnetisations $\mu_{Fe(III)-N}$ and $\mu_{Fe(II)-C}$. From those values, the effect of electron delocalisation in DFT becomes highly visible: i) Bader charges[283–285] lie far below their classical ionic lim-

86

its $q_{Fe(III)-N} = +3\ |e|$ and $q_{Fe(II)-C} = +2\ |e|$; ii) Magnetisations $\mu_{Fe(III)-N} = 0.6\ \mu_B$ and $\mu_{Fe(II)-C} = 0.4\ \mu_B$ show a large delocalisation of the electronic charge over the two metal centres.

The only difference of all the employed DFT functionals is the lattice parameter with variations of the order of 1%. This value however cannot directly compared to the experimental value 10.13–10.18 Å, as that value corresponds to an hs-ls state with average stoichiometry $Fe_4[Fe(CN)_6]_3 \cdot nH_2O$, as shown in Figure 3.1a.[259–261]

The incorrect description of the magnetic ground state results from the DFT-inherent self-interaction term, i.e. the electron interacting with itself. Especially when having closely lying magnetic minima, DFT calculations of correlated systems fail.

DFT + U

One way to correct for the electronic self-interaction is to introduce an effective Hubbard U parameter $U^{eff} = (U-J)$, as explained in Section 2.1.2.[167–170,175] In this context, U^{eff} parameters varying from 0.0 eV to 8.0 eV on both iron centres were added. Since the value of the optimal U parameter is expected not to vary significantly with ionic charge and spin state,[174,286] I have used the *same* U^{eff} parameter on all irons to maintain a greater transferability,[165,287] which is in contrast to a previous report where two different U^{eff} for PB were introduced.[276] Calculations of the hs-ls and ls-ls configurations with varying U^{eff} were performed for the functionals PBE and PBEsol. The resulting structural and electronic parameters are presented in Figures 3.4 and 3.5 and Tables 3.3 and 3.4.
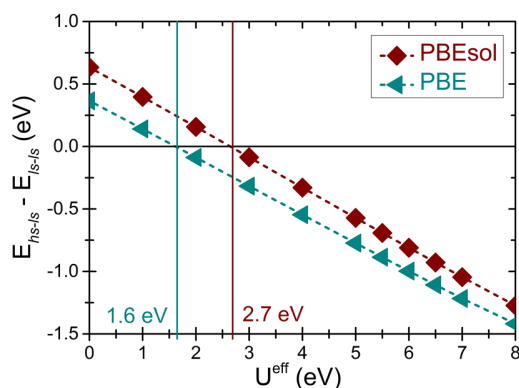
Figure 3.4: Variation of the energy difference between hs-ls and ls-ls configuration ($E_{hs-ls} - E_{ls-ls}$) with U^{eff} for the functionals PBE and PBEsol.

The relative stabilisation of the hs-ls configuration with respect to the ls-ls configuration is given by $E_{hs-ls} - E_{ls-ls}$ and shown in Figure 3.4. From Figure 3.4, it can be seen that $U^{eff} \geq 1.6$ eV for PBE and

$U^{eff} \geq 2.7$ eV for PBEsol is needed to stabilise the correct hs-ls state over the ls-ls state, i.e. for the energy difference $E_{hs-ls} - E_{ls-ls}$ to be ≥ 0.

When increasing U^{eff} on both irons, also the lattice parameter a increases, as shown in Figure 3.5a. This is due to the fact that adding U^{eff} on the metal centres leads to a higher localisation of charge density on the atoms, thus removing electronic density from the metal–ligand bond and increasing the bond length. More important though is the difference in lattice constant between hs-ls and ls-ls states. In the hs-ls configuration (see Figure 3.3) the Fe(III)–N e_g orbitals, which are slightly anti-bonding in character, are half-filled and the Fe–N bond distance enlarged. In general, the PBEsol functional gives about 1% smaller lattice parameters, which are closer to the experimentally observed result for hs-ls Prussian blue, as indicated in Figure 3.5a. This is not surprising as PBEsol was constructed to give more accurate lattice constants for solid compounds.[161,288] Therefore, in my Thesis, I mainly used PBEsol(+U) as GGA(+U) functional of choice for obtaining the geometries of the used structures.

Figure 3.5b shows the increase of the band gap E_g with increasing U^{eff} of the hs-ls $KFe[Fe(CN)_6]$. (The half-metallic ls-ls state with band gap 0 is also indicated in Figure 3.5b.) As stronger the effective on-site Coulomb interaction, as narrower get the d-bands and as larger the gap. For $U^{eff} = 6.0$ eV (PBE) and $U^{eff} = 5.5$ eV (PBEsol) a match with the experimental value of 1.75 eV is obtained (green line in Figure 3.5b). The band gap is key to opto-electronic applications and is thus taken as main criterion for evaluating the adequate functional. Consequently, I decided on PBEsol+U with $U^{eff} = 5.5$ eV as a DFT+U functional of choice in this study of Prussian blue type materials.
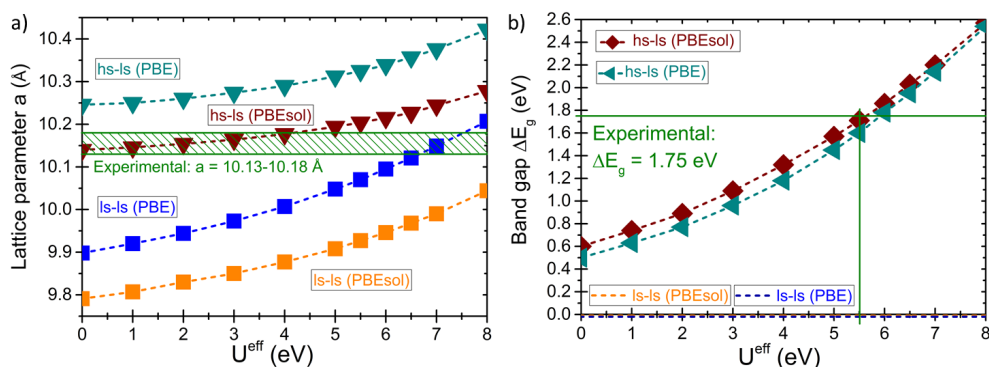
Figure 3.5: Variation of a) the lattice parameter a of both hs-ls and ls-ls configurations and b) the band gap E_g of hs-ls $KFe(III)[Fe(II)(CN)_6]$ with U^{eff} for the functionals PBE and PBEsol.

This PBEsol+U (U^{eff} = 5.5 eV) functional is also employed to investigate the possibility of different magnetic alignments, other than the hs-ls and ls-ls state of Figure 3.3. Intermediate spin states (is) with one electron occupying the e_g orbital, i.e. ls-is, hs-is, is-ls, is-hs, or an overall high-spin (hs-hs) state are compared in Table 3.2. Those states were calculated by fixing the overall magnetic moment of the unit cell to the corresponding number of unpaired electrons per unit cell: 20 μ_B for hs-ls, 4 μ_B for ls-ls, 36 μ_B for hs-hs, 12 μ_B for ls-is and is-ls, and 28 μ_B for is-hs, hs-ls. As expected all other spin configurations, in particular the is state with a singly occupied e_g, are much higher in energy and hence can be excluded for further considerations. The same applies for an anti-ferromagnetic alignment, which is disfavoured by the spin delocalisation and direct magnetic coupling.[270,271]

Table 3.2: Relative energies (per Fe centre) of different possible magnetic configurations with respect to the hs-ls ground state calculated with the functional PBEsol+U (U^{eff}) by imposing an overall magnetic moments on the $K_4Fe_4[Fe(CN)_6]_4$ unit cell.

Total magnetic moment of unit cell $\mu_{unit\,cell}$, μ_B	Possible corresponding spin configurations of $\mu_{unit\,cell}$	Relative energy w.r.t. hs-ls ground state, eV
20	hs-ls, is-is, ls-hs	0
0	ls-ls	1.44
36	hs-hs	2.17
12	is-ls, ls-is	2.54
28	hs-is, is-hs	2.81

Tables 3.3 and 3.4 show that in the case of hs-ls PB, the magnetisation on Fe(III)–N increases, whereas the magnetisation on Fe(II)–C decreases with increasing U^{eff}. Because the electrons become more localised, the value of the magnetisations approaches the classical limit with $\mu_{Fe(III)-N}$ = 5 μ_B and $\mu_{Fe(II)-C}$ = 0 μ_B.

Interestingly, for the ls-ls configuration the localisation of the magnetic moment inverses at high U^{eff} (U^{eff} > 3.5 eV for PBE+U; U^{eff} > 4.5 eV for PBEsol+U) and the unpaired electron becomes stabilised on the ls-Fe(II)–C. Adding U leads to a destabilisation of the t_{2g} states in Fe(II)–C (in the stronger crystal field; Figure 3.2), and a partial transfer of electron density from Fe(II)–C to Fe(III)–N might be favoured in that case.

Although DFT+U (PBE+U / PBEsol+U) has shown to give accurate results for the optimised U^{eff} (5.5 eV for PBEsol), the obtained data is highly dependent on the chosen U-parameter. As in turn the optimal U^{eff} depends on the system, i.e. the electronic environment of the transition metal centre, the method lacks in transferability.[174]

Table 3.3: Dependence of electronic and geometric properties (lattice constant a, band gap E_g and magnetisation μ) and relative stabilisation of the hs-ls configuration ($E_{hs-ls} - E_{ls-ls}$) on the effective U parameter $U^{eff} = (U-J)$ for the GGA functional **PBE+U**. The ls-ls configuration is conducting (*cond.*).

U^{eff}, eV	0.0		1.0		2.0		3.0		4.0		5.0		5.5		6.0		6.5		7.0		8.0	
Spin state	hs-ls	ls-ls	hs-ls	ls-ls	hs-ls	ls-ls	hs-ls	ls-ls	hs-ls	ls-ls	hs-ls	ls-ls	hs-ls	ls-ls	hs-ls	ls-ls	hs-ls	ls-ls	hs-ls	ls-ls	hs-ls	ls-ls
a, Å	10.246	9.898	10.250	9.920	10.260	9.944	10.274	9.973	10.290	10.007	10.312	10.048	10.325	10.070	10.339	10.095	10.357	10.121	10.376	10.149	10.422	10.207
$E_{hs-ls}-E_{ls-ls}$, eV	+2.93		+1.13		-0.70		-2.54		-4.37		-6.19		-7.09		-7.98		-8.86		-9.73		-11.35	
E_g, eV	0.50	cond.	0.63	cond.	0.77	cond.	0.96	cond.	1.18	cond.	1.45	cond.	1.60	cond.	1.78	cond.	1.95	cond.	2.14	cond.	2.54	cond.
$\mu_{Fe(III)-N}$, μ_B	3.85	0.61	3.94	0.61	4.01	0.60	4.09	0.58	4.15	0.52	4.21	0.49	4.24	0.45	4.27	0.41	4.30	0.36	4.32	0.29	4.37	0.17
$\mu_{Fe(II)-C}$, μ_B	0.34	0.38	0.23	0.43	0.29	0.48	0.25	0.54	0.22	0.61	0.18	0.70	0.16	0.75	0.14	0.81	0.12	0.87	0.11	0.94	0.07	1.08

Table 3.4: Dependence of electronic and geometric properties (lattice constant a, band gap E_g and magnetisation μ) and relative stabilisation of the hs-ls configuration ($E_{hs-ls} - E_{ls-ls}$) on the effective U parameter $U^{eff} = (U-J)$ for the GGA functional **PBEsol+U**. The ls-ls configuration is conducting (*cond.*).

U^{eff}, eV	0.0		1.0		2.0		3.0		4.0		5.0		5.5		6.0		6.5		7.0		8.0	
Spin state	hs-ls	ls-ls	hs-ls	ls-ls	hs-ls	ls-ls	hs-ls	ls-ls	hs-ls	ls-ls	hs-ls	ls-ls	hs-ls	ls-ls	hs-ls	ls-ls	hs-ls	ls-ls	hs-ls	ls-ls	hs-ls	ls-ls
a, Å	10.141	9.791	10.146	9.807	10.154	9.830	10.164	9.850	10.177	9.877	10.194	9.908	10.204	9.927	10.215	9.946	10.227	9.968	10.244	9.990	10.278	10.044
$E_{hs-ls}-E_{ls-ls}$, eV	+5.06		+3.18		+1.26		-0.69		-2.63		-4.57		-5.53		-6.49		-7.43		-8.37		-10.19	
E_g, eV	0.60	cond.	0.74	cond.	0.89	cond.	1.09	cond.	1.32	cond.	1.57	cond.	1.71	cond.	1.86	cond.	2.03	cond.	2.20	cond.	2.57	cond.
$\mu_{Fe(III)-N}$, μ_B	3.84	0.61	3.92	0.62	3.99	0.62	4.06	0.61	4.13	0.59	4.19	0.55	4.22	0.53	4.25	0.49	4.27	0.46	4.30	0.41	4.35	0.28
$\mu_{Fe(II)-C}$, μ_B	0.31	0.37	0.29	0.40	0.27	0.45	0.24	0.50	0.22	0.56	0.19	0.64	0.17	0.69	0.16	0.74	0.14	0.79	0.13	0.85	0.09	1.00

Hybrid functionals

Another way of overcoming the *self-interaction error*, is to include an amount of exact Hartree-Fock exchange in the exchange–correlation energy in a *hybrid* functional. In this work I used the hybrid functionals HSE03 and HSE06, which are particularly useful in simulating periodic solids, as their long-range exact exchange term is screened.[181–184] Table 3.5 compares the applicability of GGA (PBE and PBEsol), GGA+U (PBE+U and PBEsol+U), and hybrid functionals (HSE03 and HSE06) for $KFe(III)[Fe(II)(CN)_6]$.

Table 3.5: Geometric and electronic parameters, crystal filed spitting energy *CFSE* at Fe(III)-N, band gap E_g, Bader charges,[283] and magnetisations, of the ideal $KFe(III)[Fe(II)(CN)_6]$ in an hs-ls configuration, and comparison to the ls-ls configuration, $E_{hs-ls} - E_{ls-ls}$, calculated with the functionals PBE,[157,280] PBEsol,[161] PBE+U, PBEsol+U (both with $U^{eff} = 5.5$ eV), HSE03, HSE06,[181–184] and compared to experiments.[260,261,264]

Functional	PBE	PBEsol	PBE+U	PBEsol+U	HSE03	HSE06	exp.
a, Å	10.246	10.141	10.325	10.204	10.184	10.175	10.166[260]
$d(Fe-N)$, Å	2.070	2.043	2.076	2.050	2.053	2.051	2.03[260]
$d(Fe-C)$, Å	1.875	1.851	1.911	1.877	1.873	1.872	1.92[260]
$d(C-N)$, Å	1.177	1.177	1.176	1.175	1.165	1.165	1.13[260]
E_{hs-ls} - E_{ls-ls}, eV	+0.37	+0.63	-0.88	-0.53	-0.69	-0.31	
E_g, eV	0.50	0.60	1.59	1.71	1.94	2.31	1.75[264]
$CFSE_{Fe(III)-N}$, eV	1.50	1.67	1.13	1.39	1.69	1.73	
$q_{Fe(III)-N}$, $|e|$	+1.61	+1.74	+1.73	+1.87	+1.86	+1.87	
$q_{Fe(II)-C}$, $|e|$	+0.97	+0.55	+1.01	+1.08	+0.76	+0.76	
q_N, $|e|$	-1.25	-1.42	-1.31	-1.36	-1.37	-1.38	
q_C, $|e|$	+0.67	+0.88	+0.70	+0.72	+0.78	+0.79	
q_K, $|e|$	+0.93	+0.93	+0.93	+0.93	+0.94	+0.94	
$\mu_{Fe(III)-N}$, μ_B	3.86	3.84	4.24	4.22	4.15	4.16	
$\mu_{Fe(II)-C}$, μ_B	0.35	0.31	0.16	0.17	0.27	0.26	
μ_N, μ_B	0.06–0.07	0.06–0.07	0.05	0.05	0.05	0.05	
μ_C, μ_B	0.02	0.02	0.02	0.02	0.01	0.01	
μ_K, μ_B	0.00	0.00	0.00	0.00	0.00	0.00	

Both hybrids, HSE03 and HSE06, yield very similar structural parameters, bond lengths and lattice constants, in very good agreement with the X-ray data.[259]

The Bader charges[283–285] of the iron centres remain far from their ionic limits $q_{Fe(III)-N} = +3 \, |e|$ and $q_{Fe(II)-C} = +2 \, |e|$, even with DFT+U

and HSE03/06, due to metal–ligand bonding in the periodic solid. This also leads to a stabilisation to a small positive charge $q_{Fe(II)-C}$ = +0.7–0.9 $|e|$ on the carbon atoms. The completely ionised counter cation K^+, on the other hand, shows a charge close to +1 $|e|$. Adding U^{eff} on both Fe centres increases their positive charge and enhances their ionic character, while the hybrid functionals lead to a better separation of charges between Fe(III)–N and Fe(II)–C (increasing only $q_{Fe(III)-N}$). Notwithstanding, the description of partial charges, such as the Bader analysis carried out, is not straightforward and needs to be regarded with caution.[148,283] If the atoms in the structure contain unpaired electrons, the magnetisation values are generally a better descriptor of the localisation of electrons.

Also the magnetisation on Fe(III)–N is lower than the expected 5 μ_B due to spin-delocalisation through the CN π-system. It however increases from 3.8–3.9 μ_B, obtained by GGA, to around 4.2 μ_B when adding U^{eff} or applying a hybrid functional, indicating a higher ionicity of the metal–ligand bonding.

The crystal field splitting energy (CFSE) is the energy separating the t_{2g} from the e_g set on *one* metal centre in an octahedral crystal field (as shown in Figures 3.1d and 3.6). Both GGAs (PBE and PBEsol) and hybrid functionals (HSE03 and HSE06) give a similar CFSE of around 1.5 – 1.7 eV. When adding on-site Coulomb interaction with the U-parameter, the CFSE decreases significantly due to shrinking the d-band separation on the same metallic centre, which might be unphysical.

Comparing both applied hybrids, HSE03 and HSE06, which differ only in the *screening distance* of the long-range Hartree Fock exact exchange term (Equation 2.16), the results for all obtained parameters, except the band gap, are found to be almost equal. The gap E_g with HSE03 (1.94 eV) is about 0.3–0.4 eV smaller than with HSE06 (2.31 eV), and therefore closer to the experimental value of 1.75 eV. Introducing exact exchange from Hartree–Fock theory leads to larger separation of valence and conduction bands and, thus, increases the gap (see Figure 3.6); an effect often overestimated.[185] HSE03, as implemented in the VASP code,[199,200] screens the exact exchange at a shorter distance of 3.33 Å, while HSE06 has a screening distance of 5.00 Å. This smaller screening distance in HSE03 is likely to be the reason for its better evaluation of the band gap.[183,184]

Also the hybrid functionals B3LYP[289] (including 20% exact exchange) and B3LYP*[185] (including 15% exact exchange) were employed and compared to HSE03, as shown in Table 3.6. Both B3LYP and B3LYP* show a similar lattice parameter of 10.26 – 10.27 Å,

about 1% larger than the experimental value and the value obtained with HSE (10.18 Å). This is based on the fact that B3LYP (and B3LYP*) was empirically parameterised using a large test set of organic molecules, and thus does not necessarily give a good description for solids. While most electronic parameters, i.e. crystal field splitting energies, charges (not shown here), and magnetisations, are similar for all hybrid functionals, the band gap is most overestimated by B3LYP, but reduced by B3LYP*, giving 1.70 eV, which is closest to the experimental result. As mentioned in Section 2.1.2, a reduced amount of exact exchange (as in B3LYP*) may often yield more accurate band splittings in transition metal compounds, an issue which is discussed later for the case of cobalt hexacyanoferrate.

Table 3.6: Comparison of the hybrid functionals HSE03,[182,184] B3LYP[289] and B3LYP*[185] in terms of their lattice parameters a, hs-ls stabilisation energy $E_{hs-ls} - E_{ls-ls}$, crystal field-splitting energy $CFSE$ of Fe-N(III), and magnetisation of the iron centres.

Functional	HSE03	B3LYP	B3LYP*
a, Å	10.184	10.246	10.274
E_{hs-ls} - E_{ls-ls}, eV	-0.69	-2.08	-1.49
E_g, eV	1.94	2.26	1.70
$CFSE_{Fe(III)-N}$, eV	1.69	1.62	1.58
$\mu_{Fe(III)-N}$, μ_B	4.15	4.09	4.03
$\mu_{Fe(II)-C}$, μ_B	0.27	0.30	0.35

Band gap and electronic structure

The band gap results from a charge-transfer transition between the Fe(II)–C t_{2g} valence band and the Fe(III)–N t_{2g} conduction band, which is only half-occupied by unpaired α-spin electrons.[†] The transition takes therefore place in the β-spin channel.

Figure 3.6 shows the electronic structures obtained for PBEsol, PBEsol+U, and HSE03, each of which chosen to be the most adequate GGA, GGA+U, and hybrid functional, respectively. On the positive ordinate the majority α-spin is plotted, and on the negative ordinate is the minority β-spin. The potassium ions do not participate in the DOS, as they become completely ionised and are therefore omitted. It can be seen that the conveniently used orbital

---

[†]It has to be kept in mind that the discussed band gaps here are taken as the energy difference of the eigenvalues obtained for the highest occupied state (VBM) and lowest unoccupied state (CBM), hence the *eigenvalue gap*, which is not equivalent to the quasiparticle gap, as obtained by a photoemission experiment.

notation t_{2g} and e_g for the electronic states in the PB lattice is no longer exact, as the insertion of counter cations leads to a descent in symmetry. Hence, the electronic environment of the Fe centres is no longer strictly octahedral and the t_{2g} and e_g states no longer degenerate. The splitting of d-levels is most prominent in the case of the accurate hybrid functional, where the electronic bands are very sharp defined peaks.
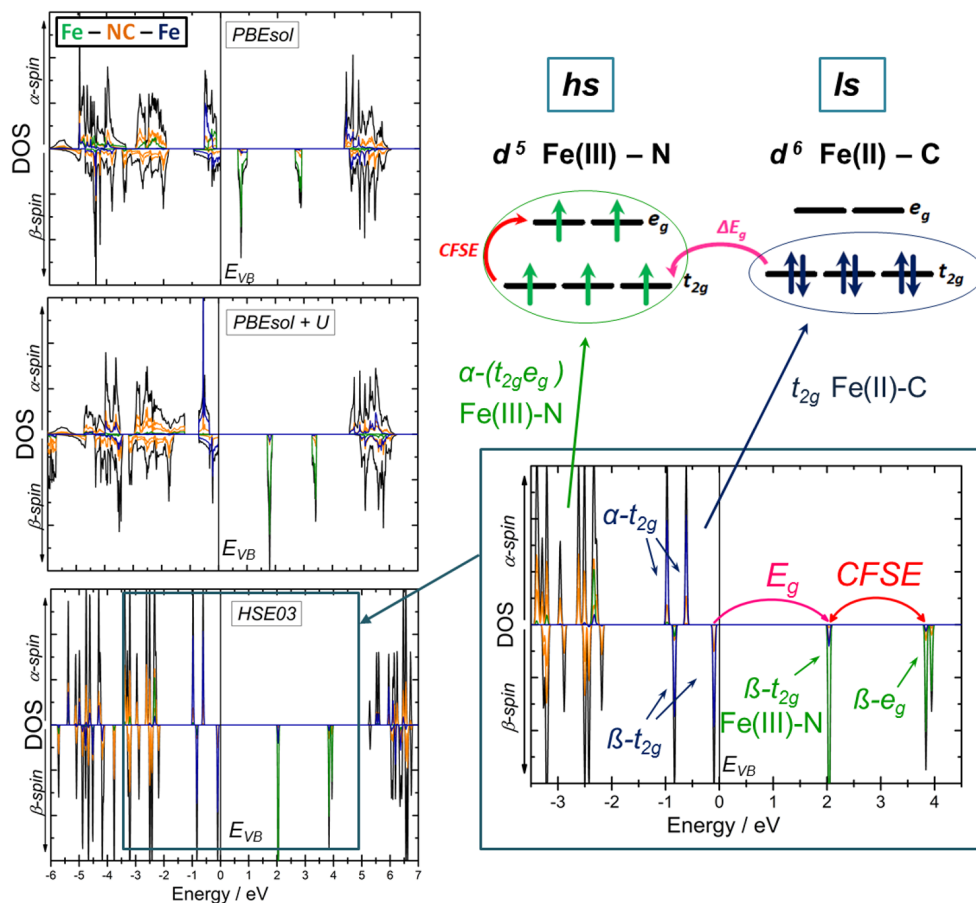
Figure 3.6: Spin-polarised projected Density of States (DOS) of hs-ls PB calculated with PBEsol, PBEsol+U (U^{eff} = 5.5 eV), and the hybrid HSE03, with α-spin density on the positive and β-spin density on the negative axis. The energy zero is defined to be at valence band maximum E_{VB}. The band gap transition E_g and crystal field splitting energy ($CFSE$) on Fe(III)–N are indicated by magenta and red arrows. In the enlarged DOS on the right (calculated with HSE03) the important valence levels α– and $\beta - t_{2g}$ and e_g are labelled.

Going from GGA to GGA+U to hybrid functionals, an increase of ionic character is seen in the DOS (Figure 3.6). Although the valence band obtained with PBEsol is mainly constituted of the t_{2g} states on

Fe(II)–C (blue), there is a high level of hybridisation with the cyanide ligand (orange) and even Fe(III)–N (green) due to a larger degree of covalency. Also the other electronic bands of metals and ligands are highly hybridised. Moreover, the splitting of the electronic bands on different atoms is lower for PBEsol than for the other functionals. In particular, the band gap E_g = 0.6 eV (Table 3.5) is largely underestimated.

Even with HSE03 a certain degree of electron delocalisation is maintained. The Fe(II)–C bands show Fe(III)–N density of states with equal symmetry due to the electronic overlap with the ligand π-orbitals.[269] Moreover, the nitrogen contribution to the charge-transfer state, i.e. the $\beta - t_{2g}$ states on both Fe centres, is seen from the DOS.

Since the electron donating Fe(II)–C and accepting Fe(III)–N lie on different points in the Brillouin zone, the band gap transition is *indirect* (see Section 2.2.5). Figure 3.7 shows the band structure (calculated with PBEsol+U) of hs-ls KFe[Fe(CN)$_6$], which indicates that the gap corresponds to an indirect $L \leftarrow \Gamma$ transition, 1.73 eV for U^{eff} = 5.5 eV, consistent with previous studies.[275] The *direct* gaps are 1.85, 1.87, 1.91, and 1.92 eV, located at Γ, K, L, and X, respectively, and lie very close to the indirect gap. Therefore, the absorption is intense and resembles a direct band transition.
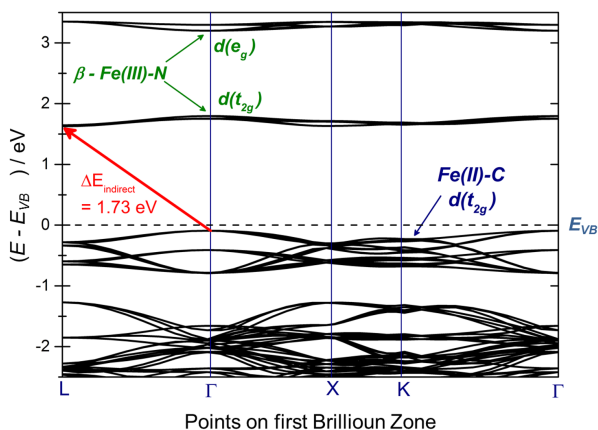
Figure 3.7: Band structure (not spin-polarised) of hs-ls PB calculated with PBEsol+U (U^{eff} = 5.5 eV). The *indirect* $L \leftarrow \Gamma$ band gap transition is shown by a red arrow.

Summarising the effect of different functionals on the simulation of Prussian blue: i) Pure DFT (on the GGA or even on the meta-GGA level of theory) has shown to be inadequate, as it incorrectly stabilises the diamagnetic ls-ls configuration of KFe(III)[Fe(II)(CN)$_6$];

ii) GGA+U (PBEsol+U^{eff} = 5.5 eV) accurately describes the structural and electronic parameters, but is not universally applicable as it was optimised particularly for the PB structure; iii) HSE03 as a hybrid functional of choice leads to a very accurate description of lattice parameters and the electronic structure of PB, but on a largely increased (2 orders of magnitude) computational cost.

In the following discussion, different Prussian blue analogues are studied and the applicability of PBEsol+U and HSE03 is assessed.

3.1.3 Redox forms: Berlin green and Prussian white

Prussian white and Berlin green are the two, thermodynamically unstable, redox forms of Prussian blue KFe(III)[Fe(II)(CN)$_6$] and are shown in Figure 3.8.[257,290,291] The oxidised Berlin green (BG) Fe(III)[Fe(III)(CN)$_6$] (Figure 3.8a), sometimes also called Prussian yellow, receives its name from its yellow-greenish appearance.[275,277] It has both iron centres oxidised to Fe(III) and is therefore charge-neutral without any intercalated counter cations. Upon reduction of PB, Prussian white (PW) K$_2$Fe(II)[Fe(II)(CN)$_6$], or Everitt's salt, forms, with both iron centres in a (formal) oxidation state of +2.[277] In this case four counter cations need to be incorporated in all the tetrahedral holes (spanned by Fe(II)–N/Fe(II)–C) of the unit cell for charge balance, as shown in Figure 3.8c.
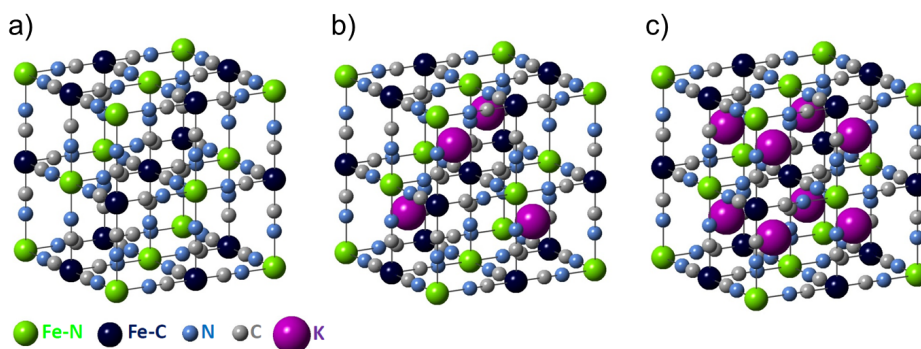
Figure 3.8: Crystal structures of a) Berlin green Fe(III)[Fe(III)(CN)$_6$], b) Prussian blue KFe(III)[Fe(II)(CN)$_6$], and c) Prussian white K$_2$Fe(II)[Fe(II)(CN)$_6$].

As it is the case for Prussian blue, two low-lying magnetic states for both BG and PW can be anticipated and are schematically illustrated in Figure 3.9a: hs-ls with a high-spin Fe–N and a low-spin Fe–C centre; ls-ls with both Fe centres in the low-spin state. Figure 3.9b shows the stabilisation of the hs-ls state w.r.t. the ls-ls state

$(E_{hs-ls} - E_{ls-ls})$ for both BG and PW with variation of the effective U-parameter U^{eff}, similar as done before for PB (Figure 3.4).
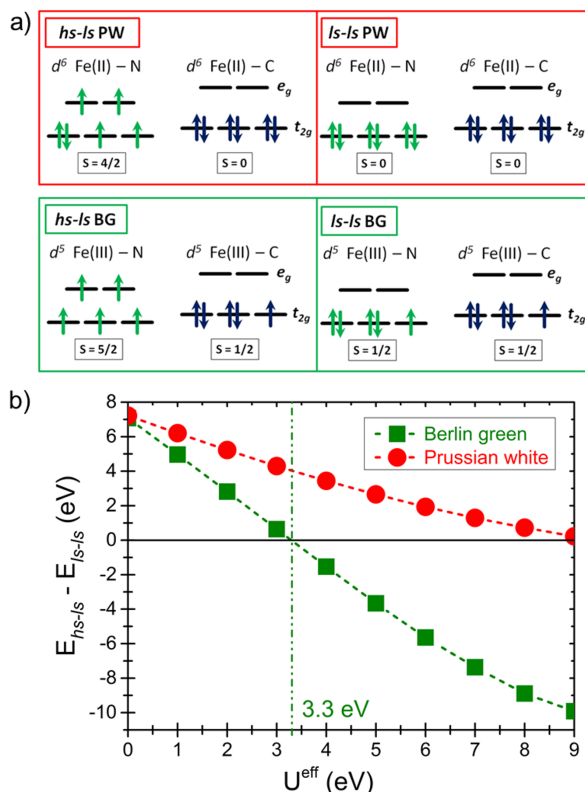
Figure 3.9: a) Possible spin configurations (hs-ls and ls-ls) and b) variation of their energy difference $E_{hs-ls} - E_{ls-ls}$ with applied U^{eff} (PBEsol+U) of Prussian white (PW) $K_2Fe(II)[Fe(II)(CN)_6]$ (red) and Berlin green (BG) $Fe(III)[Fe(III)(CN)_6]$ (green).

Table 3.7 presents the geometric and electronic parameters of Berlin green in an hs-ls configuration and Prussian white in both hs-ls and ls-ls states, calculated with PBEsol+U and HSE03, and compared to available experimental data.[290–292]

Berlin green forms upon removal of one electron from ls Fe(II)–C, giving Fe(III)–C, which stays in a a low-spin state due to the strong CN crystal field. As the hs Fe(III)–N centre is barely influenced by oxidising Fe–C, it remains in its hs configuration with constant Fe–N distance d(Fe–N) (see Tables 3.5 and 3.7). Both functionals PBEsol+U, with any U^{eff} parameter larger than 3.3 eV (Figure 3.9b) and HSE03 stabilise the hs-ls configuration w.r.t. ls-ls, as predicted from Mössbauer spectroscopy and neutron diffraction data.[293] A change of spin state from hs-ls PB upon oxidation can therefore be excluded and, in the further discussion of BG, its hs-ls ground state is as-

sumed.

For Prussian white (PW), however, the true ground state configuration cannot be determined with certainty. While Figure 3.9b shows a stabilisation of the ls-ls state, even for large Hubbard U-terms ($U^{eff} \leq 9$ eV),[†] an assessment with the hybrid functional yields a slightly more stable (by 0.1 eV) hs-ls state, as given in Table 3.7.

Table 3.7: Main parameters and energy difference $E_{hs-ls} - E_{ls-ls}$ of the Prussian blue derivatives Berlin green (hs-ls) Fe(III)[Fe(III)(CN)$_6$] and Prussian white Fe(II)[Fe(II)(CN)$_6$] in hs-ls and ls-ls configurations, calculated with the functionals PBEsol+U (U^{eff} = 5.5 eV) and HSE03, as well as experimental data.[290–294]

Functional	PBEsol + U			HSE03			exp.	
Compound	*BG*	*hs-ls PW*	*ls-ls PW*	*BG*	*hs-ls PW*	*ls-ls PW*	*BG*	*PW*
a, Å	10.217	10.289	9.978	10.237	10.363	9.982	10.218[293]	10.104-10.114[292]
$d(Fe-N)$, Å	2.049	2.086	1.926	2.055	2.083	1.936	2.003[293]	
$d(Fe-C)$, Å	1.890	1.880	1.887	1.906	1.865	1.890	1.921[293]	
$d(C-N)$, Å	1.170	1.179	1.175	1.158	1.179	1.165	1.162[293]	
E_{hs-ls} - E_{ls-ls}, eV	-0.59	+0.26		-0.91	-0.10			
E_g, eV	cond.	cond.	3.67	1.59	2.62	4.78	cond.[291]	cond.[290]
$CFSE_{Fe(III)-N}$, eV *	1.32			0.95				
q_{Fe-N}, |e|	+1.87	+1.47	+1.25	+1.79	+1.49	+1.28		
q_{Fe-C}, |e|	+0.77	+0.88	+0.77	+1.20	+0.82	+0.78		
q_N, |e|	-1.22	-1.32	-1.38	-1.33	-1.51	-1.43		
q_C, |e|	+0.78	+0.62	+0.74	+0.83	+0.82	+0.78		
q_K, |e|		+0.93	+0.92		+0.94	+0.92		
μ_{Fe-N}, μ_B	4.21	3.80	0.00	4.19	3.56	0.00	5.02[293]	
μ_{Fe-C}, μ_B	1.28	-0.05	0.00	1.11	0.06	0.00	0.8[293]	
μ_N, μ_B	0.07	0.03	0.00	0.07	0.02	0.00		
μ_C, μ_B	-0.01	0.00	0.00	-0.02	0.00	0.00		
μ_K, μ_B		0.00	0.00		0.00	0.00		

* The *CFSE* is only given for Fe(III)–N in BG as adding an electron on Fe-N upon reduction to PW, the former near-degenerate t_{2g} and e_g sets distort substantially from their octahedral symmetry and their splitting energy can no longer be extracted.

[†]Adding a higher effective U-parameter likely stabilises the hs-ls configuration as can be estimated from an extrapolation of the hs-ls stabilisation energy $E_{hs-ls} - E_{ls-ls}$ to higher U^{eff} (red line in Figure 3.9). Nonetheless, such a high on-site interaction term on the metal centres would be unphysical and therefore is avoided.

It is well-known that hybrid functionals tend to stabilise higher spin states, while DFT (+U) does not correctly take spin-pairing energies into account, which may explain the discrepancy between the obtained PBEsol+U and HSE03 results for PW.[185,187] Furthermore, difficulties in determining an unambiguous ground state of PW have been pointed out in a previous theoretical report.[276] By comparing the obtained lattice parameters to X-ray diffraction data,[292] as done in Table 3.7, no clear agreement can be found either, since the experimental value (10.1 Å) lies between the results for hs-ls (10.3–10.4 Å) and ls-ls ($\approx$10.0 Å) states. Nonetheless, hs-ls PW with its paramagnetic Fe(II)–N centres and half-metallic character (when calculated with PBEsol, not with HSE03) corresponds better to the measured conductive behaviour[290,291] and magnetic moments[292,294] at thermally accessible temperatures. The diamagnetic, closed shell ls-ls PW is insulating with a large band gap for both functionals. Although the true electronic state at 0 K cannot be determined and both hs-ls and ls-ls PW may co-exist, at room temperature hs-ls PW is likely to be predominant due to its entropic stabilisation[188] and is consequently assumed in the following discussion.

The effect of electron removal (oxidation) or insertion (reduction) on the electronic states in the Prussian blue derivatives can be explained with their respective DOS in Figure 3.10.

When removing an electron from the t_{2g} set of ls Fe(II)–C and forming Berlin green (Figure 3.10a) the Fe(III)–C t_{2g} set (blue) distorts from its near-degeneracy, because it now accommodates one unpaired electron. Therefore an empty site $\beta - t_{2g}$ is left in the minority spin-channel, which moves to higher energy. For PBEsol+U (on the top) the valence band E_{VB} (black line at $E = 0$ in Figure 3.10) cuts the $\beta - t_{2g}$ band, whereas the empty $\beta - t_{2g}$ shifts 1.59 eV above E_{VB} in the case of HSE03 (on the bottom). This, in turn, means that PBEsol-U gives a half-metal (conducting in the β-spin channel) and HSE03 gives an insulating ground state. Notwithstanding, none of these states agrees with recent experiments.[291] Temperature-dependent conductivity studies predict an increase of conductivity with temperature,[291] as opposed to (half-) metallic conduction, which decreases with temperature due to lattice vibrations. The suggested hopping mechanism between the nearest-neighbour Fe-sites would include a small band gap, which is overcome by thermal activation. The gap of 1.6 eV from HSE03 is far too large for thermal hopping to be possible ($k_B T <$ 0.003 eV at RT). Yet the splitting of occupied and unoccupied $\beta - t_{2g}$ sets by HSE03 is qualitatively correct, but overestimated, which is due to the high amount of exact

Hartree–Fock exchange energy that overvalues the spin-pairing energy.[188,295] Moreover, the oxidation of Fe(II)–C to Fe(III)–N in Berlin green results in an increase of positive charge q_{Fe-C} and magnetic moment μ_{Fe-C} in Table 3.7

Upon reduction to Prussian white, an electron is added to the Fe(III)–N centre, accompanied by cation (K$^+$) insertion. This decreases the (positive) charge q_{Fe-N} and magnetic moment μ_{Fe-N}, as given in Table 3.7. Again, this leads to loss of degeneracy due the additional β electron in the $\beta - t_{2g}$ set of Fe(II)–N. PBEsol+U (Figure 3.10b on the top) does not separate the $\beta - t_{2g}$ set and the occupied $\beta - t_{2g}$ merely moves below E_{VB}. HSE03, on the other hand, gives a splitting of the $\beta - t_{2g}$ set by 2.6 eV, which is far too large and contradictory to the observed conductivity.[290]
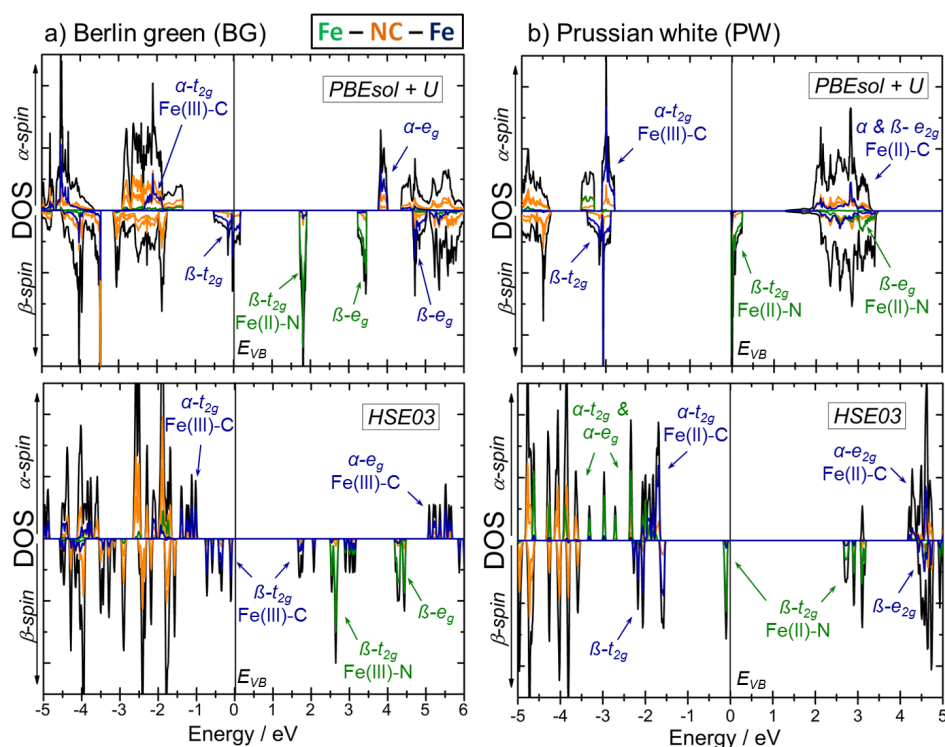
Figure 3.10: Spin-polarised projected Density of States (DOS) of a) Berlin green Fe(III)[Fe(III)(CN)$_6$] and b) Prussian white K$_2$Fe(II)[Fe(II)(CN)$_6$] calculated with PBEsol+U (U^{eff} = 5.5 eV) and the hybrid functional HSE03, with α-spin density on the positive and β-spin density on the negative axis. The energy is set to zero at the valence band maximum E_{VB} (indicated by a black line).

From the discussion on BG and PW, neither PBEsol+U nor HSE03 is found to accurately describe the electronic structure of both redox forms. On the one hand, PBEsol+U with U^{eff} = 5.5 eV has been

optimised for PB, and may not be transferable to its derivatives BG and PW, which have different charge-transfer and magnetic properties. HSE03 on the other hand lacks in overestimating the losses of degeneracy and the separation of electronic band due to its over-valuation of spin-pairing energies.

This issue is elaborated in more detail for the case of cobalt hexacyanoferrate, the cobalt iron analogue of PB (Section 3.2).

3.1.4 Intercalation derivatives of PB and PW

Analogues of PB ($KFe(III)[Fe(II)(CN)_6]$) and PW ($K_2Fe(II)[Fe(II)(CN)_6]$) can also be formed with other counter cations, replacing the intercalated potassium ions. The primary function of K^+ in the structure was to compensate for the negative charge imposed by the cyanide linkers (see Figures 3.8b and c). In many experimental studies of PB potassium containing electrolytes are used; therefore, potassium intercalation compounds are commonly found in the literature.[296, 297]

In order to test the influence of different alkali cations on the structural and electronic properties, all alkali metals A (A = Li, Na, K, Rb, Cs, Fr) were incorporated into Prussian blue and Prussian white (in hs-ls spin configurations) and calculated with both HSE03 and PBEsol+U. Henceforth a complete database of PB related compounds $AFe(III)[Fe(II)(CN)_6]$ (A-PB) and PW related compounds $A_2Fe(III)[Fe(II)(CN)_6]$ (A_2-PW) is set up and given in Tables 3.8 and 3.9.

It was found that the smaller alkali metals Li^+ and Na^+ preferentially occupy the *faces* of the lattice, instead of the tetrahedral holes, as shown in Figure 3.11. These henceforth called *face*-Li and *face*-Na PB and PW compounds are also listed in Tables 3.8 and 3.9. In the case of *face* PW various occupations can be envisaged: The cations can either occupy parallel faces, i.e. {100} and {200} sets of planes, as it is found for *face*-Na-PW (0.02 eV more stable with PBEsol+U) and shown in Figure 3.11c; or they can lie at diagonal faces, i.e. in the {222} set of planes such as in *face*-Li-PW (1.03 eV more stable with PBEsol+U) and shown in Figure 3.11b.[†]

Intercalation onto the faces of PB compounds leads to a descent from cubic symmetry because the negatively charged cyanide ligands bend towards the positively charged cation, hence distorting the structure and stabilising it due to the electrostatic ligand–cation interaction.

Larger metal cations (K^+, Rb^+, Cs^+, Fr^+) do no longer fit well

---

[†]Also other configurations than intercalation into *face* positions or tetrahedral holes may be anticipated for smaller cations, as described in a report by Ling *et al.*[298]

in the square-planar holes on the *fcc* faces and prefer to occupy the tetrahedral holes in their ground state. Indeed, *face*-K-PB, with potassium on its faces is destabilised by 0.26 eV (PBEsol+U) compared to regular K-PB with tetrahedral intercalation.
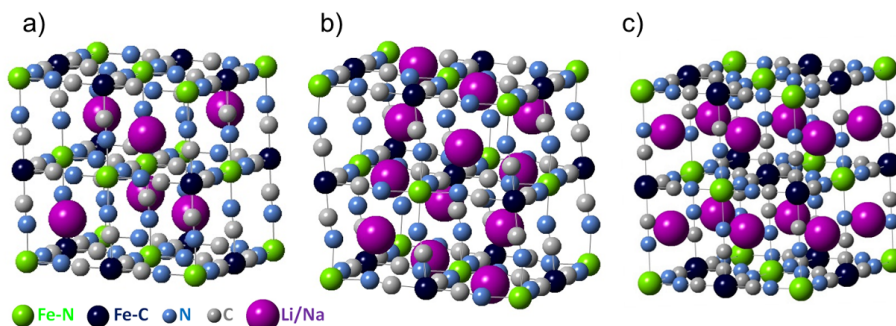
Figure 3.11: Crystal structures of the intercalation compounds with small alkali cations Li^+ and Na^+: a) *face*-Li-PB/*face*-Na-PB, b) *face*-Li-PW, and c) *face*-Na-PW.

Generally, the lattice parameter increases with alkali cation size from Li^+ to Fr^+, which is shown in Figure 3.12a. This effect is more pronounced in PW-like structures as they incorporate twice as much counter cations (in all the tetrahedral holes). Moreover, HSE03 yields a higher relative lattice expansion than PBEsol+U (see Figure 3.12a). The largest 2% expansion from about 10.2 Å to 10.4 Å is observed for A_2-PW with HSE03 when going from Li^+ to Fr^+. This demonstrates the high flexibility of the Prussian blue lattice, which is able to adapt to larger intercalation compounds by lengthening its metal–ligand coordination bonds (Fe–N and Fe–C distances increase, while the strong C–N bond remains constant). Sodium lattices, Na-PB and Na-PW, with a relative small lattice parameter compared to all other intercalation compounds, constitute an exception. The reason, however, cannot be deduced from its structural and electronic properties.

As seen in Tables 3.8 and 3.9, the charges and magnetic moments are not significantly altered for ions incorporated into tetrahedral holes, since the effect of the counter cation on the electronic structure is negligible. The charge of the alkali metal cation decreases slightly from 0.98 to 0.92 $|e|$ along the series, as the ratio q/r, thus the charge concentration decreases with cation size. Also the band gap of A-PB is merely affected by the counter cation, only with HSE03 a small decrease of $\sim$0.1 eV along the series is observed. Previous reports suggest a change in band gap either due to cation-lattice interaction[299] or lattice expansion;[276] the latter, geometric effect, is in better agreement with the obtained results.

Table 3.8: Main parameters of the Prussian blue like intercalation compounds hs-ls $AFe[Fe(CN)_6]$ (A-PB), with A occupying *half of* the tetrahedral holes, obtained with PBEsol+U (U^{eff} = 5.5 eV) and HSE03.

Functional	PBEsol + U								HSE03							
A-PB	Li	*face-Li**	Na	*face-Na**	K	Rb	Cs	Fr	Li	*face-Li**	Na	*face-Na**	K	Rb	Cs	Fr
a, Å	10.196	a=b=10.186 c=10.180†	10.194	a=b=10.251 c=10.174†	10.204	10.205	10.219	10.227	10.153	a=b=10.142 c=10.135†	10.004	a=b=10.068† c=9.981	10.184	10.191	10.211	10.223
E_g, eV	1.17	1.49	1.72	1.59	1.71	1.71	1.68	1.68	2.04	1.89	2.20	2.09	1.94	1.94	1.90	1.90
E_{face}, eV		-1.03		-0.43	+0.26					-1.02		-0.38				
q_{Fe-N}, $|e|$	+1.86	+1.83	+1.84	+1.87	+1.86	+1.86	+1.86	+1.41	+1.91	+1.88	+1.88	+1.92	+1.86	+1.91	+1.92	+1.91
q_{Fe-C}, $|e|$	+1.07	+0.95	+1.05	+1.07	+1.08	+1.08	+1.08	+0.61	+1.12	+0.99	+1.08	+1.08	+0.76	+1.13	+1.14	+1.14
q_A, $|e|$	+0.98	+0.92	+0.96	+0.89	+0.93	+0.91	+0.90	+0.92	+0.99	+0.92	+0.97	+0.89	+0.94	+0.92	+0.92	+0.93
μ_{Fe-N}, μ_B	4.22	4.21	4.22	4.22	4.22	4.22	4.22	4.22	4.15	4.15	4.13	4.13	4.15	4.15	4.15	4.15
μ_{Fe-C}, μ_B	0.17	0.17	0.17	0.17	0.17	0.17	0.17	0.17	0.27	0.27	0.27	0.27	0.27	0.27	0.27	0.27

Table 3.9: Main parameters of the Prussian white like intercalation compounds hs-ls $A_2Fe[Fe(CN)_6]$ (A_2-PW), with A occupying *all* tetrahedral holes, obtained with PBEsol+U (U^{eff} = 5.5 eV) and HSE03.

Functional	PBEsol + U								HSE03							
A_2-PW	Li	*face-Li**	Na	*face-Na**	K	Rb	Cs	Fr	Li	*face-Li**	Na	*face-Na**	K	Rb	Cs	Fr
a, Å	10.256	a=b=10.329 c=10.245†	10.289	a=b=10.412 c=10.343†	10.289	10.294	10.316	10.334	10.246	a=b=10.269 c=10.006†	9.982	a=b=10.102 c=10.004†	10.363	10.372	10.412	10.433
E_g, eV	cond.	2.48	cond.	2.74	cond.	cond.	cond.	cond.	2.53	2.75	2.40	2.61	2.62	2.67	2.60	2.70
E_{face}, eV		-1.03		-1.87						-2.32		-1.06				
q_{Fe-N}, $|e|$	+1.47	+1.50	+1.40	+1.45	+1.47	+1.47	+1.48	+1.48	+1.46	+1.54	+1.31	+1.57	+1.49	+1.49	+1.50	+1.50
q_{Fe-C}, $|e|$	+0.88	+0.85	+0.88	+1.02	+0.88	+0.88	+0.88	+0.88	+0.84	+0.88	+0.64	+1.02	+0.82	+0.83	+0.82	+0.82
q_A, $|e|$	+0.98	+0.92	+0.95	+0.90	+0.93	+0.91	+0.90	+0.88	+0.98	+0.92	+0.94	+0.90	+0.94	+0.93	+0.91	+0.91
μ_{Fe-N}, μ_B	3.80	3.59	3.80	3.62	3.80	3.80	3.81	3.80	3.54	3.54	3.52	3.54	3.56	3.56	3.56	3.56
μ_{Fe-C}, μ_B	-0.05	0.03	-0.05	0.06	-0.05	-0.05	-0.05	-0.05	0.07	0.07	0.08	0.07	0.06	0.06	0.05	0.05

* For A = Li, Na, the counter cation prefers to occupy the faces of the *fcc*-PB/PW lattices to form *face*-Li, or *face*-Na, respectively. This structure is stabilised by E_{face}, w.r.t. intercalation into tetrahedral holes.

† Two different lattice parameters and specific bond lengths are obtained for *face*-Li and *face*-Na compounds as their intercalation on the lattice faces leads to a descent from cubic to tetragonal (*face*-Li-PB, *face*-Na-PB, *face*-Na-PW) or monoclinic (*face*-Li-PW) symmetry.

In the case of *face* PB or PW, the structural distortion as seen in Figure 3.11 is accompanied by a change in electronic structure due to the electrostatic interaction of the cyanide ligand with the counter cation. This effect is represented by the DOS (calculated with HSE03) in Figures 3.12b-d. While Li-PB and Fr-PB have similar electronic densities, the DOS of *face*-Li-PB varies significantly. Due to its symmetric distortion, the Fe t_{2g} and e_g sets are no longer degenerate and split into many bands (Figure 3.12d), which also leads to a decrease in the band gap.
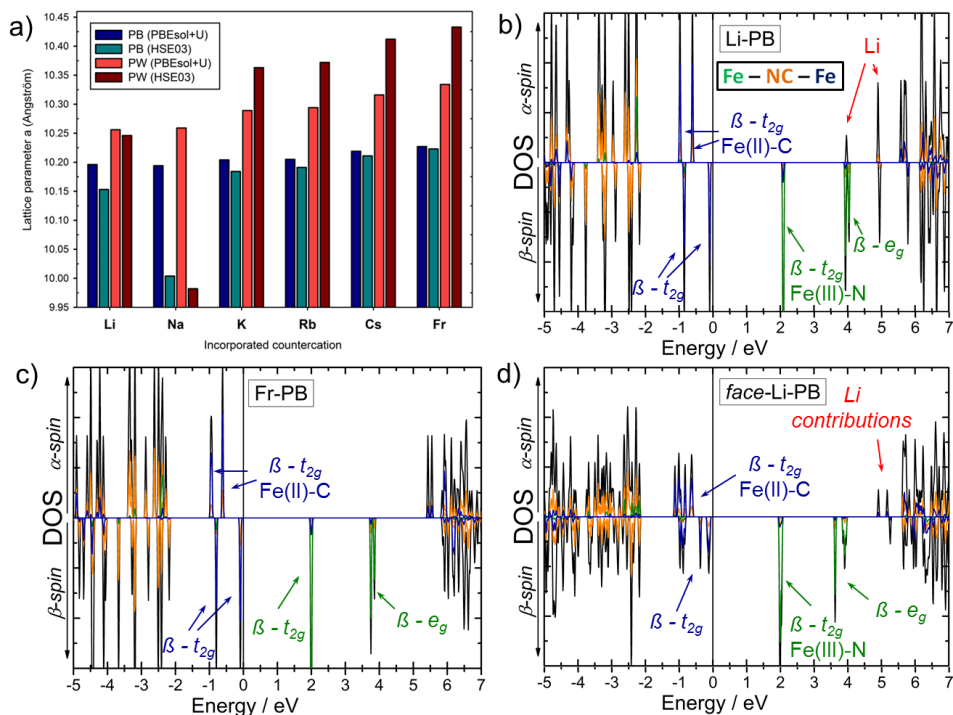
Figure 3.12: a) Variation of lattice parameter for different alkali metal cations incorporated in *half* (A-PB) or *all* (A$_2$-PW) of the tetrahedral holes, obtained by PBEsol+U (U^{eff} = 5.5 eV) and HSE03. b–d) Spin-polarised projected Density of States (DOS) of PB with Li$^+$, in both tetrahedral *face* positions, and Fr$^+$ counter cations, calculated with HSE03.

3.2 Cobalt iron Prussian blue catalysts

Cobalt hexacyanoferrate (CoFe-PB), the cobalt iron analogue of Prussian blue, is the active water oxidation catalyst in the studied photoelectrochemical systems. Instead of nitrogen coordinated irons, it contains cobalt atoms, which are assumed to be the catalytically active sites, where water oxidation takes place.[103,109,110,112] Like the parent compound iron hexacyanoferrate, it occurs a non-stoichiometric structure $A_x Co_y[Fe(CN)_6]_z \cdot nH_2O$ (with A being an alkali metal counter cation) with $Fe(CN)_6$ vacancies that lead to a Co:Fe ratio ranging from 1:1 to 3:2, which is highly dependent on the preparation conditions.[104,300,301]

A theoretical structure of regular CoFe-PB without defects (Co:Fe ratio is 1:1) is shown in Figure 3.13a (counter cations are omitted for clarity).
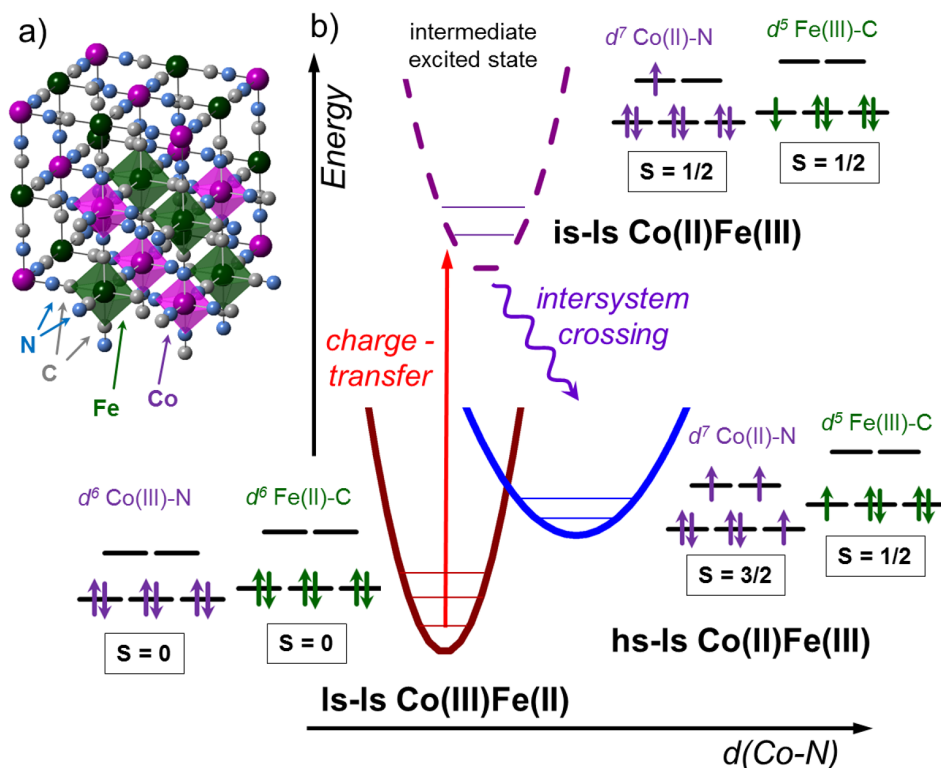
Figure 3.13: a) Regular, stoichiometric CoFe-PB ($A_x Co_y[Fe(CN)_6]_z \cdot nH_2O$, counter cations and incorporated water molecules are omitted for clarity) in crystal group $F\bar{4}3m$. b) Schematic representation of the potentials and spin states of ls-ls Co(III)Fe(II)-PB and hs-ls Co(II)Fe(III)-PB as a function of Co–N distance, which are related by charge-transfer (Fe → Co), followed by rapid intersystem-crossing. Adapted from Refs. [302] and [303].

105

It became famous as a magnetic switch,[304] in which long-range ordered magnetisation can be induced by light,[248,249,305,306] electric fields,[250] temperature,[249] or pressure.[302] The reason is that it can exist in two different magnetic configurations, which are dependent on their stoichiometry: ls-ls CoFe-PB ($A_x Co(III)_y [Fe(II)(CN)_6]_z$) and hs-ls CoFe-PB ($A_x Co(II)_y [Fe(III)(CN)_6]_z$) (Figure 3.13b).

The diamagnetic ls-ls CoFe-PB has both Co(III)–N and Fe(II)–C in a low-spin d^6 electronic state with filled t_{2g} orbitals. The ferromagnetic hs-ls CoFe-PB results when Fe(II)–C transfers a t_{2g} electron to the e_g set of Co(III)–N, which immediately (after fast spin-crossover/intersystem crossing)[303] forms a high spin $(t_{2g})^5 (e_g)^2$ state as shown in Figure 3.13.[252,307–310] This change from ls-ls CoFe-PB to hs-ls CoFe-PB, leading to *on-* and *off-* magnetisation, is therefore called a *charge-transfer induced spin transition* (CTIST) and leads to switchable magnetisation.[311]

In its hs configuration Co(II)–N has a half-filled, populated e_g set, and therefore a longer Co–N bond length as illustrated in Figure 3.13b. The potential difference of the two potential wells depends on the ratio of Co:Fe in the compound, which determines the coordination of cobalt centres,[301] as well as the counter cation,[312] which influences the relative redox potential of the $Co^{2+/3+}$ and $Fe^{2+/3+}$ redox couples. As larger the relative Co concentration, or the amount of vacant $Fe(CN)_6$ sites, respectively, as weaker is the ligand field surrounding the Co ions, hence, favouring an hs configuration.[249,302,313–315] The same argument applies for using smaller, more polarising counter cations, such as Na^+, which interact stronger with the negatively charged cyanide ligands and thus lead to a weakening of the Co-surrounding field.[312]

3.2.1 Calculations of CoFe-PB

Due to its interesting charge-transfer coupled magnetic behaviour, CoFe-PB has been challenging theoretical chemists and physicists since its discovery around two decades ago.[248,304] Verdaguer was pioneering the studies of magnetic interactions in metal hexacyanometallates, amongst them the cobalt iron derivative.[252,253,316] Also Harrison *et al.* and Nishino *et al.* investigated magnetic couplings in Prussian blue analogues. The dominant magnetic interaction was found to be double-exchange via the cyanide linker, while direct through space coupling is negligible.[317–319] Kawamoto, Asai, and Abe studied the detailed mechanisms of reversible photo-induced magnetisation in CoFe-PB, the variation of Co–N bond length and the importance of $Fe(CN)_6$ vacancies in the structure, which are key to the formation of the hs-ls CoFe-PB

configuration.[315, 320–322] Periodic DFT calculations at the GGA+U level of Kabir and van Vliet suggest that the presence of H_2O molecules is not a necessary criterion for the charge-transfer induced spin-crossover, but an intermediate symmetric distortion of the cobalt crystal field is required.[310] This deformation can be induced by structural vacancies, also confirmed by recent cluster model calculations of Krah *et al.*[323] The absorption properties of the ls → hs transition were further assessed by time-dependent studies of Kitagawa *et al.*[311]

In this work, the main interest is the function of CoFe-PB as an electrocatalyst when deposited on a semiconductor surface. Therefore, the electronic structure and its energetic alignment with the energy levels of the photoanode substrate is crucial. While the thermodynamic energy level alignment is the focus of Chapter 4, the electronic structure of CoFe-PB is discussed here.

Functional assessment

As it was shown in the Section 3.1, none of the employed functionals was able to unambiguously describe the electronic structure of Prussian blue derivatives. Not even the computationally expensive hybrid functionals, which are often used as benchmarks in periodic DFT calculations, managed to provide the correct conductive properties of reduced and oxidised PB due to overestimating the interband separations.

In this context, hybrid functional calculations for the CoFe-PB electronic structure are revised and further optimised. It is known that in the case of ligand-field splittings, such as t_{eg} and e_g in an octahedral environment, hybrid functionals with 20–25% exact exchange E_X^{HF} overstabilise high-spin states.[187, 295] The optimal amount of exact exchange depends on the interelectronic coupling, which in turn depends on the orbital symmetry. More symmetrical coordination compounds with near-degenerate ground states, and thus more correlation contributions, require less exact exchange than non-symmetric complexes with different quantum numbers on the same metal (d- or f-block) that are mainly connected by exchange.[188] Furthermore, in order to describe spin-crossover, which implies changes of the number of unpaired electrons, a smaller amount of exact exchange is often appropriate.[188]

It is mentioned that also density functionals on the GGA+U level of theory (with $U^{eff} = 3$ eV on Co and $U^{eff} = 5$ eV on Fe) have been found to give accurate electronic parameters. However, they lack in transferability. In order to compare electronic structures of the catalyst with different semiconductor materials, a unique functional,

which describes all materials is needed. For this purpose, more accurate hybrid functionals are clearly preferred.

As such, the hybrid functional HSE03 with a screening parameter of $\mu = 0.3$ Å^{-1} is chosen, as it is found most suitable for describing the band gaps of complex solids like PB.[181,182,184] The amount of introduced exact exchange E_X^{HF} is varied as shown in Table 3.10. For those calculations a regular stoichiometric *fcc* structure of KCo[Fe(CN)$_6$] is assumed (Figure 3.13a) with K$^+$ counter cations occupying half of the tetrahedral holes spanned by Co or Fe centres. The regular CoFe-PB with Co:Fe = 1:1 adopts an ls-ls ground state,[248,305,314] which is also consistently obtained for all E_X^{HF} fractions employed. As predicted though, the more E_X^{HF} is introduced, the more stable the hs-ls configuration gets with respect to the overall low-spin state.

Table 3.10: Main parameters of the ideal CoFe-PB (KCo[Fe(CN)$_6$]) obtained with HSE03[181,183] including varying amounts of exact Hartree–Fock exchange E_X^{HF}.

E_X^{HF}	E_{hs-ls}-E_{ls-ls}, eV	E_g, eV	$CFSE_{Co}$, eV	$CFSE_{Fe}$, eV	a, Å
0 %	0.88	1.17	2.34	4.16	9.862
10 %	0.84	1.96	3.49	5.02	9.853
13 %	0.77	2.21	3.86	5.24	9.852
15 %	0.69	2.38	4.09	5.44	9.852
20 %	0.49	2.81	4.71	5.89	9.851
25 %	0.27	3.24	5.32	6.37	9.855

Increasing E_X^{HF} leads to larger separation of bands. Hence, both the band gap, separating the t_{2g} *d*-bands at *different* metal centres, and the crystal field-splitting energy, separating the t_{2g} and e_g *d*-bands at *the same* metal centre, increase. The lattice parameter, on the contrary, is independent of the exact exchange introduced.

Figure 3.14 shows the increase of the band gap of KCo[Fe(CN)$_6$] with the amount of Hartree–Fock exchange E_X^{HF} introduced in a range-separated hybrid functional based on HSE03. The band gap transition (E_g = 2.25 eV),[248,305,314] which results from the electron transfer from Fe(II) t_{2g} to Co(III) e_g (Figure 3.13b), is taken as a fitting criterion to determine the optimal amount of E_X^{HF}. At E_X^{HF} = 13% a band gap of 2.26 eV is obtained, in agreement with the experimental result.[248,305] This result is consistent with the foregoing argument, that a reduced amount of exact exchange leads to a better description of complex transition metal containing solids, and with the literature values of ideal exact exchange in those

compounds, which are usually in a range of 10 to 15%.[185–190, 295]
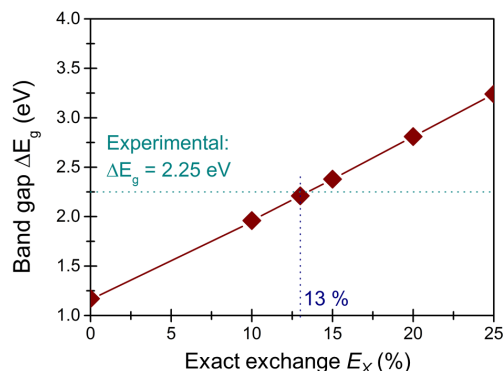
Figure 3.14: Variation of the band gap of CoFe-PB with the amount of exact Hartree-Fock exchange E_X^{HF} introduced in a range-separated hybrid functional based on HSE03.[181, 184]

As a consequence, I used this HSE03 functional with 13% exact exchange, henceforth called *HSE03-13*, for all other remaining electronic structure calculations presented in this Thesis.

3.2.2 Comparison of magnetic configurations

Figure 3.15 shows the electronic structure of the ls-ls configuration of KCo[Fe(CN)$_6$]) compared to its hs-ls state. In order to align both DOS, a H$_2$O spectator molecule is incorporated in one of the tetrahedral holes and its O 2s orbital energies were taken as common reference.[324] (The method for aligning electronic structures is further discussed in Section 4.6.2.)

In the ls-ls state on the left, the occupied Fe t_{2g} are separated by 2.26 eV (the charge-transfer band gap) from the empty Co(III) e_g set. After the electron has transferred from an Fe(II) t_{2g} orbital to Co, that Fe t_{2g} set loses its degeneracy and splits into several states. Out of those, the now empty $\beta-t_{2g}$ shifts up in energy above the valence band maximum (blue dashed line, shown on the right of Figure 3.15). After rapid spin-crossover the hs Co(II) d electrons fully populate the $\alpha-t_{2g}$ and $\alpha-e_g$ states, which shift to lower energy. The empty $\beta-t_{2g}$ state in hs-ls CoFe-PB moves around 1 eV above the valence band maximum, higher in energy than $\beta-t_{2g}$ of Fe(III).
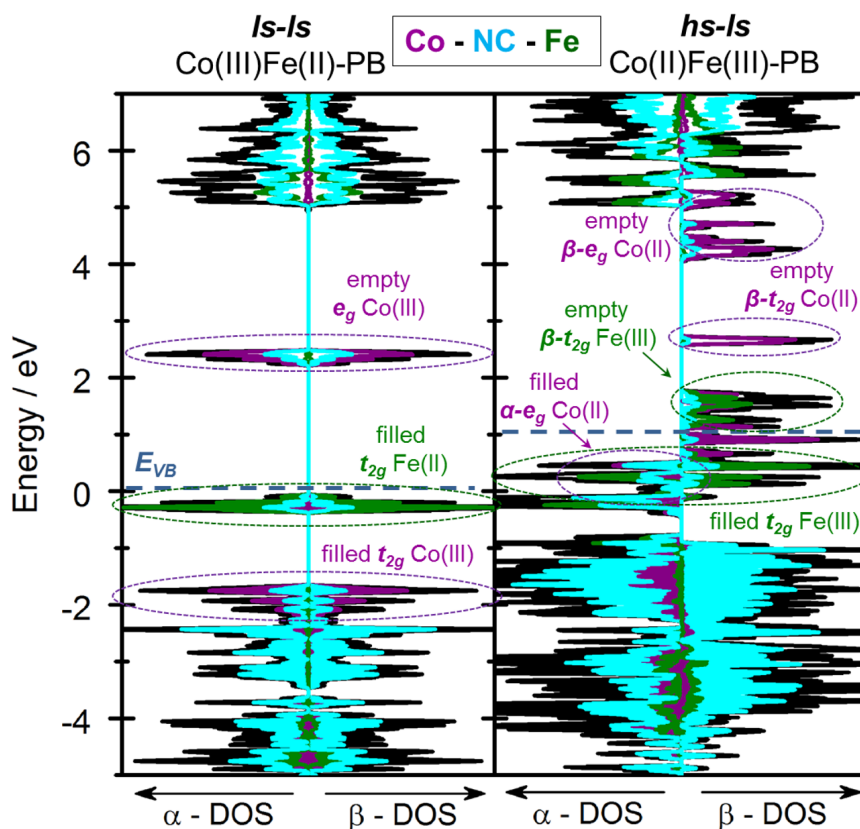
Figure 3.15: Density of States of ideal, stoichiometric ls-ls (on the left) and hs-ls (on the right) $KCo[Fe(CN)_6]$, aligned by core O $2s$ states of incorporated H_2O and with the valence band maximum (E_{VB}) of ls-ls CoFe-PB at zero eV (blue dashed line).

3.2.3 Introduction of defects

In order to understand the effect of introducing $Fe(CN)_6$ vacancies, $Co_4[Fe(CN)_6]_3 \cdot 6H_2O$ (with a Co:Fe ration of 4:3) is modelled and compared to ideal $KCo[Fe(CN)_6]$, as illustrated in Figure 3.16. Both structures are in their diamagnetic stable ls-ls ground state, with filled t_{2g} sets of Fe(II) and Co(III). Hence, only one spin channel is shown. The DOS are aligned by the cores Fe $3s$ states, which are expected to remain unchanged. In this case the O $2s$ of incorporated water could not be taken as a reference as it shifts upon coordination to Co in $Co_4[Fe(CN)_6]_3 \cdot 6H_2O$.
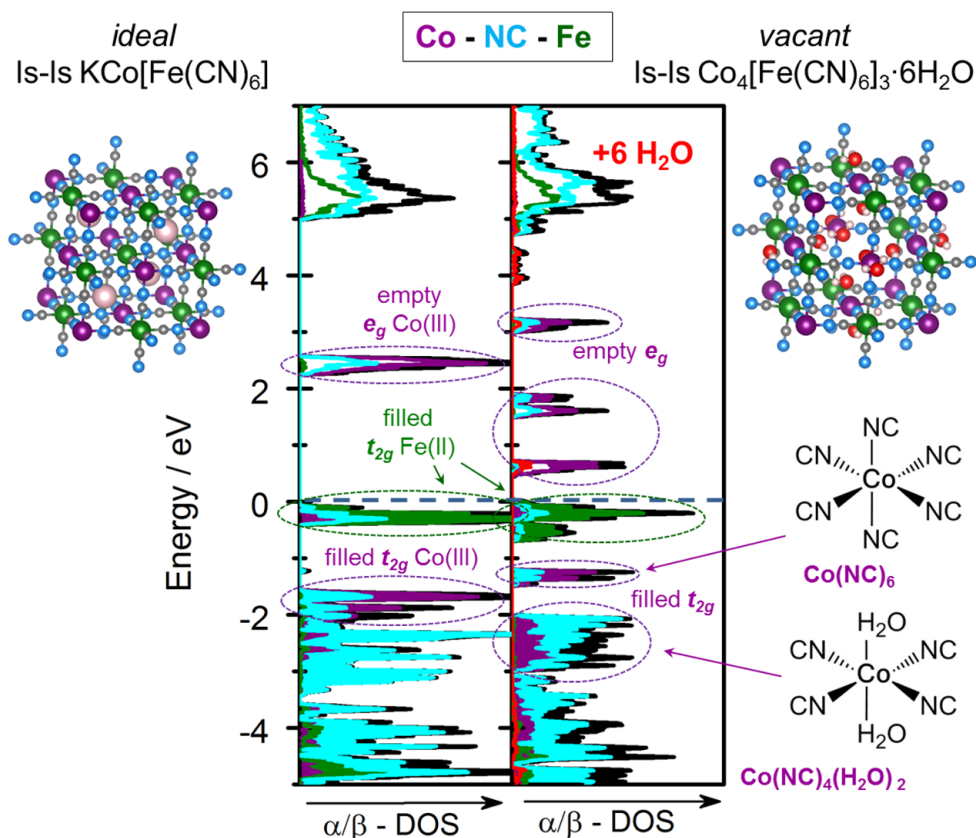
Figure 3.16: Density of States of ideal, stoichiometric ls-ls $KCo[Fe(CN)_6]$ (on the left) and ls-ls $Co_4[Fe(CN)_6]_3 \cdot 6\,H_2O$ (on the right), aligned by the core Fe $3s$ states and with the valence band maximum at zero eV (blue dashed line). The Co centres in $Co_4[Fe(CN)_6]_3 \cdot 6\,H_2O$ are no longer equivalent and divide into $Co(NC)_6$ and $Co(NC)_4 \cdot 2\,H_2O$. The energy levels of the latter are stabilised due to decreased anti-bonding metal ligand interactions.

In the case of $Co_4[Fe(CN)_6]_3 \cdot 6\,H_2O$, the four Co centres in the structure are no longer equal and have distinguishable electronic configurations, as shown on the right in Figure 3.16. Three Co atoms are coordinated by two H_2O molecules, which replace the NC-ligand, forming *trans*–$Co(NC)_4 \cdot 2\,H_2O$. One Co remains fully six-fold N-coordinated ($Co(NC)_6$).

The replacement of NC by H_2O on the $Co(NC)_4 \cdot 2\,H_2O$ centres leads to a descent of orbital symmetry, splitting the formerly degenerate t_{2g} and e_g orbital sets, while lowering their energies. Cyanide, when coordinating from its N-site, causes both t_{2g} and e_g to be slightly anti-bonding. Removing and replacing it by the only weakly coordinating H_2O decreases the anti-bonding character and thus stabilises the Co d orbitals.

The ls Fe(II) centre, on the other hand, is barely affected by the removal of one $Fe(CN)_6$ unit.

The effects of changing the electronic configuration by a charge-transfer coupled spin-crossover from an ls-ls to an hs-ls state, or introducing a $Fe(CN)_6$ vacancy into the unit cell, are summarised in Table 3.11.

Table 3.11: Main parameters of CoFe-PB in its ideal $KCo[Fe(CN)_6]$ and vacant $Co_4[Fe(CN)_6]_3 \cdot 6 H_2O$ structures, obtained with HSE03-13 and compared to experiments.[248, 305, 325, 326]

Structure	ls-ls $KCo[Fe(CN)_6]$	hs-ls $KCo[Fe(CN)_6]$	ls-ls $Co_4[Fe(CN)_6]_3$ $\cdot 6 H_2O$	exp.
a, Å	9.852	10.261	a=b=9.812 c=9.830‡	9.96(6)[305, 325]*
$d(Fe-C)$, Å	1.883	1.897	1.871–1.888‡	1.890(8)[326]†
$d(C-N)$, Å	1.166	1.167	1.159–1.174‡	1.167(7)[326]†
E_g, eV	2.26	*half-metallic*	0.38	2.25[248, 305]*
μ_{Co}, μ_B	0.0	2.80	0.00	
μ_{Fe}, μ_B	0.0	0.80	0.00	0.0*
q_{Co-N}, $|e|$	+1.39		+1.46–1.53	
q_{Fe-C}, $|e|$	+0.88		+0.96–0.98	

* CoFe-PB in ls-ls configuration.

† CoFe-PB in hs-ls configuration.

‡ When introducing an $Fe(CN)_6$ vacancy in the unit cell, the structure gets distorted and different bond lengths for all Co–N, Fe–C and C–N distances are obtained.

3.3 Metal oxide photoanodes

Metal oxides with appropriate band gaps and suitably aligned valence band levels are promising candidate materials for photoelectrochemical water oxidation.[32,34,37] This is due to their low cost device fabrication techniques, as well as their generally large resistance towards photo corrosion and low risk of toxicity.

In this work, I have studied the photoanode materials hematite (α-Fe$_2$O$_3$) and bismuth vanadate (ms-BiVO$_4$) and their interaction with cobalt iron Prussian blue. The electronic structures and computational assessment of those two oxide semiconductors are discussed in this Section.

3.3.1 Hematite: α-Fe$_2$O$_3$

Iron oxide belongs to the most abundant and cheapest materials on Earth and is therefore particularly attractive as light-harvesting semiconductor in a photoelectrochemical device.[36,38–40,327] In its hematite phase, α-Fe$_2$O$_3$, it has a band gap of around 1.9–2.2 eV, which allows for efficient light absorption in the visible region.[327] Its valence band edge, measured to be at 2.4–2.7 V vs RHE,[32,120,328] lies well below the water oxidation redox potential of 1.23 V vs RHE. Thus, hole transfer to water is thermodynamically favoured.

Yet the efficient implementation of hematite Fe$_2$O$_3$ (α is henceforth omitted) in light-activated water oxidation catalysis is hampered by its slow kinetics[120,215,222,243,329–333] and poor conduction properties.[334] The latter is due to trapping of photogenerated carriers as small polarons.[335–339]

Electronic structure of hematite

Hematite crystallises in a corundum structure with space group $R\overline{3}c$, presented in Figure 3.17a.[340] Lattice parameters are given in Table 3.12. Its iron centres are octahedrally coordinated by O atoms, but experience a longitudinal, Jahn–Teller-like distortion along the main axis in the hexagonal unit cell (Figure 3.17a).

In the formal ionic limit, Fe has an oxidation state of +3 in an electronic d^5 configuration. As the oxygen ligand field is relatively weak, a high-spin state ($t_{2g}^2 e_g^2$) is adopted with a theoretical magnetic moment of 5 μ_B. Those magnetic centres align antiferromagnetically along the principal axis due to angular superexchange interactions.[189,328,341]

The structure of Fe$_2$O$_3$ is modelled with the hybrid functional HSE03-13 (Figure 3.17), which has well described the electronic

structure of CoFe-PB. The obtained band gap of 1.95 eV matches well the experimental result (1.9–2.1 eV),[39,327] which indicates that the included 13% of exact exchange in HSE03 are also adequate for Fe_2O_3.
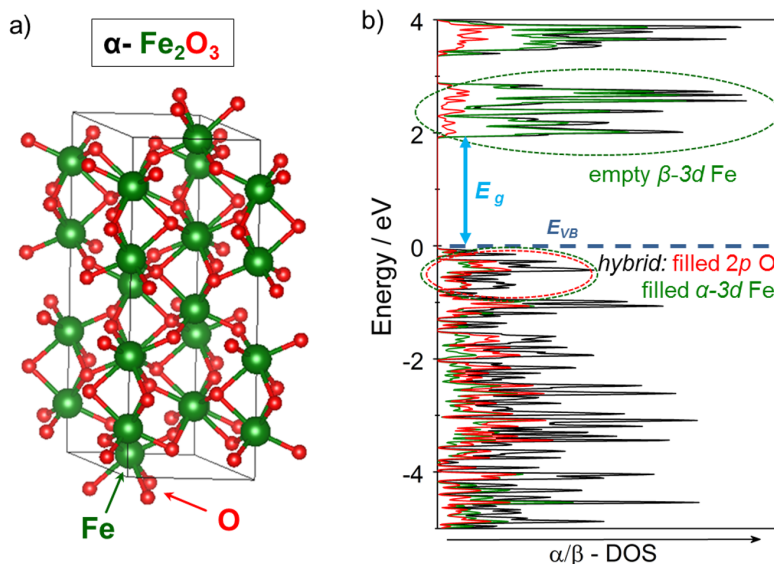
Figure 3.17: a) Crystal structure of the hexagonal unit cell (space group $R\bar{3}c$) and b) DOS (calculated with HSE03-13) of α-Fe_2O_3 referenced to the valence band maximum ($E_{VB} = 0$ eV). As the overall hematite structure is antiferromagnetic, α- and β-spin DOS are equal, but both spin states can be well distinguished at each Fe centre.

From the obtained Density of States (Figure 3.17b), it can be seen that the upper part of the valence band is composed of almost equal parts of O $2p$ states and half-filled Fe $\alpha - 3d$ states. This hybridisation of the strongly correlated Fe $3d$ levels with the band-like O $2p$ results from the symmetry distortion along the longitudinal axis,[341] which was also found by photoemission experiments.[342–345] The conduction band is mainly formed by empty $\beta - 3d$ states and a small $4s$ contribution of iron. Out of those, the d_{z^2} orbitals are slightly stabilised due to the longitudinal lattice distortion.

Because of the O $2p$ character of the valence band, the band gap absorption can be described by a ligand-to-metal $p \rightarrow d$ charge-transfer, which classifies hematite as a charge-transfer insulator (in contrast to a Mott-insulator, in which the gap is characterised by a metal $d \rightarrow d$ transition).[189,341–345] This transition hence shifts electron density from the O to the Fe centres, where it gets trapped as a small polaron.[339]

3.3.2 Bismuth vanadate: *ms*-BiVO$_4$

During the last two decades, bismuth vanadate has become one of the most important materials in photoelectrochemical systems.[42,43,52,346–349] Among the class of Earth-abundant metal oxide semiconductors, it has shown the highest performance in photoelectrocatalytic water oxidation up-to-date.[54]

Electronic structure of bismuth vanadate

Bismuth vanadate can occur in different crystalline phases, which are closely related. Although it is naturally adopting an orthogonal structure in the mineral pucherite, its monoclinic scheelite (*ms*-BiVO$_4$) structure is typically obtained under laboratory conditions and is the most catalytically active phase.[347] As it is the only phase studied in this work, the notation *ms* is usually omitted. Its crystalline structure is presented in Figure 3.18a and its lattice parameters given in Table 3.12. The space group in the conventional base-centred setting is *C/2c*, but also other settings like the body-centred *I2/b* are common to describe BiVO$_4$.[350]
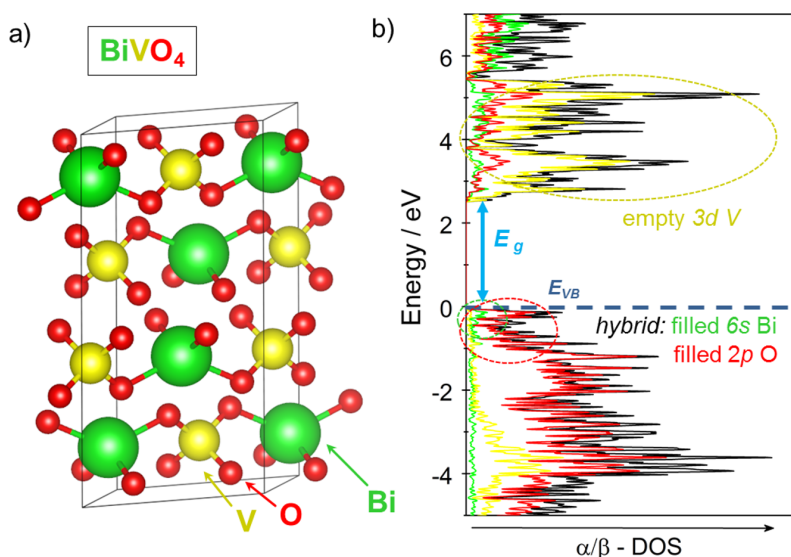
Figure 3.18: a) Crystal structure of the monoclinic-scheelite unit cell (space group *C/2c*) and b) Density of States (calculated with HSE03-13) of BiVO$_4$ referenced to the valence band maximum (E_{VB} = 0 eV).

It contains BiO$_8$ units and VO$_4$ tetrahedra, which are linked by bridging oxygens (Bi–O–V) and stacked along the main axis of the unit cell. Due to their monoclinic distortion, the metal–oxygen dis-

tances in VO_4 and BiO_8 are unequal, leading to two different V–O and three different Bi–O bonds.[351]

The electronic Density of States is given in Figure 3.18b. Since $BiVO_4$ has no unpaired electrons, it is diamagnetic and only one spin channel α/β–DOS is shown. In the delocalised limit, vanadium is in a formal oxidation state of +5 with empty $3d$ orbitals, which lie at the bottom of the conduction band. Bi has a formal oxidation state of +3. Its filled $6s$ electronic states are located at the top of the valence band where they hybridise with the oxygen $2p$ orbitals, forming a weak σ-type bond.[351,352] The impact of the $6s$ states on the VBM is enhanced by the symmetric distortion along the principal unit cell axis in the monoclinic scheelite phase.

The overlap of Bi $6s$ and O $2p$ allows for a better delocalisation of electronic density at the top of the valence band through the Bi–O bond. This facilitates transport of photogenerated holes in the VBM, which is why $BiVO_4$ is a better hole conductor than most other metal oxide semiconductors.

Comparison of Fe_2O_3 and $BiVO_4$

Table 3.12 shows a comparison between the two employed metal oxide semiconductor materials.

Table 3.12: Comparison of the calculated geometric and electronic properties of both Fe_2O_3 and $BiVO_4$, obtained with HSE03-13.

Structure	α-Fe_2O_3		$BiVO_4$	
	Calculated	Experimental	Calculated	Experimental
Lattice constants a,b,c, Å	a=b=5.025 c=13.765	a=b=5.036 c=13.749[36,39]	a=6.962 b=12.217 c=4.922	a=7.253 b=11.702 c=5.096[351,353,354]
Lattice angles α,β,γ, deg	$\alpha=\beta=90$ $\gamma=120$	$\alpha=\beta=90$ $\gamma=120$[36,39]	$\alpha=\gamma=90$ $\beta=134.99$	$\alpha=\gamma=90$ $\beta=134.07$–134.23 [351,353,354]
Metal–oxygen bond length $d(Me-O)$, Å	d(Fe–O)= 1.878– 2.222	d(Fe–O)= 1.985–2.060[355]	d(V–O)=1.709* d(Bi–O)= 2.327–2.557	d(V–O)=1.74–1.76 d(Bi–O)= 2.34–2.61[351,353,354]
Band gap E_g, eV	1.95	1.9–2.0[356]	2.46	2.4–2.5[324]
μ_{Fe}, μ_B	±3.85	±5.55[340]	-	-

* Both distinguishable V–O bond lengths, which result from monoclinic distortion, have shown only a small, nearly negligible, difference.

A good agreement between the calculated parameters and experimental data is obtained. In particular, the band gaps calculated with HSE03-13 match perfectly the experimental values.

This, in turn, highlights that HSE03-13 is not only suitable for adequately describing CoFe-PB, but also both employed metal oxide semiconductors. Indeed, the optimised fraction of 13% exact exchange E_X^{HF} is consistent with previous reports of Fe_2O_3 and $BiVO_4$; Pozun and Henkelmann employed HSE06 with 12% E_X^{HF} to describe Fe_2O_3,[189] and Kweon *et al.* included 15% E_X^{HF} to calculate polarons in $BiVO_4$.[190]

Both semiconducting metal oxides, like many other metal oxides, have O $2p$ orbitals at the top of the valence band, which appears to be a crucial to O_2 creation and hence the ability to drive efficient water oxidation.[329] Nonetheless, at the surface the electronic structure differs, and intragap states (*surface* or *trap* states) may impede efficient hole transfer and enhance electron–hole recombination, which is described later in the text.

3.4 Conclusion of Chapter 3

In summary, in the theoretical part of my Thesis, I carried out a detailed functional analysis for the case of Prussian blue. I have found that pure Density Functional approximations did not account correctly for the localised magnetic moments in the structure, leading to a wrong prediction of the ground state. With an empirically optimised Hubbard U parameter, DFT+U adequately describes PB, but is not sufficiently transferable between different PB-like compounds. Hybrid functionals have shown to overcorrect the self-interaction error of DFT by overestimating the amount of exact exchange introduced, which has led to wrong predictions of insulating behaviour in Prussian blue derivatives. The amount of exact exchange was therefore reduced and optimised to 13 % in HSE03 for cobalt iron Prussian blue. With this functional, also the properties of the photoanode materials were correctly predicted.

Moreover the electronic structures and charge-transfer properties of Prussian blue analogues and metal oxide compounds were discussed. In this context, the influence of i) spin-crossover, i.e. changing the spin state of the metal centre; ii) reducing or oxidising PB; iii) different counter cations; and iv) of hexacyanoferrate vacancies was assessed.

The energetic alignment of their electronic Densities of States, which is crucial to their function in PEC devices, is discussed in the next Chapter (in Section 4.6.2). The details of the computational methods can be found in the Appendix B.

Chapter 4

Cobalt iron Prussian blue modified photoanodes

In this Chapter the application of cobalt hexacyanoferrate, CoFe-PB, as a water oxidation co-catalyst on the photoactive metal oxides Fe_2O_3 and $BiVO_4$ is assessed. The aim of this work was to i) develop a synthetic route to modify the semiconductor materials with CoFe-PB; ii) to study the effect of CoFe-PB on the water oxidation activity; and iii) to investigate the mechanisms by which a performance enhancement occurs.

First, synthetic methods and characterisation of the combined photoanode systems are described. Their photoelectrochemical (**PEC**) behaviour is evaluated and further investigated by hole scavenger and impedance experiments. Moreover, the computed electronic structures are aligned and the thermodynamic feasibility of charge-transfer is deduced. This work has been published in *Papers II* (CoFe-PB/Fe_2O_3) and *III* (CoFe-PB/$BiVO_4$).

4.1 Importance of the semiconductor–catalyst interface

The semiconductor–catalyst interface is key to successful PEC performance. The fact that both Fe_2O_3 and $BiVO_4$ are commonly employed photoanode materials, and that CoFe-PB is an efficient water oxidation catalyst, does *not* guarantee water oxidation enhancement of the combined CoFe-PB/Fe_2O_3 and CoFe-PB/$BiVO_4$ systems. Indeed, many examples in the literature show that often the co-catalyst does not actually catalyse the OER when deposited on a light absorbing semiconductor, despite its original electrocatalytic activity.[87,101,102,132,133,217,357,358] Two of such interfaces their underlying physical mechanisms are discussed in this Chapter.

4.2 Synthesis

4.2.1 Hematite: α-Fe$_2$O$_3$

Thin films of Zr-doped hematite electrodes were prepared by a modified electrodeposition method adapted from Ref. [359] (described in Appendix A). Doping with Zr increases the n-type conductivity and thus the performance of Zr-Fe$_2$O$_3$ (the label Zr is henceforth omitted). In contrast to Ref. [359], the Zr-doped Fe films were calcined at 800 °C, instead of 450 °C,[359] in order to ensure complete oxidation of Fe and removal or organic impurities. Higher calcination temperatures are assumed to be beneficial due to passivation of surface states, as well as additional Sn-doping from the flourine-doped Sn oxide (FTO) substrate.[360] Deformation of the FTO at such high temperatures, however, adversely affects the conductivity of the substrate. Annamalai *et al.* found that an annealing time of 10 min provides an optimum compromise between those two effects.[361]

Nonetheless, this influence on heating time could not be confirmed in this study. I carried out an optimisation of calcination time for a range of times between 5 min and 1 h. Figure 4.1a shows the photocurrent evolution of two distinct Fe$_2$O$_3$ samples (denoted as (1) and (2)), heated for different times. Although there are variations of the maximum photocurrent and onset potential (nearly up to 0.2 V), those differences cannot directly be correlated with the effect of heating time. Furthermore, the high photocurrents obtained in Ref. [360] (> 1 mA/cm^2) were not reached.

Even small variations in the preparation process, i.e. in the electrodeposition conditions, or varying the exact position in the oven, and thus the heat gradient experienced, may cause a large difference in the PEC characteristics and therefore lead to bad reproducibility. In average, however, the behaviour of all prepared hematite samples is similar and well distinguishable to the performance of catalyst modified samples. In order to determine the effect of the catalyst, it is crucial though to always compare the *same* Fe$_2$O$_3$ electrode with and without catalyst.

Although Fe$_2$O$_3$ performs much better in alkaline solution (Figure 4.1b), a neutral environment was preferred in this work. In strong alkaline solution, the CoFe-PB catalyst might decompose and form oxidic Co structures (CoO$_x$, CoOOH, Co(OH)$_x$), which I wanted to avoid.[110,113] Moreover, the corresponding hydrogen evolution half-cell reaction is less favourable at high pH.[79,80] Therefore, all experiments in the following discussion are conducted in a potassium phosphate (KP$_i$) buffer at pH 7.
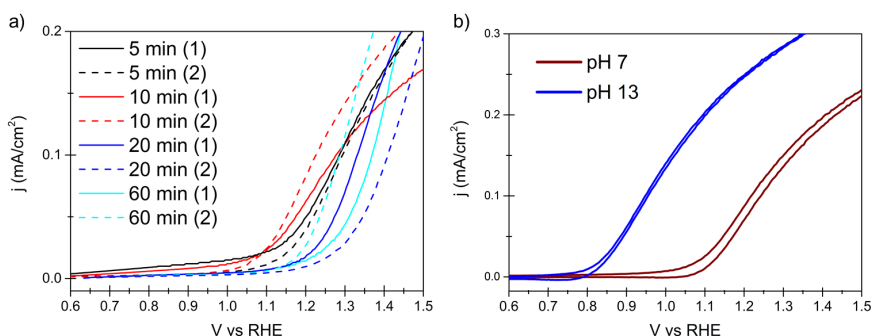
Figure 4.1: Cyclic voltammogrammes (50 mV/s) of unmodified Zr-doped Fe_2O_3 under 1 sun illumination. a) Anodic scans of Fe_2O_3 samples , which were calcined for 5 (black), 10 (red), 20 (blue) and 60 (turquoise) minutes, two for each temperature (solid (1) and dashed (2) lines) in neutral (0.1 MKP_i) buffer. b) Fe_2O_3 in pH 13 (0.1 M KOH) and pH 7 (KP_i buffer).

It has to be mentioned that in the experiment all hematite electrodes are illuminated from the front site, in order to shorten the path for the photogenerated holes to the surface. When illuminated through the FTO substrate, a drastically reduced photocurrent was obtained which is due to the very small hole diffusion lengths between 2 and 20 nm in Fe_2O_3.[40,329]

4.2.2 Bismuth vanadate: *ms*-BiVO$_4$

Thin-film *ms*-BiVO$_4$ electrodes were prepared following a simple and cost-effective electrodeposition method by Kang *et al.* (described in Appendix A).[362] Nanostructured films with thickness of about 200–250 nm (Figures 4.4e and f) were obtained.

In accordance to the observations made for hematite, variations in performance were observed for different BiVO$_4$ samples. This can be related to an inhomogeneous coverage of Bi metal during electrodeposition, or the heat gradient in the oven during the calcination process. Consequently, in order to draw a conclusion of the effect of the catalyst on BiVO$_4$, always the *same* BiVO$_4$ film before and after catalyst modification is compared.

In contrast to Fe_2O_3, BiVO$_4$ films were illuminated from the back site, through the FTO glass substrate. This is because BiVO$_4$ is a much better hole conductor, facilitated through the Bi 6s contribution to the valence band (see Section 3.3.2), but has only short electron diffusion lengths (70–100 nm).[363,364]

4.2.3 Sequential coating of CoFe-PB

The photoanodes were modified with the CoFe-PB catalyst by a se-
quential coating method, as described in the Appendix A. In brief,
the electrodes were first dipped in a $[Fe(CN)_6]^{3-}$ precursor solution,
so that the negatively charged iron cyanide complexes can bind to
the undercoordinated surface metal atoms (Fe or Bi) of the semicon-
ductor. Afterwards, the electrodes were dipped in a Co^{2+} containing
solution, in order to allow Co^{2+} to coordinate to surface oxygen or
the negatively charged N-site of the cyanide complexes, and to form
CoFe-PB. Repeating the dipping sequence gives rise to the forma-
tion of a three-dimensional complex Prussian blue structure, which
is thermodynamically largely favoured.[110, 365]

The amount of dipping cycles plays only a minor role in perfor-
mance, as shown in Figure 4.2. It was repeated at least two times
to ensure a non-negligible catalyst deposition, but for more dipping
cycles no clear trend in activity can be observed. Due to the large
variations in the PEC characteristics of the electrodeposited metal
oxide photoanodes and the inhomogeneous deposition of the cata-
lyst, a quantitative systematic assessment of the optimum deposi-
tion cycles cannot be made.
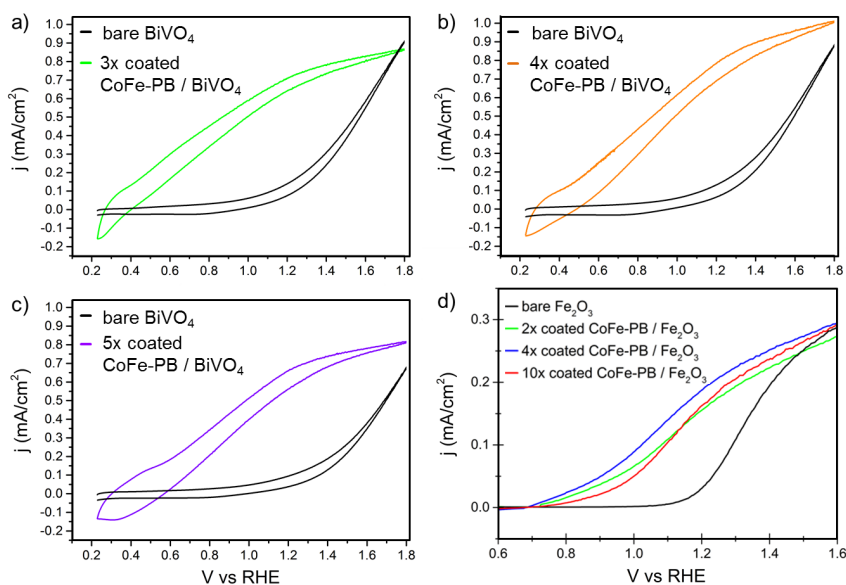
Figure 4.2: Cyclic voltammogrammes (50 mV/s) of sequentially coated
CoFe-PB photoanodes with varying dipping repetitions under 1 sun illumi-
nation at pH 7. a–c) $BiVO_4$ with a) 3x, b) 4x, and c) 5x CoFe-PB coated
$BiVO_4$. d) Anodic scans of Fe_2O_3 with 2x (green), 4x (blue), and 10x (red)
CoFe-PB coating.

This deposition method is advantageous due to its mild deposition conditions (aqueous solution at pH 7, room temperature and no applied electro(magnetic) fields), which do not damage the underlying metal oxide semiconductor. Moreover, it ensures a very thin catalyst layer (< 50 nm, see Section 4.3.1), which is desirable for a non-conducting catalyst, in order to allow for efficient charge transport and ionic permeability through the catalyst.[70]

Other deposition methods were also envisaged, namely electrodeposition and dip-coating the electrodes in a CoFe-PB nanoparticle dispersion (Figure 4.3). Electrodeposition was previously used by Pintado *et al.* for depositing CoFe-PB as an electrocatalyst on fluorine-doped tin oxide (FTO) coated glass slides.[103] Nonetheless, electrodeposition on $BiVO_4$ results in photoanode damage, which drastically decreases the photocurrent, as shown in Figure 4.3a. The loss of PEC performance is likely to be due to the applied cathodic potential (-0.28 V_{RHE}) for depositing metallic cobalt in the first step of the electrodeposition method. This potential can reduce V^{5+} and Bi^{3+} in the structure and thus decompose $BiVO_4$.
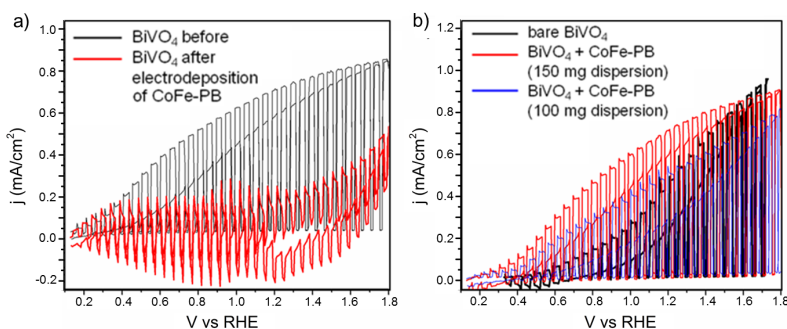
Figure 4.3: Cyclic voltammogrammes (50 mV/s) under 1 sun irradiation and chopped light (chopping frequency 1 Hz) at pH 7 of $BiVO_4$ (black) after a) electrodeposition of CoFe-PB, and b) deposition of CoFe-PB nanoparticles.

Dipping the $BiVO_4$ electrodes in a CoFe-PB small (around 50 nm) nanoparticle dispersion for several days, leads to large enhancement of PEC performance (Figure 4.3b), akin to the sequentially coated $BiVO_4$ electrodes. Notwithstanding, the sequential coating method is preferred, as it allows for chemisorption of CoFe-PB by forming coordination bonds with the surface atoms. The nanoparticles, in contrast, are electrostatically attached to the surface, and therefore may fall off over time.

Also a hydrothermal deposition method, as developed by Han *et al.*, for CoFe-PB on FTO could be considered.[110] This method yields

highly stable, thick CoFe-PB layers, which show largely enhanced *electrocatalytic* performance. Those thick (on the order of μm) catalyst layers, however, are disadvantageous for being deposited on a photoanode material as they block light absorption and hinder conduction of photogenerated charge carriers to the surface.

4.3   Characterisation

4.3.1   Scanning and transmission electron microscopy

In order to determine the morphology of the nanostructured metal oxide films and the deposited CoFe-PB catalyst, scanning electron microscopy (**SEM**) and transmission electron microscopy (**TEM**) were carried out. Figure 4.4 shows the scanning electron micrographs of bare $BiVO_4$ (Figures 4.4a,b,e) and CoFe-PB modified $BiVO_4$ (Figures 4.4c,d,f).
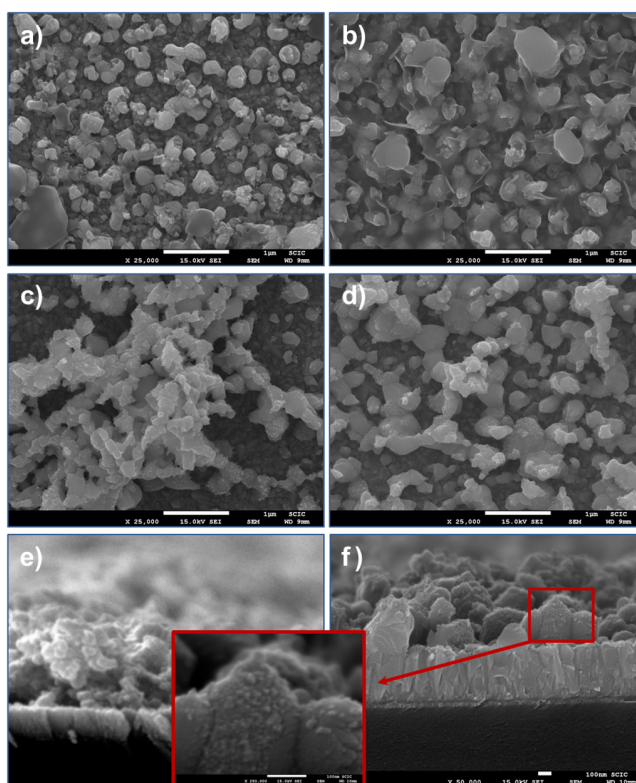
Figure 4.4: Zenithal SEM images of a) freshly prepared and b) electrochemically treated bare $BiVO_4$, and c) freshly prepared and d) electrochemically treated CoFe-PB/$BiVO_4$ (25000x magnified). Cross-sectional SEM images of d) bare $BiVO_4$ and e) CoFe-PB-modified $BiVO_4$.

In the zenithal images (Figures 4.4a–d), the application of CoFe-PB is barely visible. In the higher magnified cross-sectional image (inset in Figure 4.4f), very small surface particles can be seen, which could be identified to be CoFe-PB by energy-dispersive X-ray (**EDX**) microanalysis. The surface coverage of Co and Fe was found to be < 1%, with a slightly higher percentage of Co than of Fe. This confirms that the sequential dipcoating method leads to a very low catalyst loading.

To study the effect of ageing under photoelectrochemical water oxidation conditions, the electrodes were irradiated with 1 sun illumination at an applied voltage of 1.23 V_{RHE} for one hour and measured again (Figures 4.4b and d). It seems like the photoelectrochemical treatment softens the edges of the nanocrystallites on the surface, but no substantial change in morphology occurs, neither to bare nor to catalyst modified $BiVO_4$.

An analogous effect was obtained for the hematite electrodes, as shown in Figure 4.5. Only very small amounts of less than 1 % of CoFe-PB catalyst could be detected by EDX microanalysis.

For the sake of comparison, also the surface of the bare CoFe-PB catalyst is shown (Figure 4.5d). CoFe-PB on FTO was obtained, following the solvothermal method of Han *et al.*, as described in Appendix A. The face-centred cubic CoFe-PB forms a microporous layer of cubic crystallites of the order of 500 nm to 1 μm, consistent with literature.[110]
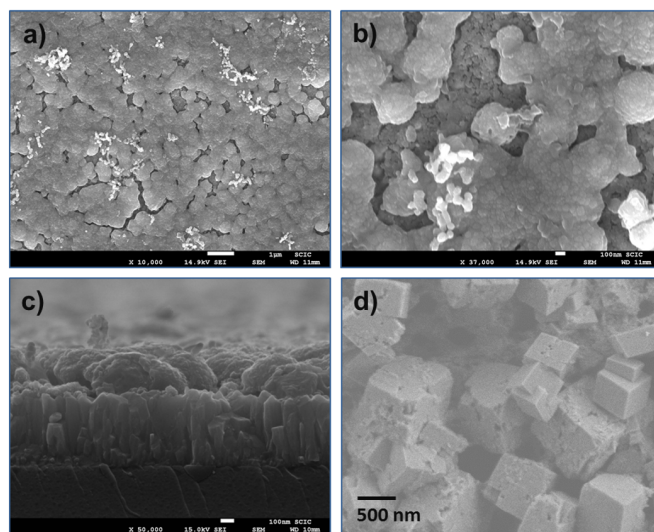
Figure 4.5: Zenithal SEM images of CoFe-PB modified Fe_2O_3 in a) 10000x and b) 37000x magnification. c) Cross-sectional SEM image of CoFe-PB/Fe_2O_3 (50000x magnified). d) Nanocubes of solvothermally deposited CoFe-PB catalyst.

High resolution TEM reveals the presence of very small (30–60 nm) CoFe-PB nanoparticles (framed in red) on the surfaces of $BiVO_4$ and Fe_2O_3, which are shown in Figures 4.6 and 4.7. In order to confirm that those small particles are indeed CoFe-PB, microanalysis with EDX was performed and their chemical composition elucidated. They are found to contain mainly Co and Fe in ratios $\gtrsim$ 1:1, which lies in the stoichiometric possible range of Co:Fe compositions between 1:1 ($KCo[Fe(CN)_6]$) and 3:2 ($Co_3[Fe(CN)_6]_2 \cdot nH_2O$).[104, 300, 301] This indicates that CoFe-PB has been successfully deposited on the metal oxides by sequential coating.
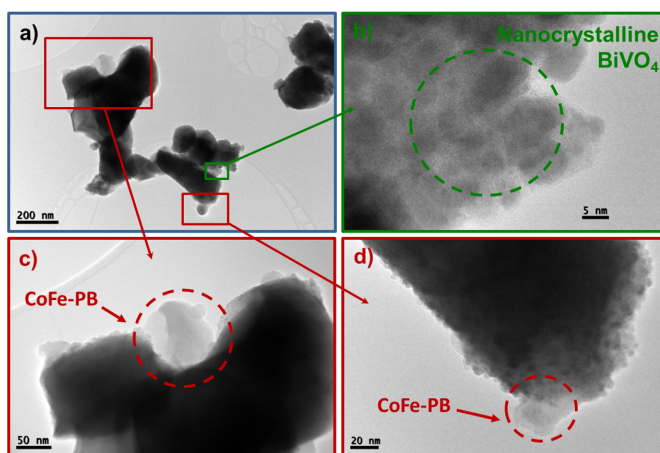
Figure 4.6: High resolution transmission electron micrographs of a) a large CoFe-PB/$BiVO_4$ particle with b) nanocrystalline surface region of $BiVO_4$, and c,d) amorphous CoFe-PB particles at different surface regions.
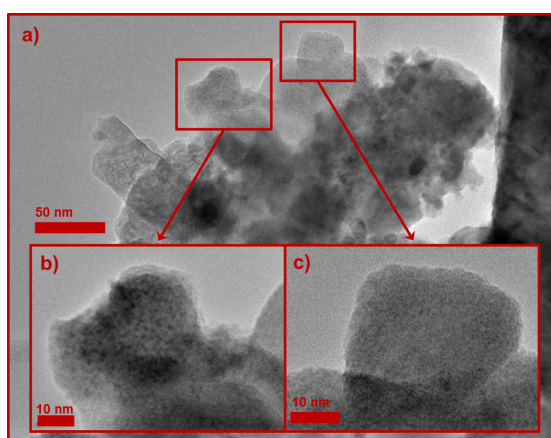
Figure 4.7: High resolution transmission electron micrographs of a) a CoFe-PB/Fe_2O_3 particle with b,c) nanocrystalline CoFe-PB.

On the $BiVO_4$ surface, CoFe-PB is formed mainly on the corners and edges as an *amorphous* phase (Figures 4.6 c and b), i.e. with no long-range ordering, detectable as lattice fringes in the TEM image. Small nanocrystalline surface formations are also found (Figure 4.6b); but they could be clearly identified as $BiVO_4$ only, since they did not contain any Co and Fe constituents. The lattice spacings of the $BiVO_4$ phase were measured to lie between 0.28–0.31 nm, corresponding to the $\{\overline{1}21\}$ and $\{040\}$ sets of planes.[324]

The composition of bismuth vanadate in the bulk was found by EDX to be 1:1, in accordance with $BiVO_4$ stoichiometry. On the surface, however, an excess of Bi was found with a detected Bi:V ratio of 1:1 to 1:6. which could be ascribed to a (partial) formation of Bi_2O_3 on the surface, and/or vacant VO_4 sites (also the O content is diminished at the surface). Such a Bi segregation at the surface was also observed by Rossell *et al.*,[366] and was seen in other Bi-containing oxides, like Bi_2SnO_7,[367] $BiMoO_6$,[368] and $BiFeO_3$.[369]

One major difference between the CoFe-PB particles on $BiVO_4$ and Fe_2O_3 is their crystallinity. While CoFe-PB on $BiVO_4$ seems to be amorphous (Figure 4.6), CoFe-PB crystallites with well-visible lattice planes (Figure 4.7) are formed on hematite. A likely explanation for this difference is the degree of *wetting*, i.e. adhesion of CoFe-PB to the metal oxide surface, which is related to the lattice (mis)matching of the crystal structures, as shown in Figure 4.8.
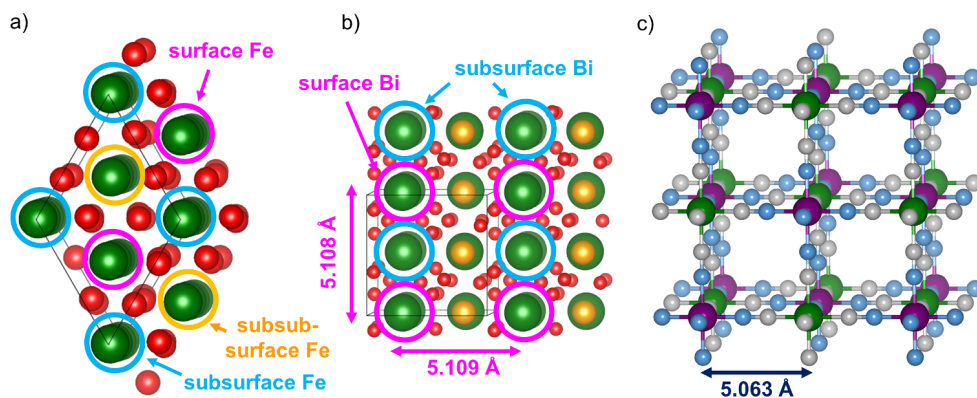
Figure 4.8: Representations of the crystal structures of a) the predominant (0001) surface of Fe_2O_3, b) the predominant (001) surface of $BiVO_4$, and c) the bulk structure of CoFe-PB (colour code: green = Fe (in a and c) or Bi (in b), yellow = V, purple = Co, red = O, blue = N, grey = C).

The most stable termination of hematite is the hexagonal (0001) surface (Figure 4.8a), which is incommensurate with the cubic CoFe-PB lattice (Figure 4.8c). This mismatch does *not* allow for the Co

and Fe centres in CoFe-PB to form Co–O–*Fe* or Fe–CN–*Fe* bridges to Fe_2O_3 (to the surface *Fe*), and to build up a well-connected three-dimensional Prussian blue network. Thus, only a few coordination bonds between Fe_2O_3 and CoFe-PB are formed, and cubic CoFe-PB crystals are more weakly attached to the surface, probably by a mixture of electrostatic attraction and metal–ligand coordination interaction.

Bismuth vanadate, on other hand, exposes surface Bi atoms in regular Bi–Bi distances of 5.11 Å (Figure 4.8b)[†], which matches well (~1%) the intermetallic distances and orientations in CoFe-PB (d_{Co-Fe} = 5.06 Å), therefore allowing epitaxy. In aqueous environment, these surface Bi will be most likely coordinated by OH or H_2O groups, depending on the pH. When dipping the $BiVO_4$ electrodes in the $[Fe(CN)_6]^{3-}$ starting solution, some of the weaker OH or H_2O ligands will be exchanged by NC, forming Bi–NC–Fe bonds. The adjacent surface Bi may bind through its coordinated hydroxy (or H_2O) group to Co^{2+}, forming a Bi–O–Co linkage. This promotes the formation of a well-attached, layered CoFe-PB structure with many coordination bonds to the surface, i.e. a good catalyst *wetting*. As the $BiVO_4$ surface is not homogeneous, the coverage does not crystallise with a well-defined long-range order and thus seems to be amorphous in the TEM image. Nonetheless, the short-range order of octahedrally coordinated metal centres linked by cyanide bridges remains preserved.

These different adhesion properties likely affect the performance of the CoFe-PB catalyst on the photoanode, since they lead to different interfacial charge-transfer pathways.[372,373] As larger the surface of the catalyst, which is in direct contact with the photoanode, as more efficient hole transfer is expected. Indeed, a different influence on PEC performance of CoFe-PB on Fe_2O_3 and on $BiVO_4$ is observed, as it is seen later in this Chapter.

4.3.2 X-ray Photoelectron Spectroscopy

To further confirm the presence of CoFe-PB on the metal oxide surfaces, X-ray Photoelectron Spectroscopy (**XPS**) was carried out. With an X-ray penetration depth of around 2–3 nm, this surface-sensitive technique was chosen as it is able to detect even very small amounts of species at the surface.[374] Moreover, shifts of XPS signals can suggest variations in the degree of oxidation due to changes in the electronic environment of a compound.

[†]In here the (001) surface of $BiVO_4$ is considered, which is the most stable in aqueous environment under PEC conditions.[350,370,371]

All the constituent elements of CoFe-PB, namely Fe, Co, N, and K could be identified on the modified electrodes, except cyanidic C, whose signal resolution is impeded by organic impurities.

Figure 4.9 shows the Fe $2p$ range of Fe_2O_3, CoFe-PB/Fe_2O_3, and CoFe-PB/$BiVO_4$ (on unmodified $BiVO_4$, no iron was detected). For the CoFe-PB modified electrodes, a clear signal between 708.2–708.4 eV could be detected, which corresponds to Fe(II) in $[Fe(CN)_6]^{4-}$.[374] This indicates that upon CoFe-PB formation, the majority of Fe(III) centres of the $[Fe(III)(CN)_6]^{3-}$ starting reagent must have become reduced to Fe(II).
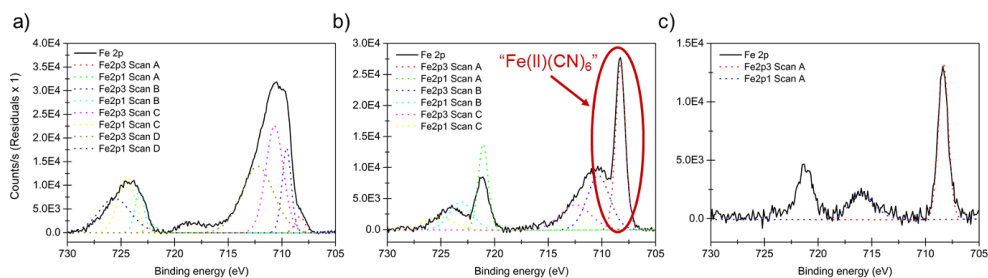
Figure 4.9: XPS spectra of the Fe $2p$ range of a) bare Fe_2O_3, b) CoFe-PB modified Fe_2O_3, and c) CoFe-PB modified $BiVO_4$.

This can also be seen in the XPS spectrum of the Co $2p$ range in Figure 4.10.
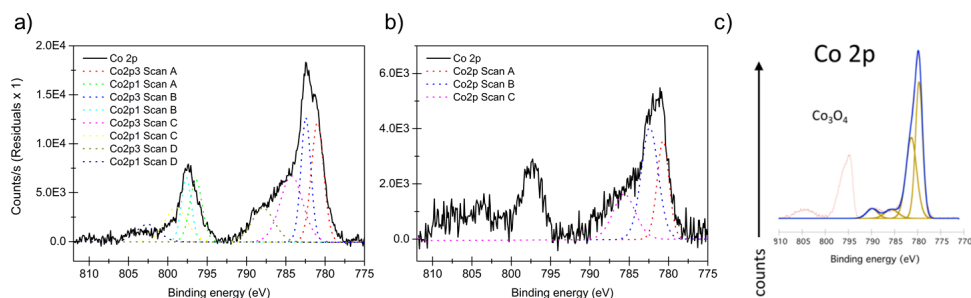
Figure 4.10: XPS spectra of the Co $2p$ range of a) CoFe-PB modified Fe_2O_3, b) CoFe-PB modified $BiVO_4$, and c) a typical Co_3O_4 spectrum for comparison.[375]

Although the Co peaks cannot clearly be deconvoluted, a broad maximum around 780–782 eV can be attributed to Co(III) in the CoFe-PB structure.[374, 376] Hence, most of the the former Co^{2+} from the dipping solution transferred an electron to $[Fe(III)(CN)_6]^{3-}$, in order to form the more stable ls-ls $K_xCo_y(III)[Fe(II)(CN)_6]_z \cdot nH_2O$ with Co in a low-spin $(t_{2g})^6$ configuration. Also the presence of

adventitious CoO_x can be ruled out, cobalt oxo-species, like Co_3O_4 and CoO would show a dominant peak below at 779.7 eV (Figure 4.10c).[375,376]

Moreover, a sharp N 1s signal is observed when CoFe-PB is deposited, which is absent for the unmodified metal oxide photoanodes (Figure 4.11).
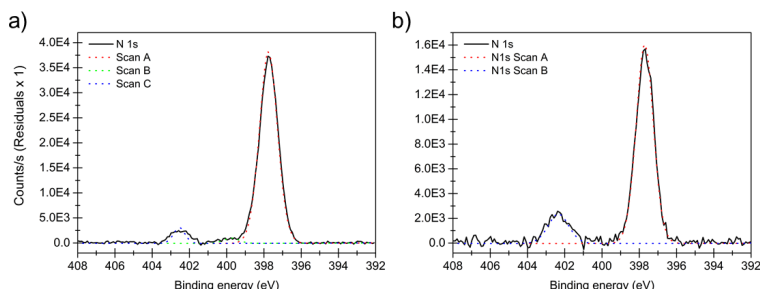
Figure 4.11: XPS spectra of the N 1s range of a) CoFe-PB modified Fe_2O_3 and b) CoFe-PB modified $BiVO_4$.

An interesting feature is observed in the case of bismuth, shown in Figure 4.12. After a long photoelectrochemical treatment, the Bi 4f peak broadens, giving rise to a second higher energy feature at 159.5–159.7 eV. This newly appearing peak could belong to a higher oxidised Bi species, which forms during a long experiment. For example Bi_2O_3 or similar structures may form at the surface, as suggested in Ref. [366]. The effect is, however, not always reproducible, and independent of the presence of CoFe-PB.[376]
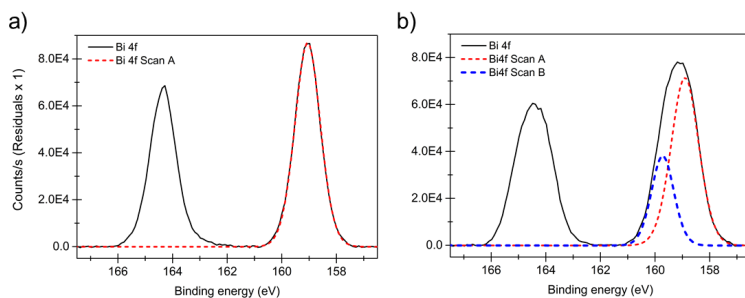
Figure 4.12: XPS spectra of the Bi 4f range of a) fresh $BiVO_4$ and b) $BiVO_4$ after a long photoelectrochemical experiment (with and without CoFe-PB modification).

The identification of detected species of bare and CoFe-PB modified Fe_2O_3, as well as of bare and CoFe-PB modified $BiVO_4$ is given in Table 4.1.

Table 4.1: XPS signals of different elements of the CoFe-PB modified and unmodified photoanodes, identification of the elemental species,[374,376] and their relative observed quantities (n.d. = not detected).

Detected species	Identity	Binding energy	Fe_2O_3	CoFe-PB /Fe_2O_3	$BiVO_4$	CoFe-PB /$BiVO_4$
		eV	average atomic % *			
Carbon (C)	Organic impurities and cyanide C (not clearly deconvoluted)	284.6–288.4	39	48	36	38
Nitrogen (N)	Cyanide N	397.6–399.8	n.d.	18	n.d.	13
Nitrogen (N)	Organic impurities on surface	402.1–402.5	n.d.	1	3	3
Oxygen (O)	Bulk O of metal oxide	529.7–529.9	26	8	46	33
Oxygen (O)	Surface O; incorporated H_2O in CoFe-PB	531.2–532.9	26	8	21	16
Bismuth (Bi)	Bi(III) in bulk $BiVO_4$	158.5–159.0	n.d.	n.d.	7	2
Bismuth (Bi)	higher oxidised Bi species, only in treated samples	159.5–159.7	n.d.	n.d.	< 1	< 1
Vanadium (V)	Partially reduced V on $BiVO_4$ surface,[366,377]	516.0–516.7	n.d.	n.d.	21	16
Iron (Fe)	Fe(III) in bulk Fe_2O_3	710.3–710.7	4	2	n.d.	n.d
Iron (Fe)	Fe(II) of $[Fe(CN)_6]^{4-}$ in CoFe-PB	708.2–708.4	n.d.	2	n.d.	2
Cobalt (Co)	Co(III) in CoFe-PB	778.9–780.4	n.d.	5	n.d.	4
Potassium (K)	Countercation in $KCo[Fe(CN)_6]$	293.4–293.6	n.d.	2	n.d.	4
Tin (Sn)	Sn from FTO (diffusion or incomplete coverage)	486.5–487.0	2	1	3	2
Zirconium (Zr)	Zr-doping of Fe_2O_3	181.8–182.1	1	1	n.d.	n.d.

* Several samples of each kind, used and unused, were tested. Average values are given here.

Typically, a higher amount of Co than Fe was observed for CoFe-PB, which is in agreement with the data from EDX microanalysis. Nonetheless, the exact Co:Fe ratio cannot be quantified, since the Fe $2p_{2/3}$ peak overlaps with Sn $2p_{2/3}$, preventing peak deconvolu-

tion. Observed Sn on Fe_2O_3 results from Sn diffusion, as Fe_2O_3 is heated up to 800 °C. In $BiVO_4$, however, this is unlikely because heating at 450 °C does not lead to significant Sn diffusion. The mesoporous $BiVO_4$ does not completely cover the underlying FTO slide, hence Sn signals from FTO can be detected in the surface-sensitive XPS experiment.

Less oxygen is found on average in the CoFe-PB modified samples, although large variations of the amount of oxygen were observed. This is due to the fact that the catalyst coverage shields the oxygens of the bulk metal oxide. A larger amount of Bi than V is found on the surface of $BiVO_4$ with an average Bi:V ratio of 1.6, which is in agreement with the EDX results and recent literature.[366,378] Moreover, the measured vanadium $2p_{3/2}$ binding energy of 516.0–516.7 eV lies more than 0.3 eV below the typical value of 517 eV for V^{5+}, which suggests a (partial) reduction to V^{4+} at the surface.[366,377] There are no significant changes of the Bi:V ratio or the V $2p_{3/2}$ peak before and after different electrochemical treatments.

Apart from the effect on Bi, photoelectrochemical treatment (irradiation with 1 sun at 1.23 V_{RHE} for 1 h) did not show any significant changes on the XPS spectra.[324] In particular, no changes in the XPS signals of Co and Fe indicate the stability of CoFe-PB towards oxidation/reduction of the metal centres under water splitting conditions. If Co or Fe were oxidised (reduced) during the PEC treatment, their XPS signals would shift to higher (lower) energies.

4.3.3 Infrared spectroscopy

Cobalt hexacyanoferrate can be uniquely identified by its characteristic cyanide stretching mode. Depending on the Co and Fe oxidation states, the bridging cyanide Co–N≡C–Fe has a stretching frequency ν_{CN} of 2070–2200 cm^{-1}.[104,300,301] Therefore, additional evidence of the formation of CoFe-PB on $BiVO_4$ was obtained through infrared (**IR**) spectroscopy.

Figure 4.13 shows the IR spectrum of CoFe-PB/$BiVO_4$, which was obtained by scratching the thin metal oxide films of several FTO electrodes and subsequently pressing it as KBr disk (see Appendix A). Since the relative amount of CoFe-PB is very small (< 1%) the observed ν_{CN} signal at around 2100 cm^{-1} is very weak. Yet it unambiguously identifies the presence of the metal hexacyano-ferrate CoFe-PB, as no other non-cyano compound can give IR signals in this region. Moreover, the broad peak ν_{CN} indicates that there are multiple, overlapping bands, which in turn suggests that the non-stoichiometric CoFe-PB adopts various oxidation states.

Units of Co(II)–N≡C–Fe(II) (ν_{CN} = 2070–2100 cm^{-1}), Co(III)–N≡C–Fe(II) (ν_{CN} = 2110–2130 cm^{-1}), and Co(II)–N≡C–Fe(III) (ν_{CN} = 2050–2160 cm^{-1}) coexist in the structure.[104,300,301]
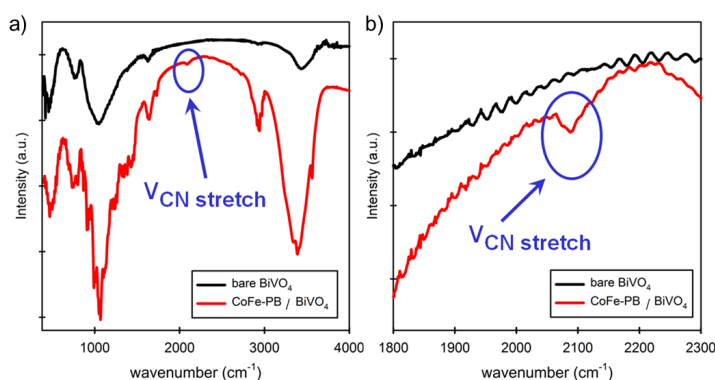
Figure 4.13: Fourier-transform (FT)-IR spectra of KBr disks of scratched particles from unmodified (black) and CoFe-PB modified (red) BiVO$_4$ of a) the complete range of the IR spectrometer and b) the cyanide stretching region between 1800 cm^{-1} and 2300 cm^{-1}.

4.3.4 UV-Vis spectroscopy

As the catalyst coverage is only around 1%, it is assumed not to interfere with the absorption of the semiconductor photoanode. Indeed, UV-Vis absorption spectra do not show the characteristic absorption signature of 520–550 nm (2.2–2.4 eV) of CoFe-PB, as seen in Figure 4.14.

The band gap of the semiconductor photoanode was approximated with the *Tauc* equation[213]

$$(h\nu\alpha)^n = C(h\nu - E_g) \qquad (4.1)$$

where α is the absorption coefficient, C is a constant, and $n = 2$ for a direct allowed transition or $n = 1/2$ for an indirect allowed transition (see Section 2.2.5).[213,221]

For hematite, the absorbance was fitted to an *indirect* (phonon-assisted) transition, in which electron density shifts from O 2p to Fe 3d (and forms a small polaron).[339] A band gap E_g of 1.9–2.0 eV was obtained, in agreement with literature values[36,40,327] and calculations (Section 3.3 in Chapter 3).

Although BiVO$_4$ is an *indirect* semiconductor, its direct band gap lies very close to the indirect one and dominates the absorption properties.[211,212,351] Therefore, fitting the absorbance to a direct transition ($n = 2$) led to a better fit. From it, a band gap of 2.40–2.45 eV was obtained, again consistent with previous literature[351,379] and HSE03-13 calculations (Section 3.3).
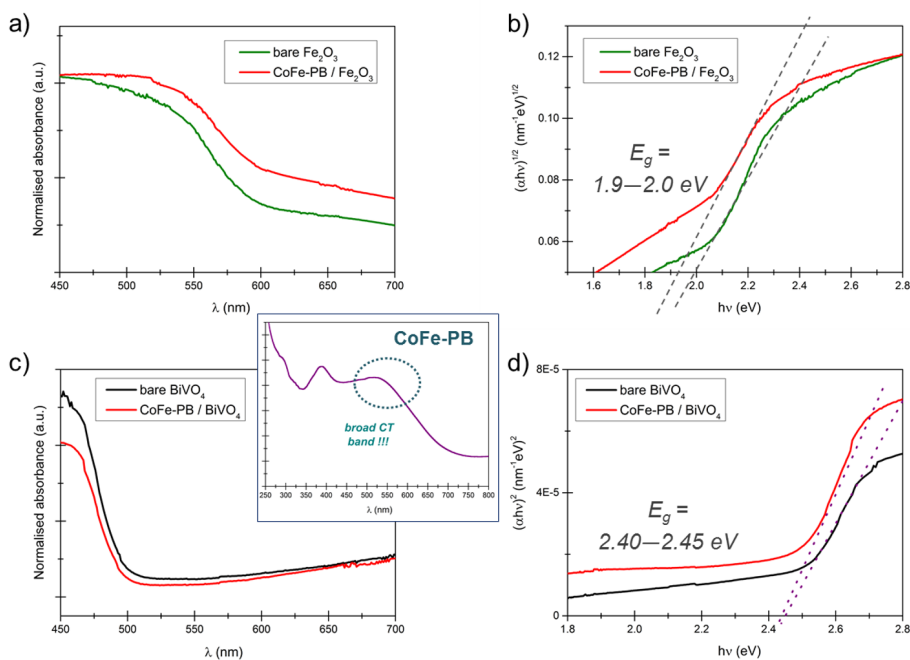
Figure 4.14: a,c) UV-Vis absorption spectra and b,d) corresponding Tauc fits of unmodified and CoFe-PB modified Fe_2O_3 (a,b) and $BiVO_4$ (c,d). The inset shows the absorption spectrum of CoFe-PB alone.

Neither the absorption nor the band gap is influenced by the CoFe-PB catalyst. The small deviations of the absorbance in Figure 4.14 is attributed to inhomogeneity of the samples. This indicates that CoFe-PB does not have a significant influence on the electronic structures of the two different underlying metal oxides.

4.3.5 Dark electrochemistry

The cyclic voltammetry (**CV**) behaviour of modified and unmodified semiconductor anodes in the dark is presented in Figure 4.15. The bare metal oxides do not show any anodic current, unless very high potentials (> 1.8 V_{RHE}) are reached. This positive current results from hole extraction from the FTO substrate (Figure 4.15d). At strong cathodic potentials, the n-type semiconductors give a negative current, as described in Section 2.3.1. The CV curve of bare $BiVO_4$ is broadened due to the V^{4+}/V^{5+} ($V^o = 0.8$–0.9 V_{RHE}) redox couple.

All electrodes, which are modified with CoFe-PB, give rise to an oxidation wave between 1.2–1.7 V_{RHE} and a reduction wave at slightly lower potentials, which may be deconvoluted into two distinct peaks. Its appearance strongly suggests the presence

of CoFe-PB on the surface. Although there is a large variation in the potential, its values lie well in the range of reported literature values for CoFe-PB redox potentials.[103,110,297,300,301] These large deviations are due to variations in preparation conditions and substrate (semiconductor metal oxide or FTO), leading to different local stoichiometries and coordinations of the metal centres, which in turn strongly influence the potential of the Co^{2+}/Co^{3+} and Fe^{2+}/Fe^{3+} redox couples (see also Section 3.2).[300,312]

Moreover, in the case of CoFe-PB deposition (Figures 4.15a,b), the anodic water oxidation current appears at a lower onset potential (around 1.5–1.6 V_{RHE}) resulting from the dark catalytic activity of CoFe-PB as an electrocatalyst.
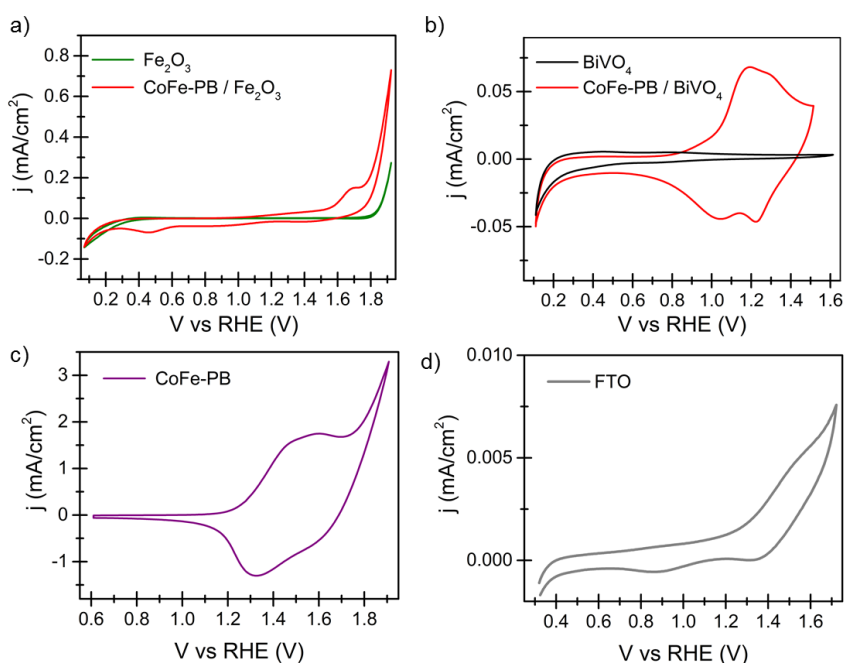
Figure 4.15: Cyclic voltammogrammes (50 mV/s) under dark conditions of a) modified (red) and bare (black) $BiVO_4$, b) modified (red) and bare (green) Fe_2O_3, c) of thick solvothermally deposited CoFe-PB alone (purple), and d) of bare FTO glass (grey) at pH 7 (0.1 M KP_i buffer).

4.4 Photoelectrochemical performance

4.4.1 Photocurrent evolution

The influence of the CoFe-PB catalyst on the photoelectrochemical behaviour of the photoanodes was first studied by cyclic voltammetry under chopped and constant illumination (1 sun) in neutral

electrolyte (0.1 M KP$_i$ buffer).

Figure 4.16 shows the CV of bare (green) and CoFe-PB modified (red) hematite. In the anodic scan (Figures 4.16a,c) an apparent cathodic shift of the photocurrent onset potential of around 0.3 V can be seen, while in the cathodic scan (Figure 4.16b) this beneficial onset potential shift is substantially decreased (to <0.1 V). For bare Fe$_2$O$_3$, however, the j–V characteristics are independent of scanning direction (anodic or cathodic). This is a first indication that the effect of the CoFe-PB layer must be to some extent capacitive, related to its oxidation/reduction in the anodic/cathodic scanning direction.
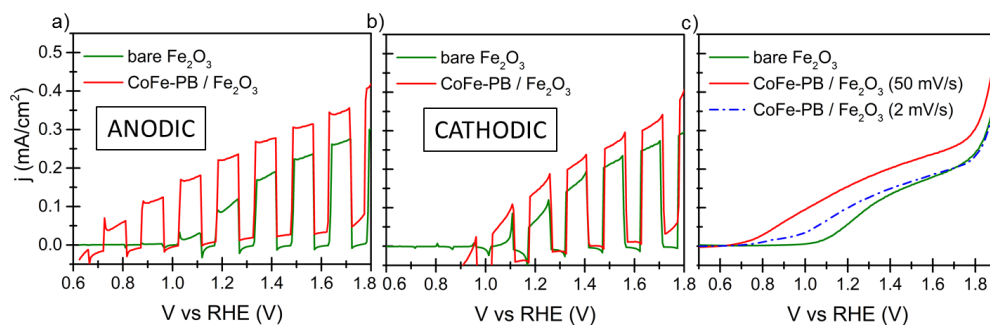
Figure 4.16: Cyclic voltammogrammes under illumination (1 sun) of modified (red) and bare (green) Fe$_2$O$_3$ at pH 7. a) anodic and b) cathodic scans under chopped light (50 mV/s), and c) anodic scans under constant light at scan rates 50 mV and 2 mV/s for CoFe-PB/Fe$_2$O$_3$.

Furthermore, performing the CV scan with 2 mV/s scanning speed (Figure 4.16c) leads to worse PEC performance than with 50 mV/s. Indeed, varying the scan rate does influence the shape of the CV of CoFe-PB/Fe$_2$O$_3$ significantly, while it has not much impact on the CV behaviour of bare Fe$_2$O$_3$, as shown in Figure 4.17.
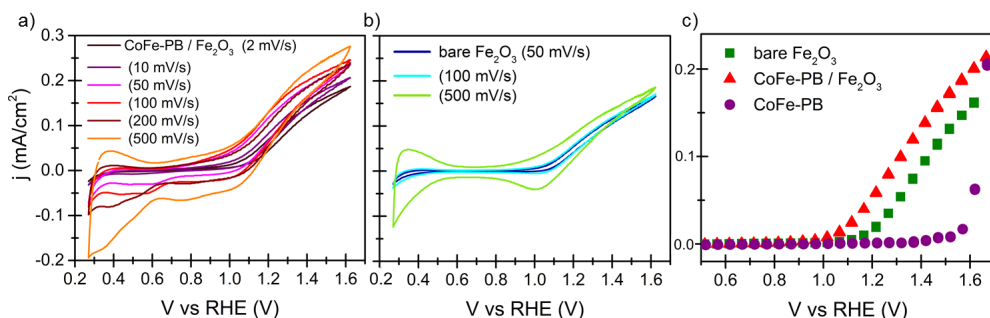
Figure 4.17: a,b) Cyclic voltammogrammes under illumination (1 sun) of a) modified and b) bare Fe$_2$O$_3$ at pH 7 at different CV scan rates. c) Steady-state j–V curve extracted from electrochemical impedance analysis data.

The photocurrent onset (in the anodic scan direction) as well as its magnitude increase with increasing scan speed (Figure 4.17a and Figure 4.16c), which further suggests a capacitive behaviour of CoFe-PB. This means that the observed current in the anodic CVs at higher scanning speeds can be ascribed to photo-induced charging of the CoFe-PB layer on the surface, and not to oxygen production. For bare Fe_2O_3, only a very high scan speed (500 mV/s) leads to a capacitive feature. From the steady-state j–V curve (Figure 4.17c) a photocurrent onset shift of 0.1 V could be determined.[†] Taken together, CoFe-PB does enhance the PEC performance of hematite, but its beneficial influence is only small.

A different behaviour is observed for CoFe-PB on $BiVO_4$, as shown in Figure 4.18 CoFe-PB largely enhances the PEC performance of $BiVO_4$ by increasing the OER current and significantly reducing the onset potential. Moreover, it can be seen, that the scanning speed of the CV scan does *not* significantly influence the shape of the j–V (Figure 4.18b).
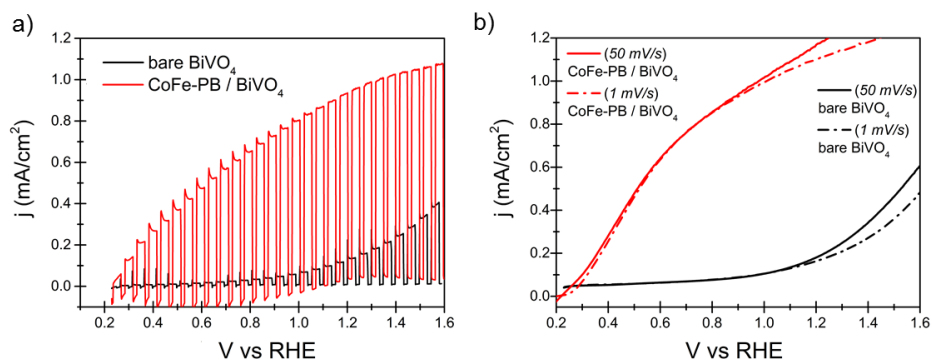
Figure 4.18: Anodic CV scans with a) chopped and b) constant light at 50 mV/s and 1 mV/s scan rates of modified (red) and bare (black) $BiVO_4$ under illumination (1 sun) at pH 7.

For determining the photocurrent onset potential, these anodic CV scans at low velocity (1 mV/s) were taken as reference and the voltage needed to attain 0.1 mA/cm^2 was set to be the onset. It has to be mentioned that the onset potential varies for different batches of prepared samples; for the best CoFe-PB/$BiVO_4$ electrodes it was measured to be around 0.3 V_{RHE}, and not larger than 0.5 V_{RHE}. For the bare $BiVO_4$ electrodes, the onset potential was found to vary a

---

[†]For the case of Fe_2O_3, the voltage to attain 0.01 mA/cm^2 photocurrent density is taken as onset potential, while for $BiVO_4$, the voltage to attain 0.1 mA/cm^2 is used. The difference is due to the much lower currents obtained for Fe_2O_3 electrodes.

lot, as much as 0.7–1.2 V_{RHE}. This indicates how sensitive $BiVO_4$ is to small variations in electrodeposition and calcination conditions, and demonstrates again the importance of always comparing the *same* electrode with and without catalyst.

Altogether, the deposition of CoFe-PB onto $BiVO_4$ shifts the onset about 0.7–0.8 V to more cathodic potentials and enhances the photocurrent density at 1.23 V_{RHE} by about 0.9–1.0 mA/cm^2. Due to the superior activity of CoFe-PB on $BiVO_4$, the rest of this work is mainly focused on the CoFe-PB/$BiVO_4$ system, albeit both photoanodes are discussed from a mechanistic perspective.

Interestingly, it appears like CoFe-PB on $BiVO_4$ first has to be activated in order to reach a stable photocurrent (Figures 4.19). The first CV scan does not give significant photocurrents at low potentials, but shows the characteristic CoFe-PB redox features (compare to Figures 4.15b,c). After several scans (generally 3 or 4), the CoFe-PB redox wave nearly completely disappears, and a stable photocurrent plateau is reached. This effect might be due to the fact that the freshly synthesised CoFe-PB contains a mixture of Co^{2+}/Co^{3+} and Fe^{2+}/Fe^{3+}, which is not yet the catalytically most active form. After various oxidation and reduction cycles a stable equilibrium of oxidation states is reached.[300,312] Consequently, in all the CV measurements presented herein, usually several scans (3–5) were carried out prior to data acquisition.
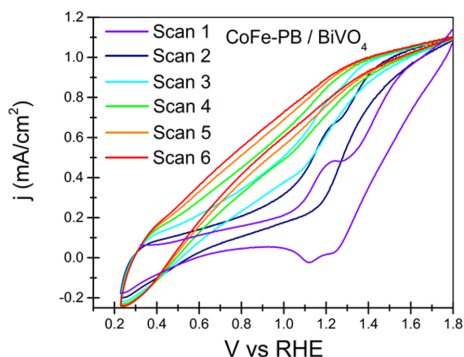
Figure 4.19: Consecutive CV scans of CoFe-PB/$BiVO_4$ under illumination (1 sun) at pH 7.

4.4.2 Photocurrent transients

In CoFe-PB/$BiVO_4$ (Figure 4.18a) and, to a small extent, in CoFe-PB/Fe_2O_3 (Figure 4.16a) *transient* currents are observed, which are seen as current spikes, when the light is switched on or off. The potential range, in which the transient currents appear, coincides

with the CoFe-PB redox potentials, as seen in Figure 4.15. Therefore the positive transients are attributed to oxidising CoFe-PB at the surface, and the negative transients to back reduction of CoFe-PB by electrons from the conduction band of the semiconductor.

Particularly pronounced is the transient cathodic dark current of CoFe-PB/BiVO$_4$ (Figures 4.18a), up to 1 V$_{RHE}$. This suggests the presence of a relatively large fraction of oxidised CoFe-PB on the surface of BiVO$_4$, which has not (yet) undergone water oxidation. In turn, this indicates that charge-transfer, and thus oxidising CoFe-PB, is faster than water oxidation catalysis on the CoFe-PB surface. The kinetics of those processes are further discussed in Chapter 5.

In the case of Fe$_2$O$_3$ (Figure 4.16b), it seems that CoFe-PB decreases the transient photocurrent peaks compared to bare Fe$_2$O$_3$, which is likely due to a suppression of surface electron–hole back recombination.[380]

4.4.3 Stability

Apart from the large photocurrent enhancement obtained by depositing CoFe-PB on BiVO$_4$, the modified photoanodes are also highly robust. Figure 4.20 shows the chronoamperometry (**CA**) curves of CoFe-PB/BiVO$_4$ under chopped (Figure 4.20a) and constant (Figure 4.20b) illumination (1 sun) at 1.23V$_{RHE}$.
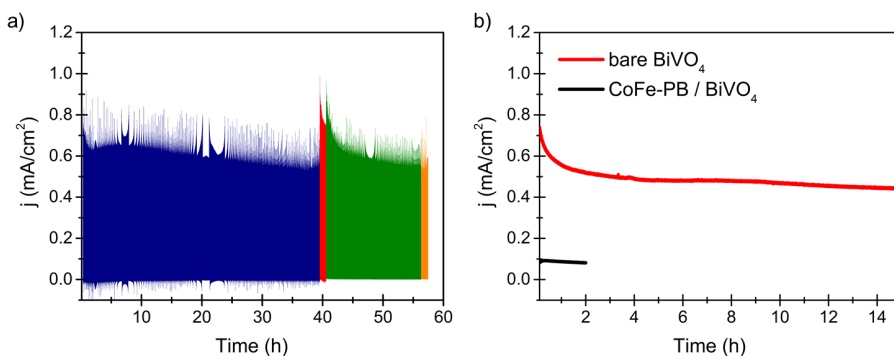
Figure 4.20: Chronoamperometric measurements of CoFe-PB modified BiVO$_4$ under a) chopped and b) constant illumination (1 sun) at 1.23V$_{RHE}$ in neutral KP$_i$ buffer. Different colours present different measurements of the *same* CoFe-PB/BiVO$_4$ electrodes at different days and after having taken the sample out of solution.

After an initial decrease of about 10% during the first hours, the photocurrent density of CoFe-PB/BiVO$_4$ remains stable over more than 55 hours (Figure 4.20a). Such an initial current drop is usually also seen for bare BiVO$_4$ and is related to its PEC instability.[378]

Hence, the initial loss is attributed to a loss of activity of the $BiVO_4$ photoanode, not to a fatigue of the catalyst.

It is important to note that the CA curve in Figure 4.20a presents *different*, consecutive measurements of the *same* photoanode, which had been performed at different days and after having taken the electrode out of solution and dried. This ex situ stability signifies that the electrode can be stored over a long time in air without losing its activity. In contrast, other catalysts, like cobalt oxide (CoO_x or CoP_i) crack easily upon drying;[86,100] this demonstrates a clear advantage of CoFe-PB.

Additionally, inductively coupled plasma optical emission spectrometry (**ICP-OES**) was carried out to rule out the possibility of material leaching. To do so, the supernatant buffer solutions of both bare $BiVO_4$ and CoFe-PB/$BiVO_4$ were analysed after different PEC experiments (multiple CVs, CAs, impedance measurements) for traces of the electrodes materials (Bi, V, Co, Fe), as well as other commonly encountered trace metals (Al, Cr, Cu, Mn, Ni, Zn). Small amounts on the order of mmol of Fe, Al, Zn, and Zr with arbitrarily varying quantities were found in the solutions. Those could neither be related to usage of the buffer solution, nor the electrode material, and are therefore ascribed to traces in the initial buffer solutions. Also the Fe content, which was found in the electrolyte, is attributed to Fe impurities in the solution, not leaching of CoFe-PB, because it was also found after measuring bare $BiVO_4$. Indeed, Fe impurities in solvents are very common and, for example, had been observed by Trotochaud *el al.*[381]

As no significant amount of constituent metal ions (<1 mmol in 30 mL) was detected in the used electrolyte, it was concluded that the catalyst is mechanically stable and not washed into solution.

4.4.4   Faradaic efficiency

The observed long-term stability (Figure 4.20) is also a strong indicator that no significant side reactions take place and that the measured photocurrent is indeed due to oxygen evolution (if not, the current would decrease). Nonetheless, in order to confirm that water oxidation occurs, the evolved oxygen is measured and quantified by gas chromatography (**GC**) under an inert argon atmosphere. Figure 4.21 shows the amount of detected molecular oxygen (red triangles), when irradiating CoFe-PB/$BiVO_4$ with 1 sun at 1.23 V_{RHE}.

If all the photogenerated holes are transferred to H_2O to create oxygen, the theoretical amount of oxygen $n_{theoretical}$ (blue line in Figure 4.21) is given by Faraday's Law

$$n_{theoretical}(\text{mol}) = \frac{It}{zF} \tag{4.2}$$

where I is the obtained photocurrent and $z = 4$ the number of transferred charges (holes). From the detected and theoretical O_2 evolution, the Faradaic efficiency can be determined (Equation 2.30), in order to assess the efficiency of oxygen production, i.e. how much of the photogenerated charges (the photocurrent) are used for oxygen production. As seen from Figure 4.21, a Faradaic efficiency of >95 % is maintained during all the experiment (1 h), from which a consistently stable oxygen production can be concluded.
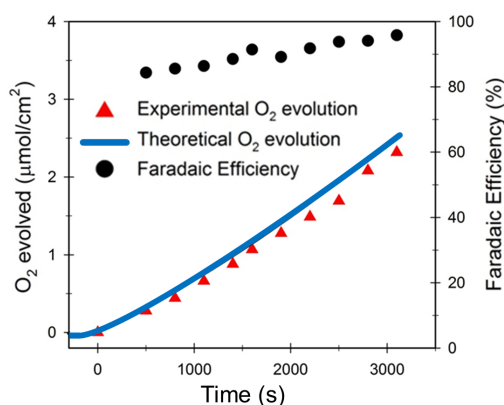
Figure 4.21: Measured $n_{evolved}$ (red triangles) and theoretical $n_{theoretical}$ (Equation 4.2, blue line) O_2 evolution and Faradaic efficiency FE (Equation 2.30, black circles).

4.4.5 Catalyst comparison

In order to compare the catalytic performance of CoFe-PB on $BiVO_4$ to other catalysts under the same experimental conditions, CoO_x and FeOOH were deposited on the same nanostructured $BiVO_4$ anodes (from the same batch). The water oxidation catalysts CoO_x (CoP_i) and FeOOH were chosen because they are stable in working conditions (pH 7)[86,382] and, mainly because they contain Co or Fe, both the metallic constituents of CoFe-PB. Hence, their catalytic mechanisms and performance may be comparable.

Figure 4.22a shows the CV behaviour of $BiVO_4$ modified with CoO_x (by electrodeposition and dipcoating) and FeOOH, as well as with CoFe-PB. The PEC performance of all Co containing systems, i.e. the two differently prepared Co oxides and CoFe-PB, is comparable, while FeOOH shows much less photoelectrochemical enhancement. CoFe-PB appears to outperform CoO_x. It has to be

noted though that neither CoO_x nor FeOOH preparations were optimised, so a direct quantitative comparison of the catalysts cannot be made. In particular, it is well-known for CoO_x that its performance depends on the deposition method.[86] Yet CoFe-PB can be said to be at least competitive with other state-of-the-art catalysts.
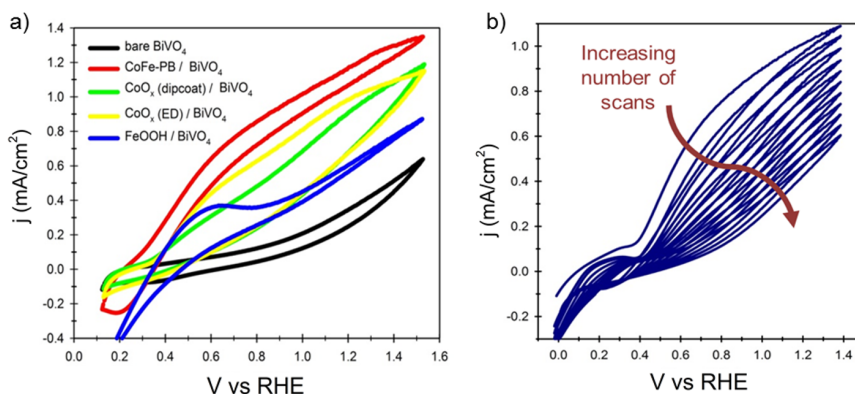
Figure 4.22: Cyclic voltammogrammes (50 mV/s) of modified $BiVO_4$ photoanodes under light (1 sun). a) Comparison of different catalysts CoFe-PB (red), dipcoated CoO_x (green), electrodeposited CoO_x (yellow), and FeOOH (blue) on $BiVO_4$ (black) in neutral buffer (0.1 M KP_i). b) Consecutive CV scans of $CoO_x/BiVO_4$ in acetate with pH 4.5.

A clear advantage of CoFe-PB as a catalyst, however, is its stability in a large range of pH ($1 < pH < 13$),[110] whereas CoO_x dissolves in acidic medium. When performing consecutive CV scans of $CoO_x/BiVO_4$ in acetate buffer (pH 4.5), the photocurrent decreases dramatically with the number of consecutive scans, as shown in Figure 4.22b. This is due to reducing Co^{3+} in CoO_x to Co_2^+ and dissolving the oxide. It is only stable in phosphate buffer KP_i due to its self-healing ability (see Section 1.4.1).[88,95]

4.4.6 Photovoltage

Modifying $BiVO_4$ with CoFe-PB also has a beneficial effect on the photovoltage, which can be regarded as the potential stored by the photogenerated electron–hole pair (see Section 2.2.7).

The photovoltage V_{Photo} was approximated as the difference in open-circuit voltage (OCV), i.e. the measured voltage when no current flows, in the dark and under light:

$$V_{Photo} = OCV(\text{dark}) - OCV(\text{light}) \qquad (4.3)$$

From Figure 4.23, it can be seen that the photovoltage increases significantly from around 0.15 to 0.60 V with CoFe-PB deposition.
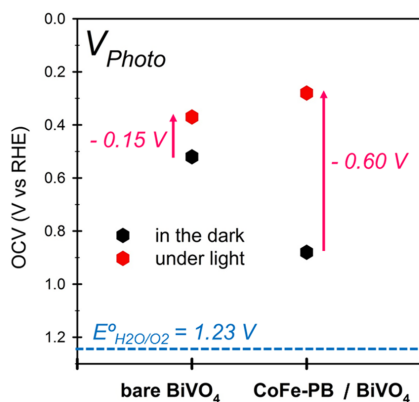
Figure 4.23: Equilibrium open-circuit voltage (OCV) measured for bare (left) and CoFe-PB modified (right) $BiVO_4$ in the dark (black hexagons) and under light (red hexagons).

A similar behaviour has been observed in other metal oxide semiconductors, where it is ascribed to surface state passivation.[383,384] If surface states are present, the Fermi level of $BiVO_4$ can no longer equilibrate with the electrolyte, an effect often referred to as *Fermi level pinning*.[383] Passivation of surface states would therefore diminish Fermi level pinning and increase the photovoltage. Nevertheless, none of the experimental techniques employed herein has further proven that such a passivation occurs.

4.5   Mechanistic studies

After having shown that CoFe-PB was successfully deposited on both Fe_2O_3 and $BiVO_4$ photoanodes, and leads to an overall increase in PEC performance, I now focus on the understanding of the mechanisms taking place at the semiconductor–catalyst interfaces. My aim was to understand the effect of the CoFe-PB catalyst, in particular, its difference on the employed Fe_2O_3 and $BiVO_4$ semiconducting metal oxides.

4.5.1   Hole scavenger experiments

Experiments in hole scavenger (*hs*) solution were carried out in order to understand the effect of electron–hole recombination and charge-transfer at the surface. An efficient hole scavenger directly withdraws photogenerated holes from the semiconductor or catalyst surface. Hence, the charge-transfer efficiency η_{CT} (Equation 2.29) can be assumed to be 100%; in other terms, surface electron–hole recombination is completely suppressed.[84,222,385]

This assumption, however, is only valid if the concentration of hole scavenger is sufficiently high, so that all surface holes are withdrawn, and a further increase of *hs* concentration does not lead to more photocurrent enhancement.[†]

Figure 4.24 shows the effect of hole scavenger Na_2SO_3 concentration on the photocurrent of $BiVO_4$. When only 0.1 M *hs* is used, a lower photocurrent density than with 1 M *hs* is obtained (Figure 4.24a), which means hole transfer at the semiconductor liquid interface is not 100% efficient for 0.1 M *hs*. Thus, at least 1 M Na_2SO_3 were needed for the conducted experiment.

After depositing the CoFe-PB catalyst, the *hs* concentration has much less impact on the PEC performance (Figure 4.24b). This indicates that the charge-transfer of CoFe-PB is already much higher and can only be increased by a smaller extent.
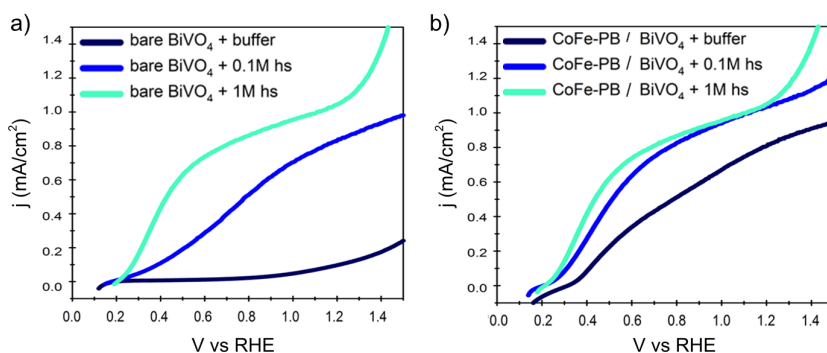
Figure 4.24: Cyclic voltammogrammes (anodic scans at 50 mV/s) of a) bare and b) CoFe-PB modified $BiVO_4$ photoanodes under light (1 sun) in 0.1 M KP_i buffer solution (dark blue) and 0.1 M and 1 M Na_2SO_3 hole scavenger solution.

Charge-transfer efficiencies

If η_{CT} = 100% is valid, it follows for the photocurrent density in *hs*,

$$j_{photo}(hs) = j_{absorption}\, \eta_{CS} \tag{4.4}$$

and with Equation 2.29 for the photocurrent in H_2O, the charge-transfer efficiency can be calculated as:

$$\eta_{CS} = \frac{j_{photo}(H_2O)}{j_{photo}(hs)} \cdot 100\,\% \tag{4.5}$$

[†]It is noted that there is also a possibility of current doubling when performing the experiment in *hs*, which is not taken into account in the present analysis. Such a current doubling effect occurs when the *hs* donates electrons into the conduction band, which leads to observed efficiencies > 100%.[386]

Figure 4.25 shows the effect of hole scavenger on CoFe-PB modified $BiVO_4$ and Fe_2O_3 photoanodes, as well as the calculated charge-transfer efficiencies (Equation 4.5). For Fe_2O_3 anodes, H_2O_2 was chosen as hole scavenger, as it was suggested by Dotan *et al.*[222]
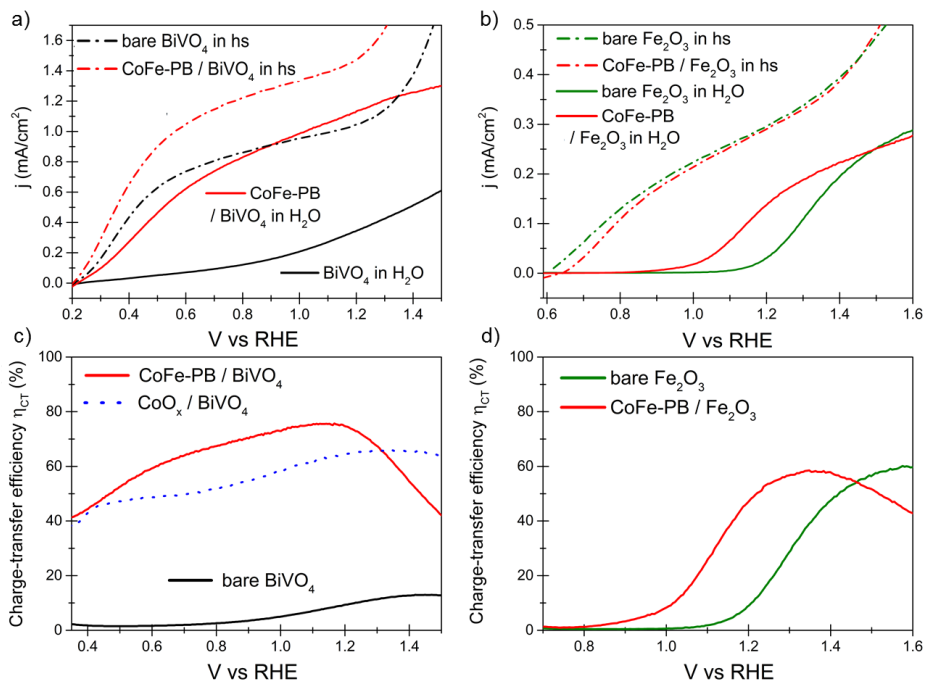
Figure 4.25: a,b) Cyclic voltammogrammes (anodic scans at 50 mV/s) of bare and CoFe-PB modified a) $BiVO_4$ and b) Fe_2O_3 photoanodes under light (1 sun) in H_2O (0.1 M KP_i) and hole scavenger (1 M Na_2SO_3 for $BiVO_4$ and 0.5 M H_2O_2 for Fe_2O_3). c,d) Calculated charge-transfer efficiencies.

Both bare $BiVO_4$ (Figure 4.25a) and bare Fe_2O_3 (Figure 4.25b) show a drastically increased photocurrent when *hs* is used. This in turn implies that the bare metal oxide anodes do *not* efficiently transfer holes in the absence of a hole scavenger. Indeed, their charge-transfer efficiencies are very low (Figure 4.25c,d), especially for $BiVO_4$ ($\eta_{CT} \lesssim 15\%$), which is consistent with previous results.[86] Efficient charge-transfer at metal oxide photoanodes is limited by electron–hole recombination at the surface, which is much faster than water oxidation.[87,122,132,217,222] Only at very anodic potentials ($>1.2\ V_{RHE}$) the charge-transfer efficiency starts to increase (to ~15% for $BiVO_4$; to ~60% for Fe_2O_3), because the large applied electric field prevents recombination.

A large difference is observed between CoFe-PB/$BiVO_4$ and CoFe-PB/Fe_2O_3, comparing their *j–V* behaviour with and without hole scavenger. The CV curve of CoFe-PB/$BiVO_4$ shows only a small pho-

tocurrent increase when utilising *hs* instead of water (buffer), which suggests that already in water charge-transfer is relatively efficient (Figures 4.24b and 4.25a). Nonetheless, the curves do not overlap, meaning charge-transfer can still be improved. This is reflected in the calculated charge-transfer efficiency η_{CT}, which reaches about 80% at 1.2 V_{RHE} (Figure 4.25c).

For Fe_2O_3, in contrast, η_{CT} of around 60% is not enhanced upon CoFe-PB deposition (Figures 4.25b,d). It is however shifted to lower potentials, reaching a maximum at 1.35 V_{RHE}, whereas for bare Fe_2O_3 it is maximal at 1.57 V_{RHE}. This cathodic shift of η_{CT} is likely related to the cathodic shift of onset potential (seen in Figures 4.16 and 4.17). The CVs of both bare Fe_2O_3 and CoFe-PB/Fe_2O_3 in *hs* overlap, which implies that an equal number of holes reaches the interface with the electrolyte. Hence, their charge-separation efficiencies, as well as their charge mobilities in the bulk, are similar and not altered upon catalyst deposition.

A comparison with CoO_x/$BiVO_4$ is given in Figure 4.25c, which shows less charge-transfer efficiency below 1.4 V_{RHE}, again indicating a better performance of CoFe-PB on $BiVO_4$. From the *j–V* behaviour in hole scavenger, also the flat band potential of the semiconductor can be approximated, as it should ideally be equal to the onset potential in *hs* (see Section 2.3.1). Therefore, from Figures 4.25a and b, flat band potentials of around 0.2 V_{RHE} for $BiVO_4$ and 0.6 V_{RHE} for Fe_2O_3, which are not affected by CoFe-PB and consistent with literature values, are deduced.[216,222,387]

Charge-separation efficiencies

The fact that the photocurrent curves of bare $BiVO_4$ and CoFe-PB/$BiVO_4$ in Figure 4.25a do *not* overlap in *hs* suggests that CoFe-PB does not only improve hole transfer to the electrolyte (in that case the *j–V* characteristics would be the same in *hs*). Another beneficial effect of CoFe-PB could be related to favouring charge-separation.

The charge-separation efficiency η_{CS} can also be extracted from the *hs* experiments, assuming Equation 4.4 to be valid.

$$\eta_{CS} = \frac{j_{photo}(hs)}{j_{absorption}} \tag{4.6}$$

The maximum absorbed photocurrent $j_{absorption}$ can be obtained from UV-Vis spectroscopy (Figure 4.14), from which the absorption coefficient α of the material can be calculated, and knowledge of the intensity spectrum of the incoming light, i.e. the wavelength-dependency of intensity, I_λ.[221]

$$j_{absorption} = \frac{e}{hc} \int I_\lambda (1 - 10^{-\alpha}) d\lambda \qquad (4.7)$$

For $BiVO_4$ $j_{absorption} = 7.25$ mA/cm^2, which is close to the theoretical maximum photocurrent 7.50 mA/cm^2.[388] This in turn suggests that the synthesised nanostructured $BiVO_4$ films are efficiently absorbing light.

Figure 4.26 presents the calculated charge-separation efficiencies for bare $BiVO_4$ and CoFe-PB/$BiVO_4$ as a function of applied bias. Upon CoFe-PB deposition, η_{CS} increases by about 5% for $V > 0.5$ V_{RHE}. Although there is a charge-separation enhancing effect of CoFe-PB, which might be of electrostatic nature, this effect is not predominating and the effect of improved charge-transfer overweights.
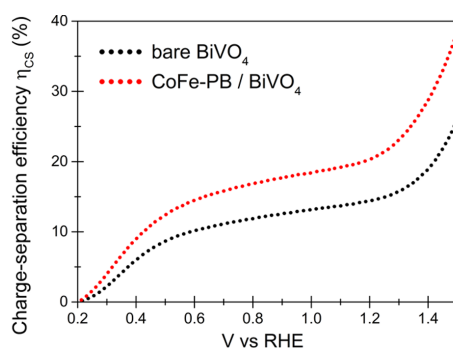
Figure 4.26: Calculated charge-separation efficiency of bare $BiVO_4$ (black) and CoFe-PB modified $BiVO_4$ (red).

4.5.2 Incident photon-to-current conversion efficiency

The incident photon-to-current conversion efficiency (**IPCE**) gives a measure of how many of the incoming photons are converted into electrical current. It is a function of incident photon wavelength λ and intensity I_λ.[†]

$$IPCE(\lambda) = \frac{h \cdot c \cdot j_{photo}}{\lambda \cdot I_\lambda} \qquad (4.8)$$

The obtained IPCE data for $BiVO_4$ and CoFe-PB/$BiVO_4$ in H_2O at 1.23 V_{RHE} is shown in Figure 4.27a.

[†]h is the Planck constant, and c the speed of light. Including the unit conversions for nm and eV, a constant of factor of 1239.87 can be used to convert between wavelengths λ and energy.
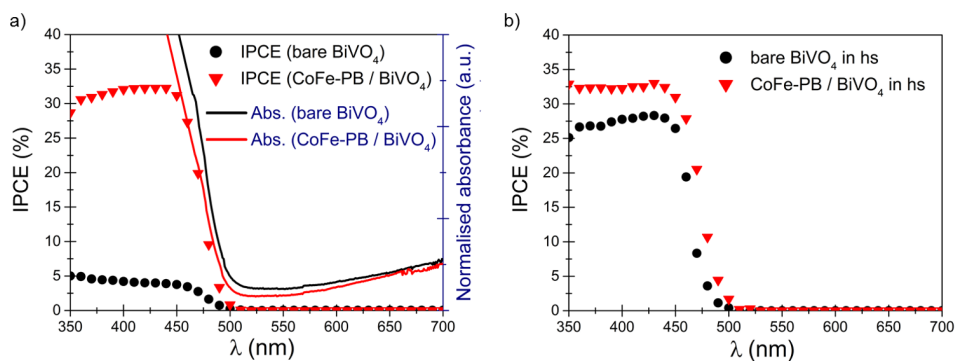
Figure 4.27: Incident photon-to-current conversion efficiency (IPCE) at 1.23 V_{RHE} of bare $BiVO_4$ (black) and CoFe-PB modified $BiVO_4$ (red) in a) 0.1 M KP_i buffer solution and b) in 1 M Na_2O_3 hole scavenger. The optical absorbance is included in a) for the sake of comparison.

The IPCE is consistent with cyclic voltammetry results (Figure 4.18); between 350 and 450 nm a 6-fold increase is obtained when depositing CoFe-PB. Moreover, the integrated photocurrents (0.38 mA/cm^2 for $BiVO_4$; 0.92 mA/cm^2 for CoFe-PB/$BiVO_4$) match perfectly the CV photocurrents at 1.23V_{RHE} (0.40 mA/cm^2 for $BiVO_4$; 0.95 mA/cm^2 for CoFe-PB/$BiVO_4$). The photocurrent threshold at 512 nm is not influenced by the catalyst, consistent with UV-Vis spectroscopy (Figure 4.14). For a better comparison, the optical absorption is shown with the IPCE in Figure 4.27a (right axis).

In presence of a hole scavenger (Figure 4.27b), the IPCE increases drastically from around 5 to 25% for bare $BiVO_4$, while it is barely changed for CoFe-PB/$BiVO_4$. The IPCE of CoFe-PB/$BiVO_4$ remains around 30–35% in water (buffer) and *hs*. This is in agreement with the previous hole scavenger studies (Figure 4.25), indicating a very high (~80%) charge-transfer efficiency.

4.5.3 Electrochemical impedance spectroscopy

In order to further evaluate the role of CoFe-PB on Fe_2O_3 and on $BiVO_4$, electrochemical impedance spectroscopy (**EIS**) was performed. It consists of measuring the complex current response of a photoanode to a frequency modulated voltage perturbation, as described in Section 2.3.2. In particular, the evaluation of different types of capacitances, and their variation upon catalyst deposition, yields important information about the mechanisms taking place at the semiconductor–catalyst interface.

For example, overlayers of Ga_2O_3[389] or Al_2O_3[390] have shown to passivate surface states, which was recognised by their decrease in surface state capacitance. Furthermore, Ga_2O_3 shifted the wa-

ter oxidation onset potential to more cathodic potentials, which was correlated to a shift of the surface state capacitance.[389] The deposition of a redox-active catalyst, such as IrO_x[53] or CoO_x,[100] on the other hand, has shown to form highly capacitive layers. The largely increased capacitance was attributed to the hole storing capability of those two catalyst, which prevents surface electron–hole back recombination.[53,100]

EIS of $BiVO_4$ photoanodes

To identify a possible effect of catalyst loading on $BiVO_4$ photoanodes, the CoFe-PB sequential coating was repeated either six (x6), eight (x8), or ten (x10) times. Figure 4.28 shows the results from EIS measurements of $BiVO_4$ photoanodes under light.
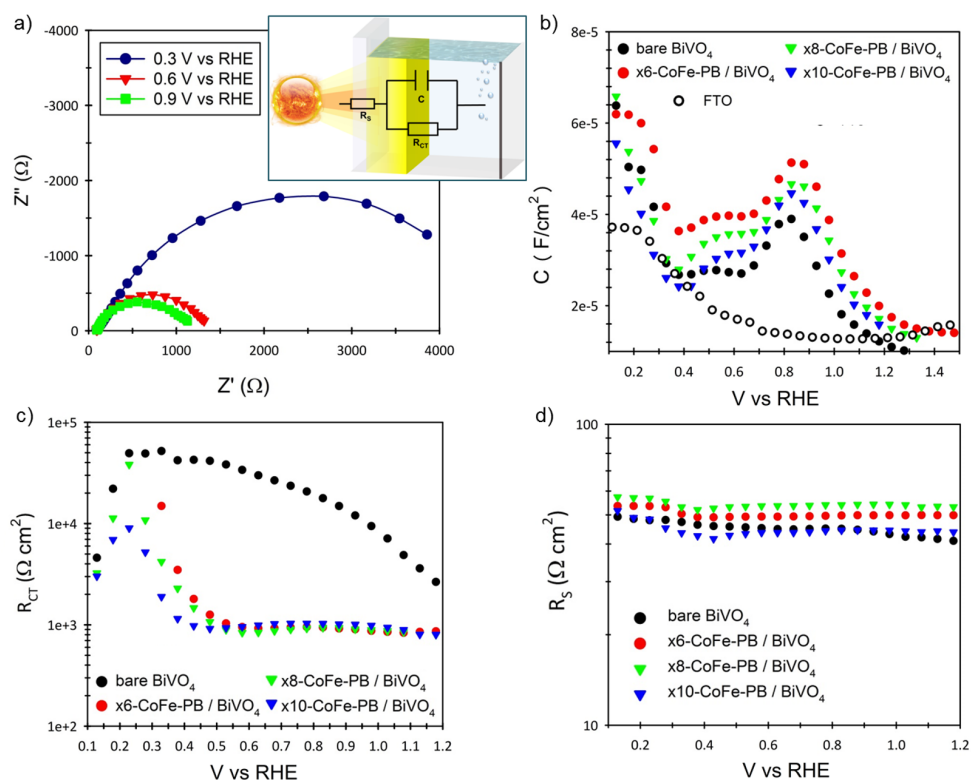
Figure 4.28: a) Nyquist plot of $Z''(\Omega)$ versus $Z'(\Omega)$ of CoFe-PB/$BiVO_4$ under illumination (1 sun) at three different potentials (pH 7). b) Capacitance C, c) charge-transfer resistance R_{CT}, and d) series resistance R_S of bare $BiVO_4$ (black), 6 times (red), 8 times (green), and 10 times (blue) sequentially coated CoFe-PB onto $BiVO_4$, obtained by fitting the complex EIS data to a Randles circuit (inset).

Imaginary and real impedance data consistently yielded a single arc in the Nyquist plot at all potentials, below and above the photocurrent onset (Figure 4.28a). Consequently, the data were fitted to a Randles' equivalent circuit model with one capacitance C, series resistance R_S, and charge-transfer resistance R_{CT}, which is presented in Figure 2.12 and the inset of Figure 4.28.[20,229]

The capacitance values in Figure 4.28b lie in the 10^{-5}–10^{-4} F/cm^2 range, which is relatively large for a typical semiconductor bulk capacitance. Those values rather correspond to the expected values for the electrical double-layer capacitance ($C_H \simeq 10^{-4}$–10^{-5} F/cm^2, see Section 2.3.2), which suggests a strong impact of such. Indeed, the capacitance measured for the bare FTO electrode (open circles in Figure 4.28b) at potentials below 0.4 V$_{RHE}$ and above 1.2 V$_{RHE}$ coincides with that of the BiVO$_4$ electrodes. Therefore, the FTO response, i.e. the electrical double-layer formed with the FTO interface, dominates the capacitance at these potentials. This is likely due to the inhomogeneous coverage of the FTO substrate by the nanostructured BiVO$_4$, as seen in the cross-sectional SEM-image in Figures 4.4e,f. At intermediate potentials, the BiVO$_4$ contribution to the capacitance overweights and gives a large capacitive feature around 0.8–0.9 V$_{RHE}$. This apparent chemical capacitance is attributed to the V^{4+}/V^{5+} redox couple, which is consistent with the CV behaviour (Figure 4.15b) and previous studies.[387]

Upon CoFe-PB modification, no change in the capacitance is apparent. Hence, the effect of CoFe-PB as either a hole accumulation layer or as passivating surface states can be ruled out. In those two cases an increase or decrease, respectively, of the capacitance at certain potentials would be expected.

In contrast, the charge-transfer resistance R_{CT} (Figure 4.15b) changes significantly when CoFe-PB is deposited. At values around 0.2–0.3 V$_{RHE}$, consistent with the photocurrent onset potential, a drop of R_{CT} to around 10^3 Ωcm^2 was observed for CoFe-PB/BiVO$_4$, whereas for bare BiVO$_4$ R_{CT} decreases only slowly. The amount of CoFe-PB, however, does not seem to have any effect on the resistances, at least not when CoFe-PB deposition is done by sequential coating. Thicker layers (>100 nm), which may be obtained through other methods, could lead to a different behaviour. The series resistance R_S (Figure 4.15d) depends mainly on the electrical contacts and wiring to the potentiostat and, therefore, is not affected by CoFe-PB.

Both the charge-transfer resistance drop and the constant capacitance suggest that holes, once photogenerated, efficiently transfer to CoFe-PB, and from there to H$_2$O, driving water oxidation. This

implies that CoFe-PB is a *true* catalyst, i.e. accepting and further transferring holes, which enhances the overall charge-transfer kinetics, as well as it suppresses surface electron–hole recombination in the $BiVO_4$ space–charge layer. Notwithstanding, neither the detailed catalytic mechanism nor the effect on catalytic and recombination rates can be deduced from the conducted EIS analysis.

EIS of Fe_2O_3 photoanodes

Impedance spectra of hematite (modified and unmodified) were recorded in the dark and under light and the acquired Nyquist plots are presented in Figure 4.29. Generally, the EIS data acquired for Fe_2O_3 were less noisy and easier to fit than for $BiVO_4$, while maintaining high stability of the photoelectrodes. This is why a larger, more complete data set for Fe_2O_3 electrodes is presented.
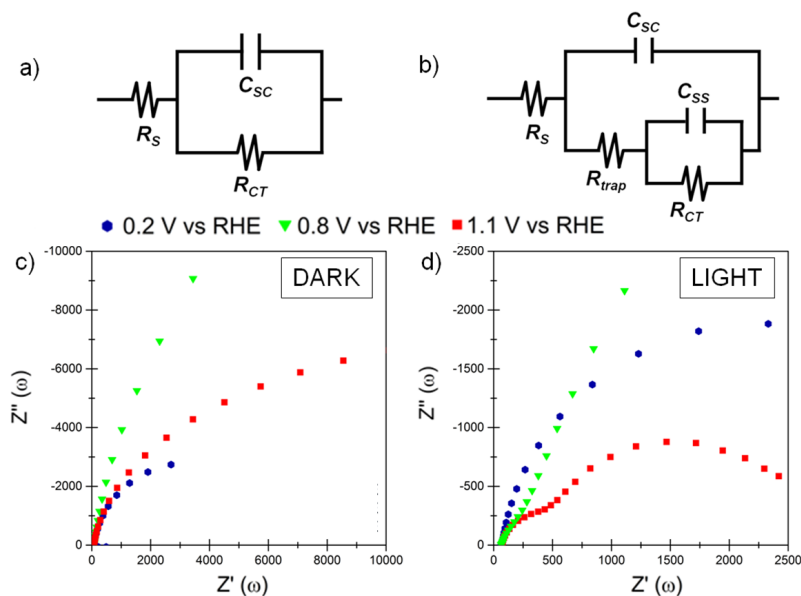
Figure 4.29: a,b) Simplified equivalent circuit models applied to fit the obtained Nyquist plots of $Z''(\Omega)$ versus $Z'(\Omega)$ of CoFe-PB/Fe_2O_3 c) in the dark and d) under illumination (1 sun) at three different potentials (pH 7). In the dark one arc is obtained at all V, while under illumination a single arc is obtained at 0.2 V_{RHE} (blue), a small second arc starts to develop at low frequencies at 0.8 V_{RHE} (green), and two arcs can clearly be distinguished at 1.1 V_{RHE} (red).

While in the dark systematically a single arc was obtained at all potentials (Figure 4.29c), a second arc appears under illumination close to the water oxidation onset (Figure 4.29d). This additional light-induced feature at lower frequencies, which is associ-

ated to the photocatalytic function of the photoanodes, allows for the extraction of a second capacitance, typically referred to as *surface state capacitance* C_{SS}.[20,216,217,331] Although the nature and role of surface states has caused some controversy in the literature,[21,215–217] I am using this notation for the sake of consistency with previous reports.[20,216] Indeed, it does not play a major role in the conducted impedance analysis, whether this capacitance is related to surface states inside the gap or to valence band states.[20,21]

The appearance of this second light-induced capacitance indicates that a change in mechanism is taking place. Water oxidation now competes with back electron–hole recombination and can be described by an *indirect* charge-transfer process, in which holes are trapped in a surface state and then transferred to the electrolyte.[21] The applied potential needed for such an indirect charge-transfer to occur is lower ($\simeq 0.8$ V_{RHE}) for CoFe-PB/Fe$_2$O$_3$ electrodes than for bare Fe$_2$O$_3$ ($\simeq 1.0$ V_{RHE}). At even higher potentials (>1.4 V_{RHE} for CoFe-PB/Fe$_2$O$_3$; >1.5 V_{RHE} for bare Fe$_2$O$_3$), the high frequency, capacitive semicircle of the surface state capacitance disappears again, since charge-transfer from the surface state to the electrolyte is no longer the rate-limiting step of water oxidation; mass transport through diffusion may become the bottleneck.

Figure 4.29b shows the equivalent circuit that was used to fit this process. Like the Randles' circuit (Figure 4.29a), it includes series and charge-transfer resistances, R_S and R_{CT}, and a capacitive element related to the space-charge layer capacitance of the semiconductor C_{SC}, to which the high frequency feature is attributed. Moreover, it includes a trapping resistance R_{trap} and the surface state capacitance C_{SS} (low frequency feature). This employed *indirect* charge-transfer model, in which charge-transfer R_{CT} takes place via surface states, is the same as for *direct* transfer from the VB.[20,21] It is commonly accepted to describe the impedance behaviour of hematite photoanodes.[216,331] Nonetheless, other equivalent circuit models might be considered, but do not affect the overall trends in the fitted resistances and capacitances.[217]

The series and charge-transfer resistances R_S and R_{CT} in the *dark* (from fitting to the Randles' circuit) of bare Fe$_2$O$_3$ (black), CoFe-PB/Fe$_2$O$_3$ (red), and CoFe-PB alone (purple) are shown in Figure 4.30. The series resistance R_S (Figure 4.30a) is independent of light irradiation and, thus, remained unchanged when illuminating the system. R_S of CoFe-PB alone is much smaller (about one half) than that of hematite. This is due to the fact that CoFe-PB was prepared by a hydrothermal method,[110] which leads to chemical bond formation with the FTO substrate, and hence a better electrical contact and reduction of R_S.

The dark charge-transfer resistance (Figure 4.30b) of bare hematite remains constant and large (around 10^5 Ωcm^2), since there is no significant charge-transfer in the applied potential range below 1.6 V_{RHE} (see dark CV, Figure 4.15a). The CoFe-PB modified Fe_2O_3, on the other hand, does show dark current and thus a reduced charge-transfer resistance, which is due to the electrocatalytic function of CoFe-PB. CoFe-PB alone shows a larger drop in R_{CT} at V >1.2 V_{RHE} because it has much more catalytically active sites available to transfer holes than the thin layer in CoFe-PB/Fe_2O_3. The small initial decrease of R_{CT} at 0.8–0.9 V_{RHE} is due to the capacitive current of the Co^{2+}/Co^{3+} and Fe^{2+}/Fe^{3+} redox couples, while the second decrease at 1.2–1.3 V_{RHE} is related to water oxidation (reflected in the dark CV, Figure 4.15c).
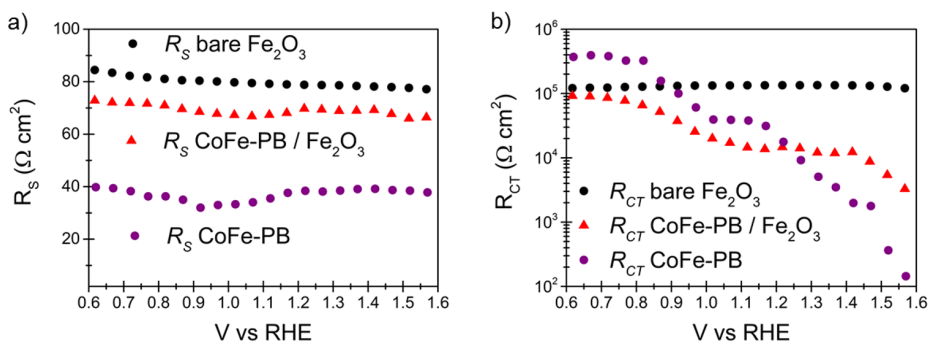
Figure 4.30: a) Series resistance R_S and b) charge-transfer resistance R_{CT} in the dark of bare Fe_2O_3 (black), CoFe-PB/$BiVO_4$ (red), and CoFe-PB alone (purple), measured in 0.1 M KP$_i$ buffer (pH 7).

Under illumination, the charge-transfer resistances of both bare Fe_2O_3 and CoFe-PB/Fe_2O_3 drop at lower potentials than in the dark and are shown in Figure 4.31a. R_{CT} of the photo-inactive CoFe-PB remains unchanged and is therefore not shown in Figure 4.31. The charge-transfer behaviour is consistent with the j–V characteristics (Figures 4.16c and 4.17c). R_{CT} of Fe_2O_3 starts to decrease around 1.0 V_{RHE}, whereas R_{CT} of CoFe-PB/Fe_2O_3 shows an initial small decrease at 0.7–0.8 V_{RHE} and a further drop around 1.0 V_{RHE}. The initial decrease can be attributed to the Co^{2+}/Co^{3+} and/or Fe^{2+}/Fe^{3+} oxidation, similar as in the dark. The potential, at which the minimum charge-transfer resistance of 10^3 Ωcm^2 is reached and significant charge-transfer occurs, is about 1.2 V_{RHE} for CoFe-PB/Fe_2O_3 and 1.3 V_{RHE} for bare Fe_2O_3. The difference corresponds to the onset potential shift observed in the CV and steady-state j–V curves (Figures 4.16c and 4.17c). The trapping resistance R_{trap} is neither influenced by the applied potential nor by catalyst modification.

The latter is consistent with the information provided by the experiments in hole scavenger (Figure 4.25b), in which the *j–V* curves with and without catalyst overlap, suggesting that charge transport to the surface, i.e. trapping, is catalyst independent.
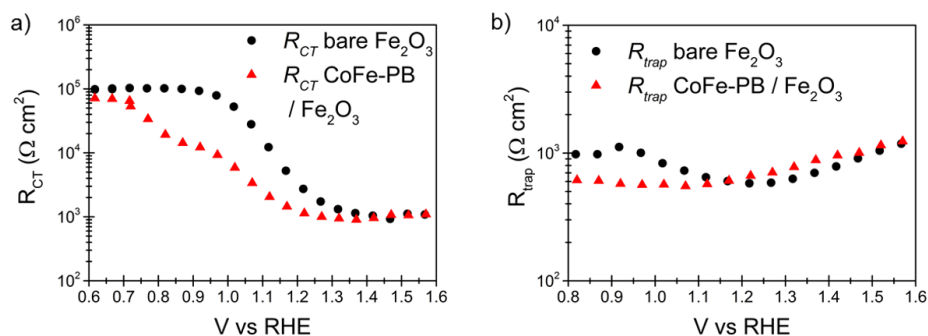
Figure 4.31: a) Charge-transfer resistance R_{CT} and b) trap resistance R_{trap} under illumination (1 sun) of bare Fe_2O_3 (black) and CoFe-PB/$BiVO_4$ (red), measured in 0.1 M KP_i buffer (pH 7).

Figure 4.32 shows the space–charge layer capacitance C_{SC} of bare and CoFe-PB modified Fe_2O_3 in the dark and under light, along with the corresponding Mott–Schottky plots. While the amount of catalyst had no influence on charge-transfer and trapping resistance, it seemed to impact the space-charge layer capacitance, which is why two times (2x, green) and ten times (10x, red) sequentially coated CoFe-PB/Fe_2O_3 electrodes are shown. C_{SC} decreases upon CoFe-PB deposition, the more (10x) catalyst, the more decrease. This is more recognisable in the Mott–Schottky plots (Figures 4.32c,d) of $1/C_{SC}^2$. The apparent decrease of C_{SC} with CoFe-PB modification is attributed to i) having less hematite surface area exposed to the electrolyte solution as more catalyst is added, or ii) reducing the surface dipole and therefore the amount of band bending. CoFe-PB is not expected to influence the dopant or donor concentration, as it resides on the surface of Fe_2O_3.

From the Mott–Schottky equation (Equation 2.34) and the dielectric permittivity ε_r, the dopant density N_d and the flat band potential V_{FB} of the semiconductor can be calculated. To allow for comparison with previous reports, $\varepsilon_r = 32$ was chosen for Fe_2O_3 (although literature values typically vary from 30 to 150).[216, 360] The resulting dopant concentration of Fe_2O_3 is around $N_d = 7$–$9 \cdot 10^{19}$ cm^{-3}, which is about 1 order of magnitude higher than observed by Klahr *et al.*,[216] resulting from both Zn-doping and Sn diffusion from the FTO substrate (see Section 4.2.1).[360] The flat band potential is given as the intercept with the x-coordinate in the Mott–Schottky plot (Figures 4.32c,d). Its fitted values $V_{FB} = 0.5$ (± 0.05) V_{RHE} are

independent of the amount of CoFe-PB, which further confirms that CoFe-PB does not change the band positions, i.e. the bulk electronic structure, of the underlying hematite. However, it differs by about 0.1 V, compared to V_{FB} obtained through hole scavenger experiments, due to inaccuracies of the used approximations. As described by Zandi *et al.*, the Mott–Schottky equation does not properly account for materials with high donor densities, as it neglects variations in the electrical double-layer.[360] This emphasises that the application of the Mott–Schottky equation is not always valid, and calculated variables should be regarded with caution.
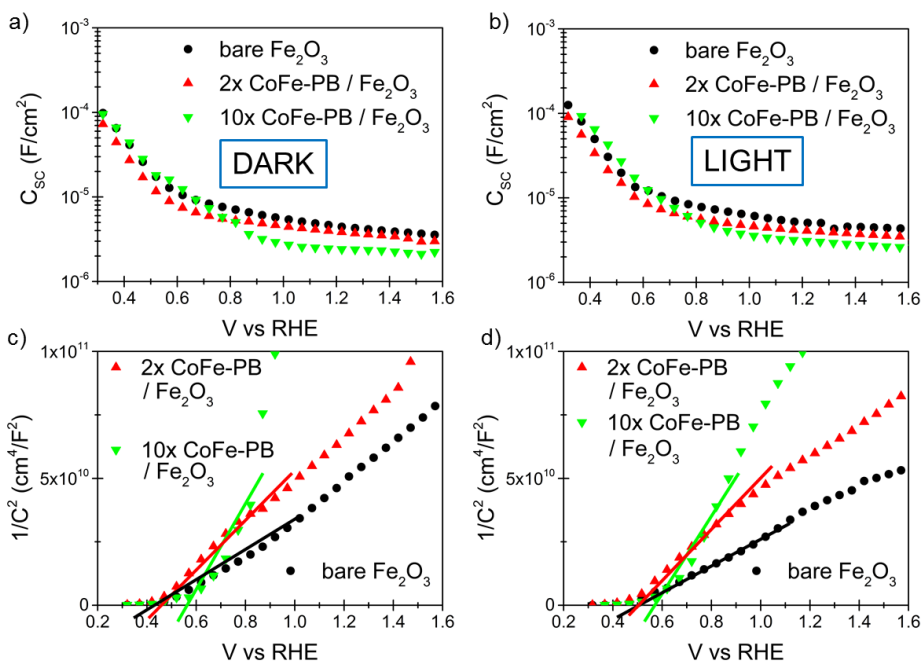
Figure 4.32: a,b) Space–charge capacitances C_{SC} of the Fe_2O_3 electrodes without (black), and with 2x (red) and 10x (green) CoFe-PB sequential coating, a) in the dark, b) under illumination (1 sun); and c,d) corresponding Mott–Schottky plots: c) in the dark, d) under light; all measured in 0.1 M KP_i buffer (pH 7).

No change of space–charge capacitance is observed under 1 sun illumination, as C_{SC} relates to an intrinsic property of the prepared semiconductor films. This is in contrast to previous studies,[216,331] in which a flattening shift in the Mott–Schottky plot was observed, when irradiating the sample. This obvious plateau-like feature has been ascribed to Fermi level pinning due to electronic trap states.[383] In the case of high annealing temperatures, such as applied, trap states may become passivated and the Fermi level *unpinned*.[360]

Figure 4.33 shows the surface state capacitance C_{SS} of bare Fe_2O_3 and CoFe-PB/BiVO$_4$, together with an illustration of the equivalent circuit elements.
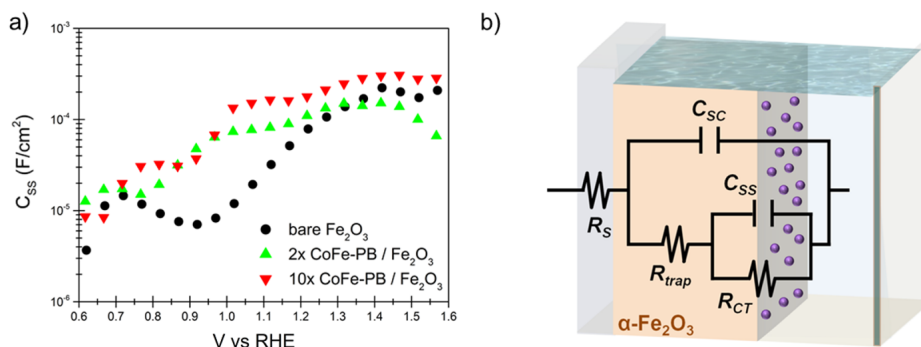
Figure 4.33: a) Surface state capacitance C_{SS} of Fe_2O_3 (black), 2x (green) and 10x (red) CoFe-PB/Fe$_2$O$_3$ under illumination (1 sun) in neutral medium (0.1 M KP$_i$), and b) corresponding *indirect CT* equivalent circuit.

For bare Fe_2O_3, C_{SS} starts to increase around 1.0 V_{RHE} until it reaches a maximum at around 1.4 V_{RHE}, in agreement with previous literature.[216,331] This surface state capacitance, which is only observed under water oxidation conditions, can be attributed to a reaction intermediate, which traps the photogenerated holes on the hematite surface.[331] Indeed, *in operando* IR spectroscopy measurements[391] and DFT calculations[333] identified an intermediate iron–oxo species Fe=O, suggested to be the bottleneck towards further completion of the water oxidation reaction (at least at pH 14).[215,333,391] This Fe=O intermediate possesses intragap electronic states,[215] which give rise to the observed capacitive behaviour.

CoFe-PB modification shifts the surface state capacitance to lower, more cathodic potentials, independent of the amount of catalyst loading. This shift of C_{SS}, which has also been observed for Ga_2O_3 overlayers on hematite,[389] appears to be responsible for the observed onset potential and charge-transfer resistance shifts (Figures 4.17 and 4.31c). C_{SS} of CoFe-PB/Fe$_2$O$_3$ begins to rise around 0.8 V_{RHE}, becomes flat between ~1.0–1.2 V_{RHE}, and then rises again and approaches the same maximum as for bare Fe_2O_3 at ~1.4 V_{RHE}. The absolute magnitude of C_{SS}, however, is not changed. Hence, surface state passivation or significant hole accumulation can be ruled out.

At ~1.4 V_{RHE} the C_{SS} curves of bare and modified Fe_2O_3 overlap, which leads to the assumption that the same water oxidation

intermediate (Fe=O) is formed on both bare and modified Fe_2O_3, where the OER takes place. The shoulder of C_{SS} at lower potentials could be ascribed to a partial oxidation of CoFe-PB on the surface, which partially suppresses surface electron–hole back recombination. Notwithstanding, this is speculative; the nature of the surface state of CoFe-PB/Fe_2O_3 cannot clearly be determined from the experiment.

Taken together EIS and other mechanistic studies, it can be concluded that CoFe-PB on hematite does *not* act as a true charge-transfer catalyst, which agrees with observations of CoO_x on hematite.[101,132] In contrast, CoFe-PB on $BiVO_4$ shows a completely different behaviour. The performed PEC measurements suggest its function as true charge-transfer catalyst. To shed more light on the reasons for the opposing behaviour of CoFe-PB on different metal oxide systems Density Functional Theory (**DFT**) calculations were carried out.

4.6   Theoretical level alignment

The electronic energy levels of the composite photoelectrodes were computed and aligned in order to evaluate the thermodynamic feasibility for interfacial charge-transfer.

4.6.1   Computational assessment of interfaces

Aligning the energy levels in heterostructures is a challenging problem, for which no single, straightforward solution exists.[127–130,392] Finding adequate structural models of the electrochemical interface is hampered by the fact that the real interface depends crucially on the synthesis conditions and is often ill-defined.[130,393] Hence, atomistic models need to take into account a manifold of possible interfacial arrangements under experimental conditions, which in turn demands extensive computational modelling, which renders the task in many cases infeasible. Moreover, as DFT poorly describes the electronic states close to the Fermi level (see Section 2.1.2), methods of higher accuracy are required, such as hybrid functionals or many-body perturbation theory (MBPT), which tremendously increase the computational cost.

Several groups successfully performed atomistic calculations of semiconductor–liquid interfaces with high accuracy.[131,394,395] Those studies, however, involve extensive *ab initio* molecular dynamics (MD) modelling of the liquid electrolyte combined with hybrid meth-

ods or MBPT. Adding a co-catalyst as a third component onto the semiconductor interface increases the level of complexity vastly, and detailed theoretical studies of such a semiconductor–catalyst–liquid junction are scarce.[129,142]

As a consequence, other alignment methods, which do *not* involve atomistic interface models, but a common reference to align the calculated electronic structures, are more feasible and chosen herein. Such methods are much faster, less cost-intensive, and also less prone to errors due to insufficient knowledge of the geometry and stoichiometry of the real interface.

For example, for highly crystalline systems with well defined lattice sites, the on-site electrostatic potentials (Madelung potentials) can be used and compared to the potential at infinite interatomic distance;[392] yet, this is only possible for certain comparable systems.

The absolute vacuum levels seems to be an obvious choice of a common reference. It can be obtained by calculating the workfunction of a solid surface, as described by Toroker *et al.*[396] Similarly, its determination allows for the computation of ionisation potentials and electron affinities, which were also used to align the band edge positions.[397,398] This method, however, requires the knowledge of the exposed and interacting surfaces, while the resulting band alignment strongly depends on the type of surface termination.[396,398] Moreover, the workfunction is highly influenced by band bending, adsorbates, and surface dipoles.[218] Therefore, such an approach is not applicable, since i) the surface of CoFe-PB is not clearly defined,[110] and ii) the workfunction of the ultrathin catalyst layer is not a physical observable.[130]

In this work, I aligned the energy levels along unperturbed core states of atoms, in this case oxygen, which has led to success in deriving the relative valence offset in several semiconductors.[130,399,400] This chosen method allows for a relatively simple extraction of band alignments without computationally very expensive MBPT calculations[401] and/or construction of a three-component interface model. Although it does not provide detailed information about the interfacial structure, it allows us to determine if the overall alignment of the band edges is favourable, which is a necessary prerequisite for charge-transfer to happen.[142]

4.6.2 Electronic structures of employed systems

For aligning the DOS of the employed photoanodes and water, the average energy of the oxygen 2*s* orbital is taken as a common reference. Since CoFe-PB does not contain any oxygen (and does not

share any other element with $BiVO_4$), one H_2O molecule was incorporated into one of its tetrahedral holes. This had no effect on the electronic structure, which is demonstrated by Figure 4.34. Also other structural and electronic properties remained unaffected.
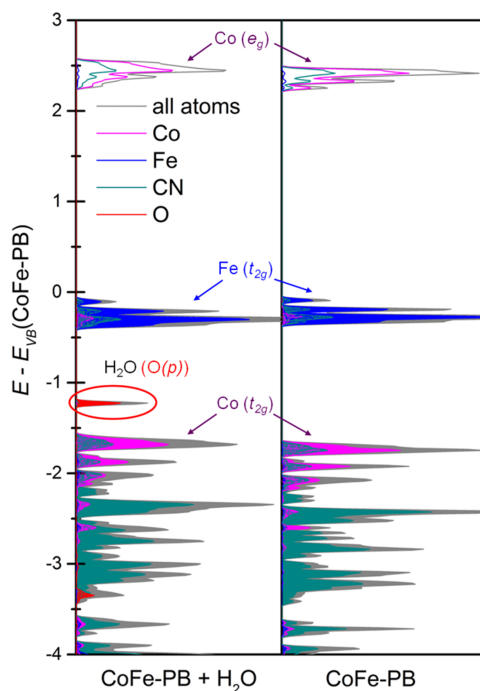
Figure 4.34: Density of States (calculated with HSE03-13) of $K[CoFe(CN)_6]$ with (on the left) and without (on the right) incorporated H_2O molecule. The reference energy was set to zero at the valence band maximum. The DOS remains unaffected by water, only a peak from the O $2p$ orbitals is appearing.

The Densities of States (DOS) of the bulk structures were calculated with the accurate hybrid functional HSE03-13, which is described in Chapter 3, and then aligned by the electronic O $2s$ core states. The average energy, which is obtained by integrating the projected DOS, is expected not to vary significantly.[402]

In order to allow for efficient charge-transfer and, thus, water oxidation catalysis, the band edges of all components need to be suitably aligned. This means that the catalyst needs to have filled electronic states at higher energy than the VBM of the photoanode, so that there is a *thermodynamic* driving force for the holes (electrons) to be transferred to (from) the catalyst. Furthermore, the highest occupied molecular orbital (HOMO) of solvent water needs to lie above that of the catalyst, so that further hole-transfer from the catalyst to water, i.e. water oxidation, can occur. The aligned energy lev-

els of both the semiconductor–catalyst–water systems are shown in Figure 4.35.
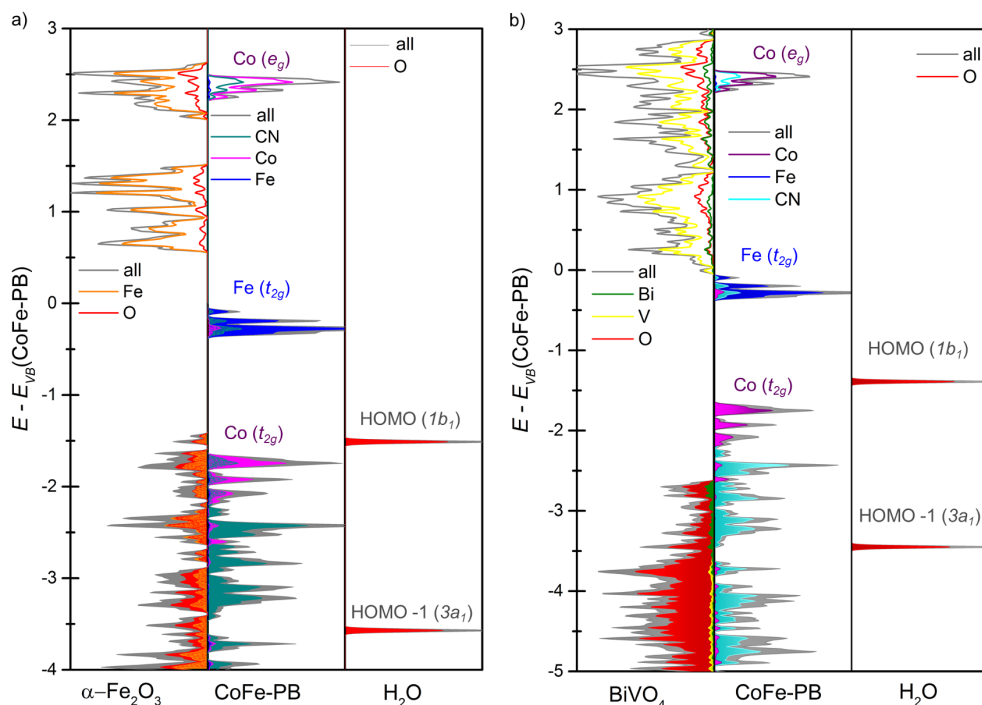
Figure 4.35: Densities of States (calculated with HSE03-13) of a) Fe_2O_3 and b) $BiVO_4$ aligned with $K[CoFe(CN)_6]$ and H_2O (aligned by core O $2s$ states). The reference energy was set to zero at the valence band maximum of CoFe-PB. Filled (empty) electronic states are represented by filled (empty) areas.

When a photon gets adsorbed by hematite (Figure 4.35a), a hole will be created in the VB, comprised of hybridised Fe $3d$ and O $2p$ states. At this energy, however, there are no electronic states in the CoFe-PB catalyst, with which the photogenerated hole may interact. The filled Co t_{2g} states, which are responsible for water oxidation lie just below the VB edge of Fe_2O_3. Hence there is no intrinsic driving force for holes to transfer from Fe_2O_3 to CoFe-PB, as shown schematically in Figure 4.36a. Nevertheless, that does not imply that hole transfer cannot happen; under reaction conditions, i.e. at room temperature and applied potential, charges may transfer to the catalyst, but with an energy penalty.

The Fe t_{2g} states of CoFe-PB, which lie about 1 eV above Co t_{2g}, do *not* directly participate in the water oxidation reaction, nor are involved in the interface formation with the semiconductor. Fe is strongly coordinated by its cyanide ligands (from the C-site), and CN ligand substitution by either H_2O or surface OH demands a lot

of energy. Hence, binding to Fe is extremely unfavourable. The Fe centres play a stabilising role in the in CoFe-PB scaffold, rather than being actively involved in the catalytic reaction.

In the case of $BiVO_4$/CoFe-PB (Figure 4.35b), the thermodynamic alignment of energy level meets the criteria for favourable hole transfer, as also schematically represented in Figure 4.36b. The catalytically active Co t_{2g} states are spread around 0.5–1.0 eV above the valence band of $BiVO_4$. This means that once a photohole is generated in the VB of $BiVO_4$, it is driven towards CoFe-PB. The HOMO ($1b_1$) of H_2O lies about 0.3–0.4 eV above those t_{2g} levels, and therefore can accept the holes transferred to Co t_{2g}; consequently, water oxidation at CoFe-PB can occur. Moreover, the $1b_1$ symmetry allows for efficient orbital overlap with Co t_{2g}, which is necessary for fast inner-sphere hole transfer.[33, 268]
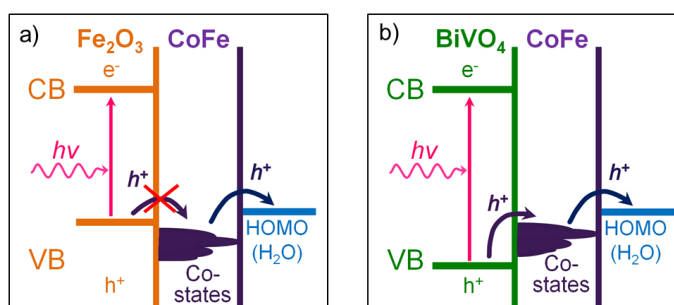
Figure 4.36: Schematic energy level alignment of a) Fe_2O_3 and b) $BiVO_4$ with K[CoFe(CN)$_6$] and H_2O.

It has to be noted that the calculated electronic levels are not directly comparable with experimentally obtained redox levels, which are typically presented in the literature in the field of photoelectrochemical water splitting, as for example in Refs. [34], [28], and [36] (and Figure 1.6). Those redox potentials are generally given versus SHE or another reference electrode (as explained in Section 2.3.1), whereas the calculated energy levels are aligned with respect to the CoFe-PB VBM (E_{VB}(CoFe-PB)) . Moreover, the water HOMO is *not* the adiabatic water oxidation potential ($V^o = 1.23\ V_{RHE}$), which is shown in Refs. [34], [28], and [36]. Indeed, considering that water oxidation is a four electron / four proton transfer involving several intermediate steps, it seems more appropriate to show the *molecular* orbital levels and to determine the likelihood of a first single hole transfer.[33]

Taken together, the different photoelectrochemical behaviour of CoFe-PB on Fe_2O_3 and $BiVO_4$ can be explained by the different thermodynamics of the catalytic interface. While the CoFe-PB/$BiVO_4$ interface allows for favourable hole transfer and water oxidation catal-

ysis, the CoFe-PB/Fe_2O_3 interface gives no thermodynamic driving force for this to happen (see Figure 4.36).

4.6.3 Reasons for performance enhancement of the catalytic interfaces

Although the deposition of CoFe-PB onto Fe_2O_3 does not lead to an advantageous charge-transfer pathway, it yet enhances the photo-electrochemical performance. The reason for the observed cathodic shift in onset potential upon CoFe-PB modification is likely due to the shift of the surface state capacitance (see Figure 4.33).

This is in line with previous studies of the Ga_2O_3/Fe_2O_3 inter-face, in which the onset potential was lowered without having a favourable band alignment.[403] Hence the effect of Ga_2O_3 can be attributed to surface state passivation and/or lowering of the surface state capacitance,[389] as for CoFe-PB. At variance, for Al_2O_3 the thermodynamic level alignment to hematite seems favourable, yet the reaction kinetics are not favoured by Al_2O_3 and OER is expected to take place on the Fe_2O_3 sites.[404]

This shows that an advantageous level alignment is a necessary but not conclusive criterion for hole transfer catalysis. Interfacial hole transfer also needs to be *kinetically* favoured, which means hole transfer from the semiconductor surface to the co-catalyst has to be faster than to H_2O. In this context, a spectroscopic study of the charge carrier kinetics in CoFe-PB/$BiVO_4$ is carried out and discussed in Chapter 5.

4.7 Conclusion of Chapter 4

In this Chapter, it was shown that the appropriate energy level alignment is crucial to the catalytic mechanism when a photocat-alytic semiconductor is modified by an electrocatalyst material. If the electronic states are not appropriately aligned for hole transfer to be thermodynamically favourable, the function of the deposited electrocatalyst is likely to be not *truly* catalytic. This means, no hole/electron transfer to/from the electrocatalyst occurs and its working mechanism is different.[87,101,102,132,133,217,357,358] The CoFe-PB/hematite interface is an example for this. In case of CoFe-PB/$BiVO_4$, however, the theoretical bulk level alignment has shown that there is a thermodynamic driving force for hole transfer to occur.

Additionally, the epitaxial deposition of CoFe-PB on $BiVO_4$ leads to a higher degree of wetting than on Fe_2O_3, likely due to the formation of chemical bonds to the metal oxide (Figures 4.6 and 4.7). Those interfacial bonds can be seen as chemical linkers between the two compounds, enabling fast and efficient charge-transfer (see Figure 4.8).

Both the fulfilment of the necessary energetic criteria and the well-matching epitaxy of the interface suggest that the function of CoFe-PB on $BiVO_4$ is to accept holes and to drive the water oxidation reaction, hence being a genuine catalyst (with the cobalt centres being the catalytically active sites). Photoelectrochemical experiments and electrochemical impedance spectroscopy strongly support such a favoured hole transfer from $BiVO_4$ to CoFe-PB.

Nonetheless, the employed photoelectrochemical techniques are based on measuring (photo)currents, i.e. extracted electrons from the back of the electrode. For a more direct determination of the hole dynamics at the semiconductor–catalyst and electrolyte interfaces, time-resolved spectroscopic methods were applied to the advantageous CoFe-PB/$BiVO_4$ system and are focus of the next Chapter.

Chapter 5

Charge carrier dynamics in modified photoanodes

In this Chapter, a complementary spectroscopic investigation of the charge-transfer dynamics in CoFe-PB modified $BiVO_4$ photoanodes is carried out. With spectroelectrochemical (**SEC**) techniques the absorption features of CoFe-PB that are important to water oxidation catalysis are determined. Further, time-dependent spectroscopy techniques, namely transient absorption spectroscopy (**TAS**) and photo-induced absorption spectroscopy (**PIAS**), are employed in order to elucidate the life times of photogenerated holes. From this, the time scales of charge-transfer and water oxidation are deduced and a mechanistic proposal is given. The results of this study have been submitted for publication in *Paper IV*.

5.1 Motivation

Although the previous findings strongly indicate that holes efficiently transfer from $BiVO_4$ to CoFe-PB, where they effectively oxidise water, results from PEC measurements cannot conclusively determine the fate of photogenerated holes. From the *j–V* response obtained by PEC, only a net current, which is the sum of the total electron and hole currents, is measured. Hence, it is not possible to discern if holes go directly into solution, or first transfer via the catalyst. Furthermore, the fractions of total applied potential, which drop at the interfaces, i.e. between conductive support and semiconductor, between semiconductor and catalyst, and at the interface with the electrolyte, cannot be determined.[126] In this context, time-dependent spectroscopy gives a means to directly access the hole dynamics at the CoFe-PB/$BiVO_4$ interface.

5.2 Dynamics of photogenerated holes in metal oxide semiconductors

5.2.1 Unmodified metal oxide photoanodes

Efficient water oxidation on metal oxide photoanodes, such as TiO_2 Fe_2O_3, WO_3, and $BiVO_4$, is mainly limited by fast electron–hole re-combination.[87,118–120,122,330,405–407] In other words, OER catalysis (typically on the time scale of tens of ms to s) is in kinetic competition with potential dependent recombination of holes accumulated at the surface, i.e. *surface* or *back* electron–hole recombination (see Section 2.3.3).[87,122,406]

In order to achieve high photoelectrochemical efficiencies, a relatively large anodic bias is required, which increases band bending and space–charge layer (SCL) separation, and thus suppresses surface recombination. This is schematically illustrated in Figure 5.1.
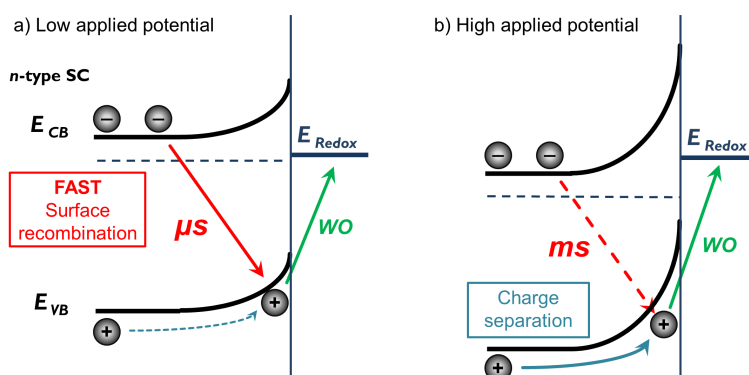
Figure 5.1: Schematic representation of the electronic processes occurring in an *n*-type photoanode under water oxidation conditions. a) At low applied bias the photogenerated holes at the surface are not well separated from the bulk electrons and recombine rapidly (∼ms in $BiVO_4$).[122] b) At high applied bias charge separation is increased and surface recombination reduced (∼0.1–1 s in $BiVO_4$).[122] Due to the larger electric field also water oxidation (WO) is enhanced.

If no or only a small positive bias is applied (Figure 5.1a), holes at the semiconductor surface are not efficiently separated and prone to fast recombination with electrons from the bulk, before they are able to oxidise water. In the case of unmodified $BiVO_4$, the rate of water oxidation lies in the range of 0.1–1 s^{-1}, whereas the rate of surface recombination is about 100–1000 times faster at potentials close to that of the flat band potential.[122,133,407] Thus, only a negligible fraction of photogenerated holes survives long enough to react with H_2O before recombining.

When a high bias is applied as in Figure 5.1b, band bending is increased, which leads to more efficient charge separation and higher density of surface accumulated holes. For surface electron–hole recombination to occur, electrons from the bulk need to tunnel through the space–charge layer. Increasing the potential drop across the space–charge layer reduces the likelihood of surface recombination, and thus its time constant, which is on the order of 0.1–1 s in $BiVO_4$ at the onset potential.[122] Moreover, increasing the potential results in a larger thermodynamic driving force for water oxidation. The water oxidation rate per catalytically active site, however, is not changed. Hence, in the case of $BiVO_4$ water oxidation now becomes kinetically competitive with surface recombination, both happening on a ms–s timescale.

A common approach to overcome the kinetic limitations of water oxidation is to deposit an efficient electrocatalyst on the surface of a photoanode, such as CoFe-PB in this study. The function of the catalyst is usually to increase the rate of water oxidation and/or to reduce the rate of recombination. Initial photoelectrochemical studies indicated that CoFe-PB acts as a true catalyst on $BiVO_4$, enhancing the rate of water oxidation by actively performing catalysis at its active sites. Nonetheless, its kinetic contributions to hole transfer and recombination could not unambiguously be discerned, and are focus of this Chapter. To provide context and to allow for a further comparison, first the case of CoO_x/semiconductor interfaces is discussed.

5.2.2 Influence of the catalyst: The case of CoO_x

Many studies address the impact of cobalt oxide catalysts, CoO_x or CoP_i, on the water oxidation enhancement when applied on different semiconductor photoanodes.[23,50,85–87,99–101,132,133,143,217,358] The deposition of CoO_x on Fe_2O_3 or $BiVO_4$ typically shifted the onset potential cathodically by about 0.1–0.4 V in neutral media, depending on the employed experimental conditions.[50,86,87,100,101,132,133,358] Several independent studies based on various PEC measurements,[50,85] including electrochemical impedance spectroscopy (EIS),[100] intensity modulated spectroscopy (IMPS),[87,102] and time-resolved spectroscopy (TAS and PIAS),[101,132,133,358] attributed this effect to reduced surface recombination, *not* enhanced catalytic activity.

When deposited on the *n*-type metal oxide, CoO_x increases the surface dipole and thus enhances the band bending, similar as represented in Figure 5.1b. This is sometimes described in the litera-

ture as Schottky barrier[87,101,143] or *p-n* heterojunction[85] formation. Its impact on the underlying semiconductor is therefore comparable to that of a strong applied external bias (within the simple model in 5.1b), which in turn reduces the need for large overpotentials. Due to the increased space–charge layer at the semiconductor/CoO_x interface, surface recombination is efficiently suppressed and hole lifetime increased. The catalysis, however, is assumed to effectively take place at the metal oxide photoanode, *not* at the catalytically active Co centres on CoO_x.

Indeed, the catalytic rate of water oxidation on CoO_x was found to be much (around 100–1000 times) slower than on most typical photoanode materials.[132,358] Turnover frequencies of CoO_x were found to lie in the order of 10^{-3}–10^{-2} s^{-1} (at 0.4 V overpotential),[90,91] while the water oxidation rate constants on Fe_2O_3 and $BiVO_4$ are on the order of 0.1–10 s^{-1}.[120,122,405,407] Also hole transfer from the semiconductor to CoO_x was found to be relatively slow, about one order of magnitude slower than direct water oxidation on $BiVO_4$.[358] This suggests that only a small fraction of photogenerated holes gets transferred across the semiconductor–catalyst interface.

Nevertheless, it has to be noted that in the case of CoO_x/Fe_2O_3, literature is not entirely conclusive about the exact role of CoO_x.[44,99,100,132] Impedance spectroscopy data suggested significant oxidation of CoO_x on top of hematite, and hence efficient transfer across the interface.[100] This seemingly contradictory result may be caused by differences in morphology, as suggested by Carrol *et al.*[143] Mesostructured, thicker hematite with electrodeposited CoO_x noduli was employed in TAS experiments,[101,132] while planar, thin films of hematite with a thick, impermeable catalyst layer were used for the impedance measurements.[100]

For the sake of comparison to the time-resolved measurements herein, the time constants as observed by Ma *et al.* for the CoO_x/$BiVO_4$ interface are taken for the following discussion.[133,358]

5.3 Spectral assignment of CoFe-PB

Before considering the effect of CoFe-PB modification on $BiVO_4$, the spectral features of CoFe-PB alone were investigated, as knowledge of those is key to interpret spectroscopic data of the interface. To do so, spectroelectrochemistry (**SEC**) of CoFe-PB on FTO under electrochemical conditions was measured. CoFe-PB electrodes were prepared by a modified solvothermal procedure developed by Han *et al.*, as described in Appendix A.[110]

Figure 5.2 shows the *ground state* absorption spectra of CoFe-PB in H_2O (KP$_i$ buffer) at different potentials, represented as difference ΔOD versus the open-circuit (resting) potential (Figure 5.2a) or the water oxidation onset potential (Figure 5.2b).
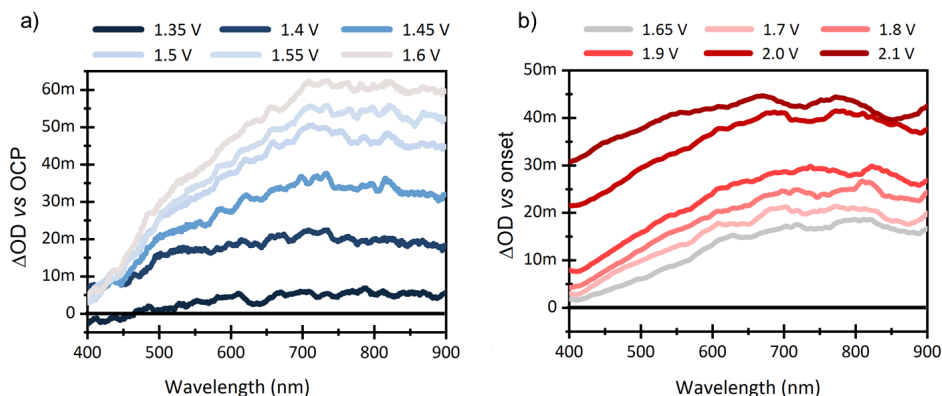
Figure 5.2: Spectroelectrochemical difference spectra of CoFe-PB from 400 to 900 nm of a) the absorption difference versus the open circuit potential (OCP, 1.15 V_{RHE}) below water oxidation onset and b) versus the onset potential (1.58 V_{RHE}) in 0.1 M KP$_i$ buffer, pH 7.

When increasing the potential above the open-circuit potential (OCP), the absorption at wavelengths larger than 500 nm rises (Figure 5.2a). This consistently observed, broad absorption feature with a maximum around 700–800 nm saturates at potentials around 2.0 V_{RHE} (Figure 5.2b). It is hence attributed to an oxidation of the CoFe-PB system, as it further correlates strongly with the oxidation and reduction waves observed by cyclic voltammetry, which is shown in Figure 5.3a.

Due to the non-stoichiometric nature of CoFe-PB (A$_x$Co$_y$[Fe(CN)$_6$]$_z$ ·nH$_2$O), containing a mixture of ls-ls Co(III)Fe(II)-PB and hs-ls Co(II)Fe(III)-PB (Figure 3.13) with both Co and Fe in different electronic environments, the redox peaks cannot clearly be assigned to either Co^{2+}/Co^{3+} or Fe^{2+}/Fe^{3+} redox couples (see Sections 3.2 and 4.3.5).[300,312] Therefore, the oxidised CoFe-PB state is simply labelled as "CoFe-PB$^+$". Since "CoFe-PB$^+$" appears *before* the catalytic water oxidation onset, it is not directly involved in the water oxidation reaction and can be regarded as a *pre-catalytic* species.

Further oxidation of CoFe-PB above the catalytic water oxidation onset potential of around 1.6 V_{RHE} (Figure 5.2b) leads to broadening of the spectrum, i.e. flattening in the long wavelength region, while absorption at shorter wavelengths increases. The appearance of the spectral feature in the region <500 nm *above* the onset is likely

169

due to a second oxidation of CoFe-PB, which is related to water oxidation. This doubly oxidised "CoFe-PB^{2+}" is therefore ascribed to as *catalytic* species.

It is noted though that the shape of the absorption spectrum of oxidised CoFe-PB differs from that in Ref. [408]. In this, a different preparation method was used, which is likely to form a different CoFe-PB stoichiometry with slightly different redox and absorption features.[408] The observed isosbestic point (where absorption is constant), is however the same (400 nm) as obtained herein.
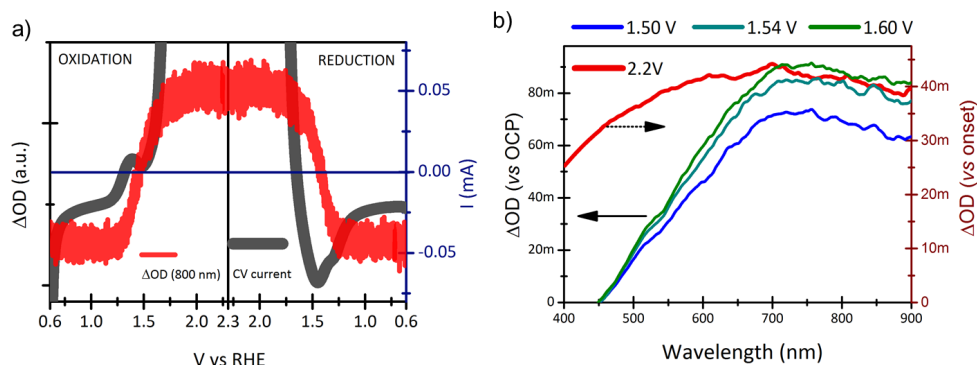
Figure 5.3: SEC of CoFe-PB: a) Potential dependence of the absorption at 800 nm (red), simultaneously recorded during a CV scan (grey) at a 1 mV/s scan rate (oxidative CV scan on the left, reductive CV scan on the right). The absorption at 800 nm, assigned to "CoFe-PB$^+$", increases/decreases with the oxidation/reduction wave. b) ΔOD vs OCP (1.15 V$_{RHE}$) corresponding to "CoFe-PB$^+$" (blue and green), and vs the onset potential (1.58 V$_{RHE}$) corresponding to "CoFe-PB^{2+}" (red) (0.1 M KP$_i$ buffer, pH 7).

As a summary, Figure 5.3b compares the absorption of CoFe-PB above and below the water oxidation onset. The asymmetric (decaying more strongly towards shorter wavelength) absorption peak around 700–800 nm (blue and green) at mild oxidative potentials corresponds to "CoFe-PB$^+$", and the blue-shifted absorption (red) at potentials exceeding the onset potential corresponds to "CoFe-PB^{2+}". Utilising the spectral fingerprint of oxidised CoFe-PB, subsequent TAS and PIAS data of the CoFe–PB/BiVO$_4$ photoanodes may be interpreted.

5.4 Time-resolved spectroscopy of CoFe-PB/BiVO$_4$

In order to investigate the dynamics of photogenerated holes in the CoFe-PB/BiVO$_4$ system time-dependent spectroscopy, namely **TAS**

(transient absorption spectroscopy) and **PIAS** (photo-induced absorption spectroscopy) were carried out.

5.4.1 Transient absorption spectroscopy

TAS measurements with a time resolution from microseconds to seconds were performed for bare and CoFe-PB modified $BiVO_4$ samples. Figure 5.4a shows the obtained TA spectrum at 10 ms after the excitation pulse. At low applied potentials (0.25 and 0.70 V_{RHE}) and at all wavelengths, no or only negligible absorption is observed 10 ms after the the sample was excited. This means the excited state has already relaxed back to the ground state, or in other words, all photogenerated charges have recombined. At larger applied bias (1.50 V_{RHE}) above the water oxidation onset, a persistent signal peaking at 550 nm is detected after 10 ms. Previous TAS studies of pristine $BiVO_4$ have shown that photogenerated holes show an absorption signal around 550 nm.[122,409] The measured 550 nm signal, which is shown in Figure 5.4b, is therefore attributed to photoholes accumulated at the surface. As those holes are responsible for water oxidation in bare $BiVO_4$, they are only observed at a bias high enough for water oxidation to become significant. At lower potentials, band bending is insufficient to drive enough charge-separation and hole accumulation at the surface, before electron–hole recombination occurs.[122,133]
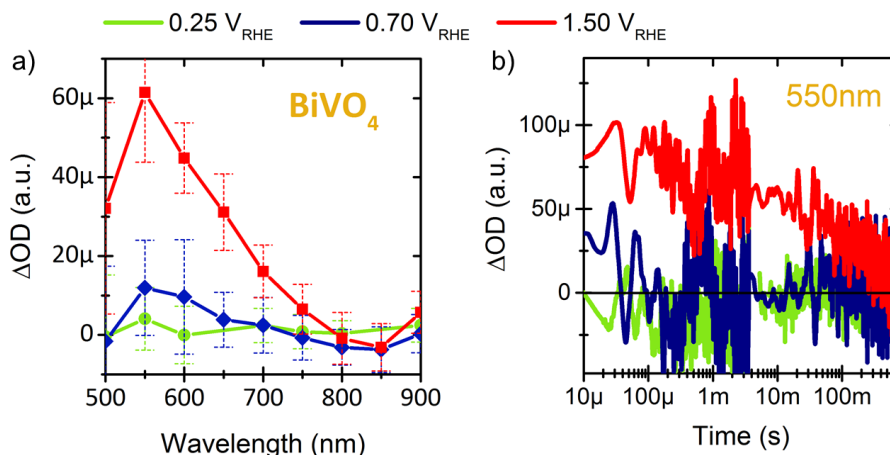
Figure 5.4: a) TA spectrum of $BiVO_4$ at 10 ms after the excitation pulse and b) TA signal decay of photogenerated holes at 550 nm at different applied potentials (in 0.1 M KP_i buffer, pH 7). Only at strong bias (1.5 V_{RHE}) a persistent transient (red) is observed.

The signal-to-noise ratio however was low, as the films were not highly transmissive. This is due to the inhomogeneous, mesostructured morphology of the electrodeposited $BiVO_4$ films, which scatter a large fraction of incoming probe light. Therefore, the measured signal could not be fitted; nevertheless, at high applied bias the decay resembles the expected biphasic decay (see Equation 2.37), consisting of a fast phase (<ms) due to bulk electron–hole recombination, and a slow phase (ms–s) due to surface recombination, which is in agreement with literature.[122,217,406] Although a quantitative assignment of the signal, such as in Ref. [122], was precluded, a qualitative comparison with modified CoFe-PB/$BiVO_4$ could be made.

When depositing CoFe-PB a significant change is obtained and shown in Figure 5.5. Instead of the 550 nm feature of $BiVO_4$ holes, a red-shifted signal around 700–800 nm is observed, persistent even at low applied potentials. This has two important implications; on one hand the apparent loss of the $BiVO_4$ hole signal indicates that the accumulated holes have been either annihilated or transferred; on the other hand, the appearing feature at ~700 nm upon CoFe-PB modification signifies the generation of a new charged species within CoFe-PB.
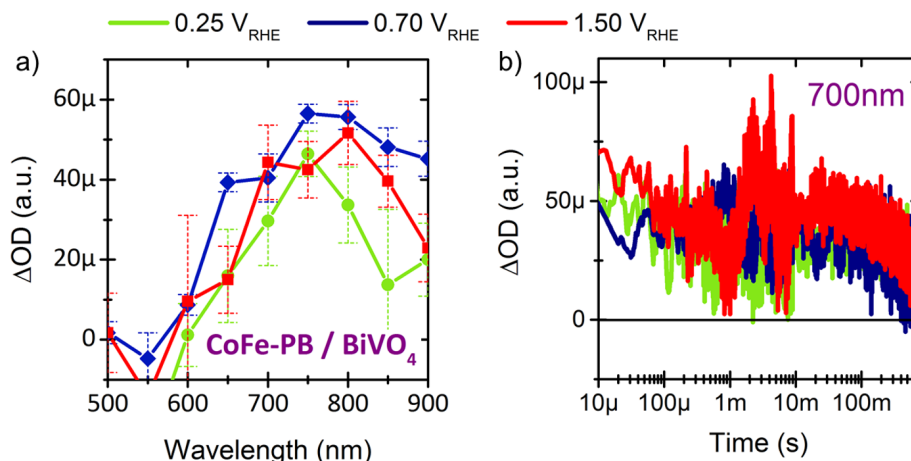
Figure 5.5: a) TA spectrum of CoFe-PB/$BiVO_4$ at 10 ms after the excitation pulse and b) TA signal decay at 700 nm at different applied potentials (in 0.1 M KP_i buffer, pH 7). Even at low applied potentials a persistent transient at 700 nm is observed, which is attributed to hole transfer to CoFe-PB, creating "CoFe-PB$^+$".

Comparing the TA spectra at 10 ms (Figure 5.5a) with that of oxidised CoFe-PB ("CoFe$^+$") from SEC (Figures 5.2a and 5.3b), a strong resemblance can be seen. This suggests that CoFe-PB on the $BiVO_4$ surface gets oxidised during the TAS experiment, mean-

ing that holes generated in $BiVO_4$ transfer to CoFe-PB, resulting in an absorption increase at 700–800 nm. Importantly, this leads to a prolonged lifetimes of photogenerated charges, even without[†] or very low applied potentials (Figure 5.5b). Hence, charge-separation across the $BiVO_4$/CoFe-PB interface is largely irreversible and efficiently preventing electron–hole recombination within $BiVO_4$.

Moreover, the amplitude of the ∼700 nm signal remains almost constant at early times, from 10 μs to tens of ms, i.e. does not increase. This indicates that the "CoFe[+]" generation has almost been completed *before* spectral acquisition, which in turn indicates that interfacial hole transfer takes place on the sub-microsecond time scale. In order to determine the exact time scale of such an efficient charge-transfer, a different TAS set-up with nano- or even picosecond time resolution would be required.

5.4.2 Photo-induced absorption spectroscopy

To correlate the occurrence of such efficient hole transfer to CoFe-PB to its implications for water oxidation catalysis, PIAS was performed. It employs a long (5 s) LED pulse to simulate steady-state PEC conditions (see Section 2.3.3). Figure 5.6a shows the obtained PIA spectra of both $BiVO_4$ and CoFe-PB/$BiVO_4$ at strong anodic potential (1.5 V_{RHE}), at which significant water oxidation occurs in both systems. Again, unmodified $BiVO_4$ (yellow) shows a clear absorption signal at 500 nm, whereas CoFe-PB/$BiVO_4$ shows a red-shifted broad absorption around 600–750 nm, concomitant with a decrease of absorption at 550 nm. This further evinces that holes, once generated in $BiVO_4$, efficiently transfer to CoFe-PB, giving rise to an absorption feature at higher wavelengths.

The appearance of the 550 nm feature in $BiVO_4$ only at high anodic potentials and under PEC water oxidation conditions (Figure 5.6b) can be directly related to enhanced band bending, which allows holes to accumulate at the surface to drive significant water oxidation. This in turn implies that surface recombination is largely suppressed at these potentials, in accordance with the TAS data (Figure 5.4 and previous reports).[122,407]

In CoFe-PB/$BiVO_4$ the spectrum is red-shifted with a broad absorption maximum at 600–750 nm, whereas the 550 nm signal vanishes (Figure 5.6a), again consistent with TAS. This broad absorption peak, which is attributed to oxidised "CoFe[+]" appears even at low potentials. Figure 5.6c shows that its decay (∼700 nm), when switching off the irradiation after 5 s, is much faster at 1.5 V_{RHE} than

---

[†]A similar signal at ∼700 nm was also observed when no external potential was applied.

at 0.3 V$_{RHE}$ due to efficient water oxidation.
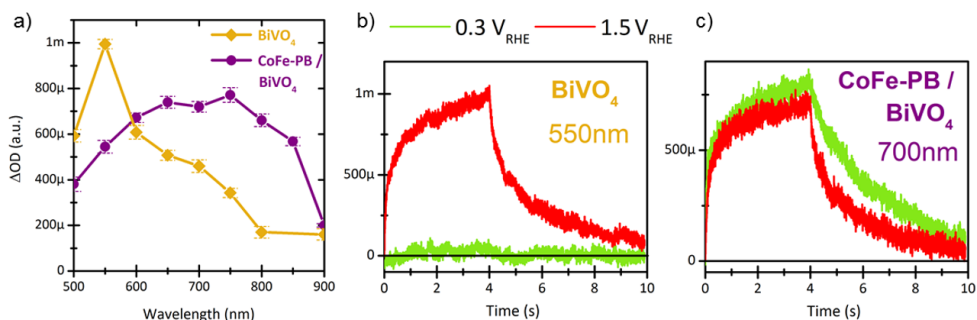
Figure 5.6: a) Comparison of PIA spectra of bare (yellow) and CoFe-PB modified (purple) BiVO$_4$ at 1.5 V$_{RHE}$. b, c) PIA signal decay curves of b) bare BiVO$_4$ at 550 nm and c) CoFe-PB/BiVO$_4$ at 700 nm (in 0.1 M KP$_i$ buffer, pH 7). Adapted from our manuscript (Ref. [410]).

Taken together the above PIAS and TAS analyses, it can be concluded that CoFe-PB modification enables fast and efficient interfacial charge-transfer, which is largely irreversible at time scales, at which surface electron–hole recombination occurs. Consequently surface recombination is inhibited by CoFe-PB modification, favouring overall water oxidation.

Considering this argument alone, it cannot be inferred that the holes transferred to CoFe-PB inevitably react with H$_2$O, meaning that CoFe-PB acts as active catalyst. The other possibility would be that CoFe-PB acts as a hole scavenger or hole capacitor, extracting holes but *not* transferring them to the electrolyte. From the previous impedance analysis (Section 4.5.3), this can largely be excluded, since the measured capacitance remained unchanged when depositing CoFe-PB (see Figure 4.28). Nonetheless, the spectral analysis given below shall further clarify this issue.

5.5 Comparison of spectra

Regarding the PIA spectrum of CoFe-PB/BiVO$_4$ at low (0.3 V$_{RHE}$) and high (1.5 V$_{RHE}$) potentials, a difference can be noticed, as shown in Figure 5.7a. At low potentials, around the water oxidation onset of CoFe-PB/BiVO$_4$ (0.3 V$_{RHE}$), the absorption appears to be more red-shifted, peaking around 600–750 nm, with an asymmetric, stronger decay towards shorter wavelengths, while at higher potentials the spectrum blue-shifts. Comparing this with the previously obtained SEC results of CoFe-PB alone, a clear similarity can be seen (Figure 5.7b). Around the onset potential (at 1.6 V$_{RHE}$), a strong asymmetric

absorption at 700–800 nm was observed and assigned to the *pre-catalytic* "CoFe-PB$^+$" (see also Figure 5.2a). During water oxidation (at sufficiently large anodic potential, 2.3 V$_{RHE}$), the spectrum shifts towards lower wavelengths due to the appearance of a catalytic doubly oxidised "CoFe-PB^{2+}" species.

Therefore, the blue shift in PIAS (Figure 5.7a), which appears at water oxidation potentials, gives rise to the assumption that catalytic "CoFe-PB^{2+}" is created under the employed *in operando* conditions. This in turn implies that CoFe-PB on top of BiVO$_4$ does become catalytic and acts as a true charge-transfer catalyst.
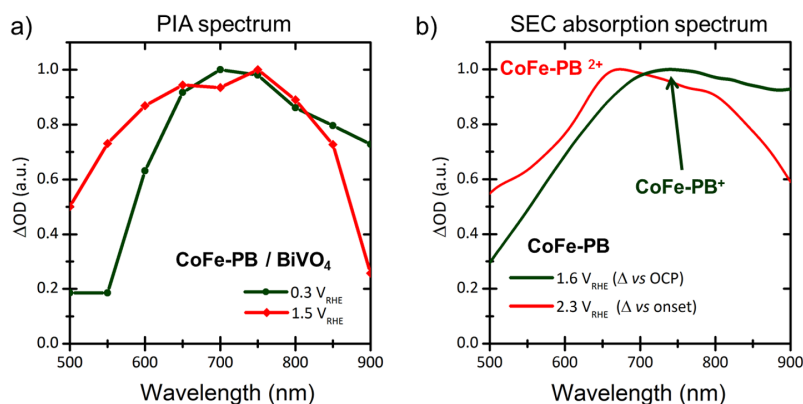
Figure 5.7: a) Comparison of PIA spectrum of CoFe-PB/BiVO$_4$ at 0.3 V$_{RHE}$ (around onset) and 1.5 V$_{RHE}$ and b) Absorption spectrum of CoFe-PB alone at 1.6 V$_{RHE}$ (around onset) and 2.3 V$_{RHE}$. Adapted from our manuscript (Ref. [410]).

It has to be noted though that the stoichiometry of the relatively thick CoFe-PB electrodes (on FTO) is likely to differ from that when deposited on BiVO$_4$. Hence a clear one-to-one mapping of the absorption of CoFe-PB/BiVO$_4$ (Figure 5.7a) with that of CoFe-PB alone (Figure 5.7b) cannot be done. However, due to the consistency of the results stemming from various methods (PEC, DFT, and spectroscopy), this assignment of a blue-shifted PIAS signal to a catalytically active species seems highly probable.

5.6 Water oxidation kinetics

Various analytic methods have been attempted in order to make a comparison between the dynamics of water oxidation on CoFe-PB alone, BiVO$_4$, and CoFe-PB modified BiVO$_4$, to that of interfacial charge-transfer. Due to the inhomogeneity of samples and the weak signals obtained, a direct quantification was hampered. Nev-

ertheless a qualitative evaluation and discussion based on different measurements is done.

5.6.1 Rate of water oxidation on CoFe-PB

At first, the rate of water oxidation on CoFe-PB alone was estimated, in order to compare it with that on $BiVO_4$, and to evaluate if it is *kinetically favourable* to catalyse the water oxidation reaction on CoFe-PB. For example, water oxidation on CoO_x was found to be 100-1000 times slower than on $BiVO_4$,[90,91,358] hence presenting a *kinetically* unfavourable semiconductor–catalyst interface.

Spectroelectrochemical evaluation

From monitoring the absorption at 440 nm, which was attributed to the appearance of catalytic "CoFe-PB^{2+}", the rate order and reaction time can be estimated. Assuming no back recombination and 100% faradaic efficiency, a rate law can be approximated by relating the absorption signals $\Delta OD(440\ nm)$ to the steady-state water oxidation current j_{WO}, as described in Ref. [236]. Similar to Equation 2.38, it follows under steady-state water oxidation conditions:

$$\frac{d[CoFe-PB^{2+}]}{dt} = 0 \ \ \text{and} \ \ j_{WO} = -k_{WO} \cdot [CoFe-PB^{2+}]^{\beta} \quad (5.1)$$

and thus

$$\lg|j_{WO}| = \lg|k_{WO}| + \beta \cdot \lg|[CoFe-PB^{2+}]| \quad (5.2)$$

Where k_{WO} is the rate constant and β the rate order. Since the concentration of the catalytic species "CoFe-PB^{2+}" and the detected 440 nm signal are directly proportional to each other, the reaction rate order β can be obtained by plotting $\lg|j_{WO}|$ against the absorption signal $(\lg|\Delta OD(440\ nm)|)$ at different applied voltages; β is the slope of the linear fit, as shown in Figure 5.8a.

However, because the absorption feature of "CoFe-PB^{2+}" is strongly overlapped by the more intense absorption of "CoFe-PB^{+}" around 700–800 nm, a quantitative correlation of ΔOD with the amount of $[CoFe-PB^{2+}]$ could not be established. Therefore, a direct evaluation of k_{WO} from this analysis was not possible. The slope of nearly two in Figure 5.8a suggests a second order rate law of water oxidation on CoFe-PB. This is rather surprising; a first order reaction is usually expected for first row transition metal complexes, resulting from a mechanism consisting of consecutive

single electron and proton transfer steps. A possible mechanistic interpretation is given below (Section 5.7).
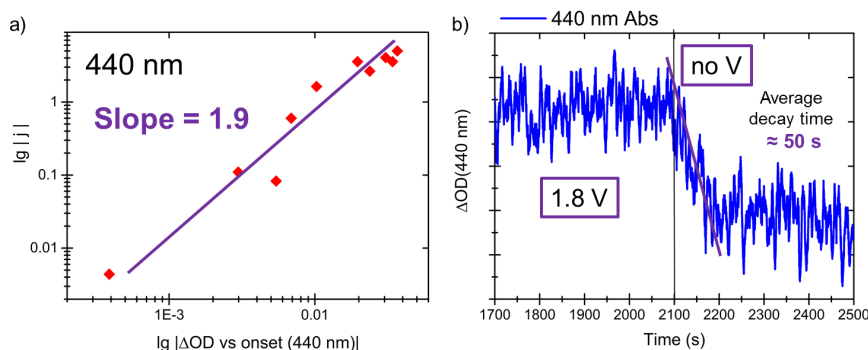
Figure 5.8: a) Logarithmic plot of water oxidation current density ($\lg|j|$) versus absorption signal at 440 nm ($\lg|\Delta OD(440\ nm)|$) for CoFe-PB. An apparent rate order of 2 (1.9) is obtained from a linear fit. b) Time evolution of the 440 nm signal, applying 1.8 V_{RHE} (above onset), and then switching off the applied bias. The absorption signal decays during times on the order of tens of seconds.

An attempt to estimate the kinetics was done by monitoring the signal at 440 nm after switching off the bias, as shown in Figure 5.8b. First a bias of 1.8 V_{RHE} ($\simeq 0.2\ V_{RHE}$ above the onset potential), at which a significant current (0.5 mA/cm^2) occurs, was applied, until a constant signal was reached. Then, the bias was switched off, and the signal decayed due to a decrease of "CoFe-PB^{2+}" concentration. The decay time, i.e. the time the signal needs to recover its initial amplitude (without bias), is approximated to be similar to the water oxidation time constant, assuming that the absorption decay is due to solely water oxidation. The signal appears to decay on a time scale of the order of tens of seconds (around 50–100 s). Since this signal is largely overlapped with other contributions, this approximation is rather vague and gives only an upper limit to the real time decay.

Electrochemical evaluation

An approximate turnover frequency (TOF) per catalytically active centre in CoFe-PB can be estimated from the concentration of redox active centres $[cat]^{\dagger}$, and relating the observed water oxidation current density j_{WO} to the TOF by

---

†The concentration of active sites $[cat]$ is *not* the same as the concentration of catalytic species $[CoFe-PB^{2+}]$. $[cat]$ refers to the total amount of active sites in the system.

$$TOF = \frac{j_{WO}}{z\,F\,[cat]} \tag{5.3}$$

with z being the number of transferred holes, hence $z = 4$, and F the Faraday constant.

The amount of catalytically active centres can be approximated from cyclic voltammetry, since the observed peak current j_{peak}[‡] of the oxidation and reduction wave is proportional to $[cat]$ (see Figure 5.9).
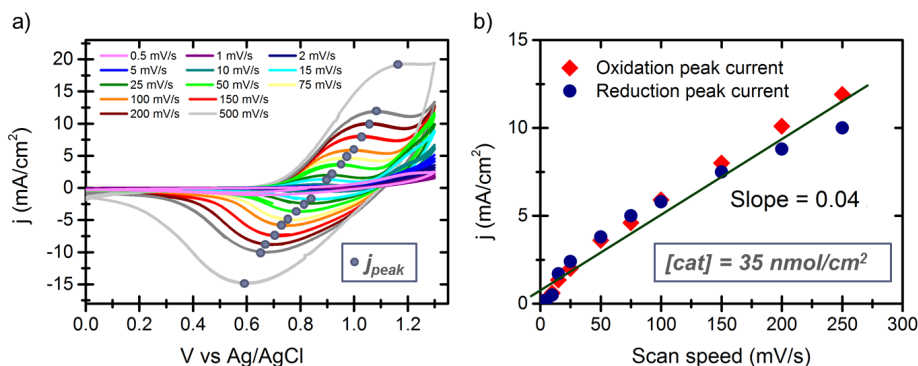
Figure 5.9: a) CV scans of CoFe-PB in buffer (pH 7) solution recorded at different scanning speeds dV/dt. b) Linear fit of both oxidation and reduction peak currents (absolute values) versus scan rate.

Assuming that all redox active centres are also catalytically active, $[cat]$ can be determined by scanning the potential at different speeds dV/dt and applying the relation:

$$j_{peak} = \frac{z^2\,F^2[cat]}{4RT}\,\frac{dV}{dt} \tag{5.4}$$

In this case $z = 1$, since one hole/electron is transferred to the redox active centres during oxidation/reduction.[103] A derivation of this expression is given in Appendix A. As shown in Figure 5.9b, $[cat]$ can then be calculated from the slope of the linear fit. Taking both oxidation and reduction peak currents into account, an average concentration of $3.5 \cdot 10^{-8}$ mol/cm^2, i.e. 35 nmol/cm^2 is obtained (see Figure 5.9).

Previous studies reported $[cat]$ values of ~1 nmol/cm^2, 2–5 nmol/cm^2, and 110 nmol/cm^2 for CoFe-PB electrodes prepared by electrodeposition,[103] nanoparticle fixation with a polymer ink,[112] or a solvothermal/chemical etching method,[110] respectively. Herein,

---

[‡]In order to avoid confusion, it is noted that the peak current j_{peak} refers to the maximum of the redox wave and is *not* related to the water oxidation current j_{WO}.

the same solvothermal method as in Ref. [110] was used, but with a shorter CoO_x formation time (3 instead of 10 h); hence, the resulting [cat] of about one third (35 instead of 110 nmol/cm^2) is reasonable. This is an *upper limit* to the real number of catalytic sites, because it takes into account *all* redox active sites. Water oxidation catalysis mainly takes place at the surface or close to the surface, at sites that are accessible by diffusion through the pores of the CoFe-PB Structure.

Therefore, the estimated TOF from Equation 5.3 is a *lower limit* to the real TOF. It is shown in Figure 5.10 along with its inverse, τ_{cat}, the time needed to complete one catalytic cycle.
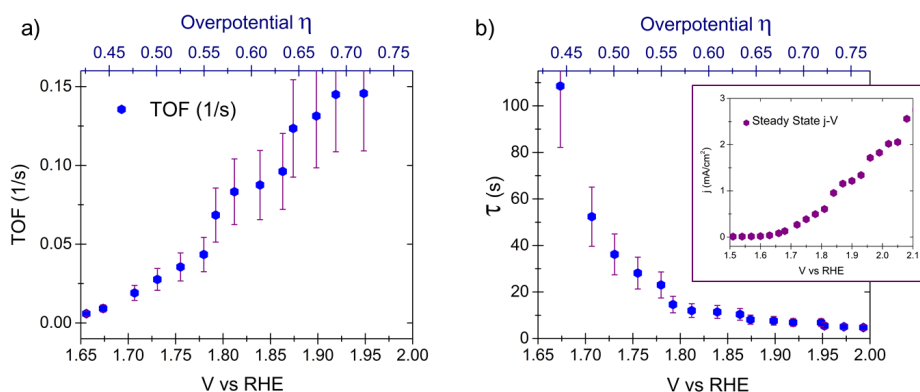
Figure 5.10: Potential dependent plots of a) the turnover frequency (TOF) per catalytically active centre, and b) the corresponding time constant τ_{cat}. The inset shows the corresponding steady state *j–V* curve of CoFe-PB in neutral (pH 7) KPi buffer, determined by chronoamperometry.

At potentials where water oxidation becomes a significant process, 1.7–1.8 V_{RHE} (see *j–V* dependence in the inset of Figure 5.10), the potential-dependent TOF is around 0.02–0.08 s^{-1} and its inverse $\tau_{cat} \simeq$ 50–10 s. This is also in agreement with previous literature; Han *et al.* and Alsaç *et al.* obtained TOFs of 0.05 and 0.06 s^{-1}, respectively, when extrapolating to 1.8 V_{RHE}.[110,112] Pintado *et al.* measured a TOF one order of magnitude higher (0.5 s^{-1} at 1.8 V_{RHE}), likely due to the fact that they used much thinner films, which expose more catalytically active species.[103] It has to be noted though that the potential dependent TOF is *not* the same as the rate constant derived in Equations 5.1 and 5.2, which is a potential-independent quantity.

Nevertheless, when considering the decay time of the SEC signal (Figure 5.8b), which was related to water oxidation, and τ_{cat} (Figure 5.10b) at the *same* potential, i.e. at 1.8 V_{RHE}, a comparison of the approximate time scale can be made. Both SEC decay and τ_{cat}, the

time needed to oxidise one water molecule per catalytically active site at 1.8 V_{RHE}, lie in the order of tens of seconds. This in turn is a good indication that water oxidation must happen on a time scale of the order of tens of seconds, or even less, regarding the fact that τ_{cat} is an upper value to the real oxidation time per catalytic centre.

RC time constant

Another characteristic time constant of an electrochemical system is its *RC* time constant, which can be obtained by impedance spectroscopy. Although this time constant τ_{RC} could not directly be related to a catalytic water oxidation rate, it is briefly discussed for the sake of completeness.[217,237]

For a *first order* electrical circuit[†] with one capacitor C and one resistor R, such as CoFe-PB alone, the time constant given by $\tau_{RC} = RC$ defines the time, at which the capacitor is 63.2% $(1 - e^{-1})$ charged and the resistor 36.8% (e^{-1}) discharged. It is shown in Figure 5.11 along with the corresponding capacitances and resistances, which were determined by fitting the impedance of CoFe-PB to a simple Randles circuit (see Sections 2.3.2 and 4.5.3).[226]
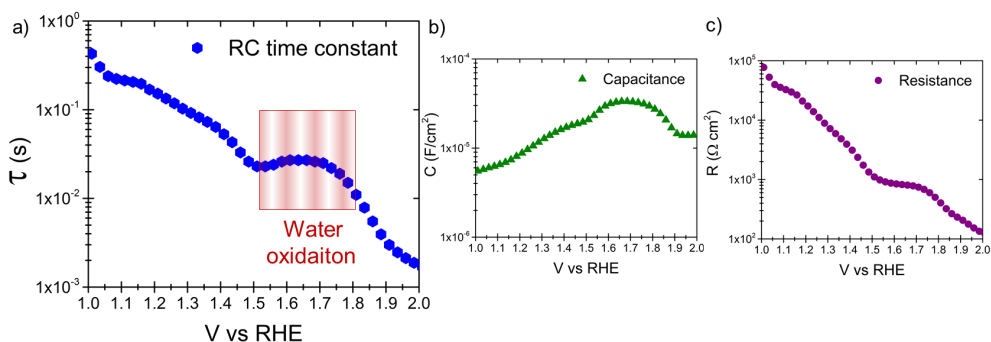
Figure 5.11: a) RC time constant, b) capacitance, and c) resistance of CoFe-PB alone, measured by EIS at pH 7 and fitted to a Randles circuit.

At small anodic potentials $V \lesssim 1.5$ V_{RHE}, below the water oxidation onset, τ_{RC} continuously decreases. This means that the time to charge/discharge CoFe-PB becomes shorter, hence CoFe-PB gets oxidised more easily when increasing the bias.

However, at larger potentials, where water oxidation starts to occur, τ_{RC} can no longer simply be interpreted as the time to charge the capacitor. Now mainly two competing processes take place, charging of CoFe-PB, as well as transferring the charge to the electrolyte, i.e. water oxidation.

[†]In this case the constant series resistance is neglected.

Between ~1.55–1.75 V_{RHE} the time constant stabilises (red box in Figure 5.11a), concomitantly with the resistance (Figure 5.11c) and the capacitance reaching a peak (Figure 5.11b). At even higher potentials ($\gtrsim$1.8 V_{RHE}), τ_{RC} further decreases, again in concordance with the resistance, indicating that hole transfer to water is not the rate limiting step anymore.

The constant value of τ_{RC} ~0.02 s at water oxidation potentials (red box in Figure 5.11a) is around 10–100 times lower than the turnover time constant per catalytic centre (Figure 5.10b) or the decay time from SEC (Figure 5.8b). This indicates that τ_{RC} comprises different components apart from hole transfer, such as charging of the CoFe-PB layer. Due to relatively fast charging of the CoFe-PB, the observed τ_{RC} of the overall system may appear faster. An interpretation of the RC time constant, however, is difficult and may be subject to further discussion.[237]

5.6.2 Rate of water oxidation on bare and CoFe-PB modified BiVO$_4$

Rate law

From the PIAS data at high applied bias a rate law can be determined, as described in Section 2.3.3 and Ref. [243]. This is done by plotting the obtained photocurrent j_{photo} at different irradiation intensities versus the corresponding PIA signal (both in logarithmic scale), as shown in Figure 5.12. According to Equation 2.38, the slope of the logarithmic plot gives the rate constant of light-induced water oxidation.

In unmodified BiVO$_4$ the photogenerated holes that absorb at 550 nm (Figure 5.6) are ultimately responsible for water oxidation, which is why this PIA signal is used to establish the rate dependency (Figure 5.12a).[407] For CoFe-PB/BiVO$_4$ the signal at 500 nm is taken, the lowest measurable wavelength, which is proportional to the amount of catalytically active "CoFe-PB^{2+}" species.[†]

Bare BiVO$_4$ shows a rate order of 1 at relatively low excitation intensities, i.e. small signal intensities ΔOD, while at high excitation intensities a rate order of 3 is observed, consistent with recent literature.[407] This trend, i.e. changing from a first order to a third order at high densities of surface accumulated holes, has also been observed for other photoactive metal oxides, such as Fe$_2$O$_3$.[217] Consistent with the fit of the SEC data of CoFe-PB alone (see Figure

---

[†]At lower wavelengths, i.e. energies much higher than the band gap excitation, various electronic processes occur, preventing the interpretation of any signal. Although the signal at 500 nm is strongly overlapping with the signal of "CoFe-PB$^+$" and cannot be deconvoluted, it is expected to rise proportionally to "CoFe-PB^{2+}".

5.8a), a slope of nearly 2 is observed in the case of CoFe-PB/BiVO$_4$, indicating a second order rate law.

The fact that the behaviour of CoFe-PB modified BiVO$_4$ differs largely from that of BiVO$_4$ alone, while being similar to that of CoFe-PB, clearly indicates that water oxidation catalysis on CoFe-PB/BiVO$_4$ does *not* take place on the BiVO$_4$ surface, but on active CoFe-PB sites.
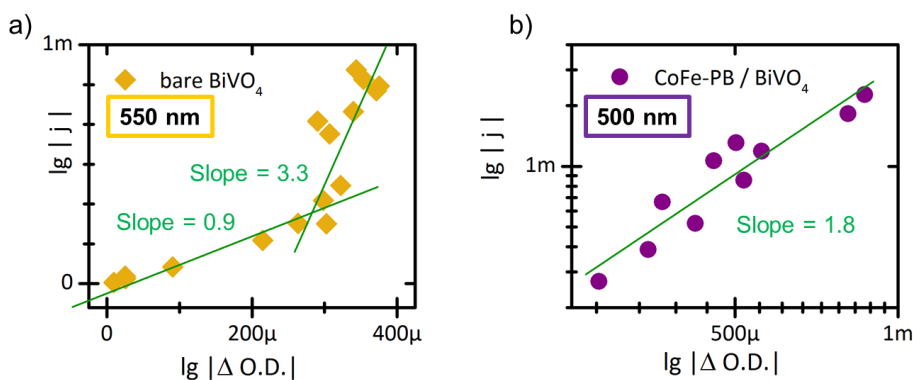
Figure 5.12: Logarithmic plot of photocurrent density ($lg|j_{photo}|$) versus PIA signal ($lg|\Delta OD|$) of a) bare BiVO$_4$ at 550 nm and b) CoFe-PB/BiVO$_4$ at 500 nm.

A comparable dependency had been observed in Ref. [236] for the hydrogen evolution reaction (HER) on a catalyst modified photocathode. Therein also a second order rate law was obtained for both the electrocatalyst RuO$_x$ alone and the photocatalytic interface CuO$_2$/RuO$_x$, which indicated that HER takes place on RuO$_x$ in both cases. Moreover, the authors concluded that the HER follows a two-step mechanism, in which RuO$_x$ first is reduced to a singly reduced pre-catalytic "RuO$_x^-$" species, which subsequently gets reduced to the catalytic "RuO$_x^{2-}$", giving rise to an apparent rate order of 2.[236] A similar conclusion might be drawn in the case of CoFe-PB/BiVO$_4$; further research on the mechanistic details, in order to clarify this issue, is still ongoing.

Timescale of water oxidation

As opposed to the steady-state approximation, the initial rates method can also give an approximation of the OER kinetics (see Section 2.3.3).[243,407] When applying a sufficiently high bias to suppress back electron–hole recombination, all photogenerated holes at the surface react with water. Hence the initial PIA decay time of the corresponding hole signal after switching off the light

source, is a direct estimate of the characteristic time scale of water oxidation (see Equation 2.39). Figure 5.13 shows the PIA signal at different light intensities of bare $BiVO_4$ (550 nm) and CoFe-PB/$BiVO_4$ (500 nm) with the average time the signal needed to decay.
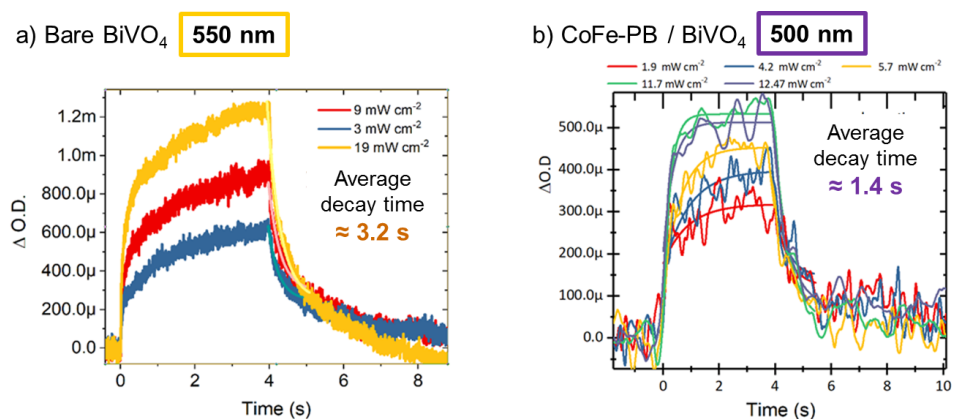
Figure 5.13: Fitting of the initial rate of decay of PIA traces for a) unmodified $BiVO_4$ at 1.6 V_{RHE} (550 nm probe) and b) CoFe-PB modified $BiVO_4$ at 1.2 V_{RHE} (500 nm probe). Average decay times from all fits at different illumination intensities were 3.2 s and 1.4 s for bare and CoFe-PB modified $BiVO_4$, respectively.

In unmodified $BiVO_4$, the initial rates analysis yields a water oxidation time on the order of seconds, in agreement with previous reports (Figures 5.13a and 5.6b).[122,407] CoFe-PB modified $BiVO_4$ shows decay times around 1 s, on a similar order of magnitude (Figures 5.13b and 5.6c). Moreover this times scale is comparable to that of electrocatalytic water oxidation on CoFe-PB alone, which happens on the order of seconds to tens of seconds.

It is noted though that the time scale of CoFe-PB/$BiVO_4$ extracted from PIAS (Figure 5.13b) seems shorter than than that of CoFe-PB alone from the SEC decay time (5.8b), or from the TOF analysis (Figure 5.10b). This variation, however, is attributed to inaccuracies and differences of the methods, considering that: (i) the SEC analysis was very rough and data were noisy; (ii) τ_{cat} (the inverse TOF) is a potential dependent quantity, and the effective potential acting on CoFe-PB in CoFe-PB/$BiVO_4$ is unknown (which is a mixture of applied potential and effective photovoltage minus potential losses at boundaries and defects); and (iii) τ_{cat} is an upper quantity to the real water oxidation time. Thus a time scale of seconds is likely and was indeed observed for thinner CoFe-PB films (at 1.8 V_{RHE}).[103]

Consequently it is reasonable to conclude that water oxidation on the catalytic active sites of CoFe-PB occurs on the order of seconds and is therefore comparable to the time scales of water oxi-

dation on $BiVO_4$.[407] This in turn allows for efficient water oxidation catalysis on CoFe-PB when deposited on $BiVO_4$, which is in contrast to observations for CoO_x,[358] and is discussed below (in Section 5.8). The fact that water oxidation on CoFe-PB happens on the same time scale as on $BiVO_4$ is indeed remarkable, considering that significant thermodynamic driving force is lost, when transferring holes to CoFe-PB. As described in Section 4.5.3, the energy levels of catalytically active Co t_{2g} states lie *above* (∼0.5–1.0 eV) the $BiVO_4$ valence band (see Figure 4.35b). Hence, when holes transfer to Co, they lose a fraction of thermodynamic potential necessary to drive water oxidation, i.e. the energy difference to the H_2O HOMO decreases. This in turn implies that CoFe-PB is an effective water oxidation catalyst, since it still catalyses water oxidation at the same rate as $BiVO_4$.

5.7 Mechanistic considerations

The high catalytic activity of CoFe-PB is likely due to its complex polymeric structure containing *molecular-like* Co centres with many vacant coordination sites. Those octahedral Co units allow a large mechanistic flexibility, unlike in other heterogeneous catalysts.

Typically, two water oxidation mechanisms are assumed, which may take place on both molecular complexes or solid surfaces, and are illustrated in Figures 5.14a and b. The rate-limiting O–O bond formation is either described by a water nucleophilic attack (WNA) or the interaction of two metal–oxo entities (I2M).[17,116] In the WNA, water acts as a nucleophile and attacks the slightly more positive oxygen of the M–O moiety (Figure 5.14a).[17,66] In the I2M, if two M–O units are in close proximity, they may interact, generating a bridging M–O–O–M peroxo species (Figure 5.14b).[17,116] This I2M mechanism, however, is excluded in CoFe-PB, as the catalytically active Co centres are too far apart, with the closest Co–Co distance >7 Å (on the *fcc* surface, see Section 3.2).

Due to the non-stoichiometric nature of CoFe-PB, comprising many vacant $Fe(CN)_6$ sites and an average of two H_2O per Co centre $(Co(NC)_4 \cdot 2\,H_2O$, see Section 3.2.3), other mechanisms may be envisaged, such as illustrated in Figures 5.14d and e. The *cis*-arrangement of the two water molecules (Figure 5.14c), ‡ which would be required for those pathways, was recently suggested in a report by Goberna-Ferron *et al.*[109] In this study the

---

‡This is in contrast to the computational model shown in Figure 3.16. Modelling *cis*-$Co(NC)_4 \cdot 2\,H_2O$ in a periodic structure calculation is challenging as it would require an extremely large supercell.

authors observed poisoning of the CoFe-PB catalyst by a bidendate, *cis*-coordinating ligand (2,2'-bipyridine), which indirectly proofs that the substituted H_2O molecules must have adapted a *cis*-configuration.
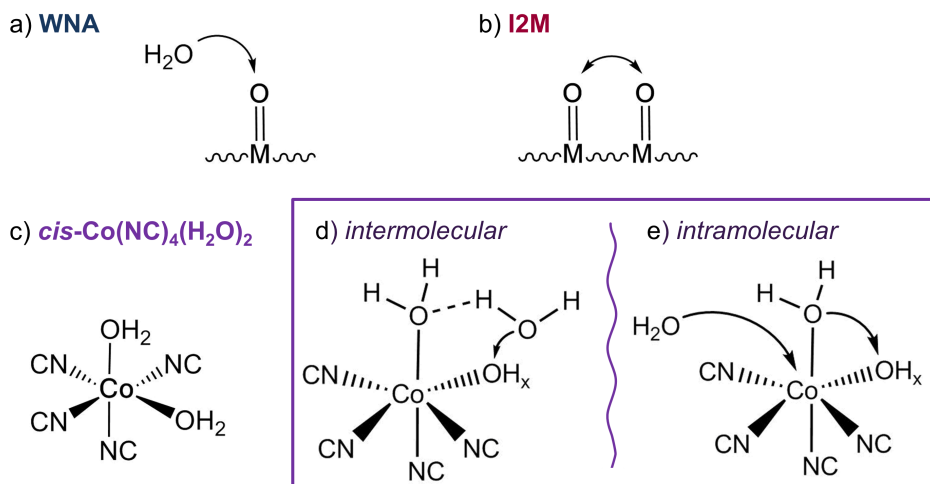
Figure 5.14: Mechanistic pathways of the rate-limiting O–O bond formation: a) Water nucleophilic attack (WNA), b) interaction between two metal–oxide entities (generally via radical coupling or reductive elimination).[17] c) *cis*-coordinated $Co(NC)_4 \cdot 2\,H_2O$, undergoing two proposed mechanisms: d) hydrogen bonded water attacks Co-OH$_x$ moiety in *cis*; e) Co-bound water interacts with Co-OH$_x$ moiety (in *cis*) and gets replaced by an incoming water molecule.

The presence of *cis*-$Co(NC)_4 \cdot 2\,H_2O$ could facilitate intermolecular water nucleophilic attack, as presented in Figure 5.14d. A solvent H_2O molecule is coordinated through hydrogen bonds to another Co-bound water, *cis* to the electrophilic Co–O moiety, at which it attacks. The mechanism is the same as typically assumed for WNA, but with a sterically favoured arrangement. Another possible, *intramolecular* pathway is shown in Figure 5.14e, in which two water molecules at the *same* Co centre interact with each other in the rate-determining O–O coupling step. The oxidation state of the Co-centre is not depicted; an equilibrium of oxidised Co and Fe centres, which are connected by charge-transfer, is likely to be present. The large multiplicities within few meV make the transitions between the diverse oxidation states so versatile that little if any energy is needed to adapt the oxidation state of the centre. The suggested mechanisms are also consistent with the apparent second order rate law; albeit, a rate order of two could also be observed for WNA or I2M, if two oxidising equivalents were needed to accumulate before the rate-determining step.

The proposed water oxidation pathway, in which two water molecules are favourably coordinated and brought in close proximity, would decrease the reaction barrier significantly and, therefore, enhance the water oxidation rate.

Apart from such a favourable mechanism, also other factors may contribute to the high catalytic activity of CoFe-PB. Those include: i) the well matching symmetry of the active Co t_{2g} and the H_2O HOMO ($1b_1$), which allows for good orbital overlap and favoured charge-transfer; ii) the wide diffusion channels in the porous network, which enables access to coordination centres within the bulk.

Taken together, this highlights the clear benefit of CoFe-PB, which despite its solid phase has catalytic properties typically associated to molecular complexes, and therefore successfully combines the advantages of both homogeneous and heterogeneous catalysis.

5.8 Comparison of charge-transfer and recombination processes

Taken together the obtained results, it can be concluded that CoFe-PB modification of $BiVO_4$ results in fast ($\sim\mu$s) hole transfer from $BiVO_4$ to CoFe-PB, even in the absence of a strong applied bias. This fast and nearly irreversible (ms–s time scale) charge-transfer forms oxidised and long-lived "CoFe$^{+/2+}$" states, the latter of which (i.e. "CoFe-PB^{2+}") react with water on the seconds time scale, similar to bare $BiVO_4$. Therefore, the origin of improved PEC performance on CoFe-PB/$BiVO_4$ is ascribed to inhibiting recombination due to spatially separating photogenerated holes from the electrons in $BiVO_4$, without a compromise in the water oxidation kinetics.

The effect on the different electronic processes is summarised in Figure 5.15 and Table 5.1, comparing bare $BiVO_4$, CoO_x/$BiVO_4$, and CoFe-PB/$BiVO_4$. In unmodified $BiVO_4$ (Figure 5.15a), surface recombination significantly limits water oxidation. A strong bias needs to be applied to slow down that recombination pathway sufficiently and to allow water oxidation to become competitive.

This requirement for a strong positive bias is reduced, when applying CoO_x (Figure 5.15b). CoO_x increases band bending and, thus, retards surface recombination, which lowers the onset potential (described in Section 5.2.2). Water oxidation on CoO_x itself is unlikely to occur; on one hand it is much (2–3 orders of magnitude) slower than on bare $BiVO_4$,[90,91,407] on the other hand charge-transfer from $BiVO_4$ to CoO_x is comparatively slow ($\sim$1–10 s) and inefficient.[358]

CoFe-PB in contrast (Figure 5.15c), leads to efficient interfacial

hole transfer and therefore prevents surface recombination within $BiVO_4$. This is coupled to effective water oxidation catalysis, facilitating the turnover of long-lived holes on CoFe-PB.

red: recombination pathway; green: favoured reaction pathway; black: disfavoured pathway; dashed lines: slow or suppressed processes
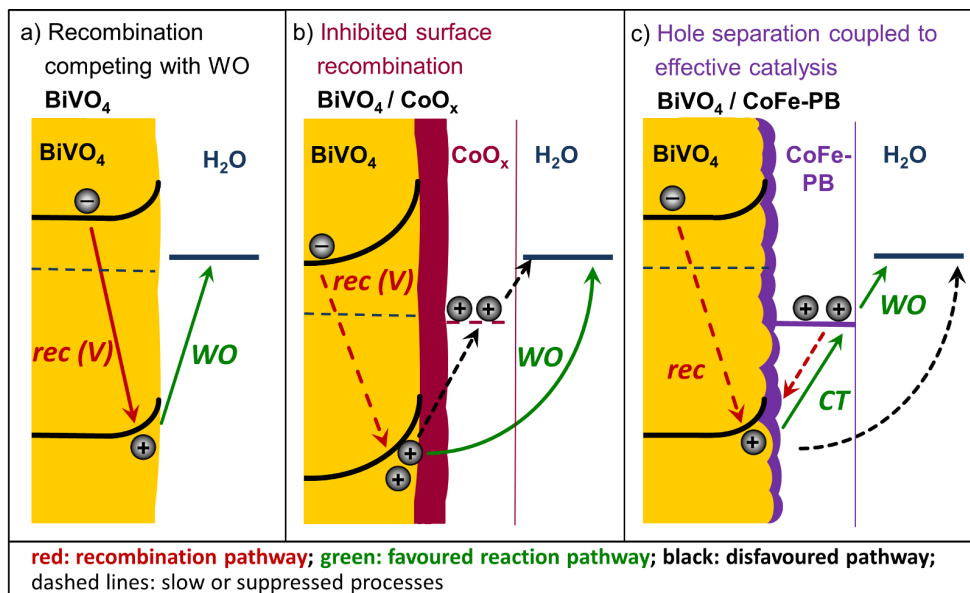
Figure 5.15: Representation of the time scales of different electronic processes in a) unmodified $BiVO_4$, b) $CoO_x/BiVO_4$, and c) CoFe-PB/$BiVO_4$: Potential dependent surface recombination ($rec(V)$), water oxidation (WO), and charge-transfer (CT). Adapted from our manuscript (Ref. [410]).

Table 5.1: Time scales of relevant electronic processes in $BiVO_4$, $CoO_x/BiVO_4$, and CoFe-PB/$BiVO_4$: potential dependent (V-dep.) surface electron–hole recombination (in $BiVO_4$), hole transfer to the catalyst, and water oxidation on the $BiVO_4$ or catalyst surface.

Characteristic time scales	$BiVO_4$	$CoO_x/BiVO_4$	CoFe-PB/$BiVO_4$
Surface recombination (in $BiVO_4$)	μs–s (V-dep.)[122]	ms–s (V-dep.)[133]	largely suppressed
Interfacial charge-transfer	–	s[358]	μs*
Water oxidation	s[407]	100's of s (via CoO_x)[90,91]	s (via CoFe-PB)

* The exact time scale of charge-transfer in CoFe-PB/$BiVO_4$ is not known, as it occurs below the time resolution ($\sim \mu$s) of the performed TAS experiment.

The reasons why CoFe-PB acts so differently on CoO_x are likely to be of *kinetic* origin. Considering the thermodynamic energy differences of CoFe-PB/$BiVO_4$ and $CoO_x/BiVO_4$, they are assumed to be similar. The catalytically active Co states in CoFe-PB lie around

0.5–1.0 eV above the $BiVO_4$ valence band (see Figure 4.35b). In CoO_x, the offset of the redox active Co states with respect to $BiVO_4$ is suggested to be around 1 eV.[87,358] Thus, the driving force of hole transfer from $BiVO_4$ to CoO_x should be similar, if not even higher, to that in CoFe-PB/$BiVO_4$. Yet, the rate of interfacial charge-transfer in CoFe-PB/$BiVO_4$ is at least one or two orders of magnitude faster.[†]

One possible explanation is the formation of strong coordination bonds, linking the surfaces of $BiVO_4$ and CoFe-PB. As discussed in Section 4.3.1, the CoFe-PB/$BiVO_4$ interface presents a favourable epitaxy, allowing for good metal–ligand coordination (Figure 4.8). This opens up an efficient charge-transfer pathway with a low barrier.

Another hypothesis is that the differences in charge-transfer kinetics are based on the different morphologies of both systems: CoFe-PB/$BiVO_4$, discussed in this work, and CoO_x/$BiVO_4$ from Refs. [133] and [358], to which they are compared. The $BiVO_4$ photoanodes, which I prepared, are nano-/mesostructured and the sequentially coated CoFe-PB layer very thin (several nm), while Ma *et al.* used flat and dense $BiVO_4$ films with a thick (200 nm) CoO_x layer.[133,358] Since the exposed surface area of the $BiVO_4$ employed herein is much larger, more interfacial contacts with CoFe-PB, and thus faster charge-transfer, are expected. Indeed there are several examples highlighting the crucial role of the interface morphology in the observed catalytic performance, as was discussed in the Introduction (Chapter 1).[126,136,139,140] Further research to clarify the impact of the morphology in the case of CoFe-PB/$BiVO_4$ interfaces on the observed fast interfacial charge transfer characteristics is still necessary and currently underway.

5.9 Conclusion of Chapter 5

In summary, in this Chapter a time-resolved spectroscopic study was carried out to unravel the dynamics of photogenerated holes in CoFe-PB/$BiVO_4$ photoanodes.

Combining transient and photo-induced absorption spectroscopy, a long-lived absorption signal at 700–800 nm was found, even at low applied bias. By comparing the obtained absorption spectra with spectroelectrochemical measurements of ground state CoFe-PB alone, this feature could be attributed to a singly oxidised "CoFe-PB$^+$" species, which is generated from fast ($\sim\mu$s) hole trans-

---

[†]It has to be noted though that a direct comparison cannot be given, since the energy level offset of $\sim$1 eV in CoO_x/$BiVO_4$ comes from the measured difference in redox potentials.

fer from $BiVO_4$ to CoFe-PB. Upon further oxidation of "CoFe-PB$^+$", doubly oxidised "CoFe-PB^{2+}" is formed, which is assumed to be the catalytically active species in the OER. Its characteristic absorption is blue-shifted and much weaker compared to that of "CoFe-PB$^+$". The fact that its absorption cannot clearly be differentiated from that of "CoFe-PB$^+$" prevented an accurate quantitative rate analysis. Nevertheless, by combining different data sets and fitting procedures, an approximate water oxidation time scale on the order of seconds was extracted.

Taken together, modification of $BiVO_4$ with CoFe-PB results in fast ($\sim\mu$s) interfacial charge-transfer, coupled to effective ($\sim$s) water oxidation, which results in efficient suppression of electron–hole recombination in the photoactive semiconductor, and therefore large photoelectrochemical water oxidation enhancement.

Chapter 6

General conclusions

Artificial photosynthesis can be realised by a photoelectrochemical (PEC) system, which combines light harvesting with effective water splitting catalysis. Nevertheless, the design of an efficient, robust, and affordable photoanode, imposes a challenge, sometimes considered as the bottleneck step to the development of economically viable PEC water splitting. A common strategy to improve the performance of semiconductor anodes is to deposit a water oxidation co-catalyst. In this context, redox catalysts based on Prussian blue derivatives (metal hexacyanoferrates), which have shown high catalytic activities, while being stable, cost-effective, and easily processable, show great promise. However, their detailed mechanisms and structure–reactivity relationships are not yet well-understood.

In this Doctoral Thesis, the Earth-abundant metal oxide semiconductors, Fe_2O_3 and $BiVO_4$, which are well-known photoanode materials, were modified with CoFe-PB, the cobalt iron analogue of Prussian blue. The main goals of this combined experimental and theoretical study were i) to find suitable theoretical methods to assess the electronic structure of Prussian blue analogues and to develop a robust computational set-up to model the employed photoanodes (Chapter 3); ii) to demonstrate the applicability of CoFe-PB as co-catalyst on metal oxide semiconducting materials as proof-of-concept and to design an efficient preparation method (Chapter 4); and iii) to investigate the mechanisms by which CoFe-PB achieves a performance enhancement, and its determining factors (Chapters 4 and 5).

In **Chapter 3**, a detailed DFT analysis was performed for Prussian blue (PB) and its analogues. In this regard, the applicability of various functionals was assessed. It was found that all pure DFT functionals on the GGA (and even meta-GGA) level of theory are not suitable to describe the complex hexacyanoferrate networks.

191

Apart from their well-known drawback of electron overdelocalisation, all tested GGA and meta-GGA functionals consistently yielded a wrong magnetic ground state. Neither GGA+U nor common hybrid functionals with 25% exact exchange were found to be adequate. GGA+U lacks in transferability; each derivative of PB with metal centres in different electronic environments requires different Hubbard U parameters. The main issues with this are that: i) the optimal U would need to be determined for each PB derivative, either empirically or through *ab initio* methods; and ii) those structures with different U parameters cannot be directly compared. The high amount of 25% exact exchange (in the range separated HSE hybrid functional) *overlocalises* electrons, leading to overestimated band gaps and false predictions of conduction properties.

In order to assess the electronic structures of CoFe-PB, a range-separated hybrid functional based on HSE03 was modified and empirically optimised with respect to the amount of exact exchange; the ideal amount was found to be 13%. This modified functional did also accurately describe the photoanode materials Fe_2O_3 and $BiVO_4$, and was consequently taken as functional of choice for further evaluation and level alignment, as done in Chapter 4.

In **Chapter 4**, CoFe-PB was deposited onto Fe_2O_3 and $BiVO_4$ photoanodes in order to study its function as a co-catalyst. First, different preparation methods were evaluated; hematite and bismuth vanadate were both prepared by a relatively simple electrode-position method, and CoFe-PB was subsequently deposited by a sequential coating procedure. Regarding the resulting photocurrent enhancement, CoFe-PB had a more significant impact on $BiVO_4$ than on Fe_2O_3, shifting the onset potential cathodically by about 0.8 V on $BiVO_4$ and 0.1 V on Fe_2O_3. Mechanistic studies based on hole scavenger experiments and electrochemical impedance spectroscopy suggested that the role of CoFe-PB on $BiVO_4$ is *truly* catalytic, while this is not the case on Fe_2O_3. The charge-transfer efficiency is largely enhanced by CoFe-PB modification on $BiVO_4$ without affecting the capacitance. Aligning the calculated Densities of States (DOS), obtained with HSE03-13, this charge-transfer appears to be *thermodynamically* favoured. Electronic Co states of CoFe-PB lie above the valence band of $BiVO_4$ and below H_2O, favouring hole transfer *via* the catalyst. Such a conclusion cannot be drawn for Fe_2O_3; the theoretical level alignment did *not* predict thermodynamically favoured hole transfer via CoFe-PB. Moreover, both the charge-transfer efficiency and the capacitance of CoFe-PB/Fe_2O_3 are not changed in magnitude with respect to bare Fe_2O_3, but are shifted towards more cathodic potentials by around 0.1–0.2 V. Therefore the observed onset potential shift in CoFe-PB/Fe_2O_3

was attributed to the shift in surface state capacitance.

In **Chapter 5**, a complementary time-resolved spectroscopy study was carried out to gain a better understanding of the hole dynamics in the successful CoFe-PB/BiVO$_4$ combination. Although in Chapter 4 it was shown that hole transfer is *thermodynamically* favoured, no direct *kinetic* information about the fate of photo-generated holes at the interface is given. In order to assign the excited state absorption spectra, first the ground state signals of holes in CoFe-PB were determined by means of spectroelectro-chemistry. Absorption features of singly oxidised "CoFe-PB$^+$" and doubly oxidised "CoFe-PB^{2+}" were detected, and attributed to a pre-catalytic and catalytic state, respectively. Transient absorption spectroscopy (TAS) shows the appearance of a long-lived oxidised "CoFe-PB$^+$" on a sub-microsecond time-scale even under low applied bias. This indicates that photogenerated holes in BiVO$_4$ transfer rapidly to CoFe-PB, further supported by the fact that the typical BiVO$_4$ hole signal vanishes in CoFe-PB/BiVO$_4$. Photo-induced absorption spectroscopy (PIAS), which emulates *in operando* water oxidation conditions, shows the appearance of "CoFe-PB$^+$" and also catalytic "CoFe-PB^{2+}". From the latter, the time scale of water oxidation on CoFe-PB was estimated to be on the order of seconds, similar to BiVO$_4$. Taken together, fast interfacial charge transfer, combined with competitive catalytic rates on CoFe-PB/BiVO$_4$, led to efficient suppression of electron–hole recombination and thus largely enhanced photoelectrochemical performance.

The reasons for such an efficient charge-transfer via the CoFe-PB catalyst could be related to a well-matching epitaxy of the inter-face, which allows for chemical bond formation between BiVO$_4$ and CoFe-PB. This in turn significantly lowers the barrier for the holes to transfer. In other words, charge-transfer occurs via metal–ligand bonds, and can thus be regarded as an *inner-sphere transfer*, whereas incommensurate lattices do not provide such a pathway, and charge-transfer may take place via a tunnelling mechanism or *outer-sphere transfer*.

The implications of the interface morphology yet requires deeper understanding and is still focus of current investigations. Moreover, further research includes a detailed mechanistic study of water ox-idation on CoFe-PB, elucidating the role of defects and the impact of different spin configurations. The mutual interplay between sto-ichiometry, magnetisation, and water oxidation enhancement due to the large structural flexibility of CoFe-PB is assumed to be key to its high catalytic activity.

Appendices

UNIVERSITAT ROVIRA I VIRGILI
EXPERIMENTAL AND THEORETICAL INVESTIGATION OF PRUSSIAN BLUE-TYPE CATALYSTS FOR ARTIFICIAL
PHOTOSYNTHESIS
Franziska Simone Hegner

Appendix A

Experimental details

A.1 Synthesis of the materials

A.1.1 Materials

The chemicals iron(II)chloride tetrahydrate ($FeCl_2 \cdot 4H_2O > 98\%$), zirconyl chloride octahydrate $ZrOCl_2 \cdot 8H_2O > 99\%$), bismuth(III) nitrate ($Bi(NO_3)_3 \cdot 5H_2O \geq 98.0\%$), vanadyl acetylacetonate ($VO(acac)_2 \geq 97.0\%$), potassium ferri(III)cyanide ($K_3[Fe(CN)_6] \geq 99.0\%$), and potassium hydroxide (KOH flakes $\geq$ 90%) were purchased from Sigma–Aldrich. Cobalt chloride hexahydrate ($CoCl_2 \cdot 6H_2O \geq 98.0\%$) was purchased from Fluka Analytical. The solvents dimethylsulfoxide (DMSO $\geq$ 99.9%), hydrogen peroxide solution (H_2O_2, 30% (w/w) in H_2O), and ethylene glycol (ethane-1,2-diol $\geq$ 98.0%) were obtained from Sigma–Aldrich. The buffer solution was prepared from potassium phosphate monobasic and dibasic ($KH_2PO_4 \geq$ 99.0% and $K_2HPO_4 \geq$ 98.0%, Sigma–Aldrich). Na_2SO_3 from J.T. Baker was used as a hole scavenger for $BiVO_4$ photoanodes. High purity (Milli-Q) water was obtained with a Millipore purification system (Synergy) and used for all solutions.

Fluorine-doped tin oxide (FTO) coated glass slides were purchased from Hartford glass (15 Ω/cm^2). Prior to usage, the FTO electrodes were ultrasonicated in soap, water, and isopropanol, for 10–15 min in each solution, and cleaned. In order to remove organic residues, the FTO glass plates were heated at 500 °C for 30 min (FTO site up). Just before depositing the materials, the FTOs were again thoroughly cleaned with ethanol or methanol, and polished with a glass wipe. This step is very important, even small impurities on the FTO glass may lead to bad adhesion when electrodepositing a material from solution. If the FTO surface is not clean, the material falls of more easily.

A.1.2   Synthesis of hematite electrodes

Zr-doped metallic Fe was deposited from a precursor solution containing 20 mM $FeCl_2 \cdot 4H_2O$ and 0.9 mM $ZrOCl_2 \cdot 8H_2O$ in DMSO by applying a constant potential of -2.0 $V_{Ag/AgCl}$ (3 M KCl) for 6 min. The Fe films were carefully rinsed with Milli-Q water. In order to form Fe_2O_3, the electrodes were calcined in air at 800 °C for 9–10 min and afterwards rapidly quenched at room temperature.[356,359]

A.1.3   Synthesis of bismuth vanadate electrodes

First, metallic Bi was electrodeposited from a solution of 20 mM $Bi(NO_3)_3 \cdot 5H_2O$ in ethylene glycol. A potential of -1.8 $V_{Ag/AgCl}$ (3 M KCl) was applied until a charge of 0.04 C/cm^2 was passed and followed by a resting time of 2 s at open circuit potential. This sequence was repeated eight times, hence a total charge of 0.32 C/cm^2 was passed. The films were carefully cleaned by rinsing the FTO slides with MilliQ water from their back site, as Bi washes off easily. Then 60 $\mu L/cm^2$ of 0.15 M $VO(acac)_2$ in DMSO was dropped on the Bi surface and heated up to about 80 °C on a hot plate, in order to evaporate the DMSO solvent. Transformation of metallic Bi and VO^{2+} to ms-$BiVO_4$ was achieved by annealing the electrodes in air at 500 °C for 2 h, after heating them up to 500 °C with a rate of 2 °C/min. Afterwards, excess V_2O_5, which is formed during the calcination process, was removed by leaching the electrodes in 1 M KOH for 20–30 min under vigorous stirring.[362]

A.1.4   Sequential coating of CoFe-PB

The CoFe-PB catalyst was deposited by sequentially dipping the photoelectrodes in reactant solutions of 0.02 M $K_3[Fe(CN)_6]$ in H_2O and 0.04 M $CoCl_2$ in H_2O, both at pH 7. First, the electrodes were dipped in the $[Fe(CN)_6]^{3-}$ solution for 10–15 min under slow stirring, then thoroughly rinsed with Milli-Q water, followed by dipping them in the Co^{2+} solution, again for 10 –15 min under stirring.[365] The sequence was repeated at least two times in order to ensure significant catalyst deposition. If not otherwise stated, four to eight repetitions were performed. The PEC behaviour did not change significantly with number of sequential coating cycles.[324,356]

A.1.5   Synthesis of CoFe-PB electrodes

In order to compare the electrochemical behaviour of the modified photoanodes CoFe-PB/Fe_2O_3 and CoFe-PB/$BiVO_4$ with that of

the CoFe-PB electrocatalyst alone, CoFe-PB was deposited on FTO glass by the procedure of Han *et al*.[110] In this method, CoO_x films were deposited solvothermally on FTO by heating 27 mM $Co(NO_3)_2$ and 135 mM carbamide ($CO(NH_2)_2$) in an autoclave for 10 h at 120 °C. CoO_x was subsequently derivatised for 4 h in hexacyanoferrate ($K_3[Fe(CN)_6]$, 12 mM) solution, to form CoFe-PB. Residual CoO_x was removed by an acid treatment, i.e. immersing the electrodes for ca. 3 hours in diluted H_2SO_4 (pH = 1).

For spectroscopic experiments thinner, transparent films of CoFe-PB were needed and the solvothermal procedure was optimised. For that purpose, the initial $Co(NO_3)_2/CO(NH_2)_2$ mixture was allowed to heat only for 3 h, so that thinner CoO_x films form.

A.1.6   Deposition of CoO_x and FeOOH on $BiVO_4$

CoO_x is prepared by two different methods, electrodeposition and dipcoating in Co^{2+} solution. Electrodeposition was done by immersing the $BiVO_4$ electrode in a 0.5 mM $Co(NO_3)_2$ and on 0.1 M KP_i buffer solution (pH 7) and by applying a constant potential of 0.9 $V_{Ag/AgCl}$ for 500 and 900 seconds (adapted from Ref [86]). The dipcoating approach is similar to the preparation of CoFe-PB modified electrodes. The $BiVO_4$ electrode was dipped in a 0.1 M $Co(NO_3)_2$ (in H_2O) solution for four times five minutes.

FeOOH was photodeposited on $BiVO_4$ by applying alternating current pulses of 10 μA/cm^2 for 3 s and 1 μA/cm^2 for 2 s, while irradiating the sample with light (1 sun), as described by Seabold *et al*.[382]

A.2   Structural and optical characterisation

A.2.1   Scanning Electron Microscopy

Scanning Electron Microscopy (SEM) was performed with a JSM-7000F JEOL FEG-SEM system (Tokyo, Japan), operating at 15 kV, which was equipped with an INCA 400 Oxford EDX (Energy-Dispersive X-ray) analyser (Oxford, U.K.). Prior to the SEM measurement, the samples were sputtered with a 2 nm thick layer of Pt to make its surface conductive.

A.2.2   Transmission Electron Microscopy

Transmission Electron Microscopy (TEM) was carried out with a JEM-2100 JEOL microscope (Tokyo, Japan) at 200 kV, also equipped with an INCA 400 Oxford EDX analyser (Oxford, U.K.).

To investigate a possible morphology change under water oxidation conditions, SEM and TEM measurements were undergone before and after PEC application. To allow for comparison all tested samples were irradiated with 100 mW/cm^2 (1 sun) at 1.23 V_{RHE} for 1 h.

A.2.3 X-ray Photoelectron Spectroscopy

In order to analyse the surface and possible changes of electronic coordination before and after the electrochemical treatment, surface-sensitive X-ray Photoelectron Spectroscopy (XPS) was performed with a Specs SAGE 150 instrument. A monochromatic Al Kα irradiation (1486.6 eV) at 20 mA and 13 kV, a constant energy pass of 75 eV for overall analysis, and 30 eV for analysis in the specific binding energy ranges of each element, were used. The pressure in the analysis chamber was $8 \cdot 10^{-9}$ hPa. The measurement area was 1x1 mm^2. The data were evaluated using the Casa XPS software. Energy corrections to the spectra were performed by considering the C 1s signal as reference, which is at 284.8 eV for organic impurities.

A.2.4 Infrared Spectroscopy

Infrared absorption spectra were collected with a Thermo-Scientific NICOLET iS50 Fourier transform infrared (FT-IR) spectrometer. For the measurement, the substrate (<1 mg) was scratched from several electrodes, finely ground with large excess of KBr, and pressed to obtain a thin transparent disk.

A.2.5 Inductively coupled plasma optical emission spectrometry

After various photoelectrochemical experiments, the supernatant buffer solutions were analysed by inductively coupled plasma optical emission spectrometry (ICP-OES), in order to confirm the stability of the materials towards leaching of metal substituents. Apart from IPC analysis of electrode materials, also other trace metals (Al, Cr, Cu, Mn, Ni, Zn) were tested.

A.3 (Photo)electrochemical measurements

Photoelectrochemical (PEC) measurements were usually conducted with a three-electrode set-up as shown in Figure 2.9 with the measured sample as working electrode, a Pt wire or mesh as counter

electrode, and an Ag/AgCl (3 M KCl) reference electrode. After the measurement, the applied potentials ($V_{Ag/AgCl}$) were converted to the pH-independent reversible hydrogen electrode (RHE) with the Nernst equation (Equation 2.28), which can be simplified to (in aqueous solution at room temperature):

$$V_{RHE} = V_{Ag/AgCl} + V^o_{Ag/AgCl} + 0.059 \cdot pH \qquad \text{(A.1)}$$

where $V^o_{Ag/AgCl}$ = 0.21 V in 3 M KCl.

The PEC experiments were performed with an Eco Chemie Autolab potentiostat coupled with the NOVA electrochemical software. To calculate the current density j in mA/cm^2, the geometrical areas of the electrodes were determined by the graphical software Image J.[411] Unless otherwise stated, the experiments were performed in a 0.1 M solution of potassium phosphate (KH_2PO_4) buffer at pH = 7($\pm$0.1). The pH was determined with a CRISON Basic 2° pH meter. For experiments in hole scavenger solution, 1 M Na_2SO_3 (pH 8) in buffer was used for $BiVO_4$ anodes, and 0.5 M H_2O_2 solution (pH 7) was used for Fe_2O_3 anodes, as it was suggested by Dotan *et al.*[222] A 450 W Xe arc lamp with an AM 1.5 solar filter (Sciencetech Inc.) was used to simulate sunlight of 100 mW/cm^2 (1 sun).

The hematite electrodes were illuminated from the surface, while $BiVO_4$ was illuminated through the FTO glass substrate. The difference is due to the different charge carrier dynamics of both metal oxides. Hematite is known to have very small hole diffusion lengths,[40,329] whereas $BiVO_4$ is a better hole conductor but has small electron diffusion lengths.[363,364]

Cyclic voltammetry (CV) was performed at a scan rate of 50 mV/s. The shutter frequency was 1 Hz during chopped light measurements. For the CoFe-PB modified anodes typically 2–4 CV scans are needed to reach a stable signal. All the CV scans presented in here were recorded after stabilisation (unless otherwise stated).

A.3.1   Electrochemical impedance spectroscopy

Electrochemical impedance spectroscopy (EIS) was measured between 10^{-1} and $4 \cdot 10^6$ Hz with a 20 mV amplitude voltage perturbation. The collected EIS data were fit with the Software ZView.[226] For the fitting a constant phase element (CPE) was assumed instead of a capacitor, in order to account for the non-ideal behaviour of the capacitance, which results in a flattening of the semi-circle in the Nyquist plot. In other words, the constant phase angle of the CPE is given by $(90 \cdot n)^o$, with n = 1 in the case of an ideal capacitor.

From the fit, the constant phase capacitance $CPE-T$ (as defined in Zview) and n ($CPE-P$ in Zview) can be obtained, and with it the capacitance can be calculated using the formula:[226]

$$C = \left[\frac{CPE-T}{\left[R_S^{-1} + R_{CT}^{-1}\right]^{(1-CPE-P)}} \right]^{\frac{1}{CPE-P}} \tag{A.2}$$

A.3.2   Determination of the turnover frequency

In order to determine the turnover frequency (TOF), according to Equation 5.3, the amount of catalytically active centres $[cat]$ (in mol/cm^2) has to be approximated.

By assuming that all redox active centres are also catalytically active, $[cat]$ can be estimated from CV scans at different speeds $\frac{dV}{dt}$, as shown in Figure 5.9.

The expression for the peak current (Equation 5.4) is derived by defining the current j in terms of the rate of change of oxidised species $\frac{d[ox]}{dt}$.*

$$j = -z F \frac{d[ox]}{dt} \tag{A.3}$$

$[ox]$ can be obtained from the Nernst equation (Equation 2.28) while assuming a constant concentration of active sites ($[cat] = [ox] + [red]$).

$$[ox] = \frac{[cat]\exp(\frac{(V-V^o)zF}{RT})}{1 + \exp(\frac{(V-V^o)zF}{RT})} \tag{A.4}$$

Where $z = 1$ in this case, since one hole/electron is transferred to the redox active centres during oxidation/reduction.[103] Differentiating and setting $V = V^o$ at the peak current, gives

$$\frac{d[ox]}{dt} = \frac{z F}{4RT} \frac{dV}{dt} \tag{A.5}$$

and substitution in Equation A.3 gives Equation 5.4:

$$j_{peak} = \frac{z^2 F^2 [cat]}{4RT} \frac{dV}{dt} \tag{A.6}$$

Consequently, when plotting the peak current of the oxidation and/or reduction wave versus the scan rate, as shown in Figure 5.9, $[cat]$ can be calculated from the slope of the linear fit.

---

*The concentration of oxidised species $[ox]$ could be seen as the amount of oxidised CoFe-PB ($[CoFe-PB^{1+}]$ and $[CoFe-PB^{2+}]$); however, to derive the expression, I prefer using the general notation $[ox]$.

$$[cat] = \frac{4RT \cdot slope \ (\text{in } \frac{A\,s}{V\,cm^2})}{z^2\,F^2} \tag{A.7}$$

Taking both oxidation and reduction peak currents into account, an average concentration of $3.5 \cdot 10^{-8}$ mol/cm^2, i.e. 35 nmol/cm^2 is obtained (see Figure 5.9).

From this the TOF can be calculated from Equation 5.3 as a function of the applied bias. The characteristic time constant is simply the inverse TOF (see Figure 5.10).

$$\tau_{cat} = \frac{1}{TOF} \tag{A.8}$$

A.4 Oxygen detection

In order to confirm that water oxidation takes place and to derive the Faradaic efficiency, the evolved oxygen was detected by gas chromatography (GC). An Agilent Technologies 490 Micro GC device was connected to the electrochemical cell, which was constantly purged with Ar. After an initial blank measurement (without applied potential in the dark), the measurement was performed under steady-state reaction conditions at 1.23 V$_{RHE}$ under 1 sun illumination. GC data were periodically sampled every 5 minutes before and after switching on the light for one hour.

A.5 Absorption spectroscopy

A.5.1 UV-Vis Spectroscopy

UV-Vis spectra of both transmittance (with FTO glass as a reference) and diffuse reflectance were recorded with a Cary 300 Bio spectrometer (UV0911 M213). The UV-Vis absorbance of the electrodes was determined from the reflectance R and transmittance T by:

$$A = -log(T + R) \tag{A.9}$$

The absorption coefficient α can then be calculated with:

$$\alpha = A \cdot l \tag{A.10}$$

Where the l is the layer thickness.

A.5.2 Spectroelectrochemistry

Spectroelectrochemical (SEC) data, which represent the absorption as a function of applied potential, were acquired by inserting the photoelectrochemical cell in a Cary 60 UV-Vis spectrometer (Aligent Technologies). The measured absorption is generally presented as difference in optical density ΔOD subtracting either the absorption measured at the open-circuit potential/voltage (OCP/OCV) or at the water oxidation onset, i.e. ΔOD vs OCV or ΔOD vs onset, respectively. Measured data points were smoothed, applying the Savitzky-Golay smoothing function.[412]

A.6 Time-resolved absorption spectroscopy

A.6.1 Transient absorption spectroscopy

Transient absorption spectroscopy (TAS) is a pump–probe technique, using a 355 nm excitation pulse (3rd harmonic) generated from a Opotek Nd:YAG laser (Big Sky Laser Technologies) with an intensity of approximately 0.4 mJ/cm^2, a repetition rate of around 0.7 Hz and a Q-switch delay of 220 μs. The effect of excitation was monitored using light from a 100 W tungsten lamp (Bentham IL1), equipped with an Oriel cornerstone 130 monochromator. The transmitted probe light was filtered by several band pass and long pass filters (Comar Optics) and detected by a silicon photodiode (Hamamatsu S3071). Collected photons were sent to an amplifier (Costronics) and recorded by an oscilloscope (Tektronics TDS 2012c) on the timescale of μs–ms, and with a DAQ card (National Instruments, NI USB-6211) on the timescale of s–ms. Data were acquired by a home-programmed LabView software.

A.6.2 Photo-induced absorption spectroscopy

For photo-induced absorption spectroscopy (PIAS), a similar set-up was employed. Instead of the pulsed laser excitation, a continuous wave LED (365 nm, 8 mW/cm^2) illumination was used to excite electrons across the band gap of $BiVO_4$. The sample was illuminated for 10 s to approach steady-state conditions, i.e. constant oxidation and recombination rates. After allowing the system to relax for another 10 s, illumination is repeated. The probe and data collection was the same as in TAS.

Appendix B

Computational details

B.1 Implementation

All electronic calculations in this work, are performed with the periodic plane wave code **VASP** (Vienna *ab initio* simulation package).[199,200]   The core electrons are approximated by projector augmented-wave (PAW)[197,198] pseudopotentials, as they are implemented in the code. For the metal atoms, valence-subshell *s* and *p* orbitals were included in the plane wave expansion, which allows for a higher accuracy and flexibility, albeit a larger computational cost. Discrete sets of *k*-points were used to sample the Brillouin zone in reciprocal space, which were chosen according to the Monkhorst-Pack scheme.[193]   Spin-polarisation was included for all performed calculations.

B.2 Methodology

In the initial studies on $KFe[Fe(CN)_6]$ a large variety of functionals, which were available in the VASP code, were applied. These include the GGA functionals PBE (Perdew-Burke-Ernzerhof),[157,280] PBEsol (PBE revised for solids),[161] RPBE (revPBE),[160] PW91 (Perdew-Wang 1991),[158] AM05 (Armiento and Mattson 2005),[281] the meta-GGA TPSS (Tao-Perdew-Staroverov-Scuseria),[282] and the hybrid functionals HSE03 and HSE06,[182,184] B3LYP[289] and B3LYP*.[185]   Moreover, the effective Hubbard term $U^{eff} = (U - J)$ is added to the functionals PBE and PBEsol, in order to account for electronic on-site interaction.[167–170,175] Out of those, PBEsol (+U) and HSE03 with a screening parameter $\mu = 0.3$ Å^{-1} were chosen to perform best for the considered system.

In the later studies of CoFe-PB ($KCo[Fe(CN)_6]$), the hybrid functional HSE03 was further optimised to give a more accurate band

gap. In this context, geometry optimisations with a kinetic cut-off energy of 500 eV of $KCo[Fe(CN)_6]$ at gamma point were carried out, while the amount of exact exchange (AEXX tag in VASP) was varied from 0% to 25%. For HSE03-13 (HSE03 with 13% V_{EX}), the results are in closest agreement with experimental observations. Hence HSE03-13 was chosen for further calculations.

For all GGA and GGA+U calculations (in the case of Prussian blue-type compounds), geometry optimisations were carried out with a cut-off energy of 700 eV and 5x5x5 k-point sampling of the Brillouin zone. Subsequent single-point calculations were performed on a 9x9x9 k-point grid and 600 eV cut-off.

For all hybrid calculations, a gamma-centred k-point grid and 500 eV cut-off were used. In the subsequent single-point calculations, 3x3x3 k-points were used for the cubic Prussian blues, 3x3x2 for Fe_2O_3, and 6x3x4 for $BiVO_4$, in order to ensure equal k-point densities.

B.3   Molecular water

Molecular water was calculated by introducing one water molecule in a symmetry-broken 14.5 x 15.0 x 15.5 Å lattice, otherwise using the same input parameters as for the solids. Solvation effects were included through a multigrid continuum model (MGCM), developed by Garcia-Ratés,[413,414] in which implicit water is treated as a polarisable dielectric continuum.

B.4   Data accessibility

All structures were uploaded to the ioChem-BD database,[205,206] where they are openly available.[207–209] They can be found under the DOIs:

- Database of Prussian blue derivatives: 10.19061/iochem-bd-1-20[207]

- CoFe-PB/Fe_2O_3 photoanodes: 10.19061/iochem-bd-1-51[208]

- CoFe-PB/$BiVO_4$ photoanodes: 10.19061/iochem-bd-1-50[209]

Bibliography

[1] Lewis, N. S.; Nocera, D. G. Powering the planet: Chemical challenges in solar energy utilization, *Proceedings of the National Academy of Sciences* **2006,** *103,* 15729–15735.

[2] United Nations Development Programme, *World energy assessment. Energy and the challenge of sustainability*, 2001
http://www.undp.org/content/undp/en/home/librarypage/environment-energy/sustainable_energy/.

[3] Kukreja, R. *What is Smog?*, 2018, Conserve Energy Future: https://www.conserve-energy-future.com/smogpollution.php.

[4] Hoffert, M. I. *et al.* Energy implications of future stabilization of atmospheric CO_2 content, *Nature* **1998,** *395,* 881.

[5] IPCC: Intergovernmental Panel on Climate Change, *Carbon Dioxide Capture and Storage*, 2005 ISBN 978-1-107-66182-0.

[6] Perkins, S. E.; Alexander, L. V.; Nairn, J. R. Increasing frequency, intensity and duration of observed global heatwaves and warm spells, *Geophysical Research Letters* **2012,** *39,* L20714.

[7] IPCC: Intergovernmental Panel on Climate Change, *Summary for Policymakers – The Physical Science Basis*, 2013 Contribution of Working Group I to the Fifth Assessment Report of the Intergovernmental Panel on Climate Change.

[8] Shepherd, A. *et al.* A reconciled estimate of ice-sheet mass balance, *Science* **2012,** *338,* 1183–1189.

[9] NASA, *Global Climate Change - Vital Signs of the Planet*, 2018
https://climate.nasa.gov/climate_resources/164/nasa-studies-an-unusual-arctic-warming-event/.

[10] Roberts, D. *International Seminar on the Climate System and Climate Change*, 2015 Conference meeting – IPCC.

[11] Butler, H. J.; A, M. S. *National Oceanic and Atmospheric Administration Earth System Research Laboratory: THE NOAA ANNUAL GREENHOUSE GAS INDEX (AGGI)*, 2017
https://www.esrl.noaa.gov/gmd/aggi/aggi.html.

[12] IPCC: Intergovernmental Panel on Climate Change, *Emissions Scenarios - Special Report of the Intergovernmental Panel on Climate Change*, 2000.

[13] Armand, M.; Tarascon, J.-M. Building better batteries, *Nature* **2008,** *451,* 652.

[14] Ciamician, G. The photochemistry of the future, *Science* **1912,** *36,* 385–394.

[15] Barber, J. Photosynthetic energy conversion: natural and artificial, *Chemical Society Reviews* **2009,** *38,* 185–196.

[16] Nocera, D. G. The Artificial Leaf, *Accounts of Chemical Research* **2012,** *45,* 767–776.

[17] Kärkäs, M. D.; Verho, O.; Johnston, E. V.; Åkermark, B. Artificial photosynthesis: molecular systems for catalytic water oxidation, *Chemical Reviews* **2014,** *114,* 11863–12001.

[18] Riedel, E. *Allgemeine und anorganische Chemie: ein Lehrbuch für Studenten mit Nebenfach Chemie;* De Gruyter: 1979.

[19] Lewis, N. S.; Crabtree, G. Basic Research Needs for Solar Energy Utilization, *Report of the Basic Energy Sciences Workshop on Solar Energy Utilization* **2005,** 18–21 April.

[20] Giménez, S.; Bisquert, J. *Photoelectrochemical Solar Fuel Production: From Basic Principles to Advanced Devices;* Springer International Publishing: 2016.

[21] Bertoluzzi, L.; Lopez-Varo, P.; Tejada, J. A. J.; Bisquert, J. Charge transfer processes at the semiconductor/electrolyte interface for solar fuel production: insight from impedance spectroscopy, *Journal of Materials Chemistry A* **2016,** *4,* 2873–2879.

[22] Walter, M. G.; Warren, E. L.; McKone, J. R.; Boettcher, S. W.; Mi, Q.; Santori, E. A.; Lewis, N. S. Solar water splitting cells, *Chemical Reviews* **2010,** *110,* 6446–6473.

[23] Galán-Mascarós, J. R. Water Oxidation at Electrodes Modified with Earth-Abundant Transition-Metal Catalysts, *ChemElectroChem* **2015,** *2,* 37–50.

[24] De Levie, R. The Electrolysis of Water, *Journal of Electroanalytical Chemistry* **1999,** *476,* 92–93.

[25] Trasatti, S. Water electrolysis: who first?, *Journal of Electroanalytical Chemistry* **1999,** *476,* 90–91.

[26] Mason, J. E.; Zweibel, K. Baseline model of a centralized pv electrolytic hydrogen system, *International Journal of Hydrogen Energy* **2007,** *32,* 2743–2763.

[27] Rashid, M. D.; Al Mesfer, M. K.; Naseem, H.; Danish, M. Hydrogen production by water electrolysis: a review of alkaline water electrolysis, PEM water electrolysis and high temperature water electrolysis, *International Journal of Engineering and Advanced Technology* **2015,** *4,* 80-93.

[28] Kudo, A.; Miseki, Y. Heterogeneous photocatalyst materials for water splitting, *Chemical Society Reviews* **2009,** *38,* 253–278.

[29] Fujishima, A.; Honda, K. Electrochemical photolysis of water at a semiconductor electrode, *Nature* **1972,** *238,* 37.

[30] Fujishima, A.; Zhang, X.; Tryk, D. A. TiO_2 photocatalysis and related surface phenomena, *Surface Science Reports* **2008,** *63,* 515–582.

[31] Bak, T.; Nowotny, J.; Rekas, M.; Sorrell, C. Photo-electrochemical hydrogen generation from water using solar energy. Materials-related aspects, *International Journal of Hydrogen Energy* **2002,** *27,* 991–1022.

[32] van de Krol, R.; Liang, Y.; Schoonman, J. Solar hydrogen production with nanostructured metal oxides, *Journal of Materials Chemistry* **2008,** *18,* 2311–2320.

[33] Bard, A. J. Inner-sphere heterogeneous electrode reactions. Electrocatalysis and photocatalysis: the challenge, *Journal of the American Chemical Society* **2010,** *132,* 7559–7567.

[34] Grätzel, M. Photoelectrochemical cells, *Nature* **2001,** *414,* 338.

[35] Osterloh, F. E. Inorganic nanostructures for photoelectrochemical and photocatalytic water splitting, *Chemical Society Reviews* **2013,** *42,* 2294–2320.

[36] Tamirat, A. G.; Rick, J.; Dubale, A. A.; Su, W.-N.; Hwang, B.-J. Using hematite for photoelectrochemical water splitting: a Review of current progress and challenges, *Nanoscale Horizons* **2016,** *1,* 243–267.

[37] Sivula, K.; Van De Krol, R. Semiconducting materials for photoelectrochemical energy conversion, *Nature Reviews Materials* **2016,** *1,* 15010.

[38] Hardee, K. L.; Bard, A. J. Semiconductor electrodes V. The application of chemically vapor deposited iron oxide films to photosensitized electrolysis, *Journal of the Electrochemical Society* **1976,** *123,* 1024–1026.

[39] Cornell, R. M.; Schwertmann, U. *The iron oxides: structure, properties, reactions, occurrences and uses;* John Wiley & Sons: 2003.

[40] Sivula, K.; Le Formal, F.; Grätzel, M. Solar water splitting: progress using hematite (α-Fe$_2$O$_3$) photoelectrodes, *ChemSusChem* **2011,** *4,* 432–449.

[41] Fàbrega, C.; Murcia-López, S.; Monllor-Satoca, D.; Prades, J.; Hernández-Alonso, M.; Penelas, G.; Morante, J.; Andreu, T. Efficient WO$_3$ photoanodes fabricated by pulsed laser deposition for photoelectrochemical water splitting with high faradaic efficiency, *Applied Catalysis B: Environmental* **2016,** *189,* 133–140.

[42] Kudo, A.; Ueda, K.; Kato, H.; Mikami, I. Photocatalytic O$_2$ evolution under visible light irradiation on BiVO$_4$ in aqueous AgNO$_3$ solution, *Catalysis Letters* **1998,** *53,* 229–230.

[43] Kim, T. W.; Choi, K.-S. Nanoporous BiVO$_4$ photoanodes with dual-layer oxygen evolution catalysts for solar water splitting, *Science* **2014,** 1245026.

[44] Zhong, D. K.; Sun, J.; Inumaru, H.; Gamelin, D. R. Solar water oxidation by composite catalyst/α-Fe$_2$O$_3$ photoanodes, *Journal of the American Chemical Society* **2009,** *131,* 6086–6087.

[45] Zhong, D. K.; Gamelin, D. R. Photoelectrochemical water oxidation by cobalt catalyst ("Co- Pi")/α-Fe$_2$O$_3$ composite photoanodes: oxygen evolution and resolution of a kinetic bottleneck, *Journal of the American Chemical Society* **2010,** *132,* 4202–4207.

[46] Kleiman-Shwarsctein, A.; Hu, Y.-S.; Stucky, G. D.; McFarland, E. W. NiFe-oxide electrocatalysts for the oxygen evolution reaction on Ti doped hematite photoelectrodes, *Electrochemistry Communications* **2009,** *11,* 1150–1153.

[47] Tilley, S. D.; Cornuz, M.; Sivula, K.; Grätzel, M. Light-induced water splitting with hematite: improved nanostructure and iridium oxide catalysis, *Angewandte Chemie International Edition* **2010,** *49,* 6405–6408.

[48] Kim, J. Y.; Magesh, G.; Youn, D. H.; Jang, J.-W.; Kubota, J.; Domen, K.; Lee, J. S. Single-crystalline, wormlike hematite photoanodes for efficient solar water splitting, *Scientific Reports* **2013,** *3,* 2681.

[49] Steinmiller, E. M.; Choi, K.-S. Photochemical deposition of cobalt-based oxygen evolving catalyst on a semiconductor photoanode for solar oxygen production, *Proceedings of the National Academy of Sciences* **2009,** *106,* 20633–20636.

[50] Zhong, D. K.; Choi, S.; Gamelin, D. R. Near-complete suppression of surface recombination in solar photoelectrolysis by "Co-Pi" catalyst-modified W:BiVO$_4$, *Journal of the American Chemical Society* **2011,** *133,* 18370–18377.

[51] Qiu, Y.; Liu, W.; Chen, W.; Zhou, G.; Hsu, P.-C.; Zhang, R.; Liang, Z.; Fan, S.; Zhang, Y.; Cui, Y. Efficient solar-driven water splitting by nanocone BiVO$_4$-perovskite tandem cells, *Science Advances* **2016,** *2,* e1501764.

[52] Park, Y.; McDonald, K. J.; Choi, K.-S. Progress in bismuth vanadate photoanodes for use in solar water oxidation, *Chemistry Society Review* **2013,** *42,* 2321–2337.

[53] Badia-Bou, L.; Mas-Marza, E.; Rodenas, P.; Barea, E. M.; Fabregat-Santiago, F.; Gimenez, S.; Peris, E.; Bisquert, J. Water Oxidation at Hematite Photoelectrodes with an Iridium-Based Catalyst, *Journal Physical Chemistry C* **2013,** *117,* 3826–3833.

[54] Pihosh, Y. *et al.* Photocatalytic generation of hydrogen by core-shell $WO_3/BiVO_4$ nanorods with ultimate water splitting efficiency, *Scientific Reports* **2015,** *5,* 11141.

[55] Liu, G.; Ye, S.; Yan, P.; Xiong, F.; Fu, P.; Wang, Z.; Chen, Z.; Shi, J.; Li, C. Enabling an integrated tantalum nitride photoanode to approach the theoretical photocurrent limit for solar water splitting, *Energy & Environmental Science* **2016,** *9,* 1327–1334.

[56] She, Z. W.; Kibsgaard, J.; Dickens, C. F.; Chorkendorff, I.; Nørskov, J. K.; Jaramillo, T. F. Combining theory and experiment in electrocatalysis: Insights into materials design, *Science* **2017,** *355,* eaad4998.

[57] Trasatti, S. Electrocatalysis by oxides—attempt at a unifying approach, *Journal of Electroanalytical Chemistry and Interfacial Electrochemistry* **1980,** *111,* 125–131.

[58] Quaino, P.; Juarez, F.; Santos, E.; Schmickler, W. Volcano plots in hydrogen electrocatalysis–uses and abuses, *Beilstein Journal of Nanotechnology* **2014,** *5,* 846.

[59] Medford, A. J.; Vojvodic, A.; Hummelshøj, J. S.; Voss, J.; Abild-Pedersen, F.; Studt, F.; Bligaard, T.; Nilsson, A.; Nørskov, J. K. From the Sabatier principle to a predictive theory of transition-metal heterogeneous catalysis, *Journal of Catalysis* **2015,** *328,* 36–42.

[60] Sabatier, P. *La catalyse en chimie organique;* Encyclopédie de science chimique appliquée aux arts industriels C. Béranger: 1913.

[61] Man, I. C.; Su, H.-Y.; Calle-Vallejo, F.; Hansen, H. A.; Martínez, J. I.; Inoglu, N. G.; Kitchin, J.; Jaramillo, T. F.; Nørskov, J. K.; Rossmeisl, J. Universality in oxygen evolution electrocatalysis on oxide surfaces, *ChemCatChem* **2011,** *3,* 1159–1165.

[62] Matsumoto, Y.; Sato, E. Electrocatalytic properties of transition metal oxides for oxygen evolution reaction, *Materials Chemistry and Physics* **1986,** *14,* 397–426.

[63] Hall, D. E. Alkaline water electrolysis anode materials, *Journal of The Electrochemical Society* **1985,** *132,* 41C–48C.

[64] Bockris, J. O.; Otagawa, T. The electrocatalysis of oxygen evolution on perovskites, *Journal of the Electrochemical Society* **1984,** *131,* 290–302.

[65] Rossmeisl, J.; Logadottir, A.; Nørskov, J. K. Electrolysis of water on (oxidized) metal surfaces, *Chemical Physics* **2005,** *319,* 178–184.

[66] Rossmeisl, J.; Qu, Z.-W.; Zhu, H.; Kroes, G.-J.; Nørskov, J. K. Electrolysis of water on oxide surfaces, *Journal of Electroanalytical Chemistry* **2007,** *607,* 83–89.

[67] Lee, Y.; Suntivich, J.; May, K. J.; Perry, E. E.; Shao-Horn, Y. Synthesis and activities of rutile IrO_2 and RuO_2 nanoparticles for oxygen evolution in acid and alkaline solutions, *The Journal of Physical Chemistry Letters* **2012,** *3,* 399–404.

[68] Seitz, L. C. *et al.* A highly active and stable $IrO_x/SrIrO_3$ catalyst for the oxygen evolution reaction, *Science* **2016,** *353,* 1011–1014.

[69] Doyle, R. L.; Lyons, M. E. An electrochemical impedance study of the oxygen evolution reaction at hydrous iron oxide in base, *Physical Chemistry Chemical Physics* **2013,** *15,* 5224–5237.

[70] Trotochaud, L.; Ranney, J. K.; Williams, K. N.; Boettcher, S. W. Solution-cast metal oxide thin film electrocatalysts for oxygen evolution, *Journal of the American Chemical Society* **2012,** *134,* 17253–17261.

[71] Zhang, B. *et al.* Homogeneously dispersed multimetal oxygen-evolving catalysts, *Science* **2016,** *352,* 333–337.

[72] Suntivich, J.; May, K. J.; Gasteiger, H. A.; Goodenough, J. B.; Shao-Horn, Y. A perovskite oxide optimized for oxygen evolution catalysis from molecular orbital principles, *Science* **2011,** *334,* 1383–1385.

[73] Han, B.; Risch, M.; Lee, Y.-L.; Ling, C.; Jia, H.; Shao-Horn, Y. Activity and stability trends of perovskite oxides for oxygen evolution catalysis at neutral pH, *Physical Chemistry Chemical Physics* **2015,** *17,* 22576–22580.

[74] Singh, R. N.; Singh, J. P.; Lal, B.; Singh, A. Preparation and characterization of $CuFe_2-xCr_xO_4$ (0 x 1.0) nano spinels for electrocatalysis of oxygen evolution in alkaline solutions, *International Journal of Hydrogen Energy* **2007,** *32,* 11–16.

[75] Singh, R. N.; Singh, J. P.; Singh, A. Electrocatalytic properties of new spinel-type $MMoO_4$ (M= Fe, Co and Ni) electrodes for oxygen evolution in alkaline solutions, *International Journal of Hydrogen Energy* **2008,** *33,* 4260–4264.

[76] Smith, R. D.; Prévot, M. S.; Fagan, R. D.; Zhang, Z.; Sedach, P. A.; Siu, M. K. J.; Trudel, S.; Berlinguette, C. P. Photochemical route for accessing amorphous metal oxide materials for water oxidation catalysis, *Science* **2013,** 1233638.

[77] Smith, R. D. L.; Prévot, M. S.; Fagan, R. D.; Trudel, S.; Berlinguette, C. P. Water oxidation catalysis: electrocatalytic response to metal stoichiometry in amorphous metal oxide films containing iron, cobalt, and nickel, *Journal of the American Chemical Society* **2013,** *135,* 11580–11586.

[78] McCrory, C. C.; Jung, S.; Peters, J. C.; Jaramillo, T. F. Benchmarking heterogeneous electrocatalysts for the oxygen evolution reaction, *Journal of the American Chemical Society* **2013,** *135,* 16977–16987.

[79] Subbaraman, R.; Tripkovic, D.; Strmcnik, D.; Chang, K.-C.; Uchimura, M.; Paulikas, A. P.; Stamenkovic, V.; Markovic, N. M. Enhancing hydrogen evolution activity in water splitting by tailoring Li^+–$Ni(OH)_2$–Pt interfaces, *Science* **2011,** *334,* 1256–1260.

[80] Subbaraman, R.; Danilovic, N.; Lopes, P.; Tripkovic, D.; Strmcnik, D.; Stamenkovic, V.; Markovic, N. Origin of anomalous activities for electrocatalysts in alkaline electrolytes, *The Journal of Physical Chemistry C* **2012,** *116,* 22231–22237.

[81] Dincă, M.; Surendranath, Y.; Nocera, D. G. Nickel–borate oxygen-evolving catalyst that functions under benign conditions, *Proceedings of the National Academy of Sciences* **2010,** *107,* 10337–10341.

[82] Frydendal, R.; Paoli, E. A.; Chorkendorff, I.; Rossmeisl, J.; Stephens, I. E. Toward an Active and Stable Catalyst for Oxygen Evolution in Acidic Media: Ti-Stabilized MnO_2, *Advanced Energy Materials* **2015,** *5,* 1500991.

[83] Kanan, M. W.; Nocera, D. G. In situ formation of an oxygen-evolving catalyst in neutral water containing phosphate and Co_2^+, *Science* **2008,** *321,* 1072–1075.

[84] Zandi, O.; Hamann, T. W. Enhanced water splitting efficiency through selective surface state removal, *The Journal of Physical Chemistry Letters* **2014, 5,** 1522–1526.

[85] Long, M.; Cai, W.; Kisch, H. Visible light induced photoelectrochemical properties of n-BiVO$_4$ and n-BiVO$_4$/p-Co$_3$O$_4$, *The Journal of Physical Chemistry C* **2008,** *112,* 548–554.

[86] Jeon, T. H.; Choi, W.; Park, H. Cobalt–phosphate complexes catalyze the photoelectrochemical water oxidation of BiVO$_4$ electrodes, *Physical Chemistry Chemical Physics* **2011,** *13,* 21392–21401.

[87] Zachäus, C.; Abdi, F. F.; Peter, L. M.; Van De Krol, R. Photocurrent of BiVO$_4$ is limited by surface recombination, not surface catalysis, *Chemical Science* **2017,** *8,* 3712–3719.

[88] Lutterman, D. A.; Surendranath, Y.; Nocera, D. G. A self-healing oxygen-evolving catalyst, *Journal of the American Chemical Society* **2009,** *131,* 3838–3839.

[89] Kanan, M. W.; Yano, J.; Surendranath, Y.; Dinca, M.; Yachandra, V. K.; Nocera, D. G. Structure and valency of a cobalt- phosphate water oxidation catalyst determined by in situ X-ray spectroscopy, *Journal of the American Chemical Society* **2010,** *132,* 13692–13701.

[90] Surendranath, Y.; Kanan, M. W.; Nocera, D. G. Mechanistic studies of the oxygen evolution reaction by a cobalt-phosphate catalyst at neutral pH, *Journal of the American Chemical Society* **2010,** *132,* 16501–16509.

[91] Klingan, K.; Ringleb, F.; Zaharieva, I.; Heidkamp, J.; Chernev, P.; Gonzalez-Flores, D.; Risch, M.; Fischer, A.; Dau, H. Water oxidation by amorphous cobalt-based oxides: volume activity and proton transfer to electrolyte bases, *ChemSusChem* **2014,** *7,* 1301–1310.

[92] Surendranath, Y.; Dinca, M.; Nocera, D. G. Electrolyte-dependent electrosynthesis and activity of cobalt-based water oxidation catalysts, *Journal of the American Chemical Society* **2009,** *131,* 2615–2620.

[93] Trasatti, S. *Electrodes of Conductive Metallic Oxides;* Electrodes of Conductive Metallic Oxides Elsevier Scientific Publishing Company: 1981.

[94] Minguzzi, A.; Fan, F.-R. F.; Vertova, A.; Rondinini, S.; Bard, A. J. Dynamic potential–pH diagrams application to electrocatalysts for water oxidation, *Chemical Science* **2012,** *3,* 217–229.

[95] Surendranath, Y.; Lutterman, D. A.; Liu, Y.; Nocera, D. G. Nucleation, growth, and repair of a cobalt-based oxygen evolving catalyst, *Journal of the American Chemical Society* **2012,** *134,* 6326–6336.

[96] Yeo, B. S.; Bell, A. T. Enhanced activity of gold-supported cobalt oxide for the electrochemical evolution of oxygen, *Journal of the American Chemical Society* **2011,** *133,* 5587–5593.

[97] Chen, J.; Selloni, A. First principles study of cobalt (Hydr)oxides under electrochemical conditions, *The Journal of Physical Chemistry C* **2013,** *117,* 20002–20006.

[98] Bajdich, M.; García-Mota, M.; Vojvodic, A.; Nørskov, J. K.; Bell, A. T. Theoretical investigation of the activity of cobalt oxides for the electrochemical oxidation of water, *Journal of the American Chemical Society* **2013,** *135,* 13521–13530.

[99] Gamelin, D. R. Water splitting: Catalyst or spectator?, *Nature Chemistry* **2012,** *4,* 965.

[100] Klahr, B.; Gimenez, S.; Fabregat-Santiago, F.; Bisquert, J.; Hamann, T. W. Photoelectrochemical and Impedance Spectroscopic Investigation of Water Oxidation with "Co–Pi"-Coated Hematite Electrodes, *Journal of the American Chemical Society* **2012,** *134,* 16693–16700.

[101] Barroso, M.; Cowan, A. J.; Pendlebury, S. R.; Grätzel, M.; Klug, D. R.; Durrant, J. R. The Role of Cobalt Phosphate in Enhancing the Photocatalytic Activity of α-Fe$_2$O$_3$ toward Water Oxidation, *Journal of the American Chemical Society* **2011,** *133,* 14868–14871.

[102] Cummings, C. Y.; Marken, F.; Peter, L. M.; Tahir, A. A.; Wijayantha, K. G. U. Kinetics and mechanism of light-driven oxygen evolution at thin film α-Fe$_2$O$_3$ electrodes, *Chemical Communications* **2012,** *48,* 2027–2029.

[103] Pintado, S.; Goberna-Ferron, S.; Escudero-Adan, E. C.; Galan-Mascaros, J. R. Fast and persistent electrocatalytic water oxidation by Co–Fe Prussian blue coordination polymers, *Journal of the American Chemical Society* **2013,** *135,* 13270–13273.

[104] de Tacconi, N. R.; Rajeshwar, K.; Lezna, R. O. Metal hexacyanoferrates: electrosynthesis, in situ characterization, and applications, *Chemistry of Materials* **2003,** *15,* 3046–3062.

[105] Karyakin, A. A. Prussian blue and its analogues: electrochemistry and analytical applications, *Electroanalysis: An International Journal Devoted to Fundamental and Practical Aspects of Electroanalysis* **2001,** *13,* 813–819.

[106] Zhang, Y.; Wilson, G. S. Electrochemical oxidation of H$_2$O$_2$ on Pt and Pt+ Ir electrodes in physiological buffer and its applicability to H$_2$O$_2$-based biosensors, *Journal of Electroanalytical Chemistry* **1993,** *345,* 253–271.

[107] Ali, S.; Bansal, V. K.; Khan, A. A.; Jain, S. K.; Ansari, M. A. Growth of zinc hexacyanoferrate nanocubes and their potential as heterogeneous catalyst for solvent-free oxidation of benzyl alcohol, *Journal of Molecular Catalysis A: Chemical* **2009,** *303,* 60–64.

[108] Jaffari, S. A.; Turner, A. P. F. Novel hexacyanoferrate (III) modified graphite disc electrodes and their application in enzyme electrodes—Part I, *Biosensors and Bioelectronics* **1997,** *12,* 1–9.

[109] Goberna-Ferron, S.; Hernandez, W. Y.; Rodríguez-García, B.; Galan-Mascaros, J. R. Light-driven water oxidation with metal hexacyanometallate heterogeneous catalysts, *ACS Catalysis* **2014,** *4,* 1637–1641.

[110] Han, L.; Tang, P.; Reyes-Carmona, A.; Rodriguez-Garcia, B.; Torrens, M.; Morante, J. R.; Arbiol, J.; Galan-Mascaros, J. R. Enhanced Activity and Acid pH Stability of Prussian Blue-type Oxygen Evolution Electrocatalysts Processed by Chemical Etching, *Journal of the American Chemical Society* **2016,** *138,* 16037–16045.

[111] Aksoy, M.; Nune, S. V. K.; Karadas, F. A novel synthetic route for the preparation of an amorphous Co/Fe Prussian blue coordination compound with high electrocatalytic water oxidation activity, *Inorganic Chemistry* **2016,** *55,* 4301–4307.

[112] Alsaç, E. P.; Ülker, E.; Nune, S. V. K.; Dede, Y.; Karadas, F. Tuning the Electronic Properties of Prussian Blue Analogues for Efficient Water Oxidation Electrocatalysis: Experimental and Computational Studies, *Chemistry - A European Journal* **2018,** *24,* 4856–4863.

[113] Indra, A.; Paik, U.; Song, T. Boosting Electrochemical Water Oxidation with Metal Hydroxide Carbonate Templated Prussian Blue Analogues, *Angewandte Chemie - Int. Ed.* **2018,** *57,* 1241–1245.

[114] Zhang, X.; He, J. Co–Fe Prussian Blue Coordination Polymer Modified Silicon Nanowires Array for Efficient Photoelectrochemical Water Oxidation, *Journal of Nanoscience and Nanotechnology* **2018,** *18,* 5674–5678.

[115] Rodríguez-García, B.; Reyes-Carmona, Á.; Jiménez-Morales, I.; Blasco-Ahicart, M.; Cavaliere, S.; Dupont, M.; Jones, D.; Rozière, J.; Galán-Mascarós, J. R.; Jaouen, F. Cobalt hexacyanoferrate supported on Sb-doped SnO_2 as a non-noble catalyst for oxygen evolution in acidic medium, *Sustainable Energy & Fuels* **2018,** *2,* 589–597.

[116] Berardi, S.; Drouet, S.; Francàs, L.; Gimbert-Suriñach, C.; Guttentag, M.; Richmond, C.; Stoll, T.; Llobet, A. Molecular artificial photosynthesis, *Chemical Society Reviews* **2014,** *43,* 7501-7519.

[117] Joya, K. S.; Joya, Y. F.; Ocakoglu, K.; van de Krol, R. Water-splitting catalysis and solar fuel devices: artificial leaves on the move, *Angewandte Chemie International Edition* **2013,** *52,* 10426–10437.

[118] Cowan, A. J.; Tang, J.; Leng, W.; Durrant, J. R.; Klug, D. R. Water splitting by nanocrystalline TiO_2 in a complete photoelectrochemical cell exhibits efficiencies limited by charge recombination, *The Journal of Physical Chemistry C* **2010,** *114,* 4208–4214.

[119] Pesci, F. M.; Cowan, A. J.; Alexander, B. D.; Durrant, J. R.; Klug, D. R. Charge carrier dynamics on mesoporous WO_3 during water splitting, *The Journal of Physical Chemistry Letters* **2011,** *2,* 1900–1903.

[120] Barroso, M.; Pendlebury, S. R.; Cowan, A. J.; Durrant, J. R. Charge carrier trapping, recombination and transfer in hematite (α-Fe_2O_3) water splitting photoanodes, *Chemical Science* **2013,** *4,* 2724–2734.

[121] Ravensbergen, J.; Abdi, F. F.; van Santen, J. H.; Frese, R. N.; Dam, B.; van de Krol, R.; Kennis, J. T. Unraveling the carrier dynamics of $BiVO_4$: A femtosecond to microsecond transient absorption study, *The Journal of Physical Chemistry C* **2014,** *118,* 27793–27800.

[122] Ma, Y.; Pendlebury, S. R.; Reynal, A.; Le Formal, F.; Durrant, J. R. Dynamics of photogenerated holes in undoped $BiVO_4$ photoanodes for solar water oxidation, *Chemical Science* **2014,** *5,* 2964–2973.

[123] Trotochaud, L.; Mills, T. J.; Boettcher, S. W. An optocatalytic model for semiconductor–catalyst water-splitting photoelectrodes based on in situ optical measurements on operational catalysts, *The Journal of Physical Chemistry Letters* **2013,** *4,* 931–935.

[124] Liu, R.; Zheng, Z.; Spurgeon, J.; Yang, X. Enhanced photoelectrochemical water-splitting performance of semiconductors by surface passivation layers, *Energy & Environmental Science* **2014,** *7,* 2504–2517.

[125] Hamann, T. W. Water splitting: An adaptive junction, *Nature Materials* **2014,** *13,* 3.

[126] Nellist, M. R.; Laskowski, F. A.; Lin, F.; Mills, T. J.; Boettcher, S. W. Semiconductor–electrocatalyst interfaces: theory, experiment, and applications in photoelectrochemical water splitting, *Accounts of Chemical Research* **2016,** *49,* 733–740.

[127] Peressi, M.; Binggeli, N.; Baldereschi, A. Band engineering at interfaces: theory and numerical experiments, *Journal of Physics D: Applied Physics* **1998,** *31,* 1273.

[128] Cheng, J.; Sprik, M. Alignment of electronic energy levels at electrochemical interfaces, *Physical Chemistry Chemical Physics* **2012,** *14,* 11245–11267.

[129] Pham, T. A.; Ping, Y.; Galli, G. Modelling heterogeneous interfaces for solar water splitting, *Nature Materials* **2017,** *16,* 401.

[130] Walsh, A.; Butler, K. T. Prediction of electron energies in metal oxides, *Accounts of Chemical Research* **2014,** *47,* 364–372.

[131] Guo, Z.; Ambrosio, F.; Chen, W.; Gono, P.; Pasquarello, A. Alignment of Redox Levels at Semiconductor–Water Interfaces, *Chemistry of Materials* **2017,** *30,* 94–111.

[132] Barroso, M.; Mesa, C. A.; Pendlebury, S. R.; Cowan, A. J.; Hisatomi, T.; Sivula, K.; Grätzel, M.; Klug, D. R.; Durrant, J. R. Dynamics of photogenerated holes in surface modified α-Fe$_2$O$_3$ photoanodes for solar water splitting., *Proceedings of the National Academy of Sciences* **2012,** *109,* 15640–5.

[133] Ma, Y.; Le Formal, F.; Kafizas, A.; Pendlebury, S. R.; Durrant, J. R. Efficient suppression of back electron/hole recombination in cobalt phosphate surface-modified undoped bismuth vanadate photoanodes, *Journal of Materials Chemistry A* **2015,** *3,* 20649–20657.

[134] Xu, J.; Herraiz-Cardona, I.; Yang, X.; Gimenez, S.; Antonietti, M.; Shalom, M. The complex role of carbon nitride as a sensitizer in photoelectrochemical cells, *Advanced Optical Materials* **2015,** *3,* 1052–1058.

[135] Ye, H.; Park, H. S.; Bard, A. J. Screening of electrocatalysts for photoelectrochemical water oxidation on W-doped BiVO$_4$ photocatalysts by scanning electrochemical microscopy, *The Journal of Physical Chemistry C* **2011,** *115,* 12464–12470.

[136] Hajibabaei, H.; Schon, A. R.; Hamann, T. W. Interface Control of Photoelectrochemical Water Oxidation Performance with Ni$_{1-x}$Fe$_x$O$_y$ Modified Hematite Photoanodes, *Chemistry of Materials* **2017,** *29,* 6674–6683.

[137] Schottky, W. Zur Halbleitertheorie der Sperrschicht-und Spitzengleichrichter, *Zeitschrift für Physik* **1939,** *113,* 367–414.

[138] Sze, S. M.; Ng, K. K. *Physics of Semiconductor Devices;* Wiley: 2006.

[139] Lin, F.; Boettcher, S. W. Adaptive semiconductor/electrocatalyst junctions in water-splitting photoanodes, *Nature Materials* **2014,** *13,* 81.

[140] Qiu, J.; Hajibabaei, H.; Nellist, M. R.; Laskowski, F. A.; Oener, S. Z.; Hamann, T. W.; Boettcher, S. W. Catalyst Deposition on Photoanodes: The Roles of Intrinsic Catalytic Activity, Catalyst Electrical Conductivity, and Semiconductor Morphology, *ACS Energy Letters* **2018,** *3,* 961–969.

[141] Nellist, M. R.; Qiu, J.; Laskowski, F. A. L.; Toma, F. M.; Boettcher, S. W. Potential-Sensing Electrochemical AFM Shows CoPi is a Hole Collector and Oxygen Evolution Catalyst on BiVO$_4$ Water-Splitting Photoanodes, *ACS Energy Letters* **2018,** *3,* 2286–2291.

[142] Ping, Y.; Goddard III, W. A.; Galli, G. A. Energetics and solvation effects at the photoanode/catalyst interface: ohmic contact versus Schottky barrier, *Journal of the American Chemical Society* **2015,** *137,* 5264–5267.

[143] Carroll, G. M.; Zhong, D. K.; Gamelin, D. R. Mechanistic insights into solar water oxidation by cobalt-phosphate-modified α-Fe$_2$O$_3$ photoanodes, *Energy & Environmental Science* **2015,** *8,* 577–584.

[144] A-Leaf, *An Artificial Leaf: a photo-electro-catalytic cell from earth-abundant materials for sustainable solar production of CO$_2$-based chemicals and fuels*, 2017–2020
http://www.a-leaf.eu.

[145] European Comission, *Community Research and Development Information Service: Project ID A-Leaf: 732840*, 2017–2020
http://cordis.europa.eu/project/rcn/206200_en.html.

[146] Sholl, D.; Steckel, J. A. *Density functional theory: a practical introduction;* John Wiley & Sons: 2011.

[147] Parr, R. G.; Weitao, Y. *Density-Functional Theory of Atoms and Molecules;* International Series of Monographs on Chemistry Oxford University Press: 1989.

[148] Cramer, C. J. *Essentials of Computational Chemistry: Theories and Models;* John Wiley & Sons: 2013.

[149] Born, M.; Oppenheimer, R. Zur Quantentheorie der Molekeln, *Annalen der Physik* **1927,** *389,* 457–484.

[150] Slater, J. C. The Theory of Complex Spectra, *Physical Review* **1929,** *34,* 1293–1322.

[151] Valatin, J. G. Generalized Hartree-Fock Method, *Physical Review* **1961,** *122,* 1012.

[152] Hohenberg, P.; Kohn, W. Inhomogeneous electron gas, *Physical Review* **1964,** *136,* B864.

[153] Kohn, W.; Sham, L. J. Self-consistent equations including exchange and correlation effects, *Physical Review* **1965,** *140,* A1133.

[154] Ceperley, D. M.; Alder, B. J. Ground state of the electron gas by a stochastic method, *Physical Review Letters* **1980,** *45,* 566.

[155] Gunnarsson, O.; Lundqvist, B. I.; Wilkins, J. W. Contribution to the cohesive energy of simple metals: Spin-dependent effect, *Physical Review B* **1974,** *10,* 1319.

[156] Perdew, J. P.; Chevary, J. A.; Vosko, S. H.; Jackson, K. A.; Pederson, M. R.; Singh, D. J.; Fiolhais, C. Atoms, molecules, solids, and surfaces: Applications of the generalized gradient approximation for exchange and correlation, *Physical Review B* **1992,** *46,* 6671.

[157] Perdew, J. P.; Burke, K.; Ernzerhof, M. Generalized gradient approximation made simple, *Physical Review Letters* **1996,** *77,* 3865–3868.

[158] Perdew, J. P.; Wang, Y. Accurate and simple analytic representation of the electron-gas correlation energy, *Physical Review B* **1992,** *45,* 13244.

[159] Becke, A. D. Density-functional exchange-energy approximation with correct asymptotic behavior, *Physical Review A* **1988,** *38,* 3098.

[160] Hammer, B.; Hansen, L. B.; Nørskov, J. K. Improved adsorption energetics within density-functional theory using Revised Perdew-Burke-Ernzerhof functionals, *Physical Review B* **1999,** *59,* 7413.

[161] Perdew, J. P.; Ruzsinszky, A.; Csonka, G. I.; Vydrov, O. A.; Scuseria, G. E.; Constantin, L. A.; Zhou, X.; Burke, K. Restoring the density-gradient expansion for exchange in solids and surfaces, *Physical Review Letters* **2008,** *100,* 136406.

[162] Tao, J.; Perdew, J. P.; Staroverov, V. N.; Scuseria, G. E. Climbing the density functional ladder: Nonempirical meta–generalized gradient approximation designed for molecules and solids, *Physical Review Letters* **2003,** *91,* 146401.

[163] Sun, J.; Remsing, R. C.; Zhang, Y.; Sun, Z.; Ruzsinszky, A.; Peng, H.; Yang, Z.; Paul, A.; Waghmare, U.; Wu, X.; Klein, M. L.; Perdew, J. P. SCAN: An Efficient Density Functional Yielding Accurate Structures and Energies of Diversely-Bonded Materials, *arXiv* **2015,** *1511.01089v1,* [cond-mat.mtrl-sci].

[164] Sun, J. *et al.* Accurate first-principles structures and energies of diversely bonded systems from an efficient density functional, *Nature Chemistry* **2016,** *8,* 831.

[165] Martin, R. M.; Reining, L.; Ceperley, D. M. *Interacting Electrons: Theory and Computational Approaches;* Cambridge University Press: 2016.

[166] Ashcroft, N. W.; Mermin, N. D. *Solid State Physics;* HRW international editions Holt, Rinehart and Winston: 1976.

[167] Hubbard, J. Electron correlations in narrow energy bands, *Proceedings of the Royal Society of London A* **1963,** *276,* 238–257.

[168] Anisimov, V.; Gunnarsson, O. Density-functional calculation of effective Coulomb interactions in metals, *Physical Review B* **1991,** *43,* 7570.

[169] Anisimov, V. I.; Aryasetiawan, F.; Lichtenstein, A. I. First-principles calculations of the electronic structure and spectra of strongly correlated systems: the LDA+ U method, *Journal of Physics: Condensed Matter* **1997,** *9,* 767.

[170] Dudarev, S. L.; Botton, G. A.; Savrasov, S. Y.; Humphreys, C. J.; Sutton, A. P. Electron-energy-loss spectra and the structural stability of nickel oxide: An LSDA+ U study, *Physical Review B* **1998,** *57,* 1505.

[171] *VASP Wiki: The VASP Manual*, 2010 http://cms.mpi.univie.ac.at/wiki/index.php.

[172] Cococcioni, M.; De Gironcoli, S. Linear response approach to the calculation of the effective interaction parameters in the LDA+ U method, *Physical Review B* **2005,** *71,* 035105.

[173] Cococcioni, M. Accurate and Efficient Calculations on Strongly Correlated Minerals with the LDA+ U Method: Review and Perspectives, *Reviews in Mineralogy and Geochemistry* **2010,** *71,* 147–167.

[174] Capdevila-Cortada, M.; Łodziana, Z.; López, N. Performance of DFT+U Approaches in the Study of Catalytic Materials, *ACS Catalysis* **2016,** *6,* 8370-8379.

[175] Kulik, H. J. Perspective: Treating electron over-delocalization with the DFT+ U method, *The Journal of Chemical Physics* **2015,** *142,* 240901.

[176] Paier, J. Hybrid density functionals applied to complex solid catalysts: successes, limitations, and prospects, *Catalysis Letters* **2016,** *146,* 861–885.

[177] Becke, A. D. Density-functional thermochemistry. IV. A new dynamical correlation functional and implications for exact-exchange mixing, *The Journal of Chemical Physics* **1996,** *104,* 1040–1046.

[178] Becke, A. D. Density-functional thermochemistry. III. The role of exact exchange, *Journal of Chemical Physics* **1993,** *98,* 5648–5652.

[179] Lee, C.; Yang, W.; Parr, R. G. Development of the Colle-Salvetti correlation-energy formula into a functional of the electron density, *Physical Review B* **1988,** *37,* 785.

[180] Perdew, J. P.; Ernzerhof, M.; Burke, K. Rationale for mixing exact exchange with density functional approximations, *The Journal of Chemical Physics* **1996,** *105,* 9982–9985.

[181] Heyd, J.; Scuseria, G. E.; Ernzerhof, M. Hybrid functionals based on a screened Coulomb potential, *The Journal of Chemical Physics* **2003,** *118,* 8207–8215.

[182] Heyd, J. *Screened Coulomb hybrid density functionals,* Thesis, Rice University, 2004.

[183] Heyd, J.; Scuseria, G. E. Efficient hybrid density functional calculations in solids: Assessment of the Heyd–Scuseria–Ernzerhof screened Coulomb hybrid functional, *The Journal of Chemical Physics* **2004,** *121,* 1187–1192.

[184] Krukau, A. V.; Vydrov, O. A.; Izmaylov, A. F.; Scuseria, G. E. Influence of the exchange screening parameter on the performance of screened hybrid functionals, *The Journal of Chemical Physics* **2006,** *125,* 224106.

[185] Reiher, M.; Salomon, O.; Hess, B. A. Reparameterization of hybrid functionals based on energy differences of states of different multiplicity, *Theoretical Chemistry Accounts* **2001,** *107,* 48–55.

[186] de PR Moreira, I.; Illas, F.; Martin, R. L. Effect of Fock exchange on the electronic structure and magnetic coupling in NiO, *Physical Review B* **2002,** *65,* 155102.

[187] Swart, M. Accurate spin-state energies for iron complexes, *Journal of Chemical Theory and Computation* **2008,** *4,* 2057–2066.

[188] Kepp, K. P. The ground states of iron (III) porphines: Role of entropy–enthalpy compensation, Fermi correlation, dispersion, and zero-point energies, *Journal of inorganic Biochemistry* **2011,** *105,* 1286–1292.

[189] Pozun, Z. D.; Henkelman, G. Hybrid density functional theory band structure engineering in hematite, *The Journal of Chemical Physics* **2011,** *134,* 224706.

[190] Kweon, K. E.; Hwang, G. S.; Kim, J.; Kim, S.; Kim, S. Electron small polarons and their transport in bismuth vanadate: a first principles study, *Physical Chemistry Chemical Physics* **2015,** *17,* 256–260.

[191] Bloch, F. Über die Quantenmechanik der Elektronen in Kristallgittern, *Zeitschrift für Physik* **1929,** *52,* 555–600.

[192] Wigner, E.; Seitz, F. On the constitution of metallic sodium, *Physical Review* **1933,** *43,* 804.

[193] Monkhorst, H. J.; Pack, J. D. Special points for Brillouin-zone integrations, *Physical Review B* **1976,** *13,* 5188.

[194] Hamann, D. R.; Schlüter, M.; Chiang, C. Norm-conserving pseudopotentials, *Physical Review Letters* **1979,** *43,* 1494.

[195] Schlipf, M.; Gygi, F. Optimization algorithm for the generation of ONCV pseudopotentials, *Computer Physics Communications* **2015,** *196,* 36–44.

[196] Vanderbilt, D. Soft self-consistent pseudopotentials in a generalized eigenvalue formalism, *Physical Review B* **1990,** *41,* 7892.

[197] Blöchl, P. E. Projector augmented-wave method, *Physical Review B* **1994,** *50,* 17953.

[198] Kresse, G.; Joubert, D. From ultrasoft pseudopotentials to the projector augmented-wave method, *Physical Review B* **1999,** *59,* 1758.

[199] Kresse, G.; Furthmüller, J. Efficiency of ab-initio total energy calculations for metals and semiconductors using a plane-wave basis set, *Computational Materials Science* **1996,** *6,* 15–50.

[200] Kresse, G.; Furthmüller, J. Efficient iterative schemes for ab initio total-energy calculations using a plane-wave basis set, *Physical Review B* **1996,** *54,* 11169–11186.

[201] Payne, M. C.; Teter, M. P.; Allan, D. C.; Arias, T.; Joannopoulos, a. J. Iterative minimization techniques for ab initio total-energy calculations: molecular dynamics and conjugate gradients, *Reviews of Modern Physics* **1992,** *64,* 1045.

[202] Marx, D.; Hutter, J. *Ab Initio Molecular Dynamics: Basic Theory and Advanced Methods;* Cambridge University Press: 2009.

[203] Bo, C.; Maseras, F.; López, N. The role of computational results databases in accelerating the discovery of catalysts, *Nature Catalysis* **2018,** *1,* 809.

[204] Butler, K. T.; Davies, D. W.; Cartwright, H.; Isayev, O.; Walsh, A. Machine learning for molecular and materials science, *Nature* **2018,** *559,* 547.

[205] Álvarez-Moreno, M.; De Graaf, C.; López, N.; Maseras, F.; Poblet, J. M.; Bo, C. Managing the computational chemistry big data problem: the ioChem-BD platform, *Journal of Chemical Information and Modeling* **2014,** *55,* 95–103.

[206] Álvarez-Moreno, M. *ioChem-BD*, 2014–2018
https://www.iochem-bd.org/.

[207] Hegner, F. S. *Link to ioChem-BD: Database Prussian blue derivatives*, 2016
https://doi.org/10.19061/iochem-bd-1-20.

[208] Hegner, F. S. *Link to ioChem-BD: Photoanodes Fe$_2$O$_3$ CoFe-PB*, 2017
https://doi.org/10.19061/iochem-bd-1-51.

[209] Hegner, F. S. *Link to ioChem-BD: Photoanodes BiVO$_4$ CoFe-PB*, 2017
https://doi.org/10.19061/iochem-bd-1-50.

[210] Würfel, P.; Würfel, U. *Physics of Solar Cells: From Basic Principles to Advanced Concepts;* Wiley: 2016.

[211] Ding, K.; Chen, B.; Li, Y.; Zhang, Y.; Chen, Z. Comparative density functional theory study on the electronic and optical properties of BiMO$_4$ (M= V, Nb, Ta), *Journal of Materials Chemistry A* **2014,** *2,* 8294–8303.

[212] Cooper, J. K.; Gul, S.; Toma, F. M.; Chen, L.; Liu, Y.-S.; Guo, J.; Ager, J. W.; Yano, J.; Sharp, I. D. Indirect bandgap and optical properties of monoclinic bismuth vanadate, *The Journal of Physical Chemistry C* **2015,** *119,* 2969–2974.

[213] Tauc, J. Optical properties and electronic structure of amorphous Ge and Si, *Materials Research Bulletin* **1968,** *3,* 37–46.

[214] Gerischer, H. Electrochemical behavior of semiconductors under illumination, *Journal of the Electrochemical Society* **1966,** *113,* 1174–1182.

[215] Yatom, N.; Neufeld, O.; Toroker, M. C. Toward settling the debate on the role of Fe$_2$O$_3$ surface states for water splitting, *The Journal of Physical Chemistry C* **2015,** *119,* 24789–24795.

[216] Klahr, B.; Gimenez, S.; Fabregat-Santiago, F.; Hamann, T.; Bisquert, J. Water oxidation at hematite photoelectrodes: the role of surface states, *Journal of the American Chemical Society* **2012,** *134,* 4294–4302.

[217] Le Formal, F.; Pendlebury, S. R.; Cornuz, M.; Tilley, S. D.; Grätzel, M.; Durrant, J. R. Back electron–hole recombination in hematite photoanodes for water splitting, *Journal of the American Chemical Society* **2014,** *136,* 2564–2574.

[218] Zhang, Z.; Yates Jr, J. T. Band bending in semiconductors: chemical and physical consequences at surfaces and interfaces, *Chemical Reviews* **2012,** *112,* 5520–5551.

[219] Hilbert, D. *Methods of Mathematical Physics;* CUP Archive: 2004.

[220] Nernst, W. Zur Kinetik der in Lösung befindlichen Körper, *Zeitschrift für Physikalische Chemie* **1888,** *2,* 613–637.

[221] Chen, Z. *et al.* Accelerating materials development for photoelectrochemical hydrogen production: Standards for methods, definitions, and reporting protocols, *Journal of Materials Research* **2010,** *25,* 3–16.

[222] Dotan, H.; Sivula, K.; Grätzel, M.; Rothschild, A.; Warren, S. C. Probing the photoelectrochemical properties of hematite (α-Fe$_2$O$_3$) electrodes using hydrogen peroxide as a hole scavenger, *Energy & Environmental Science* **2011,** *4,* 958–964.

[223] Li, J.; Peter, L. Surface recombination at semiconductor electrodes: part III. Steady-state and intensity modulated photocurrent response, *Journal of Electroanalytical Chemistry and Interfacial Electrochemistry* **1985,** *193,* 27–47.

[224] Peter, L. M.; Li, J.; Peat, R.; Lewerenz, H.; Stumper, J. Frequency response analysis of intensity modulated photocurrents at semiconductor electrodes, *Electrochimica Acta* **1990,** *35,* 1657–1664.

[225] Spyropoulos, G. *Linear System Analysis*, 2003 http://www.ee.surrey.ac.uk/Projects/CAL/control/bode.htm.

[226] Scribner Associates Inc, *ZView Version: 3.5a*, 1990–2017.

[227] Barsukov, Y.; Macdonald, J. R. Electrochemical impedance spectroscopy, *Characterization of Materials* **2012,** *2,* 898–913.

[228] Bio-Logic - Science Instruments, *EC-Lab Software V11.18*, 1997–2017.

[229] Randles, J. E. B. Kinetics of rapid electrode reactions, *Discussions of the Faraday society* **1947,** *1,* 11–19.

[230] Bertoluzzi, L. *Surface state assisted charge transfer and recombination processes at the semiconductor/electrolyte interface,* Thesis, Physics Department, Jaume I University, Castellon de la Plana, Spain, 2016.

[231] Müller, K. *On the Structure of Charged Interfaces: A Dissertation in Chemistry;* University of Pennsylvania: 1965.

[232] Gelderman, K.; Lee, L.; Donne, S. Flat-band potential of a semiconductor: using the Mott–Schottky equation, *Journal of Chemical Education* **2007,** *84,* 685.

[233] Bisquert, J. Chemical capacitance of nanostructured semiconductors: its origin and significance for nanocomposite solar cells, *Physical Chemistry Chemical Physics* **2003,** *5,* 5360–5364.

[234] Bisquert, J. Theory of the impedance of charge transfer via surface states in dye-sensitized solar cells, *Journal of Electroanalytical Chemistry* **2010,** *646,* 43–51.

[235] Kaim, W.; Fiedler, J. Spectroelectrochemistry: the best of two worlds, *Chemical Society Reviews* **2009,** *38,* 3373–3382.

[236] Pastor, E.; Le Formal, F.; Mayer, M. T.; Tilley, S. D.; Francàs, L.; Mesa, C. A.; Grätzel, M.; Durrant, J. R. Spectroelectrochemical analysis of the mechanism of (photo) electrochemical hydrogen evolution at a catalytic interface, *Nature Communications* **2017,** *8,* 14280.

[237] Ponomarev, E. A.; Peter, L. M. A generalized theory of intensity modulated photocurrent spectroscopy (IMPS), *Journal of Electroanalytical Chemistry* **1995,** *396,* 219–226.

[238] Pendlebury, S. R.; Wang, X.; Le Formal, F.; Cornuz, M.; Kafizas, A.; Tilley, S. D.; Gratzel, M.; Durrant, J. R. Ultrafast charge carrier recombination and trapping in hematite photoanodes under applied bias, *Journal of the American Chemical Society* **2014,** *136,* 9854–9857.

[239] Huang, Z. *et al.* In situ probe of photocarrier dynamics in water-splitting hematite (α-Fe$_2$O$_3$) electrodes, *Energy & Environmental Science* **2012,** *5,* 8923–8926.

[240] Nelson, J.; Haque, S. A.; Klug, D. R.; Durrant, J. R. Trap-limited recombination in dye-sensitized nanocrystalline metal oxide electrodes, *Physical Review B* **2001,** *63,* 205321.

[241] Nelson, J.; Chandler, R. E. Random walk models of charge transfer and transport in dye sensitized systems, *Coordination Chemistry Reviews* **2004,** *248,* 1181–1194.

[242] Berera, R.; van Grondelle, R.; Kennis, J. T. M. Ultrafast transient absorption spectroscopy: principles and application to photosynthetic systems, *Photosynthesis research* **2009,** *101,* 105–118.

[243] Le Formal, F.; Pastor, E.; Tilley, S. D.; Mesa, C.; Pendlebury, S. R.; Grätzel, M.; Durrant, J. R. Rate Law Analysis of Water Oxidation on a Hematite Surface, *Journal of the American Chemical Society* **2015,** 150502122150001.

[244] Wang, L. *et al.* Rhombohedral Prussian white as cathode for rechargeable sodium-ion batteries, *Journal of the American Chemical Society* **2015,** *137,* 2548–2554.

[245] Kundu, D.; Talaie, E.; Duffort, V.; Nazar, L. F. The emerging chemistry of sodium ion batteries for electrochemical energy storage, *Angewandte Chemie International Edition* **2015,** *54,* 3431–3448.

[246] Kaye, S. S.; Long, J. R. Hydrogen Storage in the Dehydrated Prussian Blue Analogues $M_3[Co(CN)_6]_2$ (M= Mn, Fe, Co, Ni, Cu, Zn), *Journal of the American Chemical Society* **2005,** *127,* 6506–6507.

[247] DeLongchamp, D. M.; Hammond, P. T. Multiple-color electrochromism from layer-by-layer-assembled polyaniline/Prussian blue nanocomposite thin films, *Chemistry of Materials* **2004,** *16,* 4799–4805.

[248] Sato, O.; Iyoda, T.; Fujishima, A.; Hashimoto, K. Photoinduced magnetization of a cobalt-iron cyanide, *Science* **1996,** *272,* 704–705.

[249] Shimamoto, N.; Ohkoshi, S.-i.; Sato, O.; Hashimoto, K. Control of charge-transfer-induced spin transition temperature on cobalt- iron Prussian blue analogues, *Inorganic Chemistry* **2002,** *41,* 678–684.

[250] Sato, O.; Kawakami, T.; Kimura, M.; Hishiya, S.; Kubo, S.; Einaga, Y. Electric-field-induced conductance switching in FeCo Prussian blue analogues, *Journal of the American Chemical Society* **2004,** *126,* 13176–13177.

[251] Ferlay, S.; Mallah, T.; Ouahes, R.; Veillet, P.; Verdaguer, M. A room-temperature organometallic magnet based on Prussian blue, *Nature* **1995,** *378,* 701.

[252] Verdaguer, M. *et al.* Molecules to build solids: high TC molecule-based magnets by design and recent Revival of cyano complexes chemistry, *Coordination Chemistry Reviews* **1999,** *190,* 1023–1047.

[253] Ruiz, E.; Rodríguez-Fortea, A.; Alvarez, S.; Verdaguer, M. Is it possible to get high TC magnets with Prussian blue analogues? A theoretical prospect, *Chemistry–A European Journal* **2005,** *11,* 2135–2144.

[254] Zhang, W.; Hu, S.; Yin, J.-J.; He, W.; Lu, W.; Ma, M.; Gu, N.; Zhang, Y. Prussian blue nanoparticles as multienzyme mimetics and reactive oxygen species scavengers, *Journal of the American Chemical Society* **2016,** *138,* 5860–5865.

[255] Yasutaka, T.; Kawamoto, T.; Kawabe, Y.; Sato, T.; Sato, M.; Suzuki, Y.; Nakamura, K.; Komai, T. Rapid measurement of radiocesium in water using a Prussian blue impregnated nonwoven fabric: Fukushima NPP Accident Related, *Journal of Nuclear Science and Technology* **2013,** *50,* 674–681.

[256] Bartoll, J. The early use of Prussian blue in paintings. In *Proceedings of the 9th International Conference on NDT of Art*; 2008.

[257] Ware, M. Prussian Blue: Artists' Pigment and Chemists' Sponge, *J. Chemical Education* **2008,** *85,* 612.

[258] Keggin, J.; Miles, F. Structures and formulae of the Prussian blues and related compounds, *Nature* **1936,** *137,* 577.

[259] Buser, H.; Ludi, A.; Petter, W.; Schwarzenbach, D. Single-crystal study of Prussian Blue: $Fe_4[Fe(CN)_6]_3 \cdot 14\,H_2O$, *Journal of the Chemical Society, Chemical Communications* **1972,** 1299–1299.

[260] Buser, H.; Schwarzenbach, D.; Petter, W.; Ludi, A. The crystal structure of Prussian blue: $Fe_4[Fe(CN)_6]_3 \cdot xH_2O$, *Inorganic Chemistry* **1977,** *16,* 2704–2710.

[261] Herren, F.; Fischer, P.; Ludi, A.; Hälg, W. Neutron diffraction study of Prussian Blue, $Fe_4[Fe(CN)_6]_3 \cdot xH_2O$. Location of water molecules and long-range magnetic order $Fe_4[Fe(CN)_6]_3 \cdot xH_2O$, *Inorganic Chemistry* **1980,** *19,* 956–959.

[262] Gmelin, L.; zur Förderung der Wissenschaften. Gmelin-Institut für Anorganische Chemie und Grenzgebiete, M.-P.-G.; Gesellschaft, D. C. *Gmelins Handbuch der Anorganischen Chemie;* Springer-Verlag: 1980.

[263] Brunschwig, B. S.; Creutz, C.; Sutin, N. Optical transitions of symmetrical mixed-valence systems in the class II–III transition regime, *Chemical Society Reviews* **2002,** *31,* 168–184.

[264] Robin, M. B. The color and electronic configurations of Prussian blue, *Inorganic Chemistry* **1962,** *1,* 337–342.

[265] Davidson, D.; Welo, L. A. The Nature of Prussian Blue., *The Journal of Physical Chemistry* **1928,** *32,* 1191–1196.

[266] Ito, A.; Suenaga, M.; Ono, K. Mössbauer study of soluble Prussian blue, insoluble Prussian blue, and Turnbull's blue, *The Journal of Chemical Physics* **1968,** *48,* 3597–3599.

[267] Orchard, A. F. *Magnetochemistry;* Oxford Chemistry Primers Oxford University Press: 2003.

[268] Ogden, J. *Introduction to Molecular Symmetry;* Oxford Chemistry Primers Oxford University Press: 2001.

[269] Herren, F.; Ludi, A.; Guedel, H.; Givord, D.; Day, P. Valence delocalization in Prussian blue, $Fe_4III[FeII(CN)_6]_3 \cdot xD_2O$, by polarized neutron diffraction, *Helv. Chim. Acta* **1980,** *63,* 148–153.

[270] Mayoh, B.; Day, P. Charge transfer in mixed valence solids. Part VII. Perturbation calculations of valence delocalization in iron (II, III) cyanides and silicates, *Journal of the Chemical Society, Dalton Transactions* **1974,** 846–852.

[271] Middlemiss, D. S.; Wilson, C. C. Ferromagnetism and spin transitions in prussian blue: A solid-state hybrid functional study, *Physical Review B* **2008,** *77,* 155129.

[272] Hansen, L. D.; Litchman, W. M.; Daub, G. H. Turnbull's blue and Prussian blue: $KFe(III)[Fe(II)(CN)_6]$, *Journal of Chemical Education* **1969,** *46,* 46–46.

[273] Cosgrove, J.; Collins, R.; Murty, D. Preparation of ferrous ferricyanide (not Turnbull's Blue), *Journal of the American Chemical Society* **1973,** *95,* 1083–1086.

[274] Wojdeł, J. C.; de PR Moreira, I.; Bromley, S. T.; Illas, F. On the prediction of the crystal and electronic structure of mixed-valence materials by periodic density functional calculations: The case of Prussian Blue, *The Journal of Chemical Physics* **2008,** *128,* 044713.

[275] Wojdeł, J. C.; Bromley, S. T. Efficient calculation of the structural and electronic properties of mixed valence materials: application to Prussian Blue analogues, *Chemical Physics Letters* **2004,** *397,* 154–159.

[276] Wojdeł, J. C.; Bromley, S. T. Band gap variation in Prussian Blue via cation-induced structural distortion, *The Journal of Physical Chemistry B* **2006,** *110,* 24294–24298.

[277] Wojdeł, J. C.; de PR Moreira, I.; Bromley, S. T.; Illas, F. Prediction of half-metallic conductivity in Prussian Blue derivatives, *Journal of Materials Chemistry* **2009,** *19,* 2032–2036.

[278] Wojdeł, J. C.; Moreira, I. d. P.; Illas, F. Periodic density functional theory study of spin crossover in the cesium iron hexacyanochromate prussian blue analog, *The Journal of Chemical Physics* **2009,** *130,* 014702.

[279] Wojdeł, J. C. First principles calculations on the influence of water-filled cavities on the electronic structure of Prussian Blue, *Journal of Molecular Modeling* **2009,** *15,* 567.

[280] Perdew, J. P.; Burke, K.; Ernzerhof, M. Generalized Gradient Approximation Made Simple [Phys. Rev. Lett. 77, 3865 (1996)], *Physical Review Letters* **1997,** *78,* 1396–1396.

[281] Mattsson, A. E.; Armiento, R.; Paier, J.; Kresse, G.; Wills, J. M.; Mattsson, T. R. The AM05 density functional applied to solids, *The Journal of Chemical Physics* **2008,** *128,* 084714.

[282] Sun, J.; Marsman, M.; Csonka, G. I.; Ruzsinszky, A.; Hao, P.; Kim, Y.-S.; Kresse, G.; Perdew, J. P. Self-consistent meta-generalized gradient approximation within the projector-augmented-wave method, *Physical Review B* **2011,** *84,* 035117.

[283] Bader, R. F. W.; Bader, R. F. *Atoms in Molecules: A Quantum Theory;* International Series of Monographs on Chemistry Clarendon Press: 1990.

[284] Henkelman, G.; Arnaldsson, A.; Jónsson, H. A fast and robust algorithm for Bader decomposition of charge density, *Computational Materials Science* **2006,** *36,* 354–360.

[285] Tang, W.; Sanville, E.; Henkelman, G. A grid-based Bader analysis algorithm without lattice bias, *Journal of Physics: Condensed Matter* **2009,** *21,* 084204.

[286] Lu, D.; Liu, P. Rationalization of the Hubbard U parameter in CeOx from first principles: Unveiling the role of local structure in screening, *The Journal of Chemical Physics* **2014,** *140,* 084101.

[287] Aykol, M.; Wolverton, C. Local environment dependent GGA+ U method for accurate thermochemistry of transition metal compounds, *Physical Review B* **2014,** *90,* 115105.

[288] Nguimdo, G. D.; Joubert, D. P. A density functional (PBE, PBEsol, HSE06) study of the structural, electronic and optical properties of the ternary compounds $AgAlX_2$ (X= S, Se, Te), *The European Physical Journal B* **2015,** *88,* 113.

[289] Becke, A. D. A new mixing of Hartree–Fock and local density-functional theories, *The Journal of Chemical Physics* **1993,** *98,* 1372–1377.

[290] Xidis, A.; Neff, V. D. On the Electronic Conduction in Dry Thin Films of Prussian Blue, Prussian Yellow, and Everitt's Sal, **1991,** *138,* 3637–3641.

[291] Pajerowski, D. M.; Watanabe, T.; Yamamoto, T.; Einaga, Y. Electronic conductivity in Berlin green and Prussian blue, *Physical Review B* **2011,** *83,* 153202.

[292] Hu, M.; Jiang, J. Facile synthesis of air-stable Prussian white microcubes via a hydrothermal method, *Materials Research Bulletin* **2011,** *46,* 702–707.

[293] Kumar, A.; Yusuf, S.; Keller, L. Structural and magnetic properties of Fe[Fe(CN)$_6$]·4H$_2$O, *Physical Review B* **2005,** *71,* 054414.

[294] Maer Jr, K.; Beasley, M.; Collins, R.; Milligan, W. Structure of the titanium-iron cyanide complexes, *Journal of the American Chemical Society* **1968,** *90,* 3201–3208.

[295] Swart, M.; Groenhof, A. R.; Ehlers, A. W.; Lammertsma, K. Validation of exchange- correlation functionals for spin states of iron complexes, *The Journal of Physical Chemistry A* **2004,** *108,* 5479–5483.

[296] Kulesza, P. J.; Galus, Z. Mixed-valence electron hopping, redox conduction and migration effects in solid-state electrochemistry of transition metal hexacyanoferrates, *Journal of Electroanalytical Chemistry* **1992,** *323,* 261–274.

[297] Kulesza, P. J.; Malik, M. A.; Berrettoni, M.; Giorgetti, M.; Zamponi, S.; Schmidt, R.; Marassi, R. Electrochemical charging, countercation accommodation, and spectrochemical identity of microcrystalline solid cobalt hexacyanoferrate, *The Journal of Physical Chemistry B* **1998,** *102,* 1870–1876.

[298] Ling, C.; Chen, J.; Mizuno, F. First-principles study of alkali and alkaline earth ion intercalation in iron hexacyanoferrate: the important role of ionic radius, *The Journal of Physical Chemistry C* **2013,** *117,* 21158–21165.

[299] Rosseinsky, D. R.; Lim, H.; Jiang, H.; Chai, J. W. Optical charge-transfer in iron (III) hexacyanoferrate (II): Electro-intercalated cations induce lattice-energy-dependent ground-state energies, *Inorganic Chemistry* **2003,** *42,* 6015–6023.

[300] Lezna, R. O.; Romagnoli, R.; de Tacconi, N. R.; Rajeshwar, K. Cobalt hexacyanoferrate: compound stoichiometry, infrared spectroelectrochemistry, and photoinduced electron transfer, *The Journal of Physical Chemistry B* **2002,** *106,* 3612–3621.

[301] Martínez-García, R.; Knobel, M.; Balmaseda, J.; Yee-Madeira, H.; Reguera, E. Mixed valence states in cobalt iron cyanide, *Journal of Physics and Chemistry of Solids* **2007,** *68,* 290–298.

[302] Cafun, J.-D.; Lejeune, J.; Baudelet, F.; Dumas, P.; Itié, J.-P.; Bleuzen, A. Room-Temperature Photoinduced Electron Transfer in a Prussian Blue Analogue under Hydrostatic Pressure, *Angewandte Chemie* **2012,** *124,* 9280–9282.

[303] Moritomo, Y.; Nakada, F.; Kamioka, H.; Hozumi, T.; Ohkoshi, S. Role of the intermediate state in the photoinduced process of Co–Fe cyanide, *Physical Review B* **2007,** *75,* 214110.

[304] Aguila, D.; Prado, Y.; Koumousi, E. S.; Mathoniere, C.; Clérac, R. Switchable Fe/Co Prussian blue networks and molecular analogues, *Chemical Society Reviews* **2016,** *45,* 203–224.

[305] Sato, O.; Einaga, Y.; Iyoda, T.; Fujishima, A.; Hashimoto, K. Reversible photoinduced magnetization, *Journal of the Electrochemical Society* **1997,** *144,* L11–L13.

[306] Sato, O.; Einaga, Y.; Fujishima, A.; Hashimoto, K. Photoinduced long-range magnetic ordering of a cobalt- iron cyanide, *Inorganic Chemistry* **1999,** *38,* 4405–4412.

[307] Kamioka, H.; Moritomo, Y.; Kosaka, W.; Ohkoshi, S.-i. Charge transfer processes in cyano-bridged transition metals, *Physica Status Solidi S* **2009,** *6,* 116–119.

[308] Kamioka, H.; Nakada, F.; Igarashi, K.; Moritomo, Y. Transient photo-induced phenomena in vacancy-controlled Co-Fe cyanides. In *Journal of Physics: Conference Series*, Vol. 148; 2009.

[309] Miyashita, S.; Konishi, Y.; Tokoro, H.; Nishino, M.; Boukheddaden, K.; Varret, F. Structures of metastable states in phase transitions with a high-spin low-spin degree of freedom, *Progress of Theoretical Physics* **2005,** *114,* 719–735.

[310] Kabir, M.; van Vliet, K. J. Reversible mechanism for spin crossover in transition-metal cyanides, *Physical Review B* **2012,** *85,* 054431.

[311] Kitagawa, Y.; Asaoka, M.; Miyagi, K.; Matsui, T.; Nihei, M.; Oshio, H.; Okumura, M.; Nakano, M. DFT and TD-DFT studies of electronic structures and one-electron excitation states of a cyanide-bridged molecular square complex, *Inorganic Chemistry Frontiers* **2015,** *2,* 771–779.

[312] Cafun, J.-D.; Champion, G.; Arrio, M.-A.; dit Moulin, C. C.; Bleuzen, A. Photomagnetic CoFe Prussian Blue Analogues: Role of the Cyanide Ions as Active Electron Transfer Bridges Modulated by Cyanide- Alkali Metal Ion Interactions, *Journal of the American Chemical Society* **2010,** *132,* 11552–11559.

[313] Bleuzen, A.; Lomenech, C.; Escax, V.; Villain, F.; Varret, F.; Cartier dit Moulin, C.; Verdaguer, M. Photoinduced ferrimagnetic systems in Prussian blue analogues $C^I_x Co_4[Fe(CN)_6]_y$ (C^I= alkali cation). 1. Conditions to observe the phenomenon, *Journal of the American Chemical Society* **2000,** *122,* 6648–6652.

[314] Escax, V.; Bleuzen, A.; Cartier dit Moulin, C.; Villain, F.; Goujon, A.; Varret, F.; Verdaguer, M. Photoinduced Ferrimagnetic Systems in Prussian Blue Analogues $CIxCo_4[Fe(CN)_6]_y$ (CI= Alkali Cation). 3. Control of the Photo-and Thermally Induced Electron Transfer by the $[Fe(CN)_6]$ Vacancies in Cesium Derivatives, *Journal of the American Chemical Society* **2001,** *123,* 12536–12543.

[315] Kawamoto, T.; Abe, S. Mechanism of Reversible photo-induced magnetization in prussian blue analogues, *Phase Transitions: A Multinational Journal* **2001,** *74,* 209–233.

[316] Eyert, V.; Siberchicot, B.; Verdaguer, M. Magnetic order and chemical bonding in the high-T C molecule-based cyanide magnets $CsM[Cr(CN)_6]$ (M= Mn, Ni) from first principles, *Physical Review B* **1997,** *56,* 8959.

[317] Harrison, N.; Searle, B.; Seddon, E. An ab initio study of the magnetic coupling in bi-metallic CrIII cyanides, *Chemical Physics Letters* **1997,** *266,* 507–511.

[318] Nishino, M.; Kubo, S.; Yoshioka, Y.; Nakamura, A.; Yamaguchi, K. Theoretical studies on magnetic interactions in Prussian blue analogs and active controls of spin states by external fields, *Molecular Crystals and Liquid Crystals Science and Technology. Section A. Molecular Crystals and Liquid Crystals* **1997,** *305,* 109–128.

[319] Nishino, M.; Yoshioka, Y.; Yamaguchi, K. Effective exchange interactions and magnetic phase transition temperatures in Prussian blue analogs: a study by density functional theory, *Chemical Physics Letters* **1998,** *297,* 51–59.

[320] Kawamoto, T.; Asai, Y.; Abe, S. Ab initio calculations on the mechanism of charge transfer in Co-Fe Prussian-blue compounds, *Physical Review B* **1999,** *60,* 12990.

[321] Kawamoto, T.; Asai, Y.; Abe, S. Novel mechanism of photoinduced Reversible phase transitions in molecule-based magnets, *Physical Review Letters* **2001,** *86,* 348.

[322] Kawamoto, T.; Asai, Y.; Abe, S. Theoretical study of the charge transfer absorption in cobalt-iron cyanide, *Molecular Crystals and Liquid Crystals* **2002,** *376,* 423–429.

[323] Krah, T.; Suaud, N.; Zanchet, A.; Robert, V.; Ben Amor, N. Vacancy-Induced Deformation in a CoFe Prussian Blue Analogue–A Theoretical Investigation, *European Journal of Inorganic Chemistry* **2012,** *2012,* 5777–5783.

[324] Hegner, F. S.; Herraiz-Cardona, I.; Cardenas-Morcoso, D.; López, N.; Galán-Mascarós, J.-R.; Gimenez, S. Cobalt Hexacyanoferrate on $BiVO_4$ Photoanodes for Robust Water Splitting, *ACS Applied Materials & Interfaces* **2017,** *9,* 37671–37681.

[325] Yokoyama, T.; Ohta, T.; Sato, O.; Hashimoto, K. Characterization of magnetic CoFe cyanides by x-ray-absorption fine-structure spectroscopy, *Physical Review B* **1998,** *58,* 8257.

[326] Giorgetti, M.; Berrettoni, M. Structure of Fe/Co/Ni hexacyanoferrate as probed by multiple edge X-ray absorption spectroscopy, *Inorganic Chemistry* **2008,** *47,* 6001–6008.

[327] Kennedy, J. H.; Frese, K. W. Photooxidation of water at α-Fe_2O_3 electrodes, *Journal of the Electrochemical Society* **1978,** *125,* 709–714.

[328] Huda, M. N.; Walsh, A.; Yan, Y.; Wei, S.-H.; Al-Jassim, M. M. Electronic, structural, and magnetic effects of 3d transition metals in hematite, *Journal of Applied Physics* **2010,** *107,* 123712.

[329] Dare-Edwards, M. P.; Goodenough, J. B.; Hamnett, A.; Trevellick, P. R. Electrochemistry and Photoelectrochemistry of Iron (III) Oxide, *Journal of the Chemical Society, Faraday Transactions 1: Physical Chemistry in Condensed Phases* **1983,** *79,* 2027–2041.

[330] Pendlebury, S. R.; Barroso, M.; Cowan, A. J.; Sivula, K.; Tang, J.; Grätzel, M.; Klug, D.; Durrant, J. R. Dynamics of photogenerated holes in nanocrystalline α-Fe_2O_3 electrodes for water oxidation probed by transient absorption spectroscopy, *Chemical Communications* **2011,** *47,* 716–718.

[331] Klahr, B.; Gimenez, S.; Fabregat-Santiago, F.; Bisquert, J.; Hamann, T. W. Electrochemical and photoelectrochemical investigation of water oxidation with hematite electrodes, *Energy & Environmental Science* **2012,** *5,* 7626–7636.

[332] Iandolo, B.; Hellman, A. The role of surface states in the oxygen evolution reaction on hematite, *Angewandte Chemie International Edition* **2014,** *53,* 13404–13408.

[333] Yatom, N.; Elbaz, Y.; Navon, S.; Toroker, M. C. Identifying the bottleneck of water oxidation by ab initio analysis of in situ optical absorbance spectrum, *Physical Chemistry Chemistry Physics* **2017,** *19,* 17278–17286.

[334] Wijayantha, K. U.; Saremi-Yarahmadi, S.; Peter, L. M. Kinetics of oxygen evolution at α-Fe_2O_3 photoanodes: a study by photoelectrochemical impedance spectroscopy, *Physical Chemistry Chemical Physics* **2011,** *13,* 5264–5270.

[335] Bosman, A. J.; van Daal, H. J. Small-polaron versus band conduction in some transition-metal oxides, *Advances in Physics* **1970,** *19,* 1–117.

[336] Ahmed, S.; Leduc, J.; Haller, S. Photoelectrochemical and impedance characteristics of specular hematite. 1. Photoelectrochemical parallel conductance, and trap rate studies, *The Journal of Physical Chemistry* **1988,** *92,* 6655–6660.

[337] Liao, P.; Toroker, M. C.; Carter, E. A. Electron transport in pure and doped hematite, *Nano Letters* **2011,** *11,* 1775–1781.

[338] Katz, J. E.; Zhang, X.; Attenkofer, K.; Chapman, K. W.; Frandsen, C.; Zarzycki, P.; Rosso, K. M.; Falcone, R. W.; Waychunas, G. A.; Gilbert, B. Electron Small Polarons and their Mobility in Iron(Oxyhydr)oxide Nanoparticles, *Science* **2012,** *337,* 1200–1203.

[339] Carneiro, L. M.; Cushing, S. K.; Liu, C.; Su, Y.; Yang, P.; Alivisatos, A. P.; Leone, S. R. Excitation-wavelength-dependent small polaron trapping of photoexcited carriers in α-Fe$_2$O$_3$, *Nature Materials* **2017,** *16,* 819.

[340] Coey, J. M. D.; Sawatzky, G. A. A study of hyperfine interactions in the system (Fe$_{1-x}$Rh$_x$)$_2$O$_3$ using the Mössbauer effect (Bonding parameters), *Journal of Physics C: Solid State Physics* **1971,** *4,* 2386.

[341] Catti, M.; Valerio, G.; Dovesi, R. Theoretical study of electronic, magnetic, and structural properties of α-Fe$_2$O$_3$ (hematite), *Physical Review B* **1995,** *51,* 7441.

[342] Fujimori, A.; Saeki, M.; Kimizuka, N.; Taniguchi, M.; Suga, S. Photoemission satellites and electronic structure of Fe$_2$O$_3$, *Physical Review B* **1986,** *34,* 7318.

[343] Dräger, G.; Czolbe, W.; Leiro, J. High-energy-spectroscopy studies of a charge-transfer insulator: X-ray spectra of α-Fe$_2$O$_3$, *Physical Review B* **1992,** *45,* 8283.

[344] Lad, R. J.; Henrich, V. E. Photoemission study of the valence-band electronic structure in Fe$_x$O, Fe$_3$O$_4$, and α-Fe$_2$O$_3$ single crystals, *Physical Review B* **1989,** *39,* 13478.

[345] Ma, Y.; Johnson, P.; Wassdahl, N.; Guo, J.; Skytt, P.; Nordgren, J.; Kevan, S.; Rubensson, J.-E.; Böske, T.; Eberhardt, W. Electronic structures of α-Fe$_2$O$_3$ and Fe$_3$O$_4$ from O K-edge absorption and emission spectroscopy, *Physical Review B* **1993,** *48,* 2109.

[346] Sharp, I. D.; Cooper, J. K.; Toma, F. M.; Buonsanti, R. Bismuth Vanadate as a Platform for Accelerating Discovery and Development of Complex Transition-Metal Oxide Photoanodes, *ACS Energy Letters* **2017,** *2,* 139–150.

[347] Tan, H. L.; Amal, R.; Ng, Y. H. Alternative strategies in improving the photocatalytic and photoelectrochemical activities of visible light-driven BiVO$_4$: a Review, *J. Materials Chemistry A* **2017,** *5,* 16498–16521.

[348] Tolod, K.; Hernández, S.; Russo, N. Recent Advances in the BiVO$_4$ Photocatalyst for Sun-Driven Water Oxidation: Top-Performing Photoanodes and Scale-Up Challenges, *Catalysts* **2017,** *7,* 13.

[349] Lamm, B.; Trzesiewski, B. J.; Dö, H.; Smith, W. A.; Stefik, M. Emerging Postsynthetic Improvements of BiVO$_4$ Photoanodes for Solar Water Splitting, *ACS Energy Letters.* **2018,** *3,* 112–124.

[350] Li, G.-L. First-principles investigation of the surface properties of fergusonite-type monoclinic BiVO$_4$ photocatalyst, *RSC Advances* **2017,** *7,* 9130–9140.

[351] Zhao, Z.; Li, Z.; Zou, Z. Electronic structure and optical properties of monoclinic clinobisvanite BiVO$_4$, *Physical Chemistry Chemistry Physics* **2011,** *13,* 4746.

[352] Walsh, A.; Yan, Y.; Huda, M. N.; Al-Jassim, M. M.; Wei, S.-H. Band edge electronic structure of $BiVO_4$: elucidating the role of the Bi s and V d orbitals, *Chemistry of Materials* **2009,** *21,* 547–551.

[353] Sleight, A. W.; Chen, H.-Y.; Ferretti, A.; Cox, D. E. Crystal growth and structure of $BiVO_4$, *Materials Research Bulletin* **1979,** *14,* 1571–1581.

[354] Liu, J. C.; Chen, J.-P.; Li, D.-Y. Crystal Structure and Optical Observations of $BiVO_4$, *Acta Physica Sinica* **1983,** *32,* 1053-1060.

[355] Pauling, L.; Hendricks, S. B. The crystal structures of hematite and corundum, *Journal of the American Chemical Society* **1925,** *47,* 781–790.

[356] Hegner, F. S.; Cardenas-Morcoso, D.; Giménez, S.; López, N.; Galan-Mascaros, J.-R. Level Alignment as Descriptor for Semiconductor/Catalyst Systems in Water Splitting: The Case of Hematite/Cobalt Hexacyanoferrate Photoanodes, *ChemSusChem* **2017,** *10,* 4552–4560.

[357] Thorne, J. E.; Jang, J.-W.; Liu, E. Y.; Wang, D. Understanding the origin of photoelectrode performance enhancement by probing surface kinetics, *Chemical Science* **2016,** *7,* 3347–3354.

[358] Ma, Y.; Kafizas, A.; Pendlebury, S. R.; Le Formal, F.; Durrant, J. R. Photoinduced absorption spectroscopy of CoPi on $BiVO_4$: the function of CoPi during water oxidation, *Advanced Functional Materials* **2016,** *26,* 4951–4960.

[359] Shaddad, M. N.; Ghanem, M. A.; Al-Mayouf, A. M.; Gimenez, S.; Bisquert, J.; Herraiz-Cardona, I. Cooperative Catalytic Effect of ZrO_2 and α-Fe_2O_3 Nanoparticles on $BiVO_4$ Photoanodes for Enhanced Photoelectrochemical Water Splitting, *ChemSusChem* **2016,** *9,* 2779–2783.

[360] Zandi, O.; Schon, A. R.; Hajibabaei, H.; Hamann, T. W. Enhanced Charge Separation and Collection in High-Performance Electrodeposited Hematite Films, *Chemistry of Materials* **2016,** *28,* 765–771.

[361] Annamalai, A.; Subramanian, A.; Kang, U.; Park, H.; Choi, S. H.; Jang, J. S. Activation of hematite photoanodes for solar water splitting: effect of FTO deformation, *The Journal of Physical Chemistry C* **2015,** *119,* 3810–3817.

[362] Kang, D.; Park, Y.; Hill, J. C.; Choi, K.-S. Preparation of Bi-based ternary oxide photoanodes $BiVO_4$, Bi_2WO_6, and $Bi_2Mo_3O_{12}$ using dendritic Bi metal electrodes, *The Journal of Physical Chemistry Letters* **2014,** *5,* 2994–2999.

[363] Abdi, F. F.; Savenije, T. J.; May, M. M.; Dam, B.; van de Krol, R. The Origin of Slow Carrier Transport in $BiVO_4$ Thin Film Photoanodes: A Time-Resolved Microwave Conductivity Study, *Journal of Physical Chemistry Letters* **2013,** *4,* 2752–2757.

[364] Rettie, A. J. E.; Lee, H. C.; Marshall, L. G.; Lin, J.-F.; Capan, C.; Lindemuth, J.; Mccloy, J. S.; Zhou, J.; Bard, A. J.; Mullins, C. B. Combined Charge Carrier Transport and Photoelectrochemical Characterization of $BiVO_4$ Single Crystals: Intrinsic Behavior of a Complex Metal Oxide, *Journal of the American Chemical Society* **2013,** *135,* 11389–11396.

[365] Szaciłowski, K.; Macyk, W.; Stochel, G. Synthesis, structure and photoelectrochemical properties of the TiO_2–Prussian blue nanocomposite, *Journal of Materials Chemistry* **2006,** *16,* 4603–4611.

[366] Rossell, M. D.; Agrawal, P.; Borgschulte, A.; Hèbert, C.; Passerone, D.; Erni, R. Direct evidence of surface reduction in monoclinic $BiVO_4$, *Chemistry of Materials* **2015,** *27,* 3593–3600.

[367] Bhattacharya, A. K.; Forster, S. F.; Pyke, D. R.; Mallick, K. K.; Reynolds, R. Surface segregation and phase separation in bismuth–tin pyrochlores, *Journal of Materials Chemistry* **1997,** *7,* 837–841.

[368] Galván, D. H.; Castillón, F. F.; Gómez, L. A.; Avalos-Borja, M.; Cota, L.; Fuentes, S.; Bartolo-Pérez, P.; Maple, M. B. Influence of preparation on the structure and co conversion of γ-Bi$_2$MoO$_6$ catalysts, *Reaction Kinetics and Catalysis Letters* **1999,** *67,* 205–211.

[369] Ihlefeld, J. F. *et al.* Optical band gap of BiFeO$_3$ grown by molecular-beam epitaxy, *Applied Physics Letters* **2008,** *92,* 142908.

[370] Zhao, Z.; Li, Z.; Zou, Z. Structure and energetics of low-index stoichiometric monoclinic clinobisvanite BiVO$_4$ surfaces, *RSC Advances* **2011,** *1,* 874.

[371] Hu, J.; Chen, W.; Zhao, X.; Su, H.; Chen, Z. Anisotropic Electronic Characteristics, Adsorption, and Stability of Low-Index BiVO$_4$ Surfaces for Photoelectrochemical Applications, *ACS Applied Materials & Interfaces* **2018,** *10,* 5475–5484.

[372] Stoerzinger, K. A.; Hong, W. T.; Azimi, G.; Giordano, L.; Lee, Y.-L.; Crumlin, E. J.; Biegalski, M. D.; Bluhm, H.; Varanasi, K. K.; Shao-Horn, Y. Reactivity of perovskites with water: role of hydroxylation in wetting and implications for oxygen electrocatalysis, *The Journal of Physical Chemistry C* **2015,** *119,* 18504–18512.

[373] Han, B.; Stoerzinger, K. A.; Tileli, V.; Gamalski, A. D.; Stach, E. A.; Shao-Horn, Y. Nanoscale structural oscillations in perovskite oxides induced by oxygen evolution, *Nature Materials* **2017,** *16,* 121.

[374] Crist, B. *Handbook of Monochromatic XPS Spectra;* Handbook of Monochromatic XPS Spectra Wiley: 2000.

[375] Chuang, T. J.; Brundle, C. R.; Rice, D. W. Interpretation of the X-Ray Photoemission Spectra of Cobalt Oxides and Cobalt Oxide Surfaces, *Surface Science* **1976,** *59,* 413–429.

[376] Thermo Fisher Scientific Inc., *XPS Simplified*, 2013–2018 https://xpssimplified.com/knowledgebase.php.

[377] Kim, J. K.; Cho, Y.; Jeong, M. J.; Levy-Wendt, B.; Shin, D.; Yi, Y.; Wang, D. H.; Zheng, X.; Park, J. H. Rapid Formation of a Disordered Layer on Monoclinic BiVO$_4$: Co-Catalyst-Free Photoelectrochemical Solar Water Splitting, *ChemSusChem* **2018,** *11,* 933–940.

[378] Toma, F. M. *et al.* Mechanistic insights into chemical and photochemical transformations of bismuth vanadate photoanodes, *Nature Communications* **2016,** *7,* 12012.

[379] Cooper, J. K.; Gul, S.; Toma, F. M.; Chen, L.; Glans, P.-A.; Guo, J.; Ager, J. W.; Yano, J.; Sharp, I. D. Electronic structure of monoclinic BiVO$_4$, *Chemistry of Materials* **2014,** *26,* 5365–5373.

[380] Peter, L.; Li, J.; Peat, R. Surface recombination at semiconductor electrodes: Part I. Transient and steady-state photocurrents, *Journal of Electroanalytical Chemistry and Interfacial Electrochemistry* **1984,** *165,* 29–40.

[381] Trotochaud, L.; Young, S. L.; Ranney, J. K.; Boettcher, S. W. Nickel–iron oxyhydroxide oxygen-evolution electrocatalysts: the role of intentional and incidental iron incorporation, *Journal of the American Chemical Society* **2014,** *136,* 6744–6753.

[382] Seabold, J. A.; Choi, K.-S. Efficient and stable photo-oxidation of water by a bismuth vanadate photoanode coupled with an iron oxyhydroxide oxygen evolution catalyst, *Journal of the American Chemical Society* **2012,** *134,* 2186–2192.

[383] Du, C.; Yang, X.; Mayer, M. T.; Hoyt, H.; Xie, J.; McMahon, G.; Bischoping, G.; Wang, D. Hematite-based water splitting with low turn-on voltages, *Angewandte Chemie* **2013,** *125,* 12924–12927.

[384] Trześniewski, B. J.; Smith, W. A. Photocharged $BiVO_4$ photoanodes for improved solar water splitting, *Journal of Materials Chemistry A* **2016,** *4,* 2919–2926.

[385] Klahr, B. M.; Hamann, T. W. Current and voltage limiting processes in thin film hematite electrodes, *The Journal of Physical Chemistry C* **2011,** *115,* 8393–8399.

[386] Kalamaras, E.; Lianos, P. Current doubling effect revisited: current multiplication in a PhotoFuelCell, *Journal of Electroanalytical Chemistry* **2015,** *751,* 37–42.

[387] Trześniewski, B. J.; Digdaya, I. A.; Nagaki, T.; Ravishankar, S.; Herraiz-Cardona, I.; Vermaas, D. A.; Longo, A.; Gimenez, S.; Smith, W. A. Near-complete suppression of surface losses and total internal quantum efficiency in $BiVO_4$ photoanodes, *Energy & Environmental Science* **2017,** *10,* 1517–1529.

[388] Liang, Y.; Tsubota, T.; Mooij, L. P. A.; Vvan de Krol, R. Highly improved quantum efficiencies for thin film $BiVO_4$ photoanodes, *The Journal of Physical Chemistry C* **2011,** *115,* 17594–17598.

[389] Steier, L.; Herraiz-Cardona, I.; Gimenez, S.; Fabregat-Santiago, F.; Bisquert, J.; Tilley, S. D.; Grätzel, M. Understanding the role of underlayers and overlayers in thin film hematite photoanodes, *Advanced Functional Materials* **2014,** *24,* 7681–7688.

[390] Le Formal, F.; Tétreault, N.; Cornuz, M.; Moehl, T.; Grätzel, M.; Sivula, K. Passivating surface states on water splitting hematite photoanodes with alumina overlayers, *Chemical Science* **2011,** *2,* 737–743.

[391] Zandi, O.; Hamann, T. W. Determination of photoelectrochemical water oxidation intermediates on haematite electrode surfaces using operando infrared spectroscopy, *Nature Chemistry* **2016,** *8,* 778.

[392] Scanlon, D. O. *et al.* Band alignment of rutile and anatase TiO_2, *Nature Materials* **2013,** *12,* 798.

[393] Tersoff, J. Theory of semiconductor heterojunctions: The role of quantum dipoles, *Physical Review B* **1984,** *30,* 4874.

[394] Pham, T. A.; Lee, D.; Schwegler, E.; Galli, G. Interfacial effects on the band edges of functionalized Si surfaces in liquid water, *Journal of the American Chemical Society* **2014,** *136,* 17071–17077.

[395] Cheng, J.; Vande Vondele, J.; Sprik, M. Identifying trapped electronic holes at the aqueous TiO_2 interface, *The Journal of Physical Chemistry C* **2014,** *118,* 5437–5444.

[396] Toroker, M. C.; Kanan, D. K.; Alidoust, N.; Isseroff, L. Y.; Liao, P.; Carter, E. A. First principles scheme to evaluate band edge positions in potential transition metal oxide photocatalysts and photoelectrodes, *Physical Chemistry Chemical Physics* **2011,** *13,* 16644–16654.

[397] Jiang, H. Electronic band structures of molybdenum and tungsten dichalcogenides by the GW approach, *The Journal of Physical Chemistry C* **2012,** *116,* 7664–7671.

[398] Stevanović, V.; Lany, S.; Ginley, D. S.; Tumas, W.; Zunger, A. Assessing capability of semiconductors to split water using ionization potentials and electron affinities only, *Physical Chemistry Chemical Physics* **2014,** *16,* 3706–3714.

[399] Wei, S.-H.; Zhang, S. B.; Zunger, A. First-principles calculation of band offsets, optical bowings, and defects in CdS, CdSe, CdTe, and their alloys, *Journal of Applied Physics* **2000,** *87,* 1304–1311.

[400] Li, Y.-H.; Walsh, A.; Chen, S.; Yin, W.-J.; Yang, J.-H.; Li, J.; Da Silva, J. L. F.; Gong, X. G.; Wei, S.-H. Revised ab initio natural band offsets of all group IV, II-VI, and III-V semiconductors, *Applied Physics Letters* **2009,** *94,* 212109.

[401] Höffling, B.; Schleife, A.; Rödl, C.; Bechstedt, F. Band discontinuities at Si-TCO interfaces from quasiparticle calculations: Comparison of two alignment approaches, *Physical Review B* **2012,** *85,* 035305.

[402] Ambrosio, F.; Miceli, G.; Pasquarello, A. Redox levels in aqueous solution: Effect of van der Waals interactions and hybrid functionals, *The Journal of Chemical Physics* **2015,** *143,* 244508.

[403] Aharon, E.; Toroker, M. C. The Effect of Covering Fe_2O_3 with a Ga_2O_3 Overlayer on Water Oxidation Catalysis, *Catalysis Letters* **2017,** *147,* 2077–2082.

[404] Neufeld, O.; Yatom, N.; Toroker, M. C. A First-Principles Study on the Role of an Al_2O_3 Overlayer on Fe_2O_3 for Water Splitting, *ACS Catalysis* **2015,** *5,* 7237–7243.

[405] Cowan, A. J.; Barnett, C. J.; Pendlebury, S. R.; Barroso, M.; Sivula, K.; Gratzel, M.; Durrant, J. R.; Klug, D. R. Activation energies for the rate-limiting step in water photooxidation by nanostructured α-Fe_2O_3 and TiO_2, *Journal of the American Chemical Society* **2011,** *133,* 10134–10140.

[406] Pendlebury, S. R.; Cowan, A. J.; Barroso, M.; Sivula, K.; Ye, J.; Grätzel, M.; Klug, D. R.; Tang, J.; Durrant, J. R. Correlating long-lived photogenerated hole populations with photocurrent densities in hematite water oxidation photoanodes, *Energy & Environmental Science* **2012,** *5,* 6304–6312.

[407] Ma, Y.; Mesa, C. A.; Pastor, E.; Kafizas, A.; Francàs, L.; Le Formal, F.; Pendlebury, S. R.; Durrant, J. R. Rate law analysis of water oxidation and hole scavenging on a $BiVO_4$ photoanode, *ACS Energy Letters* **2016,** *1,* 618–623.

[408] Kulesza, P. J.; Zamponi, S.; Malik, M. A.; Berrettoni, M.; Wolkiewicz, A.; Marassi, R. Spectroelectrochemical characterization of cobalt hexacyanoferrate films in potassium salt electrolyte, *Electrochimica Acta* **1998,** *43,* 919–923.

[409] Aiga, N.; Jia, Q.; Watanabe, K.; Kudo, A.; Sugimoto, T.; Matsumoto, Y. Electron–Phonon Coupling Dynamics at Oxygen Evolution Sites of Visible-Light-Driven Photocatalyst: Bismuth Vanadate, *The Journal of Physical Chemistry C* **2013,** *117,* 9881–9886.

[410] Moss, B.; Hegner, F. S.; Corby, S.; Selim, S.; Francàs, L.; López, N.; Giménez, S.; Galán-Mascarós, J.-R.; Durrant, J. R. *Unraveling Charge-Transfer in CoFe-PB Modified $BiVO_4$ Photoanodes.*, **2018**, Submitted.

[411] NIH, *Image J Version: 1.50*, 1997–2018, free software: https://www.imagej.nih.gov/ij.

[412] Savitzky, A.; Golay, M. J. E. Smoothing and differentiation of data by simplified least squares procedures., *Analytical Chemistry* **1964,** *36,* 1627–1639.

[413] Garcia-Ratés, M.; López, N. Multigrid-based methodology for implicit solvation models in periodic DFT, *Journal of Chemical Theory and Computation* **2016,** *12,* 1331–1341.

[414] Garcia-Ratés, M.; García-Muelas, R.; López, N. Solvation Effects on Methanol Decomposition on Pd (111), Pt (111), and Ru (0001), *The Journal of Physical Chemistry C* **2017,** *121,* 13803–13809.

Included Papers

Inorganic Chemistry

A Database of the Structural and Electronic Properties of Prussian Blue, Prussian White, and Berlin Green Compounds through Density Functional Theory

Franziska Simone Hegner,[†] José Ramón Galán-Mascarós,[†,‡] and Núria López[*,†]

[†]Institute of Chemical Research of Catalonia ICIQ, The Barcelona Institute of Science and Technology, Av. Països Catalans 16, 43007 Tarragona, Spain

[‡]Catalan Institution for Research and Advanced Studies ICREA, Passeig Lluís Companys, 08010 Barcelona, Spain

Ⓢ Supporting Information

ABSTRACT: Prussian blue and its related compounds are formed by cheap and abundant metals and have shown their importance in the generation of new fuels by renewable sources. To optimize these compounds it is important to understand their electronic structure and thus establish robust structure−activity relationships. To this end, we employed theoretical simulations based on density functional theory, employing functionals of different degree of complexity, including pure generalized gradient approximation (GGA) and GGA+U functionals, which introduce self-interaction correction terms through the Hubbard parameter, and compared those to the hybrid functionals HSE03 and HSE06. With this robust setup, we can identify an appropriate computational scheme that provides the best compromise between computational demand and accuracy. A complete database considering Berlin green and Prussian blue and white for all alkaline cations is presented.
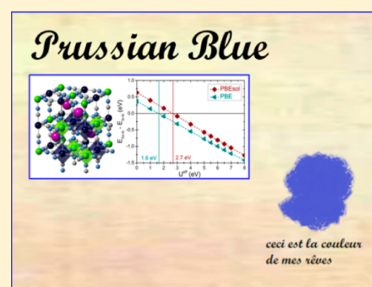
1. INTRODUCTION

Prussian blue-type compounds are a fascinating class of materials with high potential in the new energies field. These metal-hexacyanometallates have the generic formula $A_xM^a_y[M^b(CN)_6]_z$, with $M^{a,b}$ being cheap and abundant transition metals and A the countercation, typically an alkaline metal. In the lattice, the two transition-metal centers have different coordination spheres, and, as a consequence they can adapt several oxidation states and magnetic configurations. This opens up a vast variety of applications, such as electrochromism,[1] energy storage,[2,3] water-splitting catalysis,[4,5] analytical sensors,[6] radio waste detection,[7] multienzyme mimetics,[8] magnetic switches,[9,10] and room-temperature magnets.[11] The drawback of this physical and chemical versatility is that its electronic structure modeling is challenging and, thus, limiting the understanding of these materials and the establishment of structure−activity relationships. Without a proper description of their electronic structure it is impossible to rationally design the new generation of Prussian-blue (PB) derivatives with tailored properties.

The parent compound is PB $(Fe_4[Fe(CN)_6]_3 \cdot xH_2O$ ($x = 14-16$)), sometimes also called Prussian blue. The real crystal structure, which was determined by X-ray[12,13] and neutron[14] diffraction studies, is shown in Figure 1a. It consists of two octahedrally coordinated iron centers, namely, ferric Fe(III) and ferrous Fe(II), being linked by cyanide bridges with lattice constants varying from 10.13 to 10.18 Å.[12−14] Assuming classical oxidation states, the N-coordinated Fe has a charge of +3, whereas the C-coordinated iron has a charge of +2.[15−18]

In the following discussion they will therefore be denoted as Fe(III)-N and Fe(II)-C, respectively. The fact of comprising two weakly interacting metal centers of the same kind (Fe in this case) with different electronic structures classifies PB as a class(II) mixed-valence compound.[19]

Because of the strong ligand field of the cyanide C, Fe(II)-C always adopts a diamagnetic low-spin (ls) d^6 configuration with $S = 0$. Fe(III)-N is found in a paramagnetic high-spin (hs) d^5 state ($S = 5/2$) in the weaker field of the N-ligand[14,18,20,21] (see Figure 1). The Fe(III)-N moments order and align ferromagnetically below $T_c = 5.6$ K.[14,18,22] The observed ferromagnetic interaction can arise through electron delocalization via the ligand π-orbital[23] or via a direct through-space coupling of the diagonal paramagnetic Fe(III)-N centers.[24] Upon electromagnetic irradiation or changes in pressure or temperature, the iron centers might undergo transitions between their hs and ls states. This is why PB is also regarded as a spin-crossover (SCO) compound. The strong charge-transfer (CT) absorption between ls d^6 t_{2g} Fe(II)-C and hs d^5 t_{2g} Fe(III)-N at ~ 1.75 eV[25] causes the intense blue color of the compound, from which PB got its name.

In this computational study we assume an ideal stoichiometric model structure $KFe[Fe(CN)_6]$, which is shown in Figure 1b, as its main properties are expected to be similar to the real structure. As seen in Figure 1, the N-coordinated Fe(III) centers occupy the
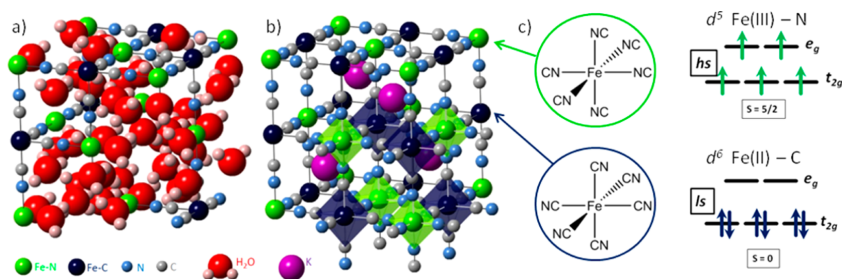
Figure 1. PB: (a) as-prepared nonstoichiometric PB ($Fe_4[Fe(CN)_6]_3 \cdot xH_2O$ ($x = 14-16$)), (b) crystalline model structure ($KFe[Fe(CN)_6]$), and (c) octahedral coordinated Fe-centers and their spin configurations. Here we used the conventional orbital notations "e_g" and "t_{2g}" for molecular octahedral point groups (local coordination), which must be regarded with caution, as a different symmetry may be superimposed by the crystalline lattice.
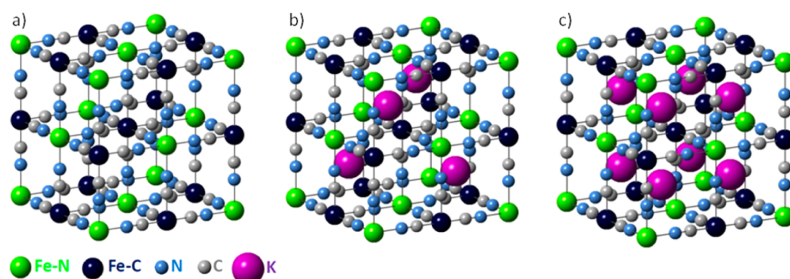
Figure 2. a Berlin Green, BG ($Fe[Fe(CN)_6]$), a Prussian Blue, PB ($KFe[Fe(CN)_6]$), and a Prussian White, PW ($K_2Fe[Fe(CN)_6]$).

corners of a face-centered cubic (*fcc*) lattice of the crystal group $F\overline{4}3m$, whereas Fe(II)-C is placed at the middle of the edges.[13,14] Alkali-metal cations, in this case potassium K^+, occupy half of the tetrahedral holes of the lattice for compensating the charge of the negatively charged cyanide complexes. In the older literature, $KFe[Fe(CN)_6]$ is often referred to as "soluble" PB, whereas $Fe_4[Fe(CN)_6]_3 \cdot xH_2O$ is named "insoluble" PB.[18,26] To our knowledge, pure $KFe[Fe(CN)_6]$ has never been synthesized. The ideal mixed-valence iron(III)–iron(II) PB has been subject of computational studies for the last two decades.[21,24,27–32] Wojdel et al. did pioneering work applying density functional theory (DFT) to PB-type compounds[21,27–30,33] and successfully reproduced experimental data while applying mixed ultrasoft pseudopotentials (USPPs)[28] and, in more recent studies, GGA+U with different Hubbard U correction terms on both iron centers.[27] To investigate magnetic interactions in PB, Middlemiss and Wilson applied hybrid functionals with different amounts of Hartree–Fock type of exchange and reported a more accurate representation of intervalence charge transfer.[24]

PB related compounds include oxidized Berlin green (BG; $Fe(III)[Fe(III)(CN)_6]$) and reduced Prussian white (PW; $K_2Fe(II)[Fe(II)(CN)_6]$) and are shown in Figure 2. BG, which is sometimes also called Prussian yellow, has both iron centers in a +3 oxidation state.[34,35] The negative charge of the cyanide ligands is balanced by the highly oxidized iron centers and, therefore, no counter cations need to be introduced in the lattice (Figure 2a). PW, or Everitt's salt, is the fully reduced counterpart with both iron centers in a +2 oxidation state and with all of its tetrahedral holes occupied by alkali cations (Figure 2b).[36] As it is the case for the parent PB $KFe(III)[Fe(II)CN_6]$, the

C-coordinated Fe center is expected to remain in a ls configuration independent of its oxidation state, which is due to the strong CN ligand field. In the intermediate field of the N-coordinating cyanide, Fe–N may change its spin configuration.[30,37] In contrast to insulating PB, both redox forms show electronic conduction.[30,35,38]

In the present work, we revise the case of PB by applying different density functional methods and testing their influence on important structural and electronic parameters. Furthermore, we applied the determined most appropriate methods to describe the fully oxidized form BG and the reduced form PW. The effect of cation insertion, when going from BG to PB and from PB to PW, as well as the influence of different counter cations, on the electronic and geometric structures were investigated and discussed.

2. COMPUTATIONAL METHODS

DFT calculations were performed using the Vienna Ab Initio Package.[39,40] To benchmark the performance of pure DFT functionals, we employed the generalized gradient approximations (GGAs) Perdew–Burke–Ernzerhof (PBE),[41,42] Perdew–Burke–Ernzerhof revised for solids (PBEsol),[43] revised Perdew–Burke–Ernzerhof (revPBE or RP),[44] Perdew–Wang 91 (PW91)[45,46] and Armiento and Mattsson 2005 (AM05).[47] Pure DFT has been shown to be insufficient in describing the correct magnetic and electronic structure of the mixed valence compound (see Supporting Information Table S1). One solution to this problem is to introduce additional on-site interaction energies on the d-metal centers, the Coulomb interaction U, and the electronic exchange J.[48] Dudarev's approach of GGA+U,[48,49] adding an effective U parameter $U^{eff} = |U − J|$ to the GGA functionals PBE and PBEsol, and examining the dependence of main parameters on the U^{eff} value, was applied in our case. In addition, hybrid functionals, which
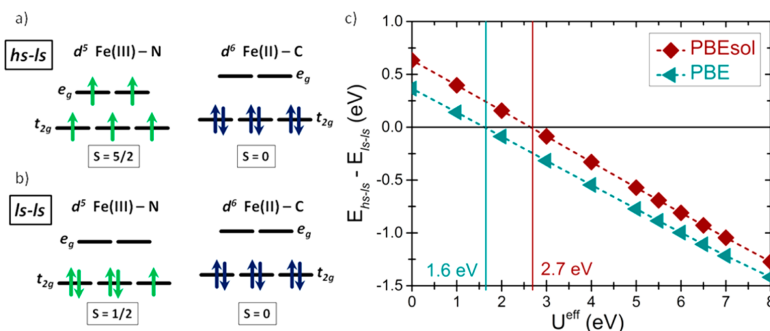
Figure 3. Energy dependence of the (a) hs-ls (hs Fe(III)-N—ls Fe(II)-C) and (b) ls-ls (ls Fe(III)-N—ls Fe(II)-C) configurations on the effective U parameter $U^{\text{eff}} = |U - J|$. (c) The energy difference $E_{\text{hs-ls}} - E_{\text{ls-ls}}$ is a measure if and how much the hs-ls ground state is stabilized over the diamagnetic ls-ls state with varying U^{eff}.
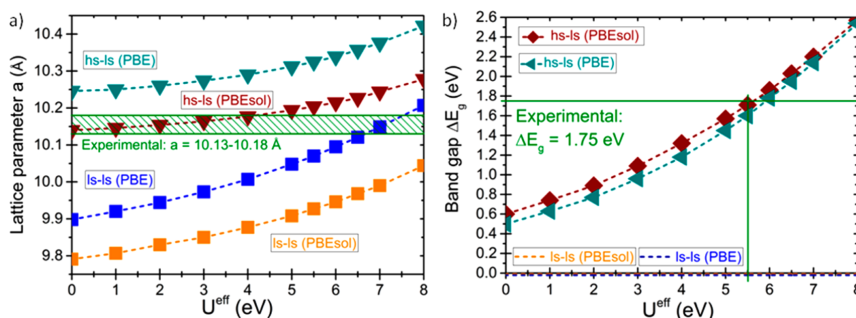
Figure 4. Variation of the effective U parameter $U^{\text{eff}} = |U - J|$ and its influence on (a) the lattice parameter and (b) the band gap.

include a defined amount of exact exchange from Hartree−Fock theory,[50] were applied. The HSE functionals (HSE03 and HSE06), which were developed especially for solids, compromise computational efficiency and accuracy.[51,52] Both HSE03 and HSE06 were used as a benchmark.[51−53] For the hybrid, as well as for PBEsol+U, functionals the geometric and electronic structures of all the systems with $K_n\text{Fe}[\text{Fe}(\text{CN})_6]$ stoichiometry representing the PB ($n = 1$), BG ($n = 0$), and PW ($n = 2$), were investigated.

All calculations assume model anhydrous structures with a face-centered $F\bar{4}3m$ unit cell, as shown in Figures 1b and 2 and with zero (BG), four (PB), or eight (PW) counter cations placed in the tetrahedral positions of the lattice. Inner electrons were replaced by plane wave projector augmented wave (PAW) method. To ensure accuracy, we applied small PAW pseudopotentials, expanding valence and valence-subshell s- and p-electrons, for all metals in the lattice.[54,55] Spin-polarized GGA and GGA+U calculations were performed using a high precision and cutoff energy (700 eV). The Brillouin zone was sampled using a Monkhorst−Pack k-point mesh[56] with $5 \times 5 \times 5$ k-points for lattice optimizations and $9 \times 9 \times 9$ k-points for static density of states (DOS) calculations, respectively. High precision static calculations were performed with a cutoff energy of 600 eV. γ-Centered hybrid calculations were performed with a cutoff energy of 500 eV, while inheriting the charge density from previous PBEsol or PBEsol+U calculations.

3. RESULTS AND DISCUSSION

3.1. Electronic Structure of the Parent Compound Prussian Blue.
3.1.1. DFT + U. The structure of KFe[Fe-(CN)$_6$] was calculated using different regular DFT functionals, which converged to an overall low-spin (ls-ls) ground state with

both Fe centers in an ls configuration, as shown in Figure 3b (Supporting Information Table S1). Also meta-GGAs, such as TPSS, stabilize the ls-ls state over the hs-ls state. (Table S1) Experimental data, however, supports a hs-ls configuration (Figures 1c and 3c), where the N-coordinated Fe centers adopt a hs d^5 state, since the crystal field of the cyanide N-site is relatively weak.[14,18,20,21] The convergence to an incorrect magnetic ground state is due to the lack of DFT describing electronic and magnetic interactions on transition-metal centers.[50] We performed a systematic scan of effective U^{eff} parameters ranging from 0.0 to 8.0 eV, applying both DFT functionals PBE and PBEsol (Supporting Information Tables S2 and S3). The U^{eff} dependence of the energies of the low-lying hs-ls and ls-ls magnetic configurations is shown in Figure 3c.

It can be seen in Figure 3 that an effective parameter $U^{\text{eff}} \geq 1.6$ eV for PBE, and $U^{\text{eff}} \geq 2.7$ eV for PBEsol, respectively, is necessary to stabilize the hs-ls state over the ls-ls state. This shows clearly the importance of electronic correlation on the magnetic configuration. It is noted that other spin combinations, such as an overall high-spin hs-hs state and mixed configurations, were excluded, as they are very high in energy (Supporting Information Table S4). The same is true for the anti-ferromagnetic alignment of the magnetic moments on separate sites, which is disfavored by spin-delocalization and, possibly, direct coupling as well.[23,24]

Complementary, Figure 4 shows the dependence of the band gap and the lattice parameter with varying U^{eff} for both DFT functionals PBE and PBEsol. The lattice constant for the hs-ls

Table 1. Structural and Electronic Parameters of the Ideal KFe(III)[Fe(II) (CN)$_6$] in a High-Spin−Low-Spin Magnetic Configuration Calculated for the Different Functionals PBE, PBEsol, PBE+U, PBEsol+U (with U^{eff} = 5.5 eV), HSE03, and HSE06^a

functional	PBE	PBEsol	PBE+U	PBEsol+U	HSE03	HSE06	expt
a, Å	10.246	10.141	10.325	10.204	10.184	10.175	10.166[13]
d(Fe−N), Å	2.070	2.043	2.076	2.050	2.053	2.051	2.03[13]
d(Fe−C), Å	1.875	1.851	1.911	1.877	1.873	1.872	1.92[13]
d(C−N), Å	1.177	1.177	1.176	1.175	1.165	1.165	1.13[13]
$E_{hs-ls} - E_{ls-ls}$,eV	+0.37	+0.63	−0.88	−5.53	−0.69	−0.31	
ΔE_g, eV	0.50	0.60	1.59	1.73	1.94	2.31	1.75[25]
$CFSE_{Fe(III)-N}$, eV	1.50	1.67	1.13	1.39	1.69	1.73	
$q_{Fe(III)-N}$, |e$^-$|	1.61	+1.74	+1.73	+1.87	+1.86	+1.87	
$q_{Fe(II)-C}$, |e$^-$|	+0.97	+0.55	+1.01	+1.08	+0.76	+0.76	
q_N, |e$^-$|	−1.25	−1.42	−1.31	−1.36	−1.37	−1.38	
q_C, |e$^-$|	+0.67	+0.88	+0.70	+0.72	+0.78	+0.79	
q_K, |e$^-$|	+0.93	+0.93	+0.93	+0.93	+0.94	+0.94	
$\mu_{Fe(III)-N}$, μ_B	3.86	3.84	4.24	4.22	4.15	4.16	5.98[14]
$\mu_{Fe(II)-C}$, μ_B	0.35	0.31	0.16	0.17	0.27	0.26	
μ_N, μ_B	0.06−0.07	0.06−0.07	0.05	0.05	0.05	0.05	
μ_C, μ_B	0.02	0.02	0.02	0.02	0.01	0.01	
μ_K, μ_B	0.00	0.00	0.00	0.00	0.00	0.00	

^{a}The energy difference $E_{hs-ls} - E_{ls-ls}$ is a measure if and how much the hs-ls ground state is stabilized over the diamagnetic ls-ls state. The band gap ΔE_g results from the charge transfer from Fe(II)-C t$_{2g}$ to Fe(III)-N t$_{2g}$. The crystal field splitting energy (CFSE$_{Fe(III)-N}$) is the energy difference of Fe(III)-N t$_{2g}$ and e$_g$.

state is much larger than for the ls-ls state, which was expected, since e$_g$-antibonding orbitals are populated, giving rise to a larger Fe(III)-N distance (Figure 4a). The ls-ls configuration always remains conducting, independent of applied U^{eff} (Figure 4b). For hs-ls PB, the bandgaps increase with the chosen value of U^{eff}. As stronger the effective on-site Coulomb interaction, as narrower get the d-bands and as larger gets the bandgap. At values of U^{eff} = 6.0 eV (PBE) and U^{eff} = 5.5 eV (PBEsol), the band gaps are closest to the experimental band gap ΔE_g = 1.75 eV[25] (Figure 4b and Supporting Information Tables S2 and S3). This finding is in relatively good agreement with the value U^{eff} = 5.3 eV, found by calculating redox energies for Fe(II) and Fe(III).[57] Especially for optoelectronics applications, a correct prediction of the band gap is crucial. Thus, it was the main criterion to choose the optimal U^{eff} parameter, which will be set to 5.5 eV throughout further discussion.

3.1.2. Functional Comparison. A comparison of the functionals PBEsol, PBEsol+U, HSE06 is shown in Table 1. We also investigated other hybrid functionals, such as, for example, B3LYP[58] and B3LYP*,[59] which generally yielded similar results. However, we chose to use HSE-type functionals, as they are optimized especially for periodic solids (see Supporting Information Table S5).

All obtained lattice parameters lie in a range of ∼1% and are in relatively good agreement with the literature values, which vary between 10.13 and 10.17 Å.[13,14] However, the experimental values correspond to the non-stoichiometric lattice Fe$_4$[Fe(CN)$_6$]$_3$·xH$_2$O. The lattice constants increase slightly with increasing U^{eff}, which can also be seen in Figure 4a. Because of the higher charge localization on the transition-metal centers, less charge density can be found in the interstitial bonding regions, leading to an increase in the metal−ligand distances and, hence, the overall lattice parameter. Compared to the hybrid functionals and literature values, PBEsol (+U) seems to perform slightly better than PBE (+U).
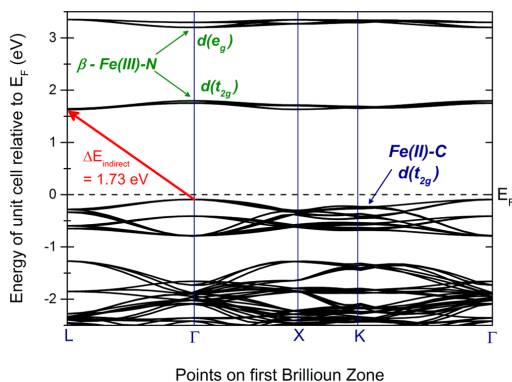
As for the Bader charges,[60−62] presented in Table 1 the Fe charges lie well below their classical, ionic limits of +3 |e$^-$|

($q_{Fe(III)-N}$) and +2 |e$^-$| ($q_{Fe(II)-C}$), due to metal−ligand bonding. This effect of charge delocalization is also reflected in a significant amount of positive charge (+0.7−0.9 |e$^-$|) on the carbon ions, while the ligand's negative charge density is borne by the nitrogen atom. Applying the U^{eff} parameter leads to a small increase of localized charges on both Fe centers and, hence, an increase in ionic character. Similar arguments apply for the magnetic moments, which are delocalized through orbital overlap with the ligand, mainly the N atom, by the so-called spin-delocalization mechanism.[23] With PBE and PBEsol alone the magnetic moment on Fe(III)-N is significantly smaller ($\mu \approx$ 3.8−3.9 μ_B) than its theoretical value of 5.92 μ_B for the isolated hs Fe(III) atom, while it is slightly larger on Fe(II)-C ($\mu \approx$ 0.3 μ_B) than for isolated ls Fe(II) (μ_B = 0). As U^{eff} increases electron correlation and, therefore, localizes electrons on the Fe centers, the magnetic moment on Fe(III)-N increases, while it decreases on Fe(II)-C with U^{eff}. This effect is slightly less pronounced in HSE03 and HSE06, which may indicate a slight overlocalization of charges with PBEsol+U.

The band gap is given as the energy difference between valence Fe(II)-C t$_{2g}$ and conduction Fe(III)-N t$_{2g}$ band (with equal spin). A calculation of the band structure (with PBEsol + U) shows that the gap corresponds to an indirect L ← Γ transition of 1.73 eV, as it is shown in Figure 5. This is in good agreement with previous theoretical studies of Wojdel et al.[28] The direct band gaps located at Γ, K, L, and X are 1.85, 1.87, 1.91, 1.92 eV, respectively, and, hence, lie very close in energy. This is why many experimental studies declare the highly absorbing PB as direct band gap semiconductor.

Pure GGA (PBE and PBEsol) lacks in describing the electronic structure around the Fermi level, which leads to a large underestimation of the band gap (ΔE_g = 0.50 and 0.60 eV). By applying an effective potential U^{eff} on the metal centers, the band gap increases, as it was already seen in Figure 4b. The more electron correlation energy is added to the transition-metal centers, the more the valence and conduction bands shift apart. Both hybrids HSE03 and HSE03 overestimate the band
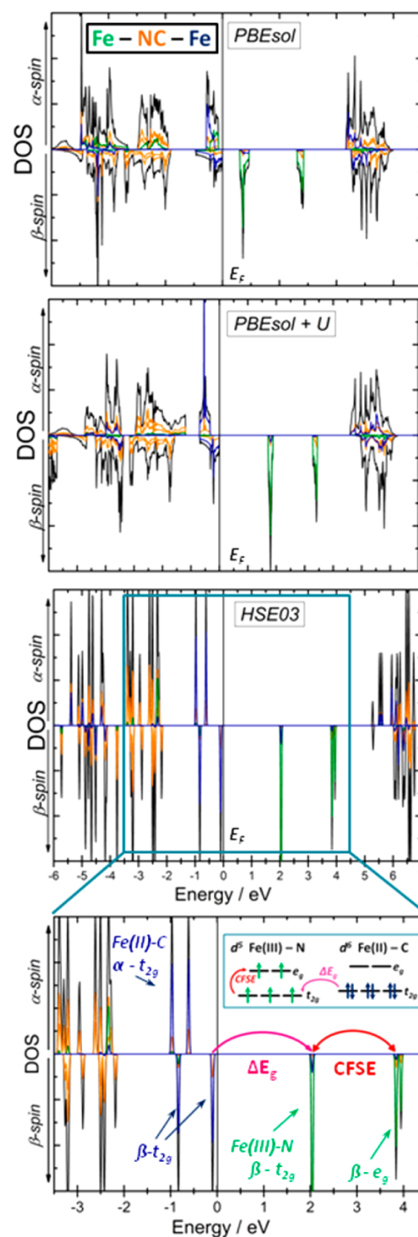
Figure 5. Band structure of hs-ls PB calculated with PBEsol + U (U = 5.5 eV).

Figure 6. Projected DOS for all atoms in the hs-ls PB lattice for the different functionals PBEsol, PBEsol+U, and HSE03.

gap, since they are overcorrecting the self-interaction error being inherent to DFT. The value 1.94 eV, obtained with HSE03, is in closer agreement to the literature value of 1.75 eV.[25] The difference between the two, otherwise similar, hybrids is due to the screening parameter μ, which defines the distance $2/\mu$ at which the short-range exact exchange becomes negligible and which strongly influences the band gap. As it was predicted by Krukau et al.,[53] HSE03 with μ = 0.3 Å^{-1}, yields a band gap closer to experiment. The crystal field splitting energy (CFSE) measures the shifts of bands one metal center. Both GGAs (PBE, PBEsol) and hybrids (HSE03, HSE06) give relatively similar crystal field splittings (1.5–1.7 eV) on the Fe(III)-N center. With the additional U correction, however, the CFSE$_{Fe(III)-N}$ decreases significantly, as U^{eff} squeezes bands on metal center together, thus leading to unphysical terms.

The electronic structures obtained for each functional are visualized as projected DOS in Figure 6. The K atoms do not participate in the DOS, as they are completely ionized, and they are not shown. PBE (+U) and HSE06 yield DOS very similar to PBEsol (+U) and HSE03, respectively, and are omitted for simplicity.

As it was seen in the variance of charges and magnetic moments, Figure 6 demonstrates that, going from pure GGA (PBEsol) to GGA+U (PBEsol+U) to hybrid (HSE03) functionals, the degree of ionic character increases. DFT alone delocalizes the charge density in the system, resulting in broad, overlapping bands that indicate a large degree of covalency. When going from PBEsol to PBEsol+U this covalency is largely decreased and, even more, in the hybrid calculations, leading to sharper bands. It must be remarked that the notation e$_g$ and t$_{2g}$ is used as a matter of convenience, as it conventionally describes octahedrally coordinated transition-metal complexes. However, the d$_{xy}$, d$_{xz}$, and d$_{yz}$ orbitals, which define the t$_{2g}$ set, are no longer degenerate due to the descent in symmetry caused by the insertion of counter cations in the lattice. The same applies for the e$_g$ set consisting of d$_{z^2}$ and d$_{x^2-y^2}$. This becomes most obvious in the highly accurate DOS plots of HSE03, where we can see a large splitting of the t$_{2g}$ sets of Fe(II)-C, as well as of the Fe(III)-N β e$_g$ set. This symmetry distortion can only be seen in the electronic structure, while the overall symmetry of the crystalline lattice remains tetrahedral. The charge-transfer state is indicated by the ls t$_{2g}$ set of the Fe(III)-N iron center,

which shows some density of the symmetry equivalent t$_{2g}$ set of Fe(II)-C, and vice versa. Moreover, the e$_g$ sets on both metal centers share some electron density, being due to a delocalization of charges via the cyanide bridge, in particular, by the nitrogen p-orbital.[22] A significant participation of nitrogen in the charge-transfer state can be seen in the DOS as well.
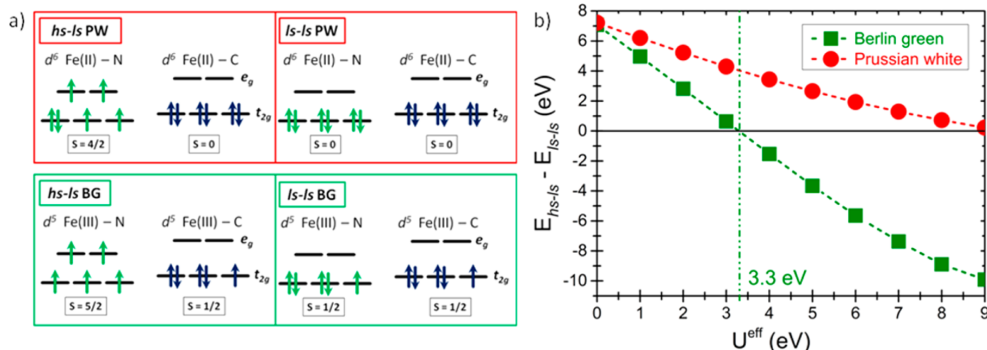
Figure 7. (a) Configurations (hs-ls and ls-ls) of BG and PW and (b) their energy dependence on the effective U parameter U^{eff}.

Table 2. Structural and Electronic Parameters of Berlin Green Fe(III)[Fe(III) (CN)$_6$] and Prussian White K$_2$Fe(II)[Fe(II) (CN)$_6$], Obtained with PBEsol+U (U^{eff} = 5.5 eV) and HSE03[a]

functional	PBEsol + U			HSE03			experimental	
compound	BG	hs-ls PW	ls-ls PW	BG	hs-ls PW	ls-ls PW	BG[34]	PW[36]
a, Å	10.217	10.289	9.978	10.237	10.363	9.982	10.218	10.104−10.114[36]
d(Fe−N), Å	2.049	2.086	1.926	2.055	2.083	1.936	2.003	
d(Fe−C), Å	1.890	1.880	1.887	1.906	1.865	1.890	1.921	
d(C−N), Å	1.170	1.179	1.175	1.158	1.179	1.165	1.162	
$E_{hs-ls} - E_{ls-ls}$, eV	−0.59	+ 0.26		−0.91	−0.10			
ΔE_g, eV	cond.	cond.	3.67	1.59	2.62	4.78	cond[35,38]	cond[38]
CFSE$_{Fe(III)-N}$, eV	1.32			0.95				
q_{Fe-N}, |e$^-$|	+1.87	+1.47	+1.25	+1.79	+1.49	+1.28		
q_{Fe-C}, |e$^-$|	+0.77	+0.88	+ 0.77	+1.19−1.20	+0.82	+0.78		
q_N, |e$^-$|	−1.22	−1.32	−1.38	−1.31−1.34	−1.51	−1.43		
q_C, |e$^-$|	+0.78	+ 0.62	+ 0.74	+0.82- 0.83	+0.82	+0.78		
q_K, |e$^-$|		+ 0.93	+0.92		+0.94	+0.92		
$\mu_{Fe(III)-N}$, μ_B	4.21	+ 3.80	0.00	4.19	3.56	0.00	5.02	
$\mu_{Fe(II)-C}$, μ_B	1.27−1.28	−0.05	0.00	1.10−1.11	0.06	0.00	0.8	
μ_N, μ_B	0.06−0.07	0.03	0.00	0.05- 0.09	0.02	0.00		
μ_C, μ_B	−0.01	0.00	0.00	−0.02- 0.01	0.01	0.00		
μ_K, μ_B		0.00	0.00		0.00	0.00		

[a]$E_{hs-ls} - E_{ls-ls}$ is a measure if and how much the hs-ls ground state is stabilized over the diamagnetic ls-ls state. The band gap ΔE_g corresponds to Fe−C t$_{2g}$ − Fe−N t$_{2g}$. CFSE$_{Fe(III)-N}$ is the energy difference of Fe(III)-N t$_{2g}$ and e$_g$ in BG.

Both the Fe(II)-C t$_{2g}$ and Fe(III)-N t$_{2g}$ peaks contain a considerable amount of nitrogen p-density.

In summary, although hybrid functionals provide a more consistent approach than GGA+U, they are often disfavored due to their huge computational cost. Furthermore, they may overcorrect the DFT-inherent self-interaction error. In the further discussion we will compare the applicability of HSE03 and compare it to GGA+U. For the DFT assessment of PB-type structures, we choose the PBEsol functional with an effective U correction of 5.5 eV, as it gives good results for the band gaps and the lattice constant.

3.2. Different Redox Forms: Prussian White and Berlin Green. The PB analogues BG and PW also have two low-lying magnetic configurations hs-ls and ls-ls, which are shown in Figure 7a. We calculated both spin states with varying U^{eff} and compared their energy differences $E_{hs-ls} - E_{ls-ls}$ in Figure 7b.

A summary of results for the most likely spin configurations of all three redox forms BG, PB, and PW for HSE03, as well as PBEsol+U (U^{eff} = 5.5 eV), is shown in Table 2. For a U^{eff} > 3.3 eV BG is stabilized in a hs-ls configuration, which is also

found in experimental studies[34,37] and hybrid calculations (Table 2). When oxidizing PB to BG, an electron is removed from the C-coordinated iron center (ls Fe(II)-C), leaving a hole in one of the electron t$_{2g}$ orbitals and remaining in a ls state due to the strong ligand field exerted by the cyanide C. The hs Fe(III)-N center is hardly influenced upon reduction from PB to BG. This is also seen in the invariance of the Fe−N bond length d(Fe−N) (Table 2). Hence, hs-ls BG is the correct magnetic ground state. On the contrary, hs-ls PW is never stabilized by PBEsol, with U^{eff} varying from 0 to 9 eV. Although higher U^{eff} parameters might yield to a stabilization of the hs-ls configuration, they are unphysical and are therefore avoided. Experimental results, however, show magnetic behavior[36,37] and conduction,[38] which are both absent in diamagnetic (S = 0) and insulating ls-ls PW. With HSE03, a slight stabilization of 0.10 eV of hs-ls PW is found. With DFT and hybrid calculations leading to contradictory results, the true electronic ground state of PW cannot be clearly determined. It is expected that both hs-ls and ls-ls configurations lie close in energy and that the hs-ls state prevails at room temperature due to entropic
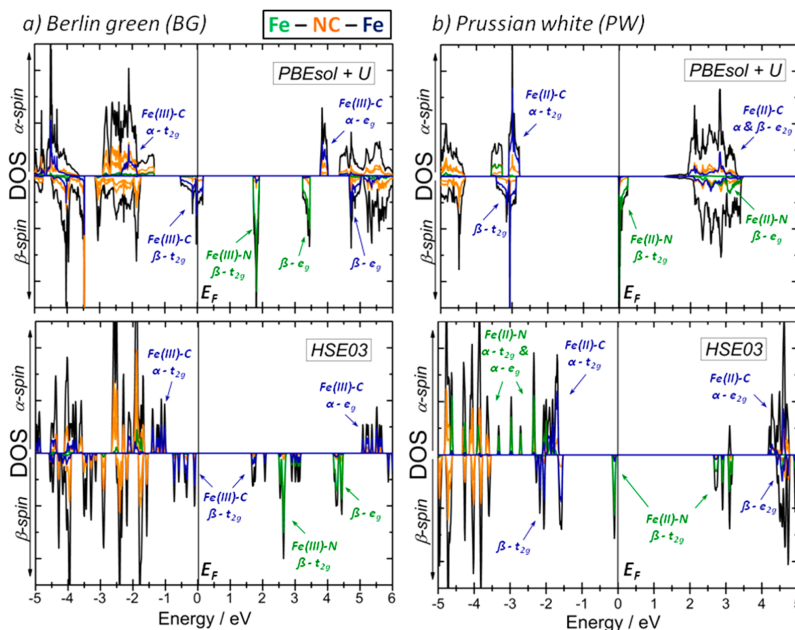
Figure 8. Projected DOS for all atoms in (a) hs-ls BG and (b) hs-ls PW calculated with PBEsol+U and HSE03.

stabilization, as it is predicted by Kepp et al.[63] To facilitate comparison with hs-ls PB, and because it is in accordance with experimental results, we will assume a hs-ls configuration in the following discussion.

The structural parameters of both BG and PW (hs-ls) are similar to those of PB. Oxidation (reduction) from PB to BG (PW), removes (adds) an electron from (to) the effectively nonbonding t_{2g} orbital of Fe(II)-C (Fe(III)-N), thus not altering the bond length. Upon reduction to PW the lattice expands by ~1%. Small structural changes may be due to the insertion or removal of the cation, which will be discussed later in the text. The charges and, more significantly, the magnetizations on the Fe centers reflect two distinct reduction steps, from BG to PB and from PB to PW (Tables 1 and 2). When BG $(Fe(III)[Fe(III)\ (CN)_6])$ is reduced to PB $(KFe(III)[Fe(II)\ (CN)_6])$, an electron is added to Fe(III)-C, filling the t_{2g} shell; hence, the positive charges and magnetic moments on Fe–C decrease. When PB $(KFe(III)[Fe(II)\ (CN)_6])$ is reduced to PW $(K_2Fe(II)[Fe(II)\ (CN)_6])$, an electron is added to Fe(III)-N, and the positive charges and magnetic moments on Fe–N decrease. Nevertheless, the charges obtained with PBEsol+U may not show this behavior being due to the U correction localizing too much charge on Fe–C. For PW no CFSE is given, since the extra electron lifts the degeneracy of the Fe(II)-N t_{2g} d-orbital, and therefore no clear gap between t_{2g} and e_g can be distinguished.

Figure 8 shows the DOS calculated with PBEsol+U and HSE03 for both compounds BG and PW (hs-ls). Also here a descent in symmetry is visible, with both t_{2g} and e_g sets being no longer degenerate and split in multiple bands. When PB is oxidized to BG, one electron is removed from the Fe–C t_{2g} set; hence, the Fe(III)-C t_{2g} band is shifted to higher energy, which can be seen in Figure 8a. For PBEsol+U this Fe(III)-C β-t_{2g}

band overlaps with the Fermi level and, thus, results in a half-metallic state.[30] HSE03, on the contrary, indicates insulating behavior with a band gap of 1.59 eV. This comes from the fact that the Fe(III)-C β-t_{2g} level is split into narrow distinct bands, with the unoccupied β-t_{2g} spin orbital lying well above the Fermi level and the two occupied β-t_{2g} spin orbitals just below (Figure 8b). Recent experimental studies on the conductivity of BG show an inverse resistance dependence on the temperature as opposed to metallic behavior.[35] Therefore, the PBEsol+U prediction of BG being a half-metal is insufficient. However, the large band gap of 1.59 eV predicted by HSE03 excludes thermally activated conduction. A different conduction mechanism might take place, such as, for example, an electron-hopping mechanism, which was proposed by Pajerowski et al.[35] The splitting of occupied and unoccupied β-t_{2g} spin orbitals, as shown by HSE03, is believed to be qualitatively correct but exaggerated. The high amount of Hartree−Fock exchange in the hybrid functional probably leads to an overestimation of the spin-pairing energy for this system. A similar effect is seen in the electronic structure of PB (Figure 8c,d). Upon reduction of PB (hs-ls) to PW (hs-ls) an extra electron with opposite spin is incorporated in the t_{2g} set of Fe−N, shifting the β-t_{2g} band toward lower energy. In the case of PBEsol+U the Fe(II)-N β-t_{2g} band overlaps with the Fermi level, while it is split into occupied and unoccupied β-t_{2g} spin orbitals with the hybrid calculation, giving rise to a large band gap of 2.62 eV. Again, HSE03 exaggerates the spin-pairing energy, therefore giving unphysical wide band gaps, which are opposed to the experimentally observed conduction.[38]

In both cases, neither HSE hybrid functionals nor GGA+U give a complete description of the accurate electronic structure. Although PBEsol + U^{eff} with U^{eff} = 5.5 eV provides a good description of the magneto-electronics of PB, it is not adequate for its redox forms, in which the electronic environment is changed.[64]

Inorganic Chemistry — Article

Table 3. Main s Parameters of the PB-like $AFe[Fe(CN)_6]$ Intercalation Compounds Obtained with PBEsol+U (U^{eff} = 5.5 eV) and HSE03[a]

A-PB	PBEsol + U								HSE03							
	Li	f-Li	Na	f-Na	K	Rb	Cs	Fr	Li	f-Li	Na	f-Na	K	Rb	Cs	Fr
a, Å	10.196	$a=b=10.168$ $c=10.180^b$	10.194	$a=b=10.251$ $c=10.174^b$	10.204	10.205	10.219	10.227	10.153	$a=b=10.142$ $c=10.135^b$	10.004	$a=b=10.068$ $c=9.981^b$	10.184	10.191	10.211	10.223
ΔE_g eV	1.71	1.49	1.72	1.59	1.71	1.71	1.68	1.68	2.04	1.89	2.20	2.09	1.94	1.94	1.90	1.90
ΔE^z_{face} eV	1.03	1.87	0.43	2.74					1.02		0.38					
q_{Fe-N} $[e^-]$	+1.86	+1.83	+1.84	+1.87	+1.86	+1.86	+1.86	+1.41	+1.91	+1.88	+1.88	+1.92	+1.86	+1.91	+1.92	+1.91
q_{Fe-C} $[e^-]$	+1.07	+0.95	+1.05	+1.07	+1.08	+1.08	+1.08	+0.61	+1.12	+0.99	+1.08	+1.08	+0.76	+1.13	+1.14	+1.14
q_Δ $|e^-|$	+0.98	+0.92	+0.96	+0.89	+0.93	+0.91	+0.90	+0.92	+0.99	+0.92	+0.97	+0.89	+0.94	+0.92	+0.92	+0.93
μ_{Fe-N} μ_B	4.22	4.21	4.22	4.22	4.22	4.22	4.22	4.22	4.15	4.15	4.13	4.13	4.15	4.15	4.15	4.15
μ_{Fe-C} μ_B	0.17	0.17	0.17	0.17	0.17	0.17	0.17	0.17	0.27	0.27	0.27	0.27	0.27	0.27	0.27	0.27

[a]The different counter cations occupy tetrahedral half of the tetrahedral holes of the lattice. For A = Li, Na the parameters are given also for all A in the face position of the lattice, which is stabilized to its tetrahedral counterpart by ΔE_{face}. The band gap ΔE_g results from the charge transfer from Fe(II)-C t_{2g} to Fe(III)-N t_{2g}. [b]Two different lattice parameters and specific bonding lengths are found for face intercalation compounds due to a descent from cubic to tetragonal crystal symmetry.

Table 4. Main Parameters of PW-like $A_2Fe[Fe(CN)_6]$ Intercalation Compounds Obtained with PBEsol+U (with U^{eff} = 5.5 eV) and HSE03[a]

A_2-PW	PBEsol + U								HSE03							
	Li	f-Li	Na	f-Na	K	Rb	Cs	Fr	Li	f-Li	Na	f-Na	K	Rb	Cs	Fr
a, Å	10.256	$a=b=10.329$ $c=10.245^b$	10.259	$a=b=10.412$ $c=10.343^b$	10.289	10.294	10.316	10.334	10.246	$a=b=10.269$ $c=10.006^b$	9.982	$a=b=10.102$ $c=10.004^b$	10.363	10.372	10.412	10.433
ΔE_g eV	cond.	2.48	cond.	2.74	cond.	cond.	cond.	cond.	2.53	2.75	2.3–2.5	2.61	2.62	2.67	2.60	2.70
ΔE^z_{face} eV	1.03	1.87							2.32		1.06					
q_{Fe-N} $[e^-]$	+1.47	+1.50	+1.40	+1.45	+1.47	+1.47	+1.48	+1.48	+1.46	+1.54	+1.31	+1.57	+1.49	+1.49	+1.50	+1.50
q_{Fe-C} $[e^-]$	+0.88	+0.85	+0.88	+1.02	+0.88	+0.88	+0.88	+0.88	+0.84	+0.88	+0.64	+1.02	+0.82	+0.83	+0.82	+0.82
q_Δ $|e^-|$	+0.98	+0.92	+0.95	+0.90	+0.93	+0.91	+0.90	+0.88	+0.98	+0.92	+0.94	+0.90	+0.94	+0.93	+0.91	+0.91
μ_{Fe-N} μ_B	3.80	3.59	3.80	3.62	3.80	3.80–3.81	3.80–3.81	3.80–3.81	3.54	3.54	3.52	3.54	3.56	3.56	3.56	3.56
μ_{Fe-C} μ_B	−0.05	0.03	−0.05	0.26	−0.05	−0.05	−0.05	−0.05	0.07	0.07	0.08	0.07	0.06	0.05–0.07	0.04–0.07	0.04–0.07

[a]The different counter cations occupy all the tetrahedral holes of the lattice. For A = Li, Na the parameters are given also for all A in the face position of the lattice, which gives a favored structure stabilized by ΔE_{face} with respect to occupying tetrahedral holes. The band gap ΔE_g results from the charge transfer from Fe(II)-C t_{2g} to Fe(III)-N t_{2g}. [b]Two different lattice parameters and specific bonding lengths are found for face intercalation compounds due to a descent from cubic to monoclinic (tetragonal for face-Na-PW) crystal symmetry.
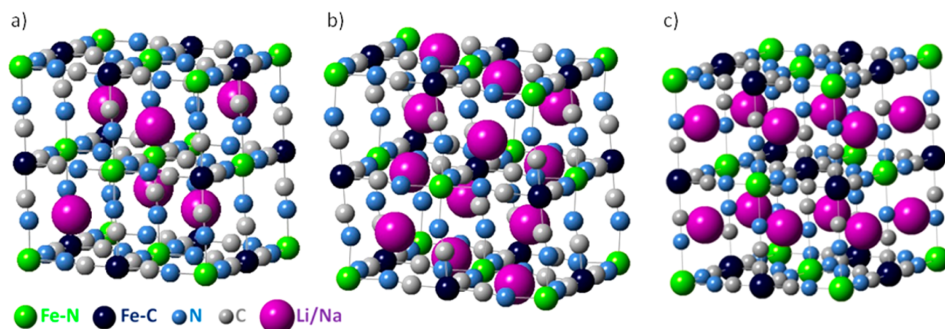
Figure 9. Intercalation compounds with small cations Li and Na: Crystal structures of the (a) *face* Li-PB and *face* Na-PB, (b) *face* Li-PW, and (c) *face* Na-PW.

It is seen that, while GGA overestimates electron delocalization and leads to large broadening of bands, HSE over corrects the self-interaction error and thus exaggerates the band splitting.

3.3. Database of Prussian White-Related Compounds with Different Alkali Atoms. To set up a complete database, as well as to test the influence of different cations on different parameters, we incorporated all alkali cations (Li, Na, K, Rb, Cs, Fr) in PB-like $(AFe(III)[Fe(II)(CN)_6])$ (Figure 2b) and PW-like $(A_2Fe(II)[Fe(II)(CN)_6])$ (Figure 2c) structures and calculated their structural and electronic properties with both PBEsol+U (U^{eff} = 5.5 eV) and HSE03 functionals (Tables 3 and 4).

For the smaller alkali metal cations, Li^+ and Na^+, it was found that the face positions in the lattice, instead of the tetrahedral holes, are preferred (Figure 9). The resulting, more stable intercalation compounds are labeled *f*-Li-PB, *f*-Li-PW and *f*-Na-PB, *f*-Na-PW, respectively, and are listed in Tables 3 and 4 as well. The larger alkali cations (K, Rb, Cs, Fr) do occupy the tetrahedral holes in the ground state. For potassium, for instance, K-PB is stabilized by 0.26 eV (PBEsol+U) with respect to *f*-K-PB. In the case of *f*-Li-PW, the structure was found to be more stable (ΔE = 1.03 eV with PBEsol+U), if all the cations lie in diagonal {222} planes (Figure 9b), instead of in parallel {100} and {200} lattice planes (Figure 9c), while the opposite is true for *face* Na-PW (ΔE = 0.02 eV with PBEsol+U). It is remarked that other positions, different than lattice faces or tetrahedral holes, may also be envisaged for Li^+ and Na^+, as did Ling et al.,[32] but this lies beyond the scope of this article.

Li and Na ionic radii are sufficiently small to occupy the square-planar holes that are spanned by four Fe-centers. Optimization of *f*-PB and *f*-PW structures leads to a distortion of cubic symmetry; hence, two different lattice parameters and bond lengths can be found. This is due to the negatively charged N-site of the cyanide ligand bending toward the positively charged countercation and thus leading to a stabilization of the distorted structure. In contrast, larger metals produce tetrahedral intercalation compounds. Along the series, the lattice expands as the alkali cation size increases (Figure 10). The Fe−N and Fe−C bonds lengthen, while the C−N distance stays the same (Supporting Information Tables S6−S9). The effect of the lattice expansion, which is of the order of 1%, has a higher impact on PW-like than PB-like structures, since all the tetrahedral holes are occupied (Figure 2). For the HSE03 calculations, this effect is more pronounced. Sodium intercalated compounds Na-PB and Na-PW seem to be exceptions, since its
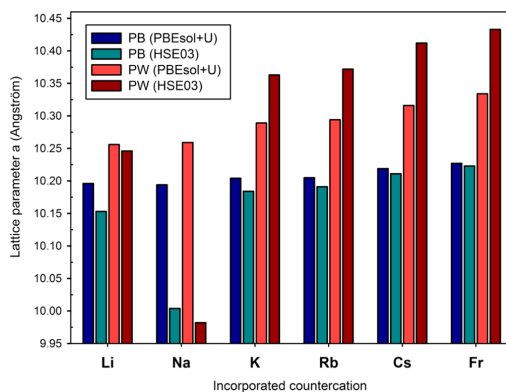
Figure 10. Variation of lattice parameter for different countercations (incorporated in the tetrahedral holes) of the PB and PW lattice for PBEsol + U and HSE03 functionals.

lattice parameter is equal (PBEsol+U) or even decreased (HSE03) compared to Li-PB or Li-PW, respectively.

The charges and magnetic moments are not significantly affected by the incorporation of the cation, if tetrahedral, since the cation is not expected to actively participate in the electronic structure (see Tables 3, 4, and S6−S9). The charge of the alkali metal itself decreases slightly from Li to Cs, which reflects the decreasing charge concentration (q/r) of the ion. If the cation is placed at the faces (*f*-PB and *f*-PW) the ionic charges vary, which is attributed to the significant structural distortion of the lattice. Moreover, the cationic charge decreases by ∼0.1 |e^-| which indicates an interaction between the CN ligand and the alkali metal when it is placed at the faces of the lattice. In all cases, the magnetic moments remain effectively unchanged (Supporting Information Tables S6−S9).

Regarding PBEsol+U calculations, the band gap and the CFSE do not vary throughout the (tetrahedral) series. In HSE03 simulations, a small decrease of the band gap of ∼0.1 eV is seen. On the one hand, Rosseinsky et al. observed a change in band gaps and attributed this to cation−lattice interactions.[65] On the other hand, Wojdel et al. reported a decrease of the band gap from K^+ to Cs^+, suggesting a lattice expansion effect.[29] Our results seem to favor the latter, geometric, effect. In the case of Na-PB (HSE03), the lattice is contracted by ∼2%, and the band

gap increased by ~20% compared to K-PB, which is supporting this assumption. Moreover, this effect of the geometry on the band gap can be observed in *f*-Li-PB and *f*−Na-P, where the lattice is distorted in the plane, in which the cations lie, leading to a decrease in band gap and CFSE.

The effect on the electronic structure is presented best by the DOS, which is shown for Li-PB, *f*-Li-PB, and Fr-PB (Figure 11)
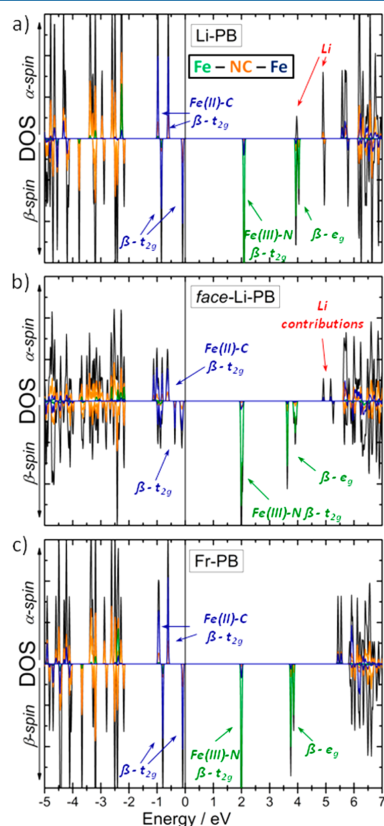
Figure 11. Projected DOS for the intercalated PB-type compounds Li-PB (a), *face*-Li-PB (b), and Fr-PB (c) calculated with HSE03.

and which was calculated by HSE03. Li-PB and Fr-PB have very similar electronic structures, again indicating that there is no major effect of the cation on the electronic structure. However, there is some antibonding cation–ligand interaction, which is shifted to higher energies with increasing cation size. The electronic structure for *f*-PB and *f*-PW, with cations on the lattice faces, varies significantly, which can be seen in Figure 11b for *f*-Li-PB. Because of the structural distortion, the former (almost-) degeneracy of orbitals is lifted, and electronic states are further split into several parts. This also influences the CFSE, which is smaller for *f*-PB and *f*-PW, respectively, because the former t_{2g} and e_g sets of Fe−N are split into smaller bands and spread apart (Figure 11b).

4. CONCLUSIONS

DFT has been shown to be insufficient in describing the correct electronic ground state of PB and its related analogues due to

many low-lying charge transfer states and magnetic configurations. GGA+U seems to be an adequate compromise to accurately assess localized charges and magnetizations on the transition-metal centers with relatively small computational effort. Nonetheless, GGA+U calculations must be treated very carefully, as they are empirically fitted to represent the experimental data of $KFe(III)[Fe(II)(CN)_6]$ PB and are not universally transferable to its derivatives. For practical use GGA+U gives good initial estimates for electronic and geometrical properties and serves as a reasonable comparison between related compounds. Hybrid functionals, such as HSE03, are clearly more accurate but also dramatically more expensive. Even hybrid functionals, however, might over correct the electronic self-interaction error and therefore overestimate band gaps and band splittings.

The insertion of cations leads to a small expansion of the lattice, if cations are inserted into the tetrahedral holes of the structure. The relative lattice expansion increases with cationic size. The smaller ions Li^+ and Na^+ give unstable structures when placed in tetrahedral holes of the lattice and prefer to move to the faces of the structure. The electronic structure is not significantly influenced when varying the type of counter-cation. It changes, however, when oxidizing or reducing the iron centers, thus along the green, blue, white series. The oxidized and reduced forms of PB, do show conducting behavior being due to a shift in Fermi level. Neither PBEsol+U nor HSE03 has shown to correctly describe the conducting behavior of those compounds, but the model for the ideal lattice might be a potential source for the discrepancy.

In summary, we have identified the challenges ahead in the modeling of PB-type compounds both increasing the counter-cation and its concentration. The modeling of the ideal lattice gives some hints pointing at the minimum computational setup to reproduce the geometries and electronic structures, but the role of impurities, partial occupancies, and other deviations from the ideal model are still ahead. A complete full database for all the compounds in the family is presented.

■ ASSOCIATED CONTENT

Ⓢ Supporting Information

The Supporting Information is available free of charge on the ACS Publications website at DOI: 10.1021/acs.inorgchem.6b02200.

Listings of extended functional tests, influence of Hubbard *U* parameter on structural and electronic parameters, energies of different magnetic configurations, complete tables of all structural and electronic parameters for PB and PW derivatives with different counter-cations (PDF)

■ AUTHOR INFORMATION

Corresponding Author

*E-mail: nlopez@iciq.es.

ORCID Ⓞ

José Ramón Galán-Mascarós: 0000-0001-7983-9762
Núria López: 0000-0001-9150-5941

Notes

Inorganic Chemistry　　　　　　　　　　　　　　　　　　　　　　　　　　　　　　Article

■ ACKNOWLEDGMENTS

■ REFERENCES

(1) DeLongchamp, D. M.; Hammond, P. T. Multiple-Color Electrochromism from Layer-by-Layer-Assembled Polyaniline/Prussian Blue Nanocomposite Thin Films. *Chem. Mater.* **2004**, *16*, 4799–4805.

(2) Wang, L.; Song, J.; Qiao, R. M.; Wray, L. A.; Hossain, M. A.; Chuang, Y. D.; Yang, W. L.; Lu, Y. H.; Evans, D.; Lee, J. J.; Vail, S.; Zhao, X.; Nishijima, M.; Kakimoto, S.; Goodenough, J. B. Rhombohedral Prussian White as Cathode for Rechargeable Sodium-Ion Batteries. *J. Am. Chem. Soc.* **2015**, *137*, 2548–2554.

(3) Kundu, D.; Talaie, E.; Duffort, V.; Nazar, L. F. The Emerging Chemistry of Sodium Ion Batteries for Electrochemical Energy Storage. *Angew. Chem., Int. Ed.* **2015**, *54*, 3431–3448.

(4) Goberna-Ferron, S.; Hernandez, W. Y.; Rodriguez-Garcia, B.; Galan-Mascaros, J. R. Light-Driven Water Oxidation with Metal Hexacyanometallate Heterogeneous Catalysts. *ACS Catal.* **2014**, *4*, 1637–1641.

(5) Pintado, S.; Goberna-Ferron, S.; Escudero-Adan, E. C.; Galan-Mascaros, J. R. Fast and Persistent Electrocatalytic Water Oxidation by Co-Fe Prussian Blue Coordination Polymers. *J. Am. Chem. Soc.* **2013**, *135*, 13270–13273.

(6) Karyakin, A. A. Prussian Blue and Its Analogues: Electrochemistry and Analytical Applications. *Electroanalysis* **2001**, *13*, 813–819.

(7) Yasutaka, T.; Kawamoto, T.; Kawabe, Y.; Sato, T.; Sato, M.; Suzuki, Y.; Nakamura, K.; Komai, T. Rapid Measurement of Radiocesium in Water Using a Prussian Blue Impregnated Nonwoven Fabric: Fukushima Npp Accident Related. *J. Nucl. Sci. Technol.* **2013**, *50*, 674–681.

(8) Zhang, W.; Hu, S.; Yin, J.-J.; He, W.; Lu, W.; Ma, M.; Gu, N.; Zhang, Y. Prussian Blue Nanoparticles as Multienzyme Mimetics and Reactive Oxygen Species Scavengers. *J. Am. Chem. Soc.* **2016**, *138*, 5860–5865.

(9) Sato, O.; Iyoda, T.; Fujishima, A.; Hashimoto, K. Photoinduced Magnetization of a Cobalt-Iron Cyanide. *Science* **1996**, *272*, 704–705.

(10) Sato, O.; Kawakami, T.; Kimura, M.; Hishiya, S.; Kubo, S.; Einaga, Y. Electric-Field-Induced Conductance Switching in FeCo Prussian Blue Analogues. *J. Am. Chem. Soc.* **2004**, *126*, 13176–13177.

(11) Ferlay, S.; Mallah, T.; Ouahes, R.; Veillet, P.; Verdaguer, M. A Room-Temperature Organometallic Magnet Based on Prussian Blue. *Nature* **1995**, *378*, 701–703.

(12) Buser, H. J.; Ludi, A. Single-Crystal Study of Prussian Blue - $Fe_4[Fe(CN)_6]_2$ $14H_2O$. *J. Chem. Soc., Chem. Commun.* **1972**, 1299–1299.

(13) Buser, H. J.; Schwarzenbach, D.; Petter, W.; Ludi, A. Crystal-Structure of Prussian Blue - $Fe_4[Fe(CN)_6]_3$ xH_2O. *Inorg. Chem.* **1977**, *16*, 2704–2710.

(14) Herren, F.; Fischer, P.; Ludi, A.; Halg, W. Neutron-Diffraction Study of Prussian Blue, $Fe_4[Fe(CN)_6]_3$ xH_2O - Location of Water-Molecules and Long-Range Magnetic Order. *Inorg. Chem.* **1980**, *19*, 956–959.

(15) The inverse redox form ferrous ferricyanide $KFe(II)[Fe(III)(CN)_6]$, also called Turnbulls blue, was not observed. Although in solution the ferrous Fe(II) cation and ferricyanide $[Fe(III)(CN)_6]$ anions are more stable, ferric ferrocyanide $KFe(III)[Fe(II)(CN)_6]$ is the more stable redox form in the solid state.

(16) Cosgrove, J. G.; Collins, R. L.; Murty, D. S. Preparation of Ferrous Ferricyanide (Not Turnbulls Blue). *J. Am. Chem. Soc.* **1973**, *95*, 1083.

(17) Hansen, L. D.; Litchman, W. M.; Daub, G. H. Turnbulls Blue and Prussian Blue - $KFe[Fe(CN)_6]$. *J. Chem. Educ.* **1969**, *46*, 46–46.

(18) Ito, A.; Suenaga, M.; Ono, K. Mossbauer Study of Soluble Prussian Blue Insoluble Prussian Blue and Turnbulls Blue. *J. Chem. Phys.* **1968**, *48*, 3597–3599.

(19) Brunschwig, B. S.; Creutz, C.; Sutin, N. Optical Transitions of Symmetrical Mixed-Valence Systems in the Class Ii-Iii Transition Regime. *Chem. Soc. Rev.* **2002**, *31*, 168–184.

(20) Davidson, D.; Welo, L. A. The Nature of Prussian Blue. *J. Phys. Chem.* **1927**, *32*, 1191–1196.

(21) Ruiz, E.; Rodriguez-Fortea, A.; Alvarez, S.; Verdaguer, M. Is It Possible to Get High T_C Magnets with Prussian Blue Analogues? A Theoretical Prospect. *Chem. - Eur. J.* **2005**, *11*, 2135–2144.

(22) Day, P.; Herren, F.; Ludi, A.; Gudel, H. U.; Hulliger, F.; Givord, D. Valence Delocalization in Prussian Blue $Fe_4(III)[Fe(II)(CN)_6]_3 \cdot XH_2O$, by Polarized Neutron-Diffraction. *Helv. Chim. Acta* **1980**, *63*, 148–153.

(23) Mayoh, B.; Day, P. Charge-Transfer in Mixed-Valence Solids 0.8. Contribution of Valence Delocalization to Ferromagnetism of Prussian Blue. *J. Chem. Soc., Dalton Trans.* **1976**, 1483–1486.

(24) Middlemiss, D. S.; Wilson, C. C. Ferromagnetism and Spin Transitions in Prussian Blue: A Solid-State Hybrid Functional Study. *Phys. Rev. B: Condens. Matter Mater. Phys.* **2008**, *77*, 1–13.

(25) Robin, M. B. Color and Electronic Configurations of Prussian Blue. *Inorg. Chem.* **1962**, *1*, 337–342.

(26) Gmelin, L. *Gmelins Handbuch Der Anorganischen Chemie;* Eisen, B., Ed.; Heidelberg, Germany, 1932.

(27) Wojdel, J. C.; de P. R. Moreira, I.; Bromley, S. T.; Illas, F. On the Prediction of the Crystal and Electronic Structure of Mixed-Valence Materials by Periodic Density Functional Calculations: The Case of Prussian Blue. *J. Chem. Phys.* **2008**, *128*, 044713–1–044713–9.

(28) Wojdel, J. C.; Bromley, S. T. Efficient Calculation of the Structural and Electronic Properties of Mixed Valence Materials: Application to Prussian Blue Analogues. *Chem. Phys. Lett.* **2004**, *397*, 154–159.

(29) Wojdel, J. C.; Bromley, S. T. Band Gap Variation in Prussian Blue Via Cation-Induced Structural Distortion. *J. Phys. Chem. B* **2006**, *110*, 24294–24298.

(30) Wojdel, J. C.; Moreira, I. D. R.; Bromley, S. T.; Illas, F. Prediction of Half-Metallic Conductivity in Prussian Blue Derivatives. *J. Mater. Chem.* **2009**, *19*, 2032–2036.

(31) Wojdel, J. C.; Moreira, I. D. R.; Illas, F. Periodic Density Functional Theory Study of Spin Crossover in the Cesium Iron Hexacyanochromate Prussian Blue Analog. *J. Chem. Phys.* **2009**, *130*, 014702.

(32) Ling, C.; Chen, J. J.; Mizuno, F. First-Principles Study of Alkali and Alkaline Earth Ion Intercalation in Iron Hexacyanoferrate: The Important Role of Ionic Radius. *J. Phys. Chem. C* **2013**, *117*, 21158–21165.

(33) Wojdel, J. C. First Principles Calculations on the Influence of Water-Filled Cavities on the Electronic Structure of Prussian Blue. *J. Mol. Model.* **2009**, *15*, 567–571.

(34) Kumar, A.; Yusuf, S. M.; Keller, L. Structural and Magnetic Properties of $Fe[Fe(CN)_6] \cdot 4H_2O$. *Phys. Rev. B: Condens. Matter Mater. Phys.* **2005**, *71*, 1–7.

(35) Pajerowski, D. M.; Watanabe, T.; Yamamoto, T.; Einaga, Y. Electronic Conductivity in Berlin Green and Prussian Blue. *Phys. Rev. B: Condens. Matter Mater. Phys.* **2011**, *83*, 1–4.

(36) Hu, M.; Jiang, J. S. Facile Synthesis of Air-Stable Prussian White Microcubes Via a Hydrothermal Method. *Mater. Res. Bull.* **2011**, *46*, 702–707.

(37) Maer, K.; Beasley, M. L.; Collins, R. L.; Milligan, W. O. Structure of Titanium-Iron Cyanide Complexes. *J. Am. Chem. Soc.* **1968**, *90*, 3201–3208.

(38) Xidis, A.; Neff, V. D. On the Electronic Conduction in Dry Thin-Films of Prussian Blue, Prussian Yellow, and Everitt Salt. *J. Electrochem. Soc.* **1991**, *138*, 3637–3642.

(39) Kresse, G.; Furthmuller, J. Efficient Iterative Schemes for Ab Initio Total-Energy Calculations Using a Plane-Wave Basis Set. *Phys. Rev. B: Condens. Matter Mater. Phys.* **1996**, *54*, 11169–11186.

(40) Hafner, J.; Kresse, G. *The Vienna Ab-Initio Simulation Program Vasp: An Efficient and Versatile Tool for Studying the Structural, Dynamic, and Electronic Properties of Materials*; Plenum Press Div Plenum Publishing Corp: New York, 1997; pp 69−82.

(41) Perdew, J. P.; Burke, K.; Ernzerhof, M. Generalized Gradient Approximation Made Simple. *Phys. Rev. Lett.* **1996**, *77*, 3865−3868.

(42) Perdew, J. P.; Burke, K.; Ernzerhof, M. Generalized Gradient Approximation Made Simple (Vol 77, Pg 3865, 1996). *Phys. Rev. Lett.* **1997**, *78*, 1396−1396.

(43) Perdew, J. P.; Ruzsinszky, A.; Csonka, G. I; Vydrov, O. A.; Scuseria, G. E.; Constantin, L. A.; Zhou, X. L.; Burke, K. Restoring the Density-Gradient Expansion for Exchange in Solids and Surfaces. *Phys. Rev. Lett.* **2009**, *102*, 1−4.

(44) Zhang, Y. K.; Yang, W. T. Comment on "Generalized Gradient Approximation Made Simple". *Phys. Rev. Lett.* **1998**, *80*, 890−890.

(45) Perdew, J. P.; Chevary, J. A.; Vosko, S. H.; Jackson, K. A.; Pederson, M. R.; Singh, D. J.; Fiolhais, C. Atoms, Molecules, Solids, and Surfaces - Applications of the Generalized Gradient Approximation for Exchange and Correlation. *Phys. Rev. B: Condens. Matter Mater. Phys.* **1992**, *46*, 6671−6687.

(46) Perdew, J. P.; Chevary, J. A.; Vosko, S. H.; Jackson, K. A.; Pederson, M. R.; Singh, D. J.; Fiolhais, C. Atoms, Molecules, Solids, and Surfaces - Applications of the Generalized Gradient Approximation for Exchange and Correlation (Vol 46, Pg 6671, 1992). *Phys. Rev. B: Condens. Matter Mater. Phys.* **1993**, *48*, 4978−4978.

(47) Mattsson, A. E.; Armiento, R.; Paier, J.; Kresse, G.; Wills, J. M.; Mattsson, T. R. The Am05 Density Functional Applied to Solids. *J. Chem. Phys.* **2008**, *128*, 084714.

(48) Anisimov, V. I; Aryasetiawan, F.; Lichtenstein, A. I. First-Principles Calculations of the Electronic Structure and Spectra of Strongly Correlated Systems: The LDA+U Method. *J. Phys.: Condens. Matter* **1997**, *9*, 767−808.

(49) Dudarev, S. L.; Botton, G. A.; Sutton, A. P. *Electron Energy Loss Spectra and the Structural Stability of Oxides with Strongly Correlated Electrons*; Iop Publishing Ltd: Bristol, England, 1998, 613−614.

(50) Parr, R. G.; Yang, W. *Density-Functional Theory of Atoms and Molecules*; Oxford University Press: Oxford, England, 1989.

(51) Heyd, J.; Scuseria, G. E.; Ernzerhof, M. Hybrid Functionals Based on a Screened Coulomb Potential. *J. Chem. Phys.* **2003**, *118*, 8207−8215.

(52) Heyd, J.; Scuseria, G. E. Assessment and Validation of a Screened Coulomb Hybrid Density Functional. *J. Chem. Phys.* **2004**, *120*, 7274−7280.

(53) Krukau, A. V.; Vydrov, O. A.; Izmaylov, A. F.; Scuseria, G. E. Influence of the Exchange Screening Parameter on the Performance of Screened Hybrid Functionals. *J. Chem. Phys.* **2006**, *125*, 224106.

(54) Blochl, P. E. Projector Augmented-Wave Method. *Phys. Rev. B: Condens. Matter Mater. Phys.* **1994**, *50*, 17953−17979.

(55) Kresse, G.; Joubert, D. From Ultrasoft Pseudopotentials to the Projector Augmented-Wave Method. *Phys. Rev. B: Condens. Matter Mater. Phys.* **1999**, *59*, 1758−1775.

(56) Monkhorst, H. J.; Pack, J. D. Special Points for Brillouin-Zone Integrations. *Phys. Rev. B* **1976**, *13*, 5188−5192.

(57) Ong, S. P. In *Materials Project*; Persson, K., Ed.; Lawrence Berkeley National Laboratory: Berkeley, CA, 2011.

(58) Becke, A. D. A New Mixing of Hartree-Fock and Local Density-Functional Theories. *J. Chem. Phys.* **1993**, *98*, 1372−1377.

(59) Reiher, M.; Salomon, O.; Artur Hess, B. Reparameterization of Hybrid Functionals Based on Energy Differences of States of Different Multiplicity. *Theor. Chem. Acc.* **2001**, *107*, 48−55.

(60) Bader, R. F. *Atoms in Molecules—A Quantum Theory*; Clarendon Press: Oxford, England, 1990; Vol. 22.

(61) Henkelman, G.; Arnaldsson, A.; Jonsson, H. A Fast and Robust Algorithm for Bader Decomposition of Charge Density. *Comput. Mater. Sci.* **2006**, *36*, 354−360.

(62) Tang, W.; Sanville, E.; Henkelman, G. A Grid-Based Bader Analysis Algorithm without Lattice Bias. *J. Phys.: Condens. Matter* **2009**, *21*, 084204.

(63) Kepp, K. P. Consistent Descriptions of Metal-Ligand Bonds and Spin-Crossover in Inorganic Chemistry. *Coord. Chem. Rev.* **2013**, *257*, 196−209.

(64) Capdevila-Cortada, M.; Lodziana, Z.; Lopez, N. On the Performance of DFT+U Approaches in the Study of Catalytic Materials. *ACS Catal.* **2016**, *6*, 8370−8379.

(65) Rosseinsky, D. R.; Lim, H.; Jiang, H. J.; Chai, J. W. Optical Charge-Transfer in Iron(III)Hexacyanoferrate(II): Electro-Intercalated Cations Induce Lattice-Energy-Dependent Ground-State Energies. *Inorg. Chem.* **2003**, *42*, 6015−6023.

(66) Alvarez-Moreno, M.; de Graaf, C.; Lopez, N.; Maseras, F.; Poblet, J. M.; Bo, C. Managing the Computational Chemistry Big Data Problem: The Iochem-Bd Platform. *J. Chem. Inf. Model.* **2015**, *55*, 95−103.

ACS AuthorChoice

Cobalt Hexacyanoferrate on BiVO$_4$ Photoanodes for Robust Water Splitting

Franziska Simone Hegner,[†] Isaac Herraiz-Cardona,[‡] Drialys Cardenas-Morcoso,[‡] Núria López,*,[†] José-Ramón Galán-Mascarós,*,[†,§] and Sixto Gimenez*,[‡]

[†]Institute of Chemical Research of Catalonia (ICIQ), The Barcelona Institute of Science and Technology (BIST), Av. Països Catalans, 16, 43007 Tarragona, Spain

[‡]Institute of Advanced Materials (INAM), Universitat Jaume I, 12006 Castelló, Spain

[§]ICREA, Pg. Lluís Companys 23, 08010 Barcelona, Spain

Ⓢ Supporting Information

ABSTRACT: The efficient integration of photoactive and catalytic materials is key to promoting photoelectrochemical water splitting as a sustainable energy technology built on solar power. Here, we report highly stable water splitting photoanodes from BiVO$_4$ photoactive cores decorated with CoFe Prussian blue-type electrocatalysts (**CoFe-PB**). This combination decreases the onset potential of BiVO$_4$ by ~0.8 V (down to 0.3 V vs reversible hydrogen electrode (RHE)) and increases the photovoltage by 0.45 V. The presence of the catalyst also leads to a remarkable 6-fold enhancement of the photocurrent at 1.23 V versus RHE, while keeping the light-harvesting ability of BiVO$_4$. Structural and mechanistic studies indicate that **CoFe-PB** effectively acts as a true catalyst on BiVO$_4$. This mechanism, stemming from the adequate alignment of the energy levels, as showed by density functional theory calculations, allows **CoFe-PB** to outperform all previous catalyst/BiVO$_4$ junctions and, in addition, leads to noteworthy long-term stability. A bare 10−15% decrease in photocurrent was observed after more than 50 h of operation under light irradiation.

KEYWORDS: photoelectrocatalysis, water splitting, oxygen evolution, electrochemistry, computational chemistry, Prussian blue
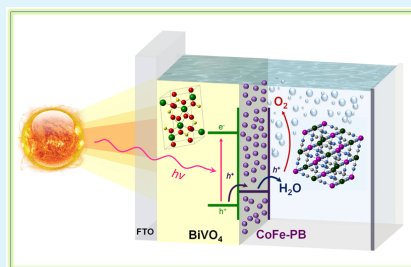
■ INTRODUCTION

The production of solar fuels (by converting the energy of solar photons into chemical bonds) stands as a promising technology to power the planet with sunlight. This approach elegantly overcomes the problems related to the intrinsically intermittent solar flux, by transforming the solar energy into compounds, which can be stored, transported, and used upon demand.[1] In this context, photoelectrochemical (PEC) water splitting offers a reliable strategy to generate solar H$_2$, which can directly power fuel cells. Alternatively, H$_2$ can be combined with CO$_2$ for the synthesis of complex hydrocarbons, leading to C-neutral energy schemes.[2] From a technoeconomical perspective, the key performance indicators, to consider the technology competitive, can be summarized as follows: (i) solar-to-hydrogen (STH) efficiency of 10%, (ii) durability of 10 years, and (iii) cost of $2−4/kg of dispensed hydrogen.[3]

These stringent requirements impose the use of Earth-abundant materials and low-cost synthetic procedures for the fabrication of photoelectrochemical (PEC) devices. In this context, n-type metal oxide semiconductor materials (TiO$_2$,[4,5] Fe$_2$O$_3$,[6−9] WO$_3$,[10−13] BiVO$_4$,[14−20] etc.) have been extensively studied as promising candidates for the development of the technology due to their relatively good stability under operation in harsh environments. From this family, BiVO$_4$ holds the

record of performance with 8.1% solar-to-hydrogen (STH) efficiency, when combined with a double-junction GaAs/InGaAsP photovoltaic device.[21] In tandem with a single perovskite solar cell, unassisted water splitting with a solar-to-hydrogen conversion efficiency of up to 6.2% for more than 10 h has been recently demonstrated.[22] Because there are some concerns on the relative abundance of bismuth in the Earth crust,[23] different compositional modifications have been explored to achieve a competitive metal vanadate based on this system.[24−26] In all of these arrangements, a water oxidation catalyst (WOC) is deposited on top of the photoactive semiconductor material to overcome the thermodynamic and kinetic barriers of the sluggish water oxidation reaction at the BiVO$_4$ surface, boosting the performance of the photoanode. Consequently, the deposition of an efficient, stable, and cost-effective WOC on the photoactive semiconductor material is key to achieving the targeted technoeconomical requirements.

Moreover, the state of the art in heterogeneous catalysis for oxygen evolution is dominated by noble metals (Ir or Ru), but their high price and scarcity preclude large technological

impact. Abundant and inexpensive oxides of first-row transition metals are also competent WOCs, although exclusively at a very high pH or with the help of ancillary electrolytes (i.e., phosphates).[27,28] Alternatively, Prussian blue (PB)-type materials have emerged as promising catalysts for water oxidation catalysis.[29−31] These coordination polymers are (i) easy to obtain and to process by soft chemistry methods; (ii) available as nanoparticles or thin films; (iii) and stable and active in a very large pH range, from neutral down to extremely acidic conditions;[32] (iv) while being non-toxic. The unique performance of these catalysts is based on their structural and electronic features. They are built from hexacyanometallate anionic complexes and a metal dication, in stoichiometric excess. These coordination networks are very robust due to the strength of cyanide bridging, with a rather high covalent character. Their structure is built following an ideal face-centered cubic (FCC) network (Scheme 1), but their

Scheme 1. Representation of the Ideal Face-Centered Cubic Structure of the CoFe-PB Prussian Blue-Type Catalyst
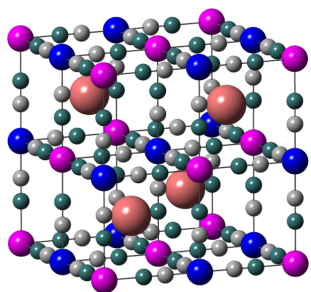
nonstoichiometric nature creates multiple voids for solvent (water) and countercations (if needed). Typically, the dication is in excess and coordinatively unsaturated due to missing $[M(CN)6]^{n-}$ moieties. This opens two to three accessible coordination sites for solvent molecules, where water oxidation catalysis is supposedly taking place. At the same time, these semiconductor materials possess versatile redox properties, allowing the metals to be in multiple oxidation states.[33] Their low absorption in the UV−vis region also makes them very good candidates to be combined with chromophores for a photocatalytic process. Indeed, light-driven water oxidation was already proven in suspension of a Co-containing PB material, using a Ru chromophore and a sacrificial electron acceptor.[34]

In the present study, we have been able to successfully combine the unique properties of these two materials, producing a BiVO$_4$ photoanode coupled to a Prussian blue-type WOC (**CoFe-PB**/BiVO$_4$). This heterostructure appears to be superior to previous examples, with a significant and robust photoelectrocatalytic performance, arising from the optimum matching of the photoactive BiVO$_4$ core and the PB system, which does not alter the capacitive properties of BiVO$_4$. This is distinct from other metal oxide WOCs on semiconductor surfaces, which appear to work mainly as charge accumulators.[35,36] Furthermore, our results are supported with state-of-the-art theoretical density functional theory (DFT) calculations that demonstrate the correct alignment of the electronic levels between the different photocatalytic units. Besides the remarkable increase of performance, the **CoFe-PB**/BiVO$_4$ system exhibits outstanding stability thanks to the intimate

interfacial connectivity achieved via a soft wet processing method.

■ EXPERIMENTAL SECTION

Materials. Chemicals bismuth(III) nitrate (Bi(NO$_3$)$_3$·5H$_2$O ≥ 98.0%), vanadyl acetylacetonate (VO(acac)$_2$ ≥ 97.0%), potassium ferri(III)cyanide (K$_3$[Fe(CN)$_6$] ≥ 99.0%), and potassium hydroxide (KOH flakes ≥ 90%) were purchased from Sigma-Aldrich and cobalt chloride hexahydrate (CoCl$_2$·6H$_2$O ≥ 98.0%) from Fluka Analytical. Solvents dimethylsulfoxide (DMSO ≥ 99.9%) and ethylene glycol (ethane-1,2-diol ≥ 99%) were obtained from Sigma-Aldrich. The buffer solution was prepared from potassium phosphate monobasic and dibasic (KH$_2$PO$_4$ ≥ 99.0% and K$_2$HPO$_4$ ≥ 98.0%, Sigma-Aldrich). As a hole scavenger, Na$_2$SO$_3$ from J.T. Baker was used. High-purity (milliQ) water was obtained with a millipore purification system (Synergy) and used for all solutions. Fluorine-doped tin oxide (FTO)-coated glass slides were purchased from Hartford glass (15 Ω/cm^2).

Synthesis of BiVO$_4$ Electrodes. Thin-film BiVO$_4$ electrodes were prepared following a simple and cost-efficient electrodeposition method, described by Kang et al.[37] Prior to deposition, fluorine-doped tin oxide (FTO) electrodes were ultrasonicated and then thoroughly cleaned with water and ethanol (isopropanol). Metallic Bi was deposited from a solution of 20 mM Bi(NO$_3$)$_3$·5H$_2$O in ethylene glycol by applying a repetitive sequence of passing 0.04 C/cm^2 at a potential of −1.8 V versus Ag/AgCl (3 M KCl), followed by a resting time of 2 s eight times. Thus, a total charge of 0.32 C/cm^2 was passed. After carefully rinsing the films with milliQ water, 60 μL/cm^2 of 0.15 M VO(acac)$_2$ in DMSO was dropped on the Bi surface and heated up to about 80 °C on a hot plate to evaporate the DMSO. The electrodes were calcined in air by heating them with a rate of 2 °C/min up to 500 °C and then at 500 °C for 2 h. During heating, metallic Bi and VO^{2+} oxidize and form BiVO$_4$. Excess V$_2$O$_5$, which is formed during the calcination process, was removed by leaching the electrodes in 1 M KOH for 20−30 min under vigorous stirring.

Sequential CoFe-PB Coating. The catalyst was deposited by sequentially dipping the BiVO$_4$ electrodes in reactant solutions of 0.02 M K$_3$[Fe(CN)$_6$] in H$_2$O and 0.04 M CoCl$_2$ in H$_2$O. First, the electrodes were dipped in a [Fe(CN)$_6$]$^{3−}$ solution for 10−15 min under slow stirring, so that the negatively charged iron cyanide complexes can bind to the BiVO$_4$ surface. Afterwards, the electrodes were thoroughly rinsed with milliQ water and then dipped in the Co^{2+} solution, again for 10−15 min under stirring, to form **CoFe-PB** complex structures. The sequence was repeated at least four times (four to eight times) to reach optimum photoelectrocatalytic enhancement.

Photoelectrochemical (PEC) Measurements. PEC experiments were performed with an Eco Chemie Autolab potentiostat coupled with the NOVA electrochemical software. A typical three-electrode cell consisted of the BiVO$_4$ photoanode as the working electrode, a Pt-wire or mesh as the counter electrode, and a Ag/AgCl (3 M KCl) reference electrode. All potentials were converted to the pH-independent reversible hydrogen electrode (RHE) by using the Nernst equation (eq 1)

$$V_{RHE} = V_{Ag/AgCl} + V^0_{Ag/AgCl} + 0.059pH \qquad (1)$$

with $V^0_{Ag/AgCl}(3\ M\ KCl) = 0.21$ V

To normalize the measured current (in ampere, A) to current density j (in mA/cm^2), the electrode geometrical areas were determined by the graphical software ImageJ 1.50i. If not stated otherwise, the experiments were performed in a 0.1 M solution of potassium phosphate (KH$_2$PO$_4$) buffer at pH = 7(±0.1). The pH was determined with a CRISON Basic 2° pH meter. Some experiments were carried out in a 1 M Na$_2$SO$_3$ solution in buffer (pH = 8), which served as a hole scavenger. A 450 W Xe arc lamp with an AM 1.5 solar filter (Sciencetech Inc.) was used to simulate sunlight of 100 mW/cm^2 (1 sun). Cyclic voltammetry (CV) was performed at a scan rate of 50 mV/s, and for chopped light experiments, the shutter frequency was 1 Hz. Because it takes typically 2−4 CVs to reach a stable signal, all
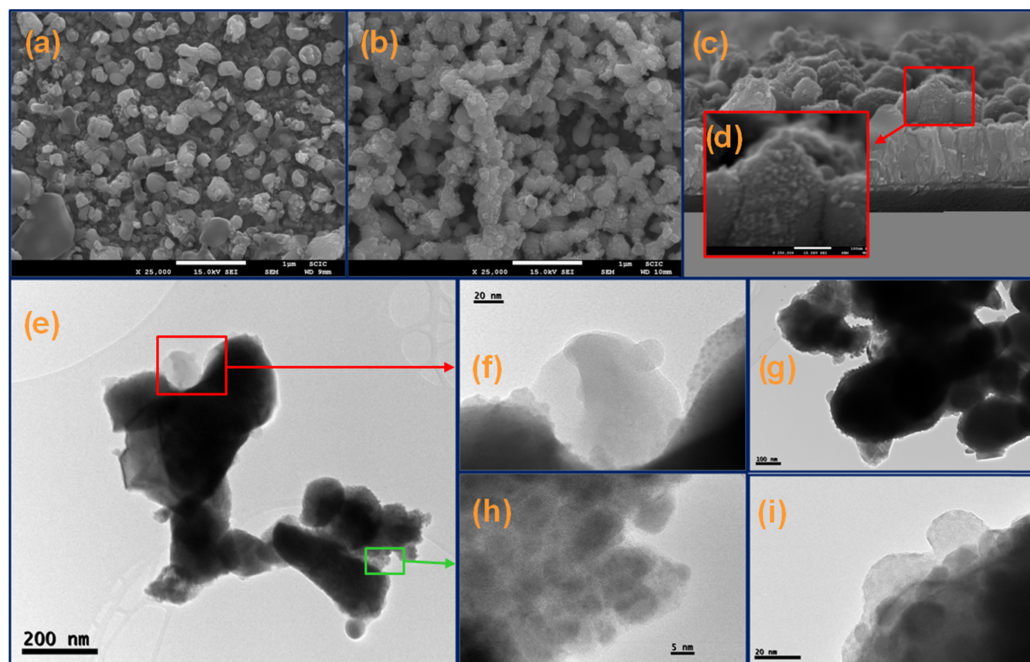
Figure 1. Electron micrographs obtained by SEM (2a−d) and TEM (2e−i): SEM images (25000× magnified) of (a) bare and (b) **CoFe-PB**-modified BiVO$_4$ surfaces and (c) cross section of **CoFe-PB**/BiVO$_4$ with (d) large (250 000×) magnification of one surface particle. High-resolution (HR)-TEM of scratched **CoFe-PB**/BiVO$_4$ particles before (e, f, h) and after (g, i) photoelectrochemical treatment (100 mW/cm^2 for 1 h at 1.23 V vs RHE). Amorphous **CoFe-PB** particles on the BiVO$_4$ surfaces before (f) and after (i) photoelectrochemical treatment (2 h) showing the nanocrystalline BiVO$_4$ structure at the surface.

experiments were generally repeated five times and the fifth scan is presented here. All BiVO$_4$ electrodes were illuminated through the FTO substrate and not, as it is usual for hematite, from the electrolyte. This ensures a small mean free path for excited electrons because conduction in BiVO$_4$ is well known to be limited by its small electron diffusion length (around 70−100 nm)[38,39] in contrast to that of hematite, where it is limited by its small hole diffusion length of 2−4 nm.[40−42] It is to be noted that the shown CVs were systematically taken after stabilization of the system. Impedance data were collected between 10^{-2} and 10^6 Hz using a 20 mV amplitude voltage perturbation and analyzed with ZView software (Scribner associates). Incident photon-to-current conversion efficiencies (IPCEs) were obtained by collecting the photocurrent recorded under monochromatic light irradiation (Newport spectrometer) using the same three-electrode setup as described above. IPCE, as a function of wavelength, is given by the ratio of the measured photocurrent, j_{photo}, to the incident monochromatic light intensity, P_{mono}

$$IPCE(\lambda) = \frac{1239.87}{\lambda} \frac{j_{photo}}{P_{mono}} \tag{2}$$

with 1239.87/λ as the wavelength-to-electronvolt conversion factor.

Structural and Optical Characterization. Morphologies, particle sizes, and chemical compositions were determined by scanning electron microscopy (SEM) with a JSM-7000F JEOL FEG-SEM system (Tokyo, Japan) equipped with an INCA 400 Oxford EDS analyzer (Oxford, U.K.) operating at 15 kV and a JEM-2100 JEOL transmission electron microscope (TEM) operating at 200 kV. Prior to the SEM experiment, the samples were sputtered with a 2 nm thick layer of Pt. To evaluate the effect of aging on the microstructural features of the samples, they were irradiated at 100 mW/cm^2 at 1.23 V

versus RHE for 1 h. X-ray photoelectron spectroscopy (XPS) was used to analyze the surface and possible changes of electronic coordination before and after the electrochemical treatment. The analyses were performed with a Specs SAGE 150 instrument using nonmonochrome Al Kα irradiation (1486.6 eV) at 20 mA and 13 kV, a constant energy pass of 75 eV for overall analysis and 30 eV for analysis in the specific binding energy ranges of each element, and a measurement area of 1 × 1 mm^2. The pressure in the analysis chamber was 8 × 10^{-9} hPa. The data were evaluated using Casa XPS software. The energy corrections of the spectra were performed considering a reference value of C 1s from the organic matter at 284.8 eV. UV−vis spectra of the electrodes were recorded with a Cary 300 Bio spectrometer (UV0911 M213). Infrared absorption spectroscopy was performed with a Thermo-Scientific NICOLET iS50 Fourier transform infrared (FT-IR) spectrometer. For the measurement, the substrate (<1 mg) was scratched from several electrodes, finely ground with large excess of KBr, and pressed to obtain a thin transparent disk. Electrolyte solutions were analyzed for trace metals using inductively coupled plasma optical emission spectrometry (ICP-OES).

Oxygen Detection. The faradaic efficiency of the photoanodes was calculated during a chronoamperometric measurement at constant potential (1.23 V vs RHE) and under illumination (100 mW/cm^2), where total oxygen evolution was determined by gas chromatography (GC). An Agilent Technologies 490 Micro GC device was connected to the electrochemical cell, which was constantly purged with Ar. After a first blank measurement (without applying any voltage and in the dark), periodic measurements of the O$_2$ content were repeated every 5 min before and after switching on the light. The detected O$_2$ amount is correlated to the measured photocurrent by its faradaic efficiency (FE) (more details in the Supporting Information)
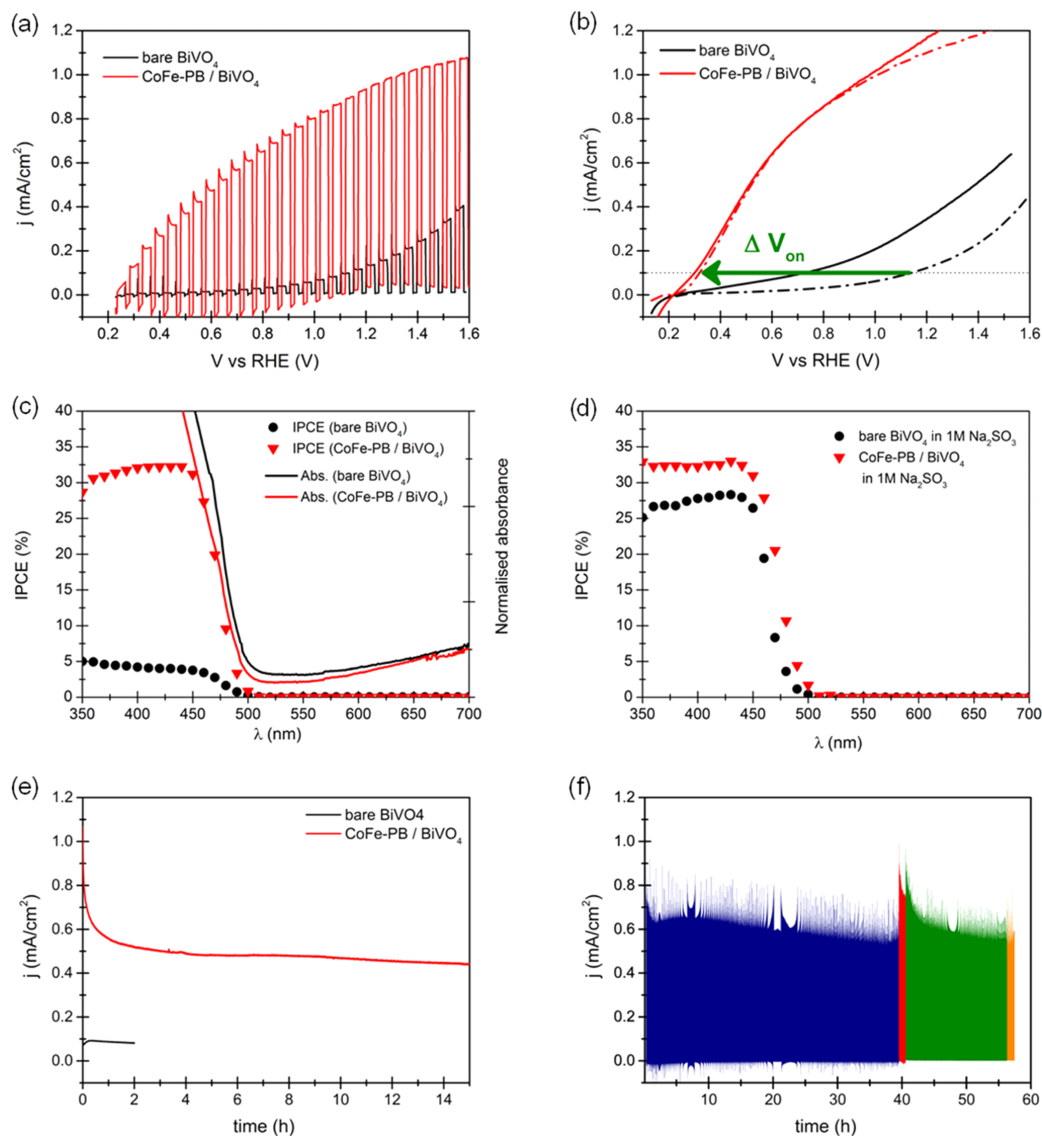
Figure 2. Anodic CV scans of **CoFe-PB**/BiVO$_4$ (red) compared to those of bare BiVO$_4$ (black) under (a) chopped ($\nu_{shutter}$ = 1 Hz) and (b) constant light irradiation (100 mW/cm^2) at scan rates of 50 mV/s (solid lines) and 1 mV/s (dashed lines) in 0.1 M KPi buffer (pH 7). Incident photon-to-current conversion efficiency (IPCE) obtained in the (c) buffer (pH 7) and (d) hole scavenger (pH 7.9) at 1.23 V vs RHE for bare BiVO$_4$ (black circles) and **CoFe-PB**-modified BiVO$_4$ (red triangles). Chronoamperometric (CA) measurements of a **CoFe-PB**-coated BiVO$_4$ photoanode at 1.23 V vs RHE under (e) constant and (f) chopped ($\nu_{shutter}$ = 0.03 Hz) irradiation (100 mW/cm^2) in 0.1 M KPi buffer (pH 7). Different colors indicate different measurements of the same **CoFe-PB** electrode at different days.

$$FE\,(\%) = \frac{n(O_2)_{evolved}\,(mol)}{n(O_2)_{theoretical}\,(mol)} \times 100\% \tag{3}$$

Computational Details. Density functional theory (DFT) calculations were carried out using the Vienna ab initio simulation package.[43,44] Pure density functional theory is insufficient in correctly describing the complex electronic structure of Prussian blue-type

materials. In contrast, hybrid functionals, which include 20−25% of exact exchange from Hartree−Fock (HF) theory, often overcorrect the DFT-inherent self-interaction error and yield exceedingly large band splittings.[45] Therefore, the required amount of exact exchange was optimized to be 13% for the hybrid functional HSE03, by fitting the optical band gap, and will be referred to as HSE03-13 in the following text. HSE03-13 gives a good description of the electronic structure for

both **CoFe-PB** and $BiVO_4$ (see Computational Modeling in Supporting Information). Projector augmented waves (PAWs) with small cores, expanding valence-subshell s- and p-electrons, ensure accuracy and were used for all metal atoms in the lattice.[46] The valence electrons were expanded in plane waves with kinetic energies up to 500 eV. The Brillouin zone was sampled using a Monkhorst–Pack k-point mesh with $3 \times 3 \times 3$ k-points for **CoFe-PB** and $6 \times 3 \times 4$ k-points for $BiVO_4$, ensuring similar k-point samplings in both compounds. Water was calculated with the same scheme, and the water solvent was represented through the MGCM method (see the Supporting Information for more details).). All structures and calculations have been uploaded to the ioChem-BD database (http://www.iochem-bd.org), where they are openly accessible.

RESULTS AND DISCUSSION

The nanostructured $BiVO_4$ films were modified with a cobalt hexacyanoferrate (**CoFe-PB**) catalyst by a sequential coating method, which has shown to be advantageous over other deposition methods (see, Supporting Information, Figure S1, for details). Mild deposition conditions were employed (aqueous solution at pH 7, room temperature, and no applied potential) to ensure that the underlying photoanode is not damaged. The optimum photoelectrochemical performance was obtained after four dipping cycles (Figure S2). Higher catalyst loading did not further improve photocurrent. This ensures a very thin deposited layer, favoring fast charge and mass transport through the catalyst.

Figure 1a,b shows zenithal SEM images of the nano-structured $BiVO_4$ film with and without the **CoFe-PB** catalyst, respectively. Figure 1c shows the cross section of the modified $BiVO_4$ photoanode, with a thickness of about 200–250 nm. The electrochemical treatment (100 mW/cm² irradiation at an applied bias of 1.23 V vs RHE for 1 h), which was done to detect the effects of aging, did not alter the morphology significantly (Figure S3).

Energy-dispersive spectrometry (EDS) microanalysis confirms the presence of the **CoFe-PB** catalyst showing about 1–2% of Fe and Co on the electrode surface. (Figures S3 and S4). High resolution transmission electron microscopy (HR-TEM) shows the presence of <50 nm nanoparticles on the surface (Figure 1e–i). The Co/Fe ratio is not homogeneous, varying between 1:1 and 3:2 (Figure S5), corresponding to the two limiting compositions $KCo[Fe(CN)_6]$ and $Co_3[Fe(CN)_6]_2$.[47] The measured lattice spacings 2.8 and 3.1 Å of $BiVO_4$ are consistent with the $(\bar{1}21)$ and (040) planes of the monoclinic scheelite structure, respectively (Figure S6).[48] No lattice fringes from the **CoFe-PB** layer were detected, probably due to a lack of long-range order, along with its very small size (Figure 1e–i). More detailed surface characterization was carried out by X-ray photoelectron spectroscopy (XPS) on different $BiVO_4$ electrodes (bare and **CoFe-PB**-modified; see Table S1 and Figures S7–S11). Quantitative analysis confirms the presence of Co and Fe on the surface of the electrodes with a higher amount of Co. Moreover, an excess of Bi with an average Bi/V ratio of 1.6 was found, in agreement with EDS/TEM data and recent mechanistic studies, which detected structural destabilization and chemical attack via vanadium loss into solution upon hole accumulation at the $BiVO_4$ surface.[49] XPS of **CoFe-PB**/$BiVO_4$ reveals a predominant Fe 2p peak at a binding energy of 708.3–708.4 eV, which can be attributed to Fe(II) as in $[Fe(CN)_6]^{4-}$.[50] Co binding energies cannot be unambiguously deconvoluted. However, an obvious peak maximum at around 780–781 eV is attributed to Co(III) in the structure. This means that upon **CoFe-PB** formation, starting reagents

$[Fe(CN)_6]^{3-}$ and $Co^{2+}(aq)$ undergo (partial) electron transfer to yield a majority of Fe^{2+} and Co^{3+} centers in the fresh electrodes (Table S1 and Figures S7–S11). XPS analysis was also carried out after photoelectrochemical treatment (1 h at 1.23 V vs RHE under 1 sun irradiation). No significant changes were detected for the Fe and Co centers, confirming the redox stability of the **CoFe-PB** material under water oxidation conditions.

Additional evidence on the formation of a PB solid structure on the surface of the $BiVO_4$ electrodes comes from infrared spectroscopy (FT-IR). The spectra (Figure S12) clearly show the characteristic and unique C–N stretching mode at frequencies in the 2070–2150 cm^{-1} range. The multiple bands also confirm the presence of both metals in multiple oxidation states, typical of these nonstoichiometric solids.

Cyclic voltammetry (CV) using **CoFe-PB**/$BiVO_4$ photoanodes was carried out under chopped (Figure 2a) and constant (Figure 2b) illumination (100 mW/cm²) in a neutral (pH 7) KPi buffer (0.1 M) solution. The photocurrent density is significantly improved when **CoFe-PB** is present, particularly at the low-voltage region, accompanied by a large cathodic shift of the onset potential. The transient cathodic dark current observed in the **CoFe-PB**/$BiVO_4$ sample in Figure 2a originates from back-reduction of oxidized Co centers by electrons from the $BiVO_4$ conduction band, after turning off the light. A similar phenomenon was previously reported for CoP$_i$-modified hematite photoanodes.[36] The onset potentials were determined from quasi steady-state j–V curves obtained at 1 mV/s (Figure 2b). The voltage needed to attain 0.1 mA/cm² photocurrent was taken as the onset potential (V_{on}).[51] The obtained values were 0.3 V versus RHE for **CoFe-PB**/$BiVO_4$ and 1.1 V versus RHE for bare $BiVO_4$, reflecting a 0.8 V gain. This is directly connected to the estimated photovoltage from open circuit measurements in the dark and under illumination. The photovoltage increases from 0.15 V for bare $BiVO_4$ to 0.60 V upon deposition of **CoFe-PB** (Figure S13). This behavior has been previously ascribed to passivation of surface states or release of Fermi-level pinning at the semiconductor–liquid junction.[6,52]

The spectral signature of the photocurrent, characterized by the incident photon-to-current conversion efficiency (IPCE), was obtained for both pristine and **CoFe-PB**-decorated $BiVO_4$ photoelectrodes (Figure 2c). The 6-fold enhancement of the photocurrent observed between 350 and 450 nm is fully consistent with the results obtained by cyclic voltammetry. Indeed, the integrated photocurrents (0.38 mA/cm² for $BiVO_4$ and 0.92 mA/cm² for **CoFe-PB**/$BiVO_4$) perfectly match those obtained at 1.23 V versus RHE by cyclic voltammetry (0.40 and 0.95 mA/cm², respectively). Moreover, the full spectral absorption range of $BiVO_4$ is not affected by the presence of the **CoFe-PB** catalyst. This should be related to the very low catalyst coverage (1–2%). Thus, the **CoFe-PB** absorption band at 520–550 nm is not fully developed and does not interfere. Indeed, it is not even detected (Figure S14). The calculated $BiVO_4$ band gap, between 2.40 and 2.45 eV, is not affected by the catalyst either, and it is in good agreement with other reports.[53] On the other hand, IPCE measurements of **CoFe-PB**/$BiVO_4$ in the presence of a hole scavenger (1 M Na_2SO_3) (Figure 2d) show almost identical values compared to those for water oxidation (in buffer), suggesting a 100% faradaic efficiency for the **CoFe-PB** catalyst.

The long-term stability of the **CoFe-PB**/$BiVO_4$ photoanodes was assessed by chronoamperometric measurements at 1.23 V

versus RHE under constant (Figure 2e) and chopped (Figure 2f) illumination (100 mW/cm^2). After an initial transient decrease of the photocurrent during 1 h, the photoanodes show a remarkable stability, with a mere decrease of about 10% current density over a time scale of more than 50 h. Remarkably, an analogous decrease is observed for bare BiVO$_4$ photoanodes. Thus, we can assign this decay to BiVO$_4$ deactivation[49] and not to catalytic fatigue. Additionally, no catalyst leaching was detected by ion plasma chromatography (IPC) analysis of the supernatant buffer solutions after water splitting, suggesting excellent catalytic stability for this system (Tables S2 and S3), in agreement with previous studies.[29,32]

The high ex situ stability of this catalyst is worth mentioning. The photoelectrodes can be stored and dried in air, for several days, while retaining their photocatalytic activity, as confirmed by subsequent measurements (Figure 2f). This outstanding stability in air constitutes a clear advantage over the widely known cobalt oxide (CoP$_i$ or CoO$_x$) systems, which easily crack upon drying, leading to fatal catalytic loss (Figure S15).[36,54]

To benchmark the performance of the **CoFe-PB** catalyst under the same experimental conditions, CoO$_x$ and FeOOH (as related WOCs containing Fe or Co) were deposited on top of our nanostructured BiVO$_4$ films (see Supporting Information for details). The photoelectrochemical behavior of **CoFe-PB** clearly outperforms both catalysts (Figure 3a). Because deposition conditions were not specifically optimized, we cannot quantitatively use these data to sustain the overall superior catalytic activity. However, it is clear that **CoFe-PB** is at least photoelectrocatalytically competitive, with the additional advantages described above.

The **CoFe-PB**/BiVO$_4$ photoelectrochemical behavior was also characterized in the presence of an efficient hole scavenger. Under these conditions, it is assumed that no electron−hole recombination takes place at the semiconductor−liquid interface.[55,57,58] The experiments were carried out in a 1 M sodium sulfite (Na$_2$SO$_3$) solution (pH = 7.9), identified as the optimum concentration of the hole scavenger in solution (see Supporting Information, Figure S16, for details). Figure 4a shows the photocurrent densities obtained in both, buffer solution and 1 M Na$_2$SO$_3$ for bare and **Co-Fe-PB**/BiVO$_4$ anodes. In good agreement with previous studies, a large difference between the obtained photocurrents with and without the hole scavenger is observed for pristine BiVO$_4$, highlighting its poor water oxidation kinetics.[54] Indeed, BiVO$_4$ yields only <15% charge transfer efficiency even at high anodic potentials (>1.4 V vs RHE), where the large electric field precludes surface recombination (Figure 4b). Upon deposition of the **CoFe-PB** catalyst, the difference between the obtained photocurrents with and without the hole scavenger is significantly narrowed, indicating enhanced charge transfer kinetics. Nonetheless, both curves do not overlap, suggesting that further optimization is still possible (some guidelines can be extracted from DFT calculations, as shown below). The charge transfer efficiency for both photoanodes together with a comparison to that of a CoO$_x$ catalyst is shown in Figure 4b. In agreement with CV data (Figure 3a), CoO$_x$ exhibits lower charge transfer/catalytic efficiency for water oxidation up to 1.4 V versus RHE when compared to that of the **CoFe-PB** catalyst. The maximum charge transfer efficiency for the **CoFe-PB**/BiVO$_4$ system ($\approx$80%) is obtained in the 1.1−1.2 V versus RHE range (Table S4). The charge separation efficiency was also evaluated, and a 5−10% enhancement is obtained after
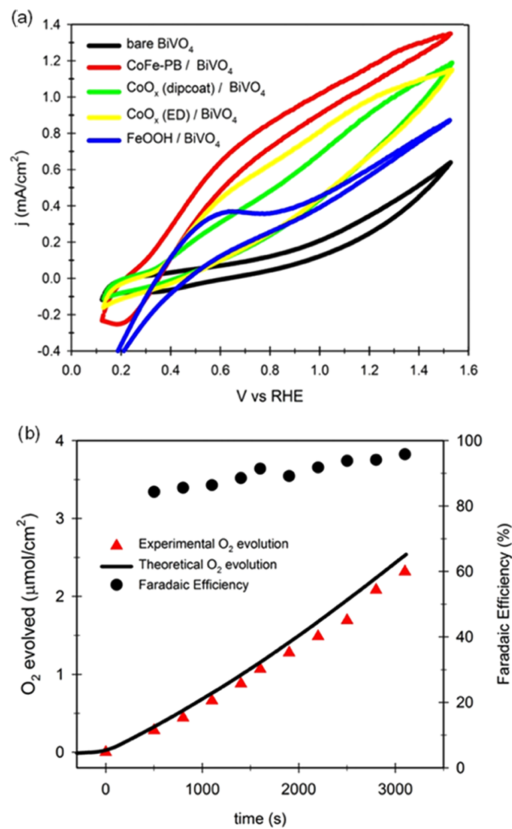

Figure 3. (a) Cyclic voltammetry curves under illumination (100 mW/cm^2) for bare BiVO$_4$ (black) and coated with different state-of-the-art catalysts: **CoFe-PB** (red), CoO$_x$ prepared by dip-coating (green) and electrodeposition (yellow),[55] and FeOOH (blue).[56] (b) Theoretical (black line) and measured (red triangles) O$_2$ evolution, as well as faradaic efficiency (black circles), of the **CoFe-PB**/BiVO$_4$ photoanode during chronoamperometry (CA) at 1.23 V vs RHE under 100 mW/cm^2 irradiation in 0.1 M KPi buffer (pH 7).

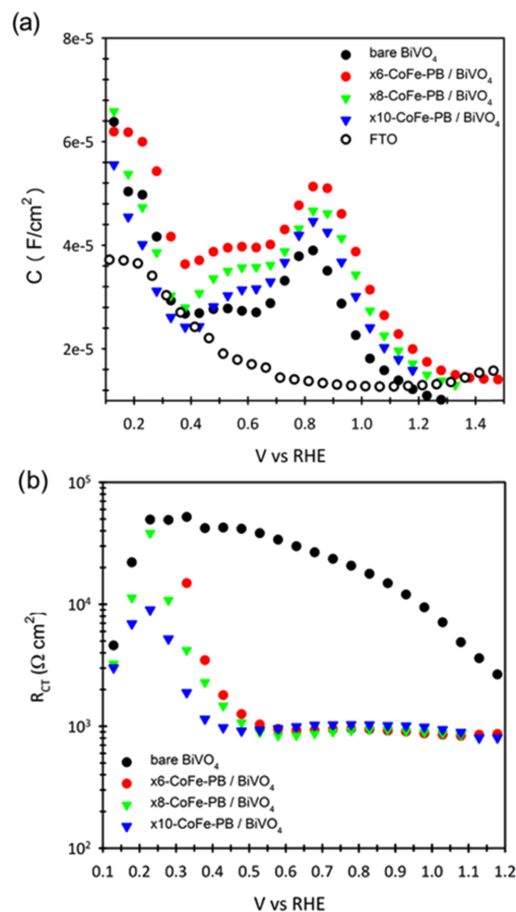**CoFe-PB** deposition (see the Supporting Information, Figure S17).

To confirm that measured photocurrents result from oxygen production at the photoanode and to exclude any contribution from side reactions, gas chromatography measurements under an inert argon atmosphere were carried out. Figure 3b shows the amount of detected oxygen (red triangles) at 1.23 V versus RHE after switching on the light source and compares it to the theoretical oxygen evolution (black line), which can be determined by the total amount of charge passed through the cell. The measured O$_2$ evolution coincides well with that theoretically estimated from the measured photocurrent by Faraday's law, maintaining >95% faradaic efficiency.

The enhanced photoelectrocatalytic behavior obtained upon deposition of the **CoFe-PB** layer can be due to several factors, such as (i) a stronger electric field at the interface leading to more favorable recombination kinetics;[59] (ii) the development of a capacitive layer,[60] which can act as a hole reservoir; (iii) the
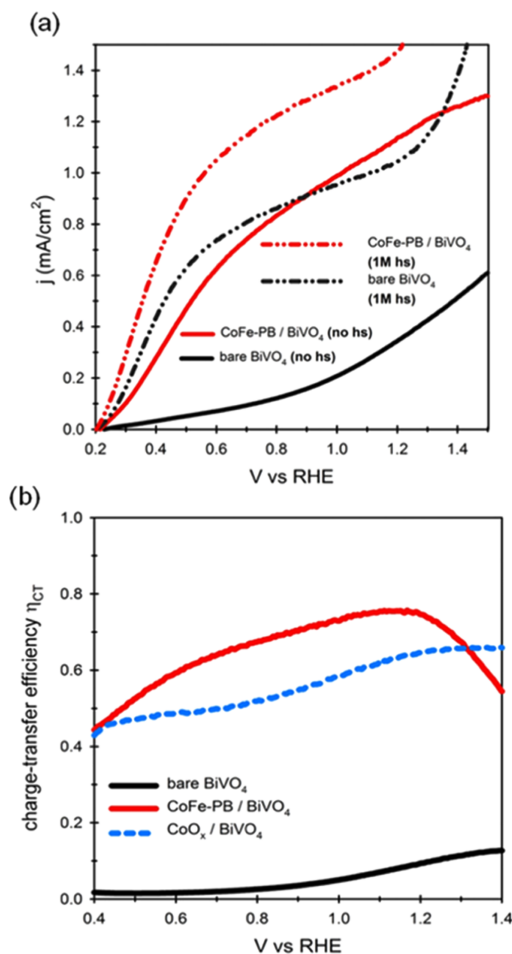
Figure 4. (a) Anodic scans (50 mV/s) of **CoFe-PB**-modified (red) and bare $BiVO_4$ (black) photoelectrodes under 1 sun irradiation in 0.1 M KPi buffer (solid lines) and after addition of hole scavenger Na_2SO_3 (dashed lines). (b) Calculated charge transfer efficiencies for both photoelectrodes as compared to those of $CoO_x/BiVO_4$ (dashed blue).

Figure 5. (a) Capacitance and (b) charge transfer resistance for bare (black solid circles) and different **CoFe-PB**-modified $BiVO_4$ electrodes, obtained by modeling the electrochemical system to a simple Randles circuit. The capacitance of the FTO substrate is also included in (a).

passivation of surface states;[61] (iv) a cathodic shift of the semiconductor bands due to a surface dipole;[62] and/or (v) suppression of surface recombination.[59,63] To gain insight into this issue, Electrochemical impedance spectroscopy (EIS) measurements were carried out on $BiVO_4$ and **CoFe-PB**/$BiVO_4$ electrodes at 0.1−1.2 V versus RHE under 100 mW/cm² illumination. Different **CoFe-PB** deposition cycles (×6, ×8, and ×10 cycles) were carried out to identify the effect of the catalyst loading on the measured response. The obtained Nyquist plots systematically showed a single arc (Figure S18) and, consequently, the data were fitted to a simple Randles circuit.[64] Independent of the **CoFe-PB** layer thickness, the capacitance of all electrodes is identical, within experimental error (Figure 5a), ruling out any significant participation of a capacitive mechanism. This is in contrast with the conclusions previously
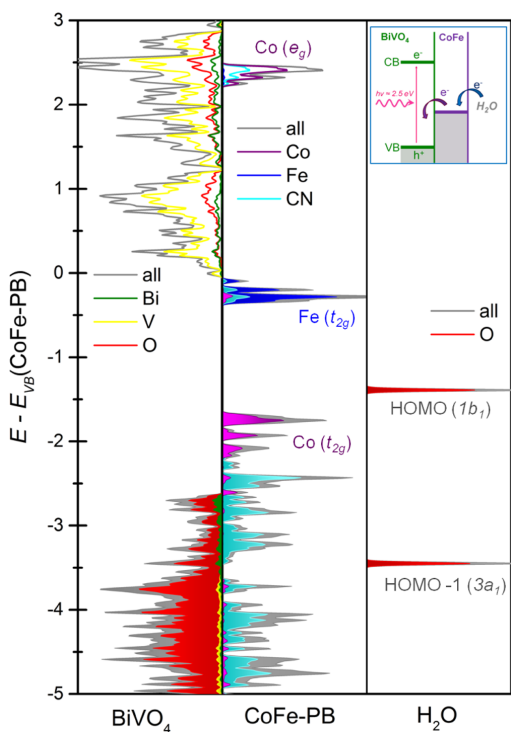
claimed for IrO_x and CoP_i when deposited on top of α-Fe_2O_3.[35,36,65] On $BiVO_4$, Durrant et al. concluded that CoP_i does not contribute significantly to the overall water oxidation current (<5%) but was essentially just retarding the electron-hole recombination.[59] In the same line, a recent study by Van de Krol et al. also claims that the photocurrent of $BiVO_4$ is limited by surface recombination rather than by surface catalysis.[63]

In the present study, the capacitance values obtained for all samples lie in the $10^{-5}-10^{-4}$ F/cm² region, suggesting an important contribution of the double layer capacitance of the electrode. For this reason, the capacitance of the bare FTO substrate is also included in Figure 5a. At applied voltages below 0.4 V and above 1.2 V versus RHE, the capacitance of the photoelectrodes is dominated by FTO. At intermediate voltages, the capacitance is dominated by $BiVO_4$. Additionally, in agreement with previous studies, a capacitive peak at 0.8 V

versus RHE is observed, which has been attributed to the V^{4+}/V^{5+} redox couple.[60] On the other hand, the charge transfer resistance drops to a constant value of ~1 kΩ at 0.5 V versus RHE for the samples coated with the **CoFe-PB** catalyst, whereas significantly higher voltages (>0.8 V) are needed for pristine $BiVO_4$ photoelectrodes (Figure 5b). Both the constant capacitance and the charge-transfer resistance drop at lower applied potentials, strongly suggests that **CoFe-PB** is acting as a true catalyst, enhancing charge transfer kinetics to the solution, although suppression of surface recombination cannot be ruled out at this stage.

The synergistic interaction between both $BiVO_4$ and **CoFe-PB** was assessed by hybrid density functional theory (DFT) calculations. Both the bulk monoclinic scheelite bismuth vanadate (ms-$BiVO_4$) and the **CoFe-PB** catalyst (topologically described as the ideal FCC structure-type $KCoFe[(CN)_6]$, Scheme 1) were modeled as well as a solvated single water molecule,[66] using a modified HSE03-13 functional (see the Supporting Information for a methodological discussion). Figure 6 shows the aligned densities of states (DOS) of the photoanode, the catalyst, and water. The $BiVO_4$ valence band (VB) edge consists of mainly O 2p and, to a smaller extent, Bi

6s contributions. This s−p hybridization is crucial as it enables ms-$BiVO_4$ to be a good hole conductor.[67−70] **CoFe-PB**, on the right-hand side, has filled valence band levels above the $BiVO_4$ VB edge, namely, the nonbonding t_{2g} states of Co (purple) and Fe (blue). The HOMO ($1b_1$) level of water, which lies about 0.34 eV above the Co t_{2g} band, is also presented in Figure 6.

The photoelectrochemical experiments can be understood as illustrated in the simplified energy diagram in Figure 6: Upon supra band gap illumination from the FTO substrate (2.55 eV from HSE03-13 calculation, in good agreement with the 2.40−2.45 eV experimental value, Figure S14) from the FTO substrate, an electron−hole pair is created at $BiVO_4$ close to the $BiVO_4$/FTO interface. Because of the applied positive bias, the electron moves to the FTO and enters the external circuit, whereas the photogenerated hole moves towards the **CoFe-PB**/$BiVO_4$ interface, where it is transferred to the **CoFe-PB** catalyst, being available for water oxidation. The $[Fe(CN)_6]$ units are coordinatively saturated and robust, as CN is a strong ligand when bonded from the C-end. Therefore, the interface between $BiVO_4$ and **CoFe-PB** is likely to be formed by the interaction of O atoms from the oxide and surface Co centers from **CoFe-PB**. The filled Co t_{2g} lies about 0.9 eV higher in energy compared with the VB of $BiVO_4$, which energetically favors the electron transfer from Co to the $BiVO_4$ VB, which is mainly formed by the O 2p band. The difference between the VB of the $BiVO_4$ substrate and the Co levels is in good agreement with the observed cathodic shift of the onset potential of 0.8 V. The subsequently created hole in the Co t_{2g} set is now available for water oxidation.

The cathodic shift of the onset potential, together with the increase of photovoltage due to the **CoFe-PB** layer, can then be interpreted as follows: Considering $BiVO_4$, the distance between the Bi 6s states and the HOMO position of water is about 1.3 eV, causing a relatively high potential needed to initiate water oxidation (1.1 V vs RHE). Thus, the $BiVO_4$ states do not overlap with the HOMO and and hence charge transfer between those states is kinetically hampered, which implies that more external energy is needed in order to overcome this barrier. In the presence of **CoFe-PB**, the situation changes and the photogenerated hole at the $BiVO_4$ surface is filled by electrons from the catalyst. In **CoFe-PB**, the energy difference to the water HOMO is reduced to 0.3−0.4 eV, facilitating water oxidation at a lower onset (0.3 V vs RHE). This smaller energy difference (as well as symmetry considerations) allows good overlap of Co t_{2g} and the water HOMO ($1b_1$). Nevertheless, there is still an energy mismatch of about 0.3 eV to be overcome, and this situation can be related to a <100% charge transfer efficiency of **CoFe-PB**/$BiVO_4$ (See Figure 4b). A more efficient charge-transfer catalyst would require catalytically active states to lie as close as possible to the HOMO level of water, while possessing an uncoordinated site with matching symmetry and further keeping the good electronic overlap with the light absorber.

Figure 6. Densities of states of $BiVO_4$ (left), $KCoFe[(CN)_6]$ (middle), and solvated H_2O molecule[64] (right) aligned by their O 2s bands. The **CoFe-PB** valence band edge is set as zero energy level, and filled electronic states are represented by filled areas. A simplified representation is given as the inset (top right). Above band gap light excitation creates a hole (h^+) in the $BiVO_4$ VB, which is filled by electron transfer from the **CoFe-PB** catalyst, which subsequently oxidizes water.

CONCLUSIONS

In summary, we have demonstrated that integrated photo-electrocatalytic systems with earth-abundant materials and low-cost synthetic procedures based on the **CoFe-PB**/$BiVO_4$ system exhibit excellent performance with (i) remarkable increase of photocurrent, (ii) low onset potentials, and (iii) excellent stability. Impedance spectroscopy analysis suggests that **CoFe-PB** is acting as a true catalyst, enhancing charge transfer kinetics to the solution, as inferred by the constant

capacitance and decreased charge transfer resistance observed. **CoFe-PB** appears to be the main catalyst in these **CoFe-PB/BiVO₄** photoelectrodes, resulting in faster oxygen evolution and significantly lower onset potentials when compared to those of bare electrodes.

Our results also highlight the importance of the interface between the catalyst and photoanode. Under general conditions, **CoFe-PB** has not been systematically faster than CoP_i or CoO_x.[28,31] However, it is intrinsically better matching the activity of the $BiVO_4$ semiconductor. Indeed, the performance of our photoanodes also exceeds those results obtained with any other decorated $BiVO_4$ photoelectrode, as discussed through the text.

Furthermore, the outstanding performance of this system can be understood on the basis of the adequate alignment of the valence levels of the $BiVO_4$ light-harvesting material and the **CoFe-PB** catalyst together with the matching symmetry and small energy difference between the Co levels in the catalyst and the HOMO of water. DFT also provides a useful guideline for further catalyst optimization to achieve 100% charge transfer efficiency for water oxidation, by achieving a closer proximity of the Co states and the HOMO level of water, while still maintaining an uncoordinated site with matching symmetry and good electronic overlap with the light absorber. Finally, the outcome of this study can be extrapolated to other metal oxides, providing that a good adsorption of **CoFe-PB** on the metal oxide surface, which leads to high mechanic stability and efficient interfacial charge transfer, is favored by the energy level alignment and orbital symmetry considerations.

■ ASSOCIATED CONTENT

ⓢ Supporting Information

The Supporting Information is available free of charge on the ACS Publications website at DOI: 10.1021/acsami.7b09449.

> Additional computational details, electrochemical data, and extensive information on the structural and photo-electrochemical characterization of the employed materials (SEM, TEM, EDS, XPS, IR, IPC, electrochemical measurements, comparison to other catalysts, EIS, and computational methods); present DFT calculations have been uploaded to the ioChem-BD database[71,72] (PDF)

■ AUTHOR INFORMATION

Corresponding Authors
*E-mail: nlopez@iciq.es (N.L.).
*E-mail: jrgalan@iciq.es (J.-R.G.-M.).
*E-mail: sjulia@uji.es (S.G.).

ORCID ⓘ
Núria López: 0000-0001-9150-5941
José-Ramón Galán-Mascarós: 0000-0001-7983-9762
Sixto Gimenez: 0000-0002-4522-3174

Notes
The authors declare no competing financial interest.

■ REFERENCES

(1) Gimenez, S.; Bisquert, J. *Photoelectrochemical Solar Fuel Production: From Basic Principles to Advanced Devices*; Springer International Publishing: Cham, 2016.

(2) Walter, M. G.; Warren, E. L.; McKone, J. R.; Boettcher, S. W.; Mi, Q.; Santori, E. A.; Lewis, N. S. Solar Water Splitting Cells. *Chem. Rev.* **2010**, *110*, 6446−6473.

(3) Pinaud, B. A.; Benck, J. D.; Seitz, L. C.; Forman, A. J.; Chen, Z.; Deutsch, T. G.; James, B. D.; Baum, K. N.; Baum, G. N.; Ardo, S.; Wang, H.; Miller, E.; Jaramillo, T. F. Technical and Economic Feasibility of Centralized Facilities for Solar Hydrogen Production via Photocatalysis and Photoelectrochemistry. *Energy Environ. Sci.* **2013**, *6*, 1983−2002.

(4) Fujishima, A.; Honda, K. Electrochemical Photolysis of Water at a Semiconductor Electrode. *Nature* **1972**, *238*, 37−38.

(5) Yang, C.; Wang, Z.; Lin, T.; Yin, H.; Lü, X.; Wan, D.; Xu, T.; Zheng, C.; Lin, J.; Huang, F.; Xie, X.; Jiang, M. Core-Shell Nanostructured "Black" Rutile Titania as Excellent Catalyst for Hydrogen Production Enhanced by Sulfur Doping. *J. Am. Chem. Soc.* **2013**, *135*, 17831−17838.

(6) Du, C.; Yang, X.; Mayer, M. T.; Hoyt, H.; Xie, J.; McMahon, G.; Bischoping, G.; Wang, D. Hematite-Based Water Splitting with Low Turn-On Voltages. *Angew. Chem., Int. Ed.* **2013**, *52*, 12692−12695.

(7) Jang, J.-W.; Du, C.; Ye, Y.; Lin, Y.; Yao, X.; Thorne, J.; Liu, E.; McMahon, G.; Zhu, J.; Javey, A.; Guo, J.; Wang, D. Enabling Unassisted Solar Water Splitting by Iron Oxide and Silicon. *Nat. Commun.* **2015**, *6*, No. 7447.

(8) Kay, A.; Cesar, I.; Graetzel, M. New Benchmark for Water Photooxidation by Nanostructured α-Fe₂O₃ Films. *J. Am. Chem. Soc.* **2006**, *128*, 15714−15721.

(9) Kim, J. Y.; Magesh, G.; Youn, D. H.; Jang, J.-W.; Kubota, J.; Domen, K.; Lee, J. S. Single-Crystalline, Wormlike Hematite Photoanodes for Efficient Solar Water Splitting. *Sci. Rep.* **2013**, *3*, No. 2681.

(10) Brillet, J.; Yum, J.-H.; Cornuz, M.; Hisatomi, T.; Solarska, R.; Augustynski, J.; Graetzel, M.; Sivula, K. Highly Efficient Water Splitting by a Dual-Absorber Tandem Cell. *Nat. Photonics* **2012**, *6*, 824−828.

(11) Alexander, B. D.; Kulesza, P. J.; Rutkowska, I.; Solarska, R.; Augustynski, J. Metal Oxide Photoanodes for Solar Hydrogen Production. *J. Mater. Chem.* **2008**, *18*, 2298−2303.

(12) Deb, S. K. Opportunities and Challenges in Science and Technology of WO₃ for Electrochromic and Related Applications. *Sol. Energy Mater. Sol. Cells* **2008**, *92*, 245−258.

(13) Ping, Y.; Goddard, W. A., III; Galli, G. A. Energetics and Solvation Effects at the Photoanode/Catalyst Interface: Ohmic Contact versus Schottky Barrier. *J. Am. Chem. Soc.* **2015**, *137*, 5264−5267.

(14) Abdi, F. F.; Han, L.; Smets, A. H. M.; Zeman, M.; Dam, B.; van de Krol, R. Efficient Solar Water splitting by Enhanced Charge Separation in a Bismuth Vanadate-Silicon Tandem Photoelectrode. *Nat. Commun.* **2013**, *4*, No. 2195.

(15) Chatchai, P.; Murakami, Y.; Kishioka, S.-Y.; Nosaka, A. Y.; Nosaka, Y. FTO/SnO₂/BiVO₄ composite Photoelectrode for Water Oxidation under Visible Light Irradiation. *Electrochem. Solid-State Lett.* **2008**, *11*, H160−H163.

(16) Kim, T. W.; Choi, K.-S. Nanoporous BiVO$_4$ Photoanodes with Dual-Layer Oxygen Evolution Catalysts for Solar Water Splitting. *Science* 2014, *343*, 990−994.

(17) Park, Y.; McDonald, K. J.; Choi, K.-S. Progress in Bismuth Vanadate Photoanodes for Use in Solar Water Oxidation. *Chem. Soc. Rev.* 2013, *42*, 2321−2337.

(18) Shi, X.; Zhang, K.; Shin, K.; Ma, M.; Kwon, J.; Choi, I. T.; Kim, J. K.; Kim, H. K.; Wang, D. H.; Park, J. H. Unassisted Photo-electroChemical Water Splitting beyond 5.7% Solar-to-Hydrogen Conversion Efficiency by a Wireless Monolithic Photoanode/Dye-Sensitised Solar Cell Tandem Device. *Nano Energy* 2015, *13*, 182−191.

(19) Shi, X.; Choi, Y.; Zhang, K.; Kwon, J.; Kim, D. Y.; Lee, J. K.; Oh, S. H.; Kim, J. K.; Park, J. H. Efficient Photoelectrochemical Hydrogen Production from Bismuth Vanadate-Decorated Tungsten Trioxide Helix Nanostructures. *Nat. Commun.* 2014, *5*, No. 4775.

(20) Chhetri, M.; Dey, S.; Rao, C. N. R. Photoelectrochemical Oxygen Evolution Reaction Activity of Amorphous Co−La Double Hydroxide-BiVO4 Fabricated by Pulse Plating Electrodeposition. *ACS Energy Lett.* 2017, *2*, 1062−1069.

(21) Pihosh, Y.; Turkevych, I.; Mawatari, K.; Uemura, J.; Kazoe, Y.; Kosar, S.; Makita, K.; Sugaya, T.; Matsui, T.; Fujita, D.; Tosa, M.; Kondo, M.; Kitamori, T. Photocatalytic Generation of Hydrogen by Core-Shell WO$_3$/BiVO$_4$ Nanorods with Ultimate Water Splitting Efficiency. *Sci. Rep.* 2015, *5*, No. 11141.

(22) Qiu, Y.; Liu, W.; Chen, W.; Zhou, G.; Hsu, P.-C.; Zhang, R.; Liang, Z.; Fan, S.; Zhang, Y.; Cui, Y.; et al. Efficient Solar-Driven Water Splitting by Nanocone BiVO$_4$-perovskite Tandem Cells. *Sci. Adv.* 2016, *2*, No. e1501764.

(23) Vesborg, P. C. K.; Jaramillo, T. F. Addressing the Terawatt Challenge: Scalability in the Supply of Chemical Elements for Renewable Energy. *RSC Adv.* 2012, *2*, 7933−7947.

(24) Guo, W.; Chemelewski, W. D.; Mabayoje, O.; Xiao, P.; Zhang, Y.; Mullins, C. B. Synthesis and Characterization of CuV2O6 and Cu$_2$V$_2$O$_7$: Two Photoanode Candidates for Photoelectrochemical Water Oxidation. *J. Phys. Chem. C* 2015, *119*, 27220−27227.

(25) Seabold, J. A.; Neale, N. R. All First Row Transition Metal Oxide Photoanode for Water Splitting Based on Cu$_3$V$_2$O$_8$. *Chem. Mater.* 2015, *27*, 1005−1013.

(26) Cardenas-Morcoso, D.; Peiro-Franch, A.; Herraiz-Cardona, I.; Gimenez, S. Chromium Doped Copper Vanadate Photoanodes for Water Splitting. *Catal. Today* 2017, *290*, 65−72.

(27) Galán-Mascarós, J. R. Water Oxidation at Electrodes Modified with Earth-Abundant Transition-Metal Catalysts. *ChemElectroChem* 2015, *2*, 37−50.

(28) Gerken, J. B.; McAlpin, J. G.; Chen, J. Y. C.; Rigsby, M. L.; Casey, W. H.; Britt, R. D.; Stahl, S. S. Electrochemical Water Oxidation with Cobalt-Based Electrocatalysts from pH 0−14: The Thermody-namic Basis for Catalyst Structure, Stability, and Activity. *J. Am. Chem. Soc.* 2011, *133*, 14431−14442.

(29) Pintado, S.; Goberna-Ferrón, S.; Escudero-Adán, E. C.; Galan-Mascarós, J. R. Fast and Persistent Electrocatalytic Water Oxidation by Co−Fe Prussian Blue Coordination Polymers. *J. Am. Chem. Soc.* 2013, *135*, 13270−13273.

(30) Yamada, Y.; Oyama, K.; Gates, R.; Fukuzumi, S. High Catalytic Activity of Heteropolynuclear Cyanide Complexes Containing Cobalt and Platinum Ions: Visible-Light Driven Water Oxidation. *Angew. Chem., Int. Ed.* 2015, *54*, 5613−5617.

(31) Aksoy, M.; Nune, S. V. K.; Karadas, F. A Novel Synthetic Route for the Preparation of an Amorphous Co/Fe Prussian Blue Coordination Compound with High Electrocatalytic Water Oxidation Activity. *Inorg. Chem.* 2016, *55*, 4301−4307.

(32) Han, L.; Tang, P. Y.; Reyes-Carmona, A.; Rodriguez-Garcia, B.; Torrens, M.; Morante, J. R.; Arbiol, J.; Galan-Mascarós, J. R. Enhanced Activity and Acid pH Stability of Prussian Blue-type Oxygen Evolution Electrocatalysts Processed by Chemical Etching. *J. Am. Chem. Soc.* 2016, *138*, 16037−16045.

(33) de Tacconi, N. R.; Rajeshwar, K.; Lezna, R. O. Metal Hexacyanoferrates: Electrosynthesis, in Situ Characterization, and Applications. *Chem. Mater.* 2003, *15*, 3046−3062.

(34) Goberna-Ferrón, S.; Hernández, W. Y.; Rodríguez-García, B.; Galan-Mascaros, J. R. Light-Driven Water Oxidation with Metal Hexacyanometallate Heterogeneous Catalysts. *ACS Catal.* 2014, *4*, 1637−1641.

(35) Badia-Bou, L.; Mas-Marza, E.; Rodenas, P.; Barea, E. M.; Fabregat-Santiago, F.; Gimenez, S.; Peris, E.; Bisquert, J. Water Oxidation at Hematite Photoelectrodes with an Iridium-Based Catalyst. *J. Phys. Chem. C* 2013, *117*, 3826−3833.

(36) Klahr, B.; Gimenez, S.; Fabregat-Santiago, F.; Bisquert, J.; Hamann, T. W. Photoelectrochemical and Impedance Spectroscopic Investigation of Water Oxidation with "Co−Pi"-Coated Hematite Electrodes. *J. Am. Chem. Soc.* 2012, *134*, 16693−16700.

(37) Kang, D.; Park, Y.; Hill, J. C.; Choi, K.-S. Preparation of Bi-Based Ternary Oside Photoanodes BiVO$_4$, Bi$_2$WO$_6$, Bi$_2$Mo$_3$O$_{12}$ Using Dendritic Bi Metal Electrodes. *J. Phys. Chem. Lett.* 2014, *5*, 2994−2999.

(38) Abdi, F. F.; Savenije, T. J.; May, M. M.; Dam, B.; van de Krol, R. The Origin of Slow Carrier Transport in BiVO$_4$ Thin Film Photoanodes: A Time-Resolved Microwave Conductivity Study. *J. Phys. Chem. Lett.* 2013, *4*, 2752−2757.

(39) Rettie, A. J. E.; Lee, H. C.; Marshall, L. G.; Lin, J.-F.; Capan, C.; Lindemuth, J.; McCloy, J. S.; Zhou, J.; Bard, A. J.; Mullins, C. B. Combines Charge Carrier Transport and Photoelectrochemical Characterization of BiVO$_4$ Single Crystals: Intrinsic Behavior of a Complex Metal Oxide. *J. Am. Chem. Soc.* 2013, *135*, 11389−11396.

(40) Ahn, H.-J.; Kwak, M.-J.; Lee, J.-S.; Yoon, K.-Y.; Jang, J.-H. Nanoporous Hematite Structures to Overcome Short Diffusion Lengths in Water Splitting. *J. Mater. Chem. A* 2014, *2*, 19999−20003.

(41) Dare-Edwards, M.-P.; Goodenough, J. B.; Hamnett, A.; Trevellick, P. R. Electrochemistry and Photoelectrochemistry of Iron(III) Oxide. *J. Chem. Soc., Faraday Trans. 1* 1983, *79*, 2027−2041.

(42) Kennedy, J.-H.; Frese, K. W. Photooxidation of Water at alpha-Fe2O3 Electrodes. *Chem. Informationsdienst* 1977, *124*, C130−C130.

(43) Hafner, J.; Kresse, G. The Vienna Ab-Initio Simulation Program VASP: An Efficient and Versatile Tool for Studying the Structural, Dynamic and Electronics Properties of Materials. Plenum Press Div Plenum Publishing Corp.: New York, 1997.

(44) Kresse, G.; Furthmuller, J. Efficient Iterative Schemes for Ab Initio Total-Energy Calculations Using a Plane-Wave Basis Set. *Phys. Rev. B: Condens. Matter Mater. Phys.* 1996, *54*, 11169−11186.

(45) Hegner, F. S.; Galan-Mascaros, J. R.; Lopez, N. A. Database of the Structural and Electronic Properties of Prussian Blue, Prussian White, and Berlin Green Compounds through Density Functional Theory. *Inorg. Chem.* 2016, *55*, 12851−12862.

(46) Kresse, G.; Joubert, D. From Ultrasoft Pseudopotentials to the Projector Augmented-Wave Method. *Phys. Rev. B: Condens. Matter Mater. Phys.* 1999, *59*, 1758−1775.

(47) Lezna, R. O.; Romagnoli, R.; de Tacconi, N. R.; Rajeshwar, K. Cobalt Hexacyanoferrate: Compound Stoichiometry, Infrared Spec-troelectrochemistry, and Photoinduced Electron Transfer. *J. Phys. Chem. B* 2002, *106*, 3612−3621.

(48) Sleight, A. W.; Chen, H. Y.; Ferretti, A.; Cox, D. E. Crystal Growth and Structure of BiVO$_4$. *Mater. Res. Bull.* 1979, *14*, 1571−1581.

(49) Toma, F. M.; Cooper, J. K.; Kunzelmann, V.; McDowell, M. T.; Yu, J.; Larson, D. M.; Borys, N. J.; Abelyan, C.; Beeman, J. W.; Yu, K. M.; Yang, J. H.; Chen, L.; Shaner, M. R.; Spurgeon, J.; Houle, F. A.; Persson, K. A.; Sharp, I. D. Mechanistic Insights into Chemical and Photochemical Transformations of Bismuth Vanadate Photoanodes. *Nat. Commun.* 2016, *7*, No. 12012.

(50) Cris, B. V. *Handbook of Monochromatic XPS Spectra*; Wiley: Weinheim, 2000.

(51) Bourgeteau, T.; Tondelier, D.; Geffroy, B.; Brisse, R.; Cornut, R.; Artero, V.; Jousselme, B. Enhancing the Performances of P$_3$HT:PCBM-MoS$_3$-Based H$_2$-Evolving Photocathodes with Interfacial Layers. *ACS Appl. Mater. Interfaces* 2015, *7*, 16395−16403.

(52) Trzesniewski, B. J.; Smith, W. A. Photocharged BiVO$_4$ Photoanodes for Improved Solar Water Splitting. *J. Mater. Chem. A* **2016**, *4*, 2919–2926.

(53) Cooper, J. K.; Gul, S.; Toma, F. M.; Chen, L.; Liu, Y.-S.; Guo, J.; Ager, J. W.; Yano, J.; Sharp, I. D. Indirect Bandgap and Optical Properties of Monoclinic Bismuth Vanadate. *J. Phys. Chem. C* **2015**, *119*, 2969–2974.

(54) Jeon, T. H.; Choi, W.; Park, H. Cobalt-Phosphate Complexes Catalyze the Photoelectrochemical Water Oxidation of BiVO$_4$ electrodes. *Phys. Chem. Chem. Phys.* **2011**, *13*, 21392–21401.

(55) Zhong, D. K.; Choi, S.; Gamelin, D. R. Near-Complete Suppression of Surface Recombination in Solar Photoelectrolysis by "Co-Pi" Catalyst-Modified W:BiVO$_4$. *J. Am. Chem. Soc.* **2011**, *133*, 18370–18377.

(56) Seabold, J. A.; Choi, K.-S. Efficient and stable Photo-Oxidation of Water by a Bismuth Vanadate Photoanode Coupled with an Iron Oxyhydroxide Oxygen Evolution Catalyst. *J. Am. Chem. Soc.* **2012**, *134*, 2186–2192.

(57) Dotan, H.; Sivula, K.; Graetzel, M.; Rothschild, A.; Warren, S. C. Probing the Photoelectrochemical Properties of Hematite (α-Fe$_2$O$_3$) Electrodes Using Hydrogen Peroxide as a Hole Scavenger. *Energy Environ. Sci.* **2011**, *4*, 958–964.

(58) Shaddad, M. N.; Ghanem, M. A.; Al-Mayouf, A. M.; Gimenez, S.; Bisquert, J.; Herraiz-Cardona, I. Cooperative Catalytic Effect of ZrO$_2$ and α-Fe$_2$O$_3$ Nanoparticles on BiVO$_4$ Photoanodes for Enhanced Photoelectrochemical Water Splitting. *ChemSusChem* **2016**, *9*, 2779–2783.

(59) Ma, Y.; Kafizas, A.; Pendlebury, S. R.; Le Formal, F.; Durrant, J. R. Photoinduced Absorption Spectroscopy of CoPi on BiVO$_4$: The Function of CoPi during Water Oxidation. *Adv. Funct. Mater.* **2016**, *26*, 4951–4960.

(60) Trześniewski, B. J.; Digdaya, I. A.; Nagaki, T.; Ravishankar, S.; Herraiz-Cardona, I.; Vermaas, D. A.; Longo, A.; Gimenez, S.; Smith, W. A. Near-Complete Suppression of Surface Losses and Total Internal Quantum Efficiency in BiVO$_4$ Photoanodes. *Energy Environ. Sci.* **2017**, *10*, 1517–1529.

(61) Steier, L.; Herraiz-Cardona, I.; Gimenez, S.; Fabregat-Santiago, F.; Bisquert, J.; Tilley, S. D.; Graetzel, M. Understanding the Role of Underlayers and Overlayers in Thin Film Hematite Photoanodes. *Adv. Funct. Mater.* **2014**, *24*, 7681–7688.

(62) Xu, J.; Herraiz-Cardona, I.; Yang, X.; Gimenez, S.; Antonietti, M.; Shalom, M. The Complex Role of Carbon Nitride as a Sensitizer in Photoelectrochemical Cells. *Adv. Opt. Mater.* **2015**, *3*, 1052–1058.

(63) Zachäus, C.; Abdi, F. F.; Peter, L. M.; van de Krol, R. Photocurrent of BiVO$_4$ Is Limited by Surface Recombination, not Surface Catalysis. *Chem. Sci.* **2017**, *8*, 3712–3719.

(64) Randles, J. E. B. Kinetics of Rapid Electrode Reactions. *Discuss. Faraday Soc.* **1947**, *1*, 11–19.

(65) Barroso, M.; Cowan, A. J.; Pendlebury, S. R.; Grätzel, M.; Klug, D. R.; Durrant, J. R. The Role of Cobalt Phosphate in Enhancing the Photocatalytic Activity of α-Fe$_2$O$_3$ toward Water Oxidation. *J. Am. Chem. Soc.* **2011**, *133*, 14868–14871.

(66) Garcia-Ratés, M.; López, N. Multigrid-Based Methodology for Implicit Solvation Models in Periodic DFT. *J. Chem. Theory Comput.* **2016**, *12*, 1331–1341.

(67) Cooper, J. K.; Gul, S.; Toma, F. M.; Chen, L.; Glans, P.-A.; Guo, J.; Ager, J. W.; Yano, J.; Sharp, I. D. Electronic Structure of Monoclinic BiVO$_4$. *Chem. Mater.* **2014**, *26*, 5365–5373.

(68) Zhao, Z.; Li, Z.; Zou, Z. Electronic Structure and Optical Properties of Monoclinic Clinobisvanite BiVO$_4$. *Phys. Chem. Chem. Phys.* **2011**, *13*, 4746–4753.

(69) Walsh, A.; Yan, Y.; Huda, M. N.; Al-Jassim, M. M.; Wei, S.-H. Band Edge Electronic Structure of BiVO$_4$: Elucidating the Role of the Bi and V d Orbitals. *Chem. Mater.* **2009**, *21*, 547–551.

(70) Kweon, K. E.; Hwang, G. S. Structural Phase-Dependent Hole Localization and Transport in Bismuth Vanadate. *Phys. Rev. B* **2013**, *87*, No. 205202.

(71) Álvarez-Moreno, M.; de Graaf, C.; López, N.; Maseras, F.; Poblet, J. M.; Bo, C. Managing the Computational Chemistry Big Data Problem: The ioChem BD Platform. *J. Chem. Inf. Model.* **2015**, *55*, 95–103.

(72) DOI:10.19061/iochem-bd-1-50.

Level Alignment as Descriptor for Semiconductor/Catalyst Systems in Water Splitting: The Case of Hematite/Cobalt Hexacyanoferrate Photoanodes

Franziska Simone Hegner,[a] Drialys Cardenas-Morcoso,[b] Sixto Giménez,*[b] Núria López,*[a]
and Jose Ramon Galan-Mascaros*[a, c]

The realization of artificial photosynthesis may depend on the efficient integration of photoactive semiconductors and catalysts to promote photoelectrochemical water splitting. Many efforts are currently devoted to the processing of multicomponent anodes and cathodes in the search for appropriate synergy between light absorbers and active catalysts. No single material appears to combine both features. Many experimental parameters are key to achieve the needed synergy between both systems, without clear protocols for success. Herein, we show how computational chemistry can shed some light on this cumbersome problem. DFT calculations are useful to predict adequate energy-level alignment for thermodynamically favored hole transfer. As proof of concept, we experimentally confirmed the limited performance enhancement in hematite photoanodes decorated with cobalt hexacyanoferrate as a competent water-oxidation catalyst. Computational methods describe the misalignment of their energy levels, which is the origin of this mismatch. Photoelectrochemical studies indicate that the catalyst exclusively shifts the hematite surface state to lower potentials, which therefore reduces the onset for water oxidation. Although kinetics will still depend on interface architecture, our simple theoretical approach may identify and predict plausible semiconductor/catalyst combinations, which will speed up experimental work towards promising photoelectrocatalytic systems.

Introduction

The production of solar fuels consists of harvesting sunlight as an energy source to transform a substrate into an energy-rich chemical through reduction. The reducing equivalents (electrons) are extracted from the complementary semireaction, in which another substrate (ideally water) gets oxidized. Hence, the efficiency and kinetics of the overall process undoubtedly depends on the latter, although the oxidation products typically have no commercial value. Without a fast and robust oxidation process, solar fuels will never reach market interests.

This is the reason why water-oxidation catalysis has become such a hot topic, as it is generally considered the major bottleneck towards the realization of artificial photosynthesis. Beyond electric potential requirements, water oxidation is a very slow process that includes a four-electron transfer and the chemically challenging formation of an oxygen–oxygen bond.

Several photoactive semiconductors possess appropriately aligned valence-band levels and a suitable band gap to drive water oxidation in their photoexcited state.[1] In this context, n-type metal-oxide semiconductor materials (e.g., TiO_2,[2] Fe_2O_3,[3] WO_3,[4] $BiVO_4$,[5] etc.) have been extensively studied as promising candidates to develop this technology, as they present relatively good stability under operation in harsh environments. From this family, α-Fe_2O_3 (hematite) is particularly appealing, not only because its favorable band gap of 1.9–2.2 eV allows for light absorption in the visible region but mainly because "rust" is one of the most abundant and cheap materials on earth.[3, 6–9]

However, its application in photoelectrochemical water oxidation is severely limited owing to its unfavorable conduction band-edge level as well as its short carrier lifetimes and slow oxygen evolution kinetics.[8] Recombination in the bulk as a result of small polaron trapping impedes hole transport to the semiconductor–electrolyte interface,[10–12] whereas surface-state trapping causes electron–hole recombination before the oxidation reaction is able to proceed.[13–20]

To overcome the latter, that is, to enhance water-oxidation kinetics with respect to surface recombination, a common strategy is to modify the semiconductor surface with a water-oxidation catalyst (WOC).[9] An efficient hole-transfer catalyst

[a] F. S. Hegner, Dr. N. López, Dr. J. R. Galan-Mascaros
    Institute of Chemical Research of Catalonia (ICIQ)
    Av. Paisos Catalans, 16 Tarragona, 43007 (Spain)
    E-mail: nlopez@iciq.es
            jrgalan@iciq.es

[b] D. Cardenas-Morcoso, Dr. S. Giménez
    Institute of Advanced Materials (INAM)
    Universitat Jaume I
    Castellon, 12006 (Spain)
    E-mail: sjulia@uji.es

[c] Dr. J. R. Galan-Mascaros
    ICREA
    Pg. Lluís Companys, 23. Barcelona, 08010 (Spain)

⊡ Supporting Information and the ORCID identification number(s) for the
ⓘ author(s) of this article can be found under https://doi.org/10.1002/
   cssc.201701538.

☀ This publication is part of a Special Issue on the topic of Artificial Photo-
   synthesis for Sustainable Fuels. To view the complete issue, visit:
   http://dx.doi.org/10.1002/cssc.v10.22.

on top of a photoactive semiconductor is thought to overcome the kinetic barriers of the sluggish water-oxidation reaction, which boosts the performance of the photoanode.[21,22] Consequently, the deposition of a stable and cost-effective WOC on a photoactive semiconductor material is crucial to achieve the targeted technoeconomical requirements.

Notwithstanding, the simple combination of such two systems does not guarantee success. Indeed, detailed studies on the mechanism of WOCs on iron-oxide photoanodes have pointed out that most "catalysts", although enhancing photoelectrochemical behavior, do not act as genuine catalysts, that is, they do not provide an effective hole-transfer pathway to increase the rate of water oxidation by lowering the activation barrier of the reaction. In many cases, the formation of the semiconductor/catalyst interface "only" increases the lifetime of surface recombination by acting as a capacitive layer or by passivating surface states.[20,23–25] A thick catalyst layer may even counteract photoelectrochemical activity by blocking light absorption or by inhibiting charge transport and ion diffusion from the electrolyte.[26,27] Moreover, an improvement in the photoelectrochemical (PEC) performance was also observed for noncatalytic overlayers, such as Al_2O_3 and Ga_2O_3, which either passivate surface states, as in the case of Ga_2O_3,[28–30] or change the energetic levels favorably, as in the case of Al_2O_3.[31]

The extent to which any semiconductor/catalyst combination has a chance of success can be predicted by computational methods, which in turn can save much time and efforts towards appropriate interface constructions.

We recently reported that cobalt hexacyanoferrate (CoFe-PB), a competitive WOC, acted preferentially as a genuine catalyst on top of photoactive $BiVO_4$ thin films.[32] Through DFT calculations, we assigned this behavior to favorable alignment of the energy levels, allowing CoFe-PB to participate as a viable bridge between the semiconductor and the water molecules. This synergy was experimentally assessed with CoFe-PB-decorated photoanodes, which exhibited a +0.8 V gain in photocurrent and a hole-extraction efficiency above 80%.[32]

Herein, we report the DFT analysis and experimental validation of a similar system, the hematite/CoFe-PB (Figure 1) composite photoanode. Computational models indicate that there

is an intrinsic mismatch between these two materials, which implies that photoelectrocatalytic synergy should not occur. Indeed, our experiments are in excellent agreement with these predictions. CoFe-PB-decorated hematite electrodes show only a small improvement in photoelectrocatalytic water-oxidation activity that cannot be assigned to genuine catalytic behavior of CoFe-PB. Most probably, this is due to a surface-state shift that also shifts the water-oxidation onset to a lower potential. Such robust computational analysis will be very useful for any other semiconductor/catalyst ensemble by allowing for prior assessment of the validity of a proposed interface combination. These theoretical analyses will facilitate, and even push, future experimental research in the right direction towards final optimization of interfaces in photoelectrodes.

Results and Discussion

For efficient hole-transfer catalysis to occur, the catalyst needs to have its energy levels correctly aligned with the photoactive material, as schematized in Figure 2a for the case of the synergetic $BiVO_4$/CoFe-PB system.[32] In particular, this indicates that once the electron–hole pair is formed, the hole needs to be transferred to the catalyst; therefore, the corresponding levels in the catalyst need to be higher in energy than the valence band (VB) of the photoanode. This energy-alignment requisite is at the core of the process. If this thermodynamic condition is not fulfilled, as shown in Figure 2b, the "catalyst" will not exert efficient hole transfer.

Hybrid density functional theory (DFT) was used to calculate the electronic structures of α-Fe_2O_3, CoFe-PB ($KCo[Fe(CN)_6]$), and a solvated water molecule, as further described in the Experimental Section. Figure 2c shows the aligned densities of states (DOS) of the photoelectrochemical system: the hematite photoanode (left), the catalyst (middle), and water (right). To avoid confusion, it has to be noted that the calculated HOMO must not be mistaken with the electrochemical H_2O redox potential, although a linear relationship may exist.[33–35]

The calculated band gap of 1.95 eV for α-Fe_2O_3 matches well with its experimental value of 1.9–2.1 eV (Figure S6 in the Supporting Information).[6,7] This shows that the hybrid functional HSE03-13%, which includes 13% of exact exchange and which was previously optimized to match the electronic properties of CoFe-PB,[32] is also adequate to describe the electronic structure of α-Fe_2O_3 and follows previous indications by Pozun and Henkelman.[36] The VB edge of hematite consists of both O2p and Fe3d t_{2g} antibonding orbitals, which hybridize as a result of longitudinal lattice distortion along the main axis of the hexagonal unit cell (Figure 1). Hybridization of the strongly correlated Fe3d levels and the bandlike O2p levels in the VB was also found by photoemission studies and allows ligand-to-metal charge transfer by photoexcitation.[37,38] The distortion of the FeO_6 octahedra in the lattice also stabilizes the empty Fed_{z^2} orbitals along the principal axis, which thus forms the conduction band (CB) minimum (together with a small Fe4s contribution).

If a photon is absorbed, an electron of the O2p VB will be excited to the Fe CB by a charge-transfer transition, as was
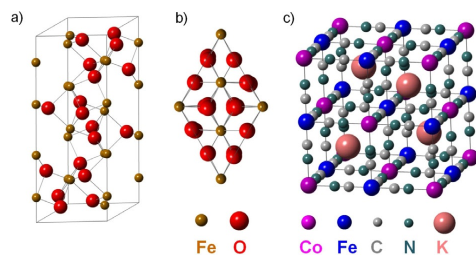
Figure 1. Representation of the crystal structures of a) the trigonal-hexagonal unit cell (space group $R\bar{3}6$), b) the predominant (001) surface facet (top view) of hematite (α-Fe_2O_3), and c) the cubic unit cell (space group $F\bar{4}3m$) of CoFe-PB ($KCo[Fe(CN)_6]$).
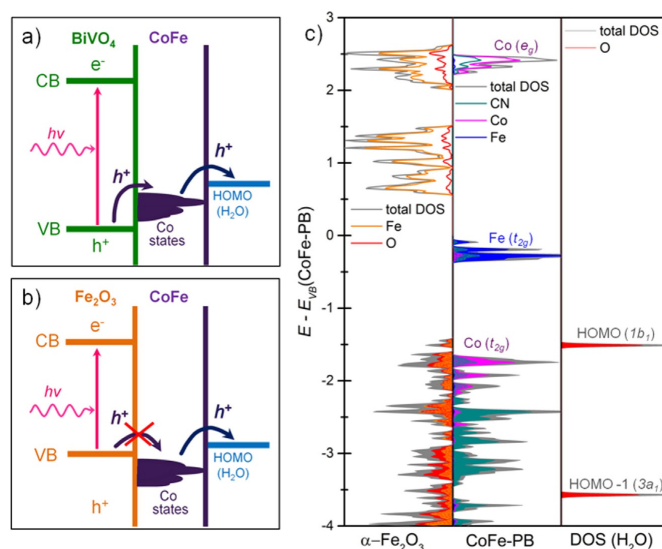
Figure 2. Energy-level alignment of a) a synergetic photoanode/catalyst interface: BiVO₄/CoFe-PB and b) a noncatalytic photoanode/catalyst combination: Fe₂O₃/CoFe-PB. c) Densities of states of α-Fe₂O₃ (left), KCoFe[(CN)₆] (middle), and a solvated H₂O molecule (right) aligned by their O 2s bands. Filled electronic states are represented by filled areas. The CoFe-PB valence band edge is set as the zero energy level, that is, the given electronic levels do not coincide with electrochemical potentials, which are potential differences measured against a reference electrode.

seen in several X-ray photoemission and absorption studies, which hence leaves a hole in the VB that is then available for water oxidation.[37,39–41] The highest electronic state, that is, the highest occupied molecular orbital (HOMO), of water lies at the same energy (within the computational error of ±0.1 eV) and, thus, is readily available to accept the hole at the Fe_2O_3 VB. From a thermodynamic viewpoint, disregarding kinetic effects and surface requirements, the hematite VB edge and the H_2O HOMO levels match adequately to induce electronic overlap, which is a necessary requirement for efficient electron (hole) transfer to take place. Nonetheless, small polaron effects and surface recombination prevent the efficient use of the hole.[10–20]

The CoFe-PB catalyst, however, has its filled Co d t_{2g} states, responsible for water oxidation,[32,42] slightly below the Fe_2O_3 VB edge (Figures 2 b, c). Therefore, there is no thermodynamic driving force to favor hole transfer from Fe_2O_3 to CoFe-PB and, subsequently, to H_2O. This, in turn, does not mean that charge transfer to the catalyst will not occur. The Fe t_{2g} states, which lie approximately 1 V above the Fe_2O_3 VB, do not directly participate in the water-oxidation catalytic reaction, nor are they involved in the formation of the CoFe-PB/Fe_2O_3 interface. The strong CN binding from cyanide's C site makes the Fe centers inaccessible to coordination. Moreover, their electronic levels are far above the water HOMO, which excludes electronic overlap, required for water oxidation to occur. At finite temperatures and in an electrochemical environment, the CoFe-PB electronic levels, which lie close to the Fe_2O_3 VB, may accept/donate holes from/to Fe_2O_3/H_2O. All the same, the probability

of CoFe-PB to have a true catalytic function, providing a faster hole-transfer pathway, on top of a hematite photoanode is negligible owing to level-alignment considerations. According to the DOS levels (Figure 2 c), it is clear that there is an intrinsic mismatch, as the Co t_{2g} hole-acceptor level of CoFe-PB is at lower energy than the valence band of hematite. This indicates that hole transfer is neutral or slightly uphill and, thus, does not favor catalysis. Nevertheless, other beneficial effects of a CoFe-PB "catalyst" on hematite cannot be excluded. Tunneling[43] and hopping between sub-band-edge states within the barrier layer[44] have also been reported to describe charge transfer between photoactive and catalytic materials if the energy levels are not correctly aligned.
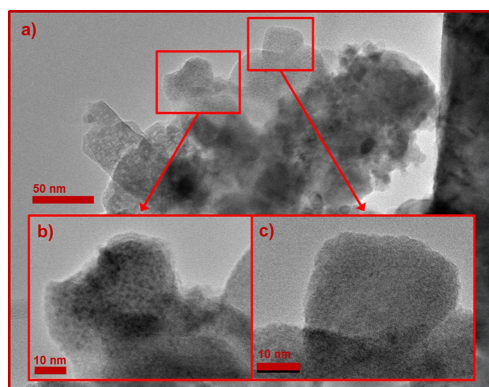
We also performed experiments to assess the validity of such a prediction. Nanostructured Zr-doped hematite films (see the Supporting Information for more details) were modified with the CoFe-PB catalyst by a sequential coating method at room temperature, as previously described.[32] The hematite electrode was submerged first in a ferricyanide solution and then in a cobalt chloride solution (both at neutral pH), which promoted the growth of the insoluble cobalt hexacyanoferrate. For our experiments, we generally used between three and six dipping cycles. Increasing the number of cycles did not significantly alter the photoelectrochemical performance of the photoanodes (as shown in Figure S3).

The electrodes were characterized by scanning electron microscopy (SEM) (Figure S4) and high-resolution transmission electron microscopy (HRTEM, Figure 3), both combined with energy-dispersive X-ray (EDX) spectroscopy. A total Fe/O ratio
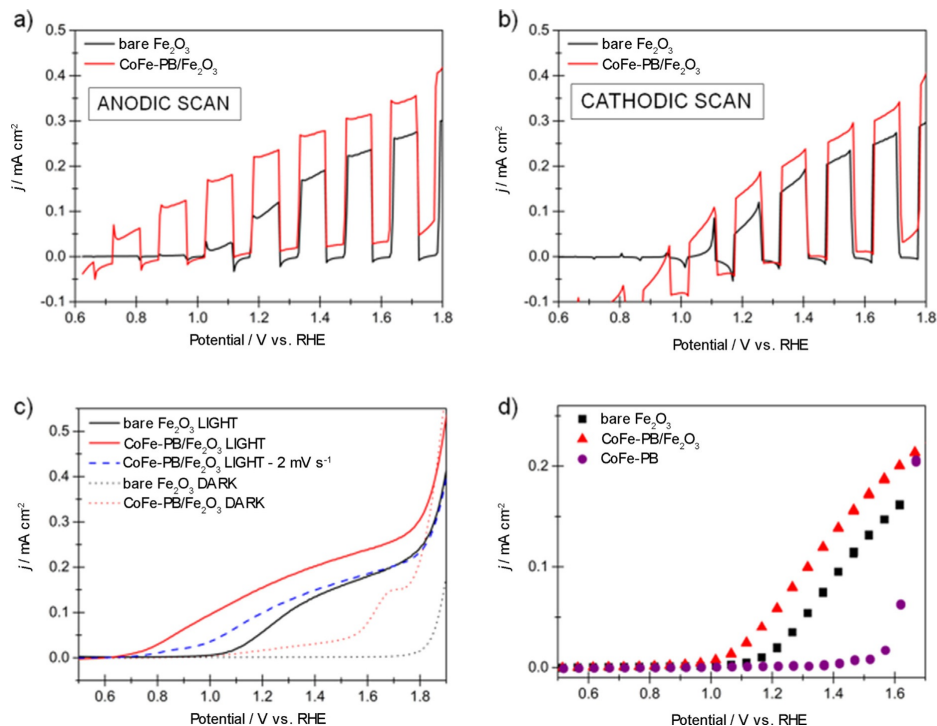
of 32:68 is found, which is in good agreement with the Fe_2O_3 stoichiometry. More consistent evidence for the formation of Fe_2O_3 is provided by X-ray photoelectron spectroscopy (XPS) analysis (see Figure S5 and Table S2). The amount of the CoFe-

PB catalyst is less than 1% and cannot be detected under SEM conditions. With HRTEM, however, cubic CoFe-PB crystallites can clearly be found on the Fe_2O_3 surface (Figure 3 b, c). Their Co/Fe ratios are found to be between 50:50 and 60:40 by EDX spectroscopy, and they all lie in the stoichiometric possible range of 1:1 ($KCo[Fe(CN)_6]$) and 3:2 ($Co_3[Fe(CN)_6]_2$).[32,45,46] The presence of CoFe-PB on the surface is further confirmed by XPS, as described in the Supporting Information. Catalyst deposition does not show a significant influence on the optical UV/Vis absorption or band gap of the hematite semiconductor (Figure S6).

The photoelectrochemical behavior of the photoanodes was examined by cyclic voltammetry (CV) under chopped and constant illumination (Figure 4) in neutral (pH 7) potassium phosphate (KPi) buffer (0.1 M) solution. In the anodic scans at $50 \, mV \, s^{-1}$ (Figure 4 a, c) an apparent cathodic shift in the photocurrent onset potential of 0.3 V can be seen. Nevertheless, scanning in the cathodic direction (Figure 4 b) reveals a much smaller improvement in the photocurrent, which indicates that the apparent shift in the water-oxidation onset in the anodic direction is the result of the capacitive effect of the CoFe-PB layer, as the difference in anodic and cathodic scans for bare Fe_2O_3 is negligible. Indeed, scanning the CoFe-PB/α-Fe_2O_3 electrode at lower scan rates (Figures 4 c and S7) significantly de-

Figure 3. a) Electron micrographs obtained by HRTEM of a scratched CoFe-PB/α-Fe_2O_3 electrode with b, c) magnifications of the CoFe-PB crystallites found on the surface.

Figure 4. The j–V curves of CoFe-PB/Fe_2O_3 (red) and bare Fe_2O_3 (black) in 0.1 M KPi buffer solution at pH 7. a) Anodic and b) cathodic CV scans under chopped light (1 sun) at a scan rate of $50 \, mV \, s^{-1}$. c) Anodic CV curve in the dark (dotted thin lines) and under light (thick solid lines) collected at scan rates of 50 (thick solid lines) and $2 \, mV \, s^{-1}$ (blue dashed line). d) Steady-state j–V curve extracted from the electrochemical impedance analysis data.

creases the observed photocurrent, whereas the scan rate barely affects the current density–voltage (*j*–*V*) behavior of bare hematite (Figure S7). Moreover, from the steady-state *j*–*V* curve (Figure 4 d), which can be extracted from electrochemical impedance spectroscopy (EIS) analysis, as well as from scans at very low scan rates, the "real" photocurrent onset potential shift of 0.1 V can be determined. In here, the voltage needed to attain a photocurrent of 0.01 mA cm^{-2} was taken as the onset potential.

To gain mechanistic understanding of the effect of CoFe-PB on hematite photoelectrodes, PEC experiments were performed in the presence of hydrogen peroxide (0.5 M), which was found to be an optimal hole scavenger for hematite.[15] Under these conditions it is assumed that all holes that reach the surface will be rapidly injected into solution and no electron–hole recombination will take place at the semiconductor–liquid interface.[15] Figure 5 a shows the photocurrents obtained with and without a hole scavenger under illumination at pH 7, and Figure 5 b shows the calculated charge-transfer efficiencies as a function of applied potential (see Supporting Information for calculation details).

The measured CV curves in hole scavenger solution do not show significant differences, which implies that an equal number of holes reaches the semiconductor/electrolyte interface for both bare and CoFe-PB-modified hematite; thus, their charge-separation efficiencies are similar. This, in turn, implies that charge mobilities in the bulk and band bending are not affected by surface catalyst modification. Consequently, it can be safely claimed that surface modification of Fe$_2$O$_3$ by CoFe-PB does not alter its bulk properties. The photocurrent onset in hole scavenger, that is, without surface recombination, is equal to the flat band potential (V_{FB}) and is approximately 0.6 V versus reversible hydrogen electrode (RHE).[47]

The charge-transfer efficiency of CoFe-PB/Fe$_2$O$_3$ reaches its maximum at approximately 1.35 V versus RHE, whereas for bare Fe$_2$O$_3$ it is maximal at 1.57 V versus RHE. The magnitude of 60%, however, is equal for both bare and modified Fe$_2$O$_3$. This indicates that the CoFe-PB catalyst does not improve charge transfer to the electrolyte but that the catalyst shifts it

to a lower potential, which is in line with the observed cathodic shift in the onset potential.

EIS measurements were performed to further investigate the effect of the catalyst layer on the photocurrent. The obtained Nyquist plots systematically show a single arc in the dark and, thus, were fit to a simple Randles' circuit,[48] whereas two arcs are obtained under illumination at high potential (see Figure S8). This is due to a different, indirect charge-transfer mechanism taking place, in which holes are trapped in surface states and are then transferred to the electrolyte.[17,23,49] It is apparent that the potential at which indirect charge transfer starts to occur is lower for CoFe-PB/Fe$_2$O$_3$ electrodes than for bare Fe$_2$O$_3$, as also described in the Supporting Information. These EIS data can be fit to a previously established equivalent circuit that accounts for indirect hole transfer via hematite surface states and that is shown in Figure 6 a.[17,23,47,49] The equivalent circuit elements include the contact-dependent series resistance (R_S); the trapping resistance (R_{trap}) (Figure 6 b), which describes trapping of charges into the surface state; the charge-transfer resistance (R_{CT}) from the surface state to the electrolyte (Figure 6 b); the space-charge capacitance (C_{SC}) of the bulk semiconductor (Figure 6 c); and the surface-state capacitance (C_{SS}) of the hematite surface traps (Figure 6 d).

The resistances R_{trap} and R_{CT} (Figure 6 a, b) are not influenced by the amount of catalyst on the surface. The trapping of holes into the surface state (described by R_{trap}) is not affected by the catalyst at all; this is in good agreement with the information provided by the experiments with the hole scavenger (Figure 5), for which no significant changes in the bulk properties of Fe$_2$O$_3$ are identified. On the other hand, hole transfer from the surface states occurs at lower potentials, in accordance with the cathodic shift of the onset potential (Figure 4) and the calculated charge-transfer efficiency (Figure 5).

The bulk capacitance of hematite C_{SC} (Figure 6 c), which results from band bending in the space-charge region, seems to decrease slightly upon increasing the number of dipping cycles during deposition. This, however, can be attributed to having less Fe$_2$O$_3$ surface area exposed to the solution in the CoFe-PB/Fe$_2$O$_3$ anode as more CoFe-PB is added. With Mott–Schottky (MS) analysis (see the Supporting Information), the
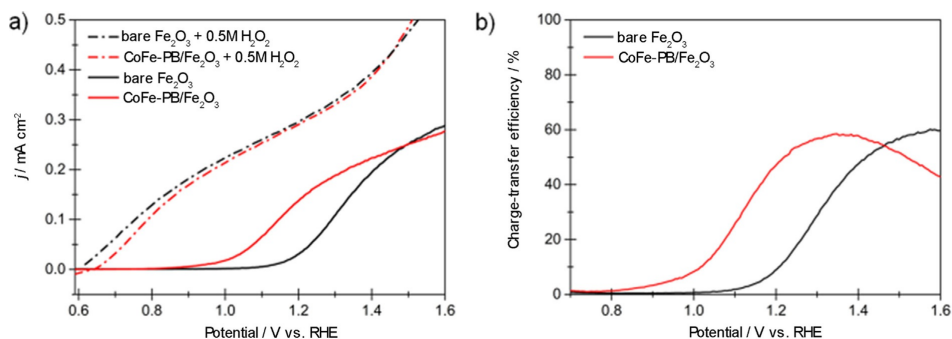
Figure 5. a) Anodic CV curves of CoFe-PB/ Fe$_2$O$_3$ (red) and bare Fe$_2$O$_3$ (black) in 0.1 M KPi buffer (solid lines) and 0.5 M H$_2$O$_2$ (dashed lines) solutions (both at pH 7) recorded at a slow scan rate of 2 mV s^{-1} to exclude catalytic, nonfaradaic current. b) Calculated charge-transfer efficiencies for both systems at pH 7.
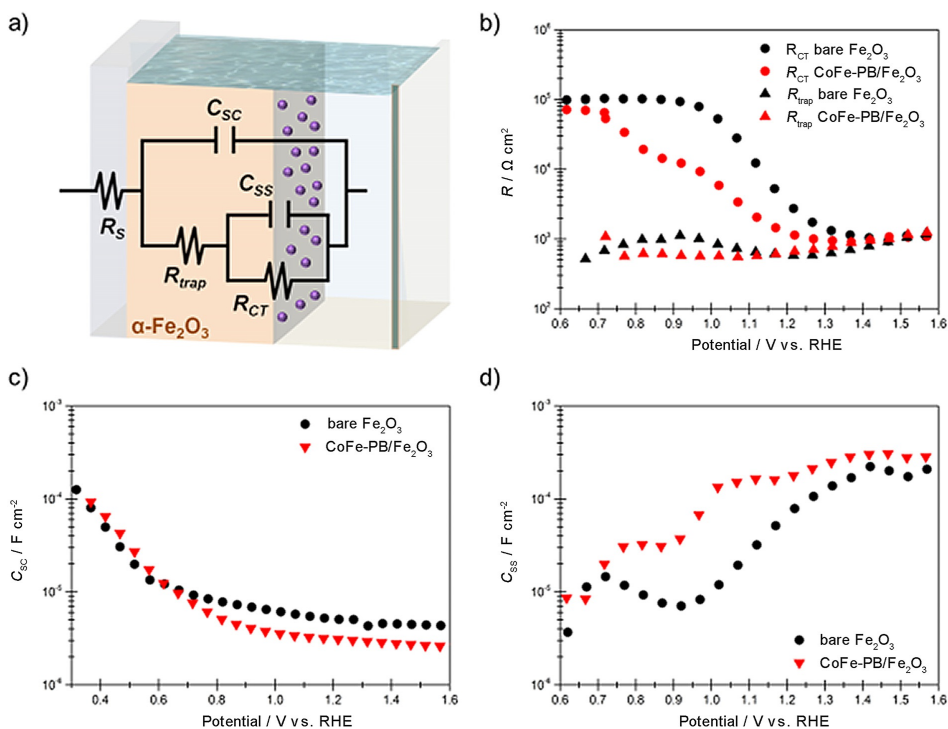
Figure 6. a) Equivalent circuit model used to fit EIS results obtained under 1 sun irradiation at higher potentials when indirect hole-transfer occurs. b) Charge-transfer (circles) and trapping (triangles) resistances of bare Fe_2O_3 (black) and CoFe-PB/Fe_2O_3 (red). c) Bulk and d) surface state capacitances of bare (black) and CoFe-PB coated (red) Fe_2O_3 semiconductor photoanodes. All spectra were obtained at pH 7 (0.1 M KPi buffer) and 1 sun irradiation.

flat band potential and the doping density of hematite were determined. As expected, the flat band potential, $V_{FB} = (0.5 \pm 0.05)$ V versus RHE, is independent of the CoFe-PB catalyst, which proves that CoFe-PB does not change the band positions. It differs by approximately 0.1 V from the photocurrent onset potential in the presence of a hole scavenger (which gives $V_{FB} = 0.6$ V vs. RHE) (Figure 5) owing to inaccuracies in the MS description for highly doped materials, as described by Zandi et al.[50] A flattening or horizontal shift in the MS curves, which was previously attributed to Fermi-level pinning,[17, 23] is not observed here. The high annealing temperatures (800 °C) employed in this study are partially thought to passivate surface states and unpin the Fermi level, an effect that is also seen in the comparatively small photocurrent transients (Figure 3 a, b).

Figure 6 d shows the surface-state capacitance (C_{SS}) values of bare and CoFe-PB-modified hematite photoanodes. The magnitude of C_{SS} is not affected by CoFe-PB; hence, the "catalyst" does not passivate surface states. It can be seen clearly though, that the deposition of CoFe-PB shifts the surface state to lower potential. Hence, we conclude that the observed cathodic onset potential shift originates from shifting the surface state, which initiates indirect charge transfer through the surface states at a lower potential than for bare Fe_2O_3, and

this, in turn, is due to oxidation of the CoFe-PB catalyst. A similar effect was found for Ga_2O_3 overlayers on hematite.[28] Furthermore, the trends followed by the two capacitances included in the model validate the selection of this equivalent circuit to fit our experimental results.

Although the energy-level alignment (Figure 2) does not favor hole transfer to the catalyst in its ground state, an applied external potential can initiate charge transfer to the catalyst in the surface, and this creates the oxidized $Co^{III}Fe^{III}$ states in CoFe-PB.[46, 51] This transfer takes place at lower potentials than hole transfer to the surface state, which could also explain the cathodic shift in the surface-state capacitance.

Another important issue is related to the interfacial adhesion of Fe_2O_3 and the CoFe-PB catalyst. The larger the surface in contact between the photoanode and the catalyst, the more paths available for hole scavenging. As shown in a recent study by Shao-Horn et al., water wetting strongly influences the charge-transfer properties from/to the electrolyte/catalyst interface and, therefore, crucially determines the dynamics of the catalytic surface reaction.[52] A similar principle applies to the "wetting" of the catalyst on the semiconductor surface, which leads to hole transfer to the solution.

The micrographs in Figure 3 show that the nanoparticles are essentially nonwetting the oxide surface, which thus limits the

number of hole-transfer paths. The reasons behind the poor wetting can be traced back to the crystal structure of the compounds. The most common surface termination of hematite is hexagonal (Figure 1 b); however, the termination of PB is cubic, and this leads to lattice mismatch. Having incommensurate crystal facets minimizes the number of Co—O—Fe bridges at the interface, which are needed to enable hole transfer. Hence, catalyst "wetting" is another aspect that may be studied in silico and is linked to interface engineering that is crucial to its performance.

Conclusions

Light-harvesting semiconductors, which can transform sunlight into an electric-field potential as the driving force to produce fuels, are promising candidates for large-scale application of artificial photosynthesis technologies. However, they need to be coupled to an appropriate catalyst for the reaction to be efficient and fast enough. Generally, electron–hole recombination is faster than chemical transformations.

Beyond interfacial engineering requirements, there will be an important contribution from the correct alignment between the electronic levels from both the semiconductor and the catalyst. In this manuscript, we demonstrated how appropriate level alignment could be used to shed some light on possible charge-transfer pathways and, hence, to determine the applicability of a possible co-catalyst, as exemplified in the hematite/cobalt hexacyanoferrate case.

Although the applied DFT analysis used the simplified model of bulk structures only and did not include real electrochemical interfaces, it clearly showed that there was an intrinsic mismatch, as the catalyst hole-acceptor level was below the valence band of hematite in the energy diagram. Consequently, hole transfer to the catalyst was neutral or slightly uphill, and thus there was no thermodynamic pathway for the generated holes in hematite to be transferred to the catalyst. This suggests that hole transfer to water, and thus water oxidation catalysis, is more likely to occur directly at the semiconductor surface. Nonetheless, different hole-transfer pathways, such as tunneling or hopping between sub-band-edge states, may be considered.[43, 44] In good agreement, our experiments indicated that CoFe-PB decoration on top of hematite electrodes did not lead to a relevant enhancement in the photoelectrocatalytic performance. We assigned the small enhancement to longer lifetimes of electron–hole surface recombination as a result of the hole-scavenging character of the interface, which shifted the surface-state capacitance to more cathodic potentials. Water oxidation still preferentially occurred on the hematite surface as observed in different hematite/catalyst systems.[23, 24] Therefore, the theoretical model of simple energy diagrams could predict the feasibility of this (and any other) junction. Interfaces may be engineered and improved, but if the process is thermodynamically uphill, their improvement is not due to an improvement in catalytic efficiency. For bare hematite in particular, finding a suitable true catalyst is a difficult task, as hematite has its valence band edge maximum very close to the HOMO of water. An appropriate co-catalyst would need to

have filled electronic states between the valence band (VB) of Fe_2O_3 and the HOMO of H_2O, which are available for water oxidation (next to having accessible coordination sites). A better strategy could involve shifting the VB of Fe_2O_3 to lower energies, which could be achieved by suitable dopants[36] or surface modification with overlayers.[31]

In this line, analogous computational studies indicate that the favorable alignment of a photoactive semiconductor and catalyst (e.g., CoFe-PB/$BiVO_4$) leads to a remarkable increase in performance,[32] which corroborates the validity of our theoretical approach.

Experimental Section

Materials

Iron(II) chloride tetrahydrate ($FeCl_2 \cdot 4H_2O$, >98%), zirconyl chloride octahydrate ($ZrOCl_2 \cdot 8H_2O$ >99%), and potassium ferricyanide ($K_3[Fe(CN)_6]$, ≥99.0%) were purchased from Sigma–Aldrich, and cobalt chloride hexahydrate ($CoCl_2 \cdot 6H_2O$, ≥98.0%) was purchased from Fluka Analytical. Dimethyl sulfoxide (DMSO, ≥99.9%) and hydrogen peroxide solution [H_2O_2, 30% (w/w) in H_2O] were obtained from Sigma–Aldrich. The buffer solution was prepared from potassium phosphate monobasic and dibasic (KH_2PO_4, ≥99.0%; K_2HPO_4, ≥98.0%; Sigma-Aldrich). High-purity (Milli-Q) water was obtained with a Millipore purification system (Synergy) and was used for all solutions. Fluorine-doped tin oxide (FTO)-coated glass slides were purchased from Hartford glass (15 Ω cm^{-2}).

Synthesis of hematite electrodes

Thin-film hematite electrodes were prepared by a simple and cost-efficient electrodeposition method, based on a description by Shaddad et al.,[53] but with varying calcination conditions as in Refs. [50, 54]. Prior to deposition, FTO electrodes were ultrasonicated and then thoroughly cleaned with water and ethanol (isopropyl alcohol). Zr-doped metallic Fe was deposited from a solution of 20 mm $FeCl_2 \cdot 4H_2O$ and 0.9 mm $ZrOCl_2 \cdot 8H_2O$ in DMSO by applying a constant potential of −20. V vs. Ag/AgCl (3 m KCl) for 6 min. After carefully rinsing the films with Milli-Q water, the electrodes were calcined in air by heating up to 800 °C for 9–10 min, which was followed by rapid quenching at room temperature.

Sequential CoFe-PB coating

The CoFe-PB catalyst was deposited by sequentially dipping the hematite electrodes in reactant solutions of 0.02 m $K_3[Fe(CN)_6]$ in H_2O and 0.04 m $CoCl_2$ in H_2O, as we recently reported for $BiVO_4$ photoanodes.[32] First, the electrodes were dipped in [$Fe(CN)_6$]$^{3-}$ solution for 10–15 min with slow stirring, so that the negatively charged iron cyanide complexes could bind to the Fe_2O_3 surface. Afterwards, the electrodes were thoroughly rinsed with Milli-Q water and were then dipped in the Co^{2+} solution, again for 10–15 min with stirring to form CoFe-PB complex structures. The sequence was repeated at least two times to ensure significant CoFe-PB deposition. In all shown measurements, 3–6 repetitions were applied, which did not change the PEC behavior of the electrodes (see Figure S3 b).

Synthesis of CoFe-PB electrodes

For the sake of comparison, CoFe-PB/FTO electrodes were prepared by following the hydrothermal method described by Han et al.[42] In this method, CoO_x was first deposited by heating $Co(NO_3)_2$ and carbamide in an autoclave at 120° (10 h) and was afterwards derivatized to CoFe-PB in $K_3[Fe(CN)_6]$ solution at 60° (1–3 h).

Photoelectrochemical (PEC) measurements

PEC experiments were performed with an Eco Chemie Autolab potentiostat coupled with NOVA electrochemical software. A typical three-electrode cell consisted of the hematite photoanode as the working electrode, a Pt wire or mesh as the counterelectrode, and a Ag/AgCl (3 M KCl) reference electrode. All potentials were converted into the pH-independent reversible hydrogen electrode (RHE) by using the Nernst equation [Eq. (1)]:

$$V_{RHE} = V_{Ag/AgCl} + V^0_{Ag/AgCl} + 0.059 \cdot pH$$
$$\text{with } V^0_{Ag/AgCl}(3\text{ M KCl}) = 0.21 \text{ V} \tag{1}$$

To normalize the measured current (in A) to a current density j in $mA\,cm^{-2}$, the electrode geometrical areas were determined by the graphical software ImageJ 1.50i. If not stated otherwise, the experiments were performed in a 0.1 M solution of potassium phosphate (KH_2PO_4) buffer at pH (7 ± 0.1). The pH was determined with a CRISON Basic 2° pH meter. Hole-scavenger experiments were performed in 0.5 M H_2O_2 solution (pH 7), which was described to be an effective hole scavenger by Warren et al.[15] A 450 W Xe arc lamp with an AM 1.5 solar filter (Sciencetech Inc.) was used to simulate sunlight of 100 mW cm⁻² (1 sun). If not otherwise mentioned, cyclic voltammetry (CV) scans were typically performed at a scan rate of 50 mV s⁻¹ until a stable signal was reached. For the CoFe-PB modified electrodes, approximately 2–3 CV scans were needed to stabilize the signal, but not for bare hematite. All hematite electrodes were illuminated from the electrolyte from the top of the hematite surface. This ensured a small mean free path for photogenerated holes, as hematite is well known to have very small hole-diffusion lengths between 2–4[55] and 20 nm.[56] Impedance data were collected between 10^{-1} and 40^6 Hz by using a 20 mV amplitude voltage perturbation and were analyzed with ZView software (Scribner associates). Steady-state j–V curves were extracted by monitoring the stabilized current at each applied voltage during the impedance measurement.

Structural and optical characterization

Morphologies, particle sizes, and chemical compositions were determined by scanning electron microscopy (SEM) with a JSM-7000F JEOL FEG-SEM system (Tokio, Japan) equipped with an INCA 400 Oxford EDX analyzer (Oxford, UK) and operating at 15 kV and a JEM-2100 JEOL transmission electron microscope operating at 200 kV that also contained an INCA 400 Oxford EDX analyzer (Oxford, UK). Prior to the SEM experiment, the samples were sputtered with a 2 nm thick layer of Pt. Surface analysis was performed by X-ray photoelectron spectroscopy (XPS) by using a Specs SAGE 150 instrument. The analyses were performed by using non-monochromatic AlK$_\alpha$ irradiation (1486.6 eV) at 20 mA and 13 kV, a constant energy pass of 75 eV for overall analysis, 30 eV for analysis in the specific binding energy ranges of each element, and a measurement area of 1×1 mm². The pressure in the analysis chamber was 8×10^{-9} hPa. The data were evaluated by using Casa XPS software. The energy corrections of the spectra were performed considering a reference value of C 1s from the organic matter at 284.8 eV. UV/Vis spectra of the electrodes was recorded with a Cary 300 Bio spectrometer (UV0911M213). Absorbance and band gaps were calculated as described in the Supporting Information.

Computational details

Density functional theory (DFT) calculations were performed by using the Vienna Ab Initio Package (VASP)[57,58] on the model structures of stoichiometric $KCo[Fe(CN)_6]$ and α-Fe_2O_3 (Figure 1). Although real CoFe-PB is a nonstoichiometric compound, its electronic structure is not expected to vary from the ideal $KCo[Fe(CN)_6]$ structure.[59] However, a difference occurs owing to a change in the magnetic configuration, which is discussed in the Supporting Information. As pure density functional theory has proven insufficient to describe correctly the electronic structure of Prussian Blue type materials[60] and as DFT$+$U cannot unambiguously predict an explicit U-term needed to compare materials with different transition-metal centers,[60,61] a modified hybrid functional based on the HSE03 functional,[62,63] but including only 13% of exact Hartree–Fock (HF) exchange, was employed.[32] More information about the functional is given in the Supporting information. Projector Augmented Wave (PAW) pseudopotentials with small cores, expanding valence-subshell containing s and p electrons, ensured sufficient flexibility and were used for all metal atoms in the lattice.[64,65] For structure optimizations, a Γ-centered k-point mesh was used, and valence electrons were expanded in plane waves with kinetic energies up to 500 eV. Single-point calculations to obtain more accurate electronic structures were performed with a kinetic cutoff energy of 600 eV and denser Monkhorst–Pack k-point grids with $3\times3\times3$ (CoFe-PB) or $3\times3\times2$ (Fe_2O_3) k-points.[66] Water was calculated with the same scheme. For this, a single H_2O molecule in an asymmetric box (14.5 Å×15 Å×15.5 Å) was solvated through a continuum model. The implicit solvated water was represented through the MGCM method.[67,68]

All structures and calculations were uploaded to the ioChem-BD database, from which they are openly accessible.[69–71]

Acknowledgements

Conflict of interest

The authors declare no conflict of interest.

ChemPubSoc Europe

CHEMSUSCHEM Full Papers

[1] K. Sivula, R. van de Krol, *Nat. Rev. Mater.* **2016**, *1*, 15010.
[2] A. Fujishima, K. Honda, *Nature* **1972**, *238*, 37–38.
[3] K. L. Hardee, A. J. Bard, *J. Electrochem. Soc.* **1976**, *123*, 1024–1026.
[4] C. Fàbrega, S. Murcia-Lopez, D. Monllor-Satoca, J. D. Prades, M. D. Hernandez-Alonso, G. Panelas, J. R. Morante, T. Andreu, *Appl. Catal. B* **2016**, *189*, 133–140.
[5] T. W. Kim, K. S. Choi, *Science* **2014**, *343*, 990–994.
[6] J. H. Kennedy, K. W. Frese, *J. Electrochem. Soc.* **1978**, *125*, 709–714.
[7] R. M. Cornell, U. Schwertmann in *The Iron Oxides: Structure, Properties, Reactions, Occurrences and Uses, 2nd ed.*, Wiley-VCH, Weinheim, **2003**, pp. 9–38.
[8] K. Sivula, F. Le Formal, M. Grätzel, *ChemSusChem* **2011**, *4*, 432–449.
[9] A. G. Tamirat, J. Rick, A. A. Dubale, W.-N. Su, B.-J. Hwang, *Nanoscale Horiz.* **2016**, *1*, 243–267.
[10] S. M. Ahmed, J. Leduc, S. F. Haller, *J. Phys. Chem.* **1988**, *92*, 6655–6660.
[11] A. J. Bosman, H. J. Vandaal, *Adv. Phys.* **1970**, *19*, 1–117.
[12] L. M. Carneiro, S. C. Cushing, C. Liu, Y. Sude, P. Yang, A. P. Alivisatos, S. R. Leone, *Nat. Mater.* **2017**, *16*, 819–824.
[13] M. Barroso, S. R. Pendlebury, A. J. Cowan, J. R. Durrant, *Chem. Sci.* **2013**, *4*, 2724–2734.
[14] F. Le Formal, S. R. Pendlebury, M. Cornuz, S. D. Tilley, M. Grätzel, J. R. Durrant, *J. Am. Chem. Soc.* **2014**, *136*, 2564–2574.
[15] H. Dotan, K. Sivula, M. Grätzel, A. Rothschild, S. C. Warren, *Energy Environ. Sci.* **2011**, *4*, 958–964.
[16] B. Klahr, S. Gimenez, F. Fabregat-Santiago, T. Hamann, J. Bisquert, *J. Am. Chem. Soc.* **2012**, *134*, 4294–4302.
[17] B. Klahr, S. Gimenez, F. Fabregat-Santiago, J. Bisquert, T. Hamann, *Energy Environ. Sci.* **2012**, *5*, 7626–7636.
[18] B. Iandolo, A. Hellman, *Angew. Chem. Int. Ed.* **2014**, *53*, 13404–13408; *Angew. Chem.* **2014**, *126*, 13622–13626.
[19] N. Yatom, O. Neufeld, M. C. Toroker, *J. Phys. Chem. C* **2015**, *119*, 24789–24795.
[20] N. Yatom, Y. Elbaz, S. Navon, M. C. Toroker, *Phys. Chem. Chem. Phys.* **2017**, *19*, 17278–17286.
[21] F. Ning, M. Shao, S. Xu, Y. Fu, R. Zhang, M. Wei, D. G. Evans, X. Duan, *Energy Environ. Sci.* **2016**, *9*, 2633–2643.
[22] W. Liu, H. Liu, L. Dang, H. Zhang, X. Wu, B. Yang, Z. Li, X. Zhang, L. Lei, S. Jin, *Adv. Funct. Mater.* **2017**, *27*, 1603904.
[23] B. Klahr, S. Gimenez, F. Fabregat-Santiago, J. Bisquert, T. Hamann, *J. Am. Chem. Soc.* **2012**, *134*, 16693–16700.
[24] M. Barroso, A. J. Cowan, S. R. Pendlebury, M. Grätzel, D. R. Klug, J. R. Durrant, *J. Am. Chem. Soc.* **2011**, *133*, 14868–14871.
[25] L. Badia-Bou, E. Mas-Marza, P. Rodenas, E. M. Barea, F. Fabregat-Santiago, S. Gimenez, E. Peris, J. Bisquert, *J. Phys. Chem. C* **2013**, *117*, 3826–3833.
[26] D. K. Zhong, D. R. Gamelin, *J. Am. Chem. Soc.* **2010**, *132*, 4202–4207.
[27] G. Wang, Y. Ling, X. Lu, T. Zhai, F. Qian, Y. Tong, Y. Li, *Nanoscale* **2013**, *5*, 4129–4133.
[28] L. Steier, I. Herraiz-Cardona, S. Gimenez, F. Fabregat-Santiago, J.- Bisquert, S. D. Tilley, M. Grätzel, *Adv. Funct. Mater.* **2014**, *24*, 7681–7688.
[29] E. Aharon, M. C. Toroker, *Catal. Lett.* **2017**, *147*, 2077–2082.
[30] K. Ulman, M. T. Nguyen, N. Seriani, R. Gebauer, *J. Phys. Chem.* **2016**, *144*, 094701.
[31] O. Neufeld, N. Yatom, M. C. Toroker, *ACS Catal.* **2015**, *5*, 7237–7243.
[32] F. S. Hegner, I. Herraiz-Cardona, D. Cardenas-Morcoso, N. López, J. R. Galán-Mascarós, S. Gimenez, *ACS Appl. Mater. Interfaces* **2017**, DOI: 10.1021/acsami.7b09449.
[33] J. Conradie, *J. Phys. Conf. Ser.* **2015**, *633*, 012045.
[34] A. V. Marenich, J. Ho, M. L. Coote, C. J. Cramer, D. G. Truhlar, *Phys. Chem. Chem. Phys.* **2014**, *16*, 15068–15106.
[35] C. P. Kelly, C. J. Cramer, D. G. Truhlar, *J. Phys. Chem.* **2006**, *110*, 16066–16081.
[36] Z. D. Pozun, G. Henkelman, *J. Chem. Phys.* **2011**, *134*, 224706.
[37] A. Fujimori, M. Saeki, N. Kimizuka, M. Taniguchi, S. Suga, *Phys. Rev. B* **1986**, *34*, 7318–7328.
[38] M. Catti, D. Valerio, R. Dovesi, *Phys. Rev. B* **1995**, *51*, 7441–7450.

[39] G. Dräger, W. Czolbe, J. A. Leiro, *Phys. Rev. B* **1992**, *45*, 8283–8287.
[40] R. J. Lad, V. E. Henrich, *Phys. Rev. B* **1989**, *39*, 13478–13485.
[41] Y. Ma, P. D. Johnson, N. Wassdahl, J. Guo, P. Skytt, J. Nordgren, S. D. Kevan, J.-E. Rubensson, T. Böske, W. Eberhardt, *Phys. Rev. B* **1993**, *48*, 2109–2111.
[42] L. J. Han, P. Y. Tang, A. Reyes-Carmona, B. Rodriguez-Garcia, M. Torrens, J. R. Morante, J. Arbiol, J. R. Galan-Mascaros, *J. Am. Chem. Soc.* **2016**, *138*, 16037–16045.
[43] Y. W. Chen, J. D. Prange, S. Dühnen, Y. Park, M. Gunji, C. E. D. Chidsey, P. C. McIntyre, *Nat. Mater.* **2011**, *10*, 539–544.
[44] J. R. Avila, M. J. Katz, O. K. Farha, J. T. Hupp, *J. Phys. Chem. C* **2016**, *120*, 20922–20928.
[45] R. O. Lezna, R. Romagnoli, N. R. de Tacconi, K. Rajeshwar, *J. Phys. Chem. B* **2002**, *106*, 3612–3621.
[46] N. R. de Tacconi, K. Rajeshwar, R. O. Lezna, *Chem. Mater.* **2003**, *15*, 3046–3062.
[47] J. Bisquert, S. Gimenez, L. Bertoluzzi, I. Herraiz-Cardona in *Photoelectrochemical Solar Fuel Production: From Basic Principles to Advanced Devices* (Eds.: S. Gimenez, J. Bisquert), Springer International, Cham, Switzerland, **2016**, Chap. 6.
[48] J. E. B. Randles, *Discuss. Faraday Soc.* **1947**, *1*, 11–19.
[49] L. Bertoluzzi, P. Lopez-Varo, J. A. Jimenéz Tejada, J. Bisquert, *J. Mater. Chem. A* **2016**, *4*, 2873–2879.
[50] O. Zandi, A. R. Schon, H. Maihibabaei, T. W. Hamann, *Chem. Mater.* **2016**, *28*, 765–771.
[51] R. Martínez-García, M. Knobel, J. Balmaseda, H. Yee-Madeira, E. Reguera, *J. Phys. Chem. Solids* **2007**, *68*, 290–298.
[52] B. Han, K. A. Stoerzinger, V. Tileli, A. D. Gamalski, E. A. Stach, Y. Shao-Horn, *Nat. Mater.* **2017**, *16*, 121–126.
[53] M. N. Shaddad, M. A. Ghanem, A. M. Al-Mayouf, S. Gimenez, J. Bisquert, I. Herraiz-Cardona, *ChemSusChem* **2016**, *9*, 2779–2783.
[54] A. Annamalai, A. Subramanian, U. Kang, H. Park, S. H. Choi, J. S. Jang, *J. Phys. C* **2015**, *119*, 3810–3817.
[55] K. Sivula, R. Zboril, F. Le Formal, R. Robert, A. Weidenkaff, J. Tucek, J. Frydruch, M. Grätzel, *J. Am. Chem. Soc.* **2010**, *132*, 7436–7444.
[56] M. P. Dare-Edwards, J. B. Goodenough, A. Hemnett, P. R. Trevellick, *J. Chem. Soc. Faraday Trans. 1* **1983**, *79*, 2027–2041.
[57] J. Hafner, G. Kresse, *The Vienna Ab-Initio Simulation Program VASP: An Efficient and Versatile Tool for Studying the Structural, Dynamic, and Electronic Properties of Materials*, Plenum Press, New York, **1997**, pp. 69–82.
[58] G. Kresse, J. Furthmüller, *Phys. Rev. B* **1996**, *54*, 11169–11186.
[59] J. C. Wojdel, I. D. R. Moreira, S. T. Bromley, F. Illas, *J. Chem. Phys.* **2008**, *128*, 044713.
[60] F. S. Hegner, J. R. Galán-Mascarós, N. López, *Inorg. Chem.* **2016**, *55*, 12851–12862.
[61] M. Capdevila-Cortada, Z. Lodziana, N. Lopez, *ACS Catal.* **2016**, *6*, 8370–8379.
[62] J. Heyd, G. E. Scuseria, *J. Chem. Phys.* **2004**, *120*, 7274–7280.
[63] J. Heyd, G. E. Scuseria, M. Ernzerhof, *J. Chem. Phys.* **2003**, *118*, 8207–8215.
[64] P. E. Blöchl, *Phys. Rev. B* **1994**, *50*, 17953–17979.
[65] G. Kresse, D. Joubert, *Phys. Rev. B* **1999**, *59*, 1758–1775.
[66] H. J. Monkhorst, J. D. Pack, *Phys. Rev. B* **1976**, *13*, 5188–5192.
[67] M. Garcia-Ratés, N. López, *J. Chem. Theory Comput.* **2016**, *12*, 1331–1341.
[68] M. Garcia-Ratés, R. García-Muelas, N. López, *J. Phys. Chem. C* **2017**, *121*, 13803–13809.
[69] ioChem-BD software, http://www.iochem-bd.org/, Institute of Chemical Research of Catalonia (ICIQ), **2014**.
[70] M. Álvarez-Moreno, C. de Graaf, N. López, F. Maseras, J. M. Poblet, C. Bo, *J. Chem. Inf. Model.* **2015**, *55*, 95–103.
[71] F. S. Hegner, link to database: Photoanodes_Fe2O3_CoFe-PB, https://doi.org/10.19061/iochem-bd-1-51.

Unraveling Charge-Transfer in CoFe-Prussian Blue Modified BiVO$_4$ Photoanodes

Benjamin Moss, [a] ‡ *Franziska Simone Hegner,* [b] ‡ *Sacha Corby,* [a] *Shababa Selim,* [a] *Laia Francàs* [a]* *Núria López,* [b]* *Sixto Giménez,* [c] *J.R. Galán-Mascarós* [b],[d]* *and James R. Durrant* [a]*

AUTHOR ADDRESSES:

[a]   Department of chemistry, Imperial College London, Imperial College Rd, London, SW7 2AZ, United Kingdom.
[b]   Institut Català d'Investigació Química (ICIQ), The Barcelona Institute of Science and Technology (BIST), Avinguda Països Catalans 16, 43007 Tarragona, Spain.
[c]   Institute of Advanced Materials (INAM). Universitat Jaume I, 12006 Castelló, Spain.
[d]   ICREA. Pg. Lluís Companys 23, 08010 Barcelona, Spain.
‡   Equal contributors to this work.

ABSTRACT. The reasons for improved photoelectrochemical performance upon catalyst modification are often controversial. When depositing the efficient CoFe Prussian blue (CoFe-PB) water oxidation catalyst on BiVO$_4$, a large photocurrent increase and onset potential shift (up to 0.8 V) is observed, while maintaining staibility for over 50 hours. To elucidate the origin of such an enhancement, we used time-resolved spectroscopies to compare the dynamics of photogenerated holes in modifed and unmodified BiVO$_4$ films. Even in the absence of strong positive bias, a fast fast (pre-ms), largely irreversible, hole transfer from BiVO$_4$ to CoFe-PB is observed. This process retards recombination, enabling holes to accumulate in the catalyst. These holes in CoFe-PB remain reactive, oxidising water at a similar rate to holes in pristine BiVO$_4$. CoFe-PB therefore enhances performance by presenting a favourable interface for efficient hole transfer, combined with the catalytic function necessary to drive water oxidation.
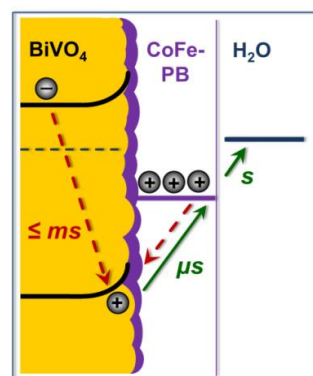
TEXT. Metal oxides, such as TiO_2 [1], Fe_2O_3 [2], WO_3 [3] and $BiVO_4$ [4] have been extensively studied as candidate photoanodes for water oxidation (WO). Despite their ideally aligned valence bands, which provide a large driving force for WO,[5] large additional positive applied potentials are still required to access high photon-to-current conversion efficiencies. A common approach to reduce the need for such strong positive potentials is to deposit an electrocatalyst on the surface of the photoanode to act as a co-catalyst. This strategy is often successful, yielding enhanced photocurrents and reduced WO onset potentials.[4,6–11] However, those observed improvements in performance are not necessarily linked to improved WO kinetics. Different mechanisms, such as slowing down electron-hole recombination in the semiconductor, may dominate. For example, deposition of cobalt phosphate (CoP_i) on dense $BiVO_4$ leads to a 100-250 mV negative shift in the onset potential of WO.[11] Independent studies of CoP_i modified films using electrochemical impedance spectroscopy (EIS), transient absorption spectroscopy (TAS),[11] and intensity modulated photocurrent spectroscopy (IMPS)[12] indicate that this improvement is not related to hole transfer to CoP_i (i.e charge separation) and/or WO catalyzed by CoP_i, but rather stems from retarded surface recombination within $BiVO_4$. Intriguingly, unfavorable interfacial kinetics for hole transfer to CoP_i are observed despite this transfer having an apparently large driving force[13] with the timescale of hole transfer from $BiVO_4$ to CoP_i observed to be 2-10 times slower than direct water-oxidation on the $BiVO_4$ surface (which has a characteristic time constant of ca. 0.5 s).[11,14,15] Although oxidation of CoP_i was observed under WO conditions, this oxidation of CoP_i did not contribute significantly to the overall water oxidation flux,[13] due to CoP_i's relatively slow water oxidation kinetics ($\sim 2 \times 10^{-3}$ s^{-1} per active site.[16] As such, finding a co-catalyst, which is directly a key challenge remains to demonstrate enhanced photoanode performance directly attributable to the water oxidation properties of an added co-catalyst. Whilst studies have reported *indirect* evidence for such performance enhancement[17], we focus herein on a *direct* kinetic study of a promising candidate system; cobalt iron Prussian blue on $BiVO_4$.

Cobalt hexacyanoferrate, the cobalt-iron analogue of Prussian blue (CoFe-PB), is a robust, effective and inexpensive electrocatalyst. CoFe-PB shows low WO onset potentials and exceptional stability, even in acidic media, whilst being simple and cost-effective to prepare.[18–21] Critically, CoFe-PB exhibits much faster WO kinetics than CoP_i (1.4 s^{-1} for CoFe-PB *vs* 2×10^{-3} s^{-1} for CoP_i per active site).[16,18] It has recently been demonstrated that CoFe-PB modification of mesostructured $BiVO_4$ photoanodes produces substantial improvements in both onset potential and photocurrent, maintaining stability for over 50 h.[17] Preliminary investigation of CoFe-PB modified $BiVO_4$, using photoelectrochemical impedance and hole scavenger studies, suggests that the origin of this improvement is distinct from the effect of CoP_i (i.e. suppression of surface recombination within $BiVO_4$), and related to more efficient hole transfer to water, presumably via CoFe-PB.[17,22] These findings are consistent with hybrid density functional theory calculations, which predict the existence of a strong energetic offset (thermodynamic driving force) for hole transfer between the valence band of $BiVO_4$ and CoFe-PB.[17,23]

Herein, we present the first study of the effect of CoFe-PB modification of $BiVO_4$ electrodes on the kinetics of photogenerated holes. Using time-resolved absorption spectroscopies, we demonstrate that $BiVO_4$ holes quickly and efficiently transfer to CoFe-PB, leading to persistent oxidised CoFe-PB states even at modest applied potentials. This capacity to separate charges at modest applied potential is coupled with effective catalytic functionality. Accumulated holes in

CoFe-PB form multiply oxidised states, which react with water with similar kinetics to unmodified $BiVO_4$, despite a significant loss of oxidising potential during charge separation.

Nanostructured $BiVO_4$ photoanodes were fabricated by a previously described electrodeposition method and modified with CoFe-PB by sequential coating.[17] Details of this synthesis and the film morphology (including SEM and TEM images of unmodified and CoFe-PB modified $BiVO_4$) can be found in the Supporting Information (Figure S1). CoFe-PB on FTO was prepared using a modified hydrothermal method, developed by Han *et al.* (See SI for details).[21] Consistent with previous reports, a thin (< 20 nm) co-catalyst layer is observed on $BiVO_4$ after sequential coating (Figure S1e and S1f).[17] Due to the thinness of this layer, the ground state absorption spectra of CoFe-PB modified and unmodified $BiVO_4$ films (Figure S2) do not significantly differ. We thus conclude that the enhancements in photocurrent are not caused by increased photon absorption - i.e that photons are predominantly absorbed by the $BiVO_4$.

Cyclic voltammograms of CoFe-PB modified and unmodified $BiVO_4$ in the dark and under simulated AM1.5 illumination are compared in (**Figure 1a**). Negligible current was observed in unmodified $BiVO_4$ in the dark. Upon CoFe-PB modification, a semi-reversible redox couple is observed in the dark around 1.2 V_{RHE}, with electrocatalytic WO occurring after 1.6 V_{RHE} (a value similar to that observed for CoFe-PB/FTO electrocatalysis).[17] Taking the voltage required to attain 0.1 mA/cm^2 as the onset potential for photocurrent under 1 sun irradiation, a negative shift of 0.8 V of the onset potential is achieved upon CoFe-PB deposition (Figure S3) - a result in agreement with previous reports.[17]
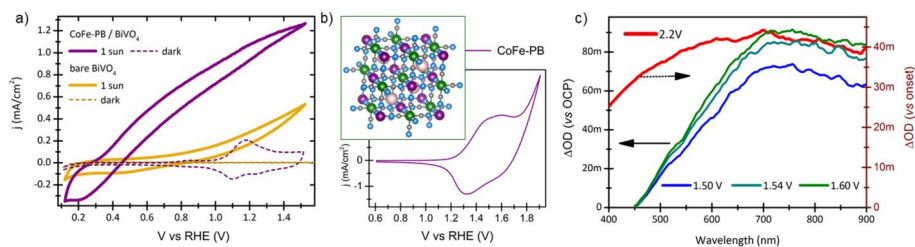

Figure 1: a) Cyclic voltammograms of bare $BiVO_4$ (yellow) and CoFe-PB modified $BiVO_4$ (purple) with and without illumination (1 sun) and b) CoFe-PB alone (in the dark) at pH 7 (0.1 M KP_i buffer). Inset: Ideal (fcc) crystal structure of CoFe-PB with octahedrally coordinated Co (purple) and Fe (green) centres. c) Differential absorbance spectra observed upon the oxidation of CoFe-PB/FTO. When potentials positive of the open circuit potential are applied (green/blue lines, referenced against OCP) an asymmetric peak with a broad maximum around 700-800 nm is observed. At potentials exceeding the onset potential of water oxidation electrocatalysis, a broader spectrum is observed with a maximum between 600 and 700 nm (red line, referenced against WO onset potential).

Before considering the effect of CoFe-PB modification on the transient absorption of $BiVO_4$, we first determined the effect of positive applied potential (oxidation) on the ground state absorption of CoFe-PB/FTO (employing a thicker, CoFe-PB film to yield a measurable ground state absorption spectrum). When potentials positive of the open-circuit (resting) potential (1.1 V_{RHE}) are applied, a broad and asymmetric (decaying more strongly towards shorter wavelengths) absorption difference spectrum is observed, peaking around 700 – 800 nm, (blue and green lines in **Figure 1c**, a full data set can be found in Figure S4). We attribute this to the oxidation of CoFe-PB as it increases with applied potential and correlates strongly with the semi-reversible redox wave observed before the onset of catalytic current. (**Figures 1b** and S4c). CoFe-PB films are non-stoichiometric, likely containing a mixture of neighbouring Co^{2+} and Fe^{2+}, Co^{3+} and Fe^{2+} (and possibly Co^{2+} and Fe^{3+}) centres, each with different coordination environments and redox potentials.[24,25] Consequently, this redox wave cannot clearly be assigned uniquely to either a Co^{2+}/Co^{3+} or a Fe^{2+}/Fe^{3+} couple. For simplicity, we hereafter refer to this oxidised state as "CoFe-PB+".[26] At potentials positive of the electrocatalytic WO onset potential (1.6 V_{RHE}), a smaller, flatter difference spectrum, with increased amplitude towards blue wavelengths is observed (red line in **Figure 1c**). This second spectrum exhibits a blue shifted maximum compared to CoFe-PB+. We assign this change in spectral shape to a further oxidation of CoFe-PB+, which again for simplicity we label "CoFe-PB2+". The appearance of this second spectrum correlates with the onset of water oxidation catalysis (**Figure 1b**.).

Utilising the spectral fingerprints of oxidised CoFe-PB states to interpret our results, we now turn to transient absorption spectroscopy (TAS, see SI for details), which we use to assess the effect of CoFe-PB modification on the kinetics of photogenerated holes in $BiVO_4$ photoanodes. **Figure 2a** presents a comparison of the transient absorption spectra (at 10 ms) of CoFe-PB modified and unmodified $BiVO_4$ films, both at strong positive bias, whilst **Figures 2b** and **2c** shows kinetics at selected wavelengths as a function of applied bias. Consistent with previous reports [11,15], unmodified $BiVO_4$ exhibits a transient absorption spectrum peaking at 550 nm and decaying towards the near IR. This spectrum has previously been assigned to $BiVO_4$ surface holes. [11, 15] After CoFe-PB modification, amplitude at 550 nm is lost, and a new peak bearing a strong resemblance to the absorption of CoFe-PB+ ($\approx$ 700 nm, decaying more strongly towards shorter wavelengths), is observed. Taken together, these results demonstrate efficient hole transfer from the $BiVO_4$ surface to CoFe-PB.

An increase in the lifetime of photogenerated charges upon CoFe-PB modification is clearly visible in the TA kinetics of the electrodes at low applied potentials (**Figure 2b** and **2c**). Concordant with previous transient studies, strong positive bias (1.5 V_{RHE}) is required to produce persistent ($\tau > 10$ ms) photogenerated holes in unmodified $BiVO_4$ (**Figure 2b**).[15] However, after CoFe-PB modification, persistent transient absorption is observed even at low applied potentials (0.25 V_{RHE}, **Figure 2c,** see also spectra in Figure S5). **Figure 2c** also shows that the signal amplitude at early times (10 μs) remains almost unchanged for 10's of ms. This data indicates that hole transfer from $BiVO_4$ to CoFe-PB is largely complete by 10 μs. We attribute this increased hole lifetime to fast and efficient hole transfer. This is because hole transfer to CoFe-PB corresponds to a spatial separation of charge; it is apparent this supresses recombination even in the absence of a strong applied potential.
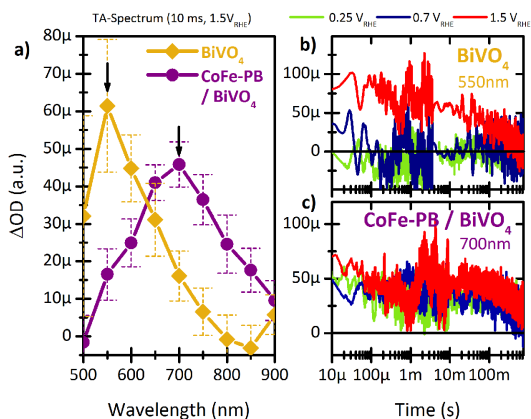
Figure 2: Comparison of the TA spectra of persistent photogenerated charges (recorded at 10 ms) in CoFe-PB modified and unmodified $BiVO_4$ (3a). In unmodified $BiVO_4$, a persistent transient related to surface holes is only observed at strong positive potential (1.5 V_{RHE}) (3b). Upon CoFe-PB modification, a persistent transient in observed even at 0.25 V_{RHE} (3c).

To better understand the fate of persistent separated holes in CoFe-PB under operational conditions, we utilise photo-induced absorption spectroscopy (PIAS) employing 5 s LED pulse to simulate *in operando* conditions (details can be found in the SI and previous publications)[13]. Unmodified $BiVO_4$ again shows a peak at 550 nm, assigned to the accumulation of $BiVO_4$ surface holes facilitated by strong positive applied potential (**Figure 3a**)[13–15] Upon CoFe-PB modification, amplitude at 550 nm decreases and a new peak consistent with oxidised CoFe-PB ($\approx$ 650 - 750 nm, see the following section for discussion of spectral shape and CoFe-PB oxidation state) is observed (**Figure 3a**). This change is broadly similar to the spectral change observed in TAS upon CoFe-PB modification, further supporting the conclusion that photogenerated holes transfer to, and accumulate in, CoFe-PB rather than $BiVO_4$.
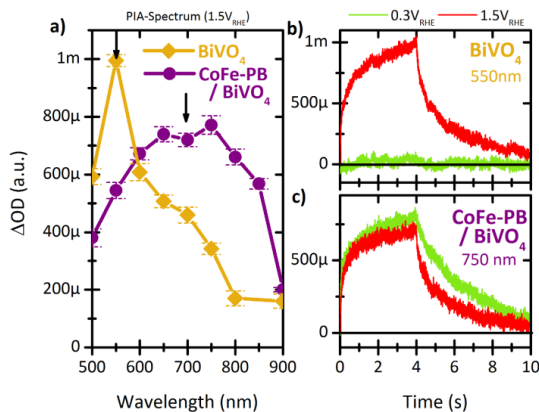
Figure 3: Comparison of the PIA spectra of CoFe-PB modified and unmodified $BiVO_4$ films (4a). In unmodified $BiVO_4$, strong positive potential (1.5 V_{RHE}) is required to observe a large growing transient, related to the accumulation $BiVO_4$ surface holes to under illumination (4b). Upon CoFe-PB modification, photogenerated charge accumulates even at potentials close to the onset potential of photocurrent, such as 0.3 V_{RHE} (4c).

The effect of the CoFe-PB layer on the dynamics of accumulated charges can be found by examining the PIA kinetics as a function of applied bias (**Figures 3b and c**). At lower applied potentials, a negligible PIA signal is observed for unmodified $BiVO_4$, indicating the few holes accumulate (**Figure 3b**). Under strong positive applied potentials, a strong PIA signal is observed, indicative of the accumulation of surface holes under *in operando* conditions - consistent with our TAS studies (**Figure 2b**). After CoFe-PB modification, strong positive potentials are no longer required to observe large PIA signals **(Figure 3c)**, again consistent with our TAS data (**Figure 3c**). The decay kinetics of the PIA traces under strong positive potential (where recombination processes are strongly supressed for both electrodes) gives a direct indication of the WO kinetics under these in operando conditions. [13] In unmodified $BiVO_4$, an initial rates analysis yields a WO time constant from $BiVO_4$ surface holes on the order of seconds (**Figures 3b** and S6a); consistent with our previous reports.[14,15] .
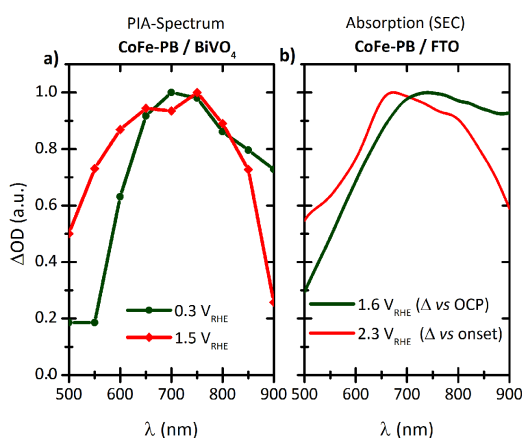

Figure 4: Normalised absorption spectra of (a) CoFe-PB modified $BiVO_4$ obtained from photoinduced absorption spectroscopy (PIA) and (b) of solely CoFe-PB on FTO obtained from spectro-electrochemistry (SEC) at low (below onset) bias (dark green) and high (above onset) bias (red).

PIA signal decays for CoFe-PB modified $BiVO_4$, assigned to oxidised CoFe-PB states, exhibit broadly similar decay kinetics to $BiVO_4$ holes, indicative of similar WO oxidation kinetics on both $BiVO_4$ and CoFe-PB (**Figure 3c**). However, in contrast to $BiVO_4$, significant PIA signal is observed for CoFe-PB modified $BiVO_4$ even at 0.3 V_{RHE}, with the PIA decay kinetics accelerating with increasing applied potential. Such an acceleration cannot be attributed to suppression of recombination losses, as this would result in a retardation of this decay. This acceleration with increased positive bias coincides with a blue shift of the PIA spectrum (**Figure 4a**). This is analogous to the blue shift observed with increased positive bias in our spectroelectrochemical data for CoFe-PB on FTO (**Figures 4b** and **1c**), assigned to the subsequent generation of CoFe-PB^{2+} states. These data thus indicate that under modest applied potential (0.3 V_{RHE}), hole transfer from $BiVO_4$ to CoFe-PB results primarily in the generation of unreactive (and therefore slowly decaying) CoFe-PB$^+$ states. However, as the applied potential (and photocurrent) increases, irradiation results in the generation of CoFe-PB^{2+} states capable of driving water oxidation. The greater reactivity of these states is consistent with their faster PIA

decay kinetics. Fitting the decay of PIA traces at gives a time constant for WO by CoFe-PB^{2+} states on the order of 1.4 s (Figure S6b), in agreement with a previously reported timescale for electrocatalytic water oxidation on CoFe-PB.[18]

In summary, and as illustrated in **Scheme 1**, our kinetic studies indicate that the enhanced photoelectrochemical water oxidation performance of CoFe-PB modified BiVO$_4$ results from fast (~ μs) hole transfer from BiVO$_4$ to CoFe-PB. This charge transfer enables the generation of long lived photogenerated holes (i.e CoFe-PB$^{+/2+}$ states in CoFe-PB) in the absence of strong anodic bias. WO kinetics are on the order of seconds on both BiVO$_4$ and CoFe-PB, despite the more oxidising nature of BiVO$_4$ holes. The resultant suppression of recombination losses, without any compromise in water oxidation kinetics, is the origin of the remarkable shift of the water oxidation onset potential following CoFe-PB deposition.
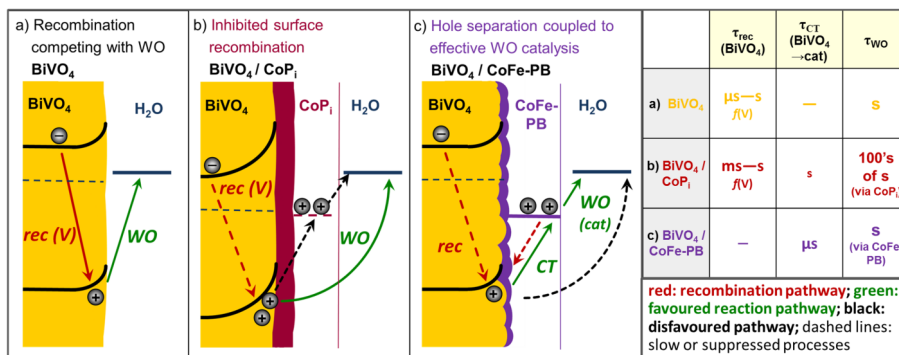
Scheme 1: Photon conversion efficiency in unmodified BiVO$_4$ (a) is limited by the kinetic competition between potential-dependent surface recombination (rec (V)) and water oxidation (WO). CoPi modification (b) reduces the applied potential needed to effectively supress surface recombination, allowing holes to react via the BiVO4 surface. Hole transfer (CT) to CoPi and water oxidation via CoPi is slow and does not contribute to photocurrent. CoFe-PB enhances efficiency via a different mechanism (c): efficient hole charge transfer to CoFe-PB separates holes from electrons in the BiVO4 surface (thereby supressing this recombination pathway). This is coupled to effective WO catalysis.

The kinetics we report herein for CoFe-PB modified BiVO$_4$ differ substantially from those we have reported previously for CoP$_i$ modified dense BiVO$_4$ films (**Scheme 1b**). Water oxidation on CoP$_i$ is 2-3 orders of magnitude slower than water oxidation via the BiVO$_4$ surface or water oxidation via CoFe-PB. This slow catalysis results in the accumulation of large amounts of relatively unreactive charge in CoP$_i$ when used as a co-catalyst, observed as slowly decaying PIA signals, with amplitudes 2 orders of magnitude greater than those observed in CoFe-PB, where holes in the catalyst are removed from the catalyst by water oxidation.[15] However, these large

signals arise from a CoP_i layer 10 times thicker than the CoFe-PB layer studied herein (200 *vs* 20 nm). Consequently, despite larger signals, only singly oxidised (i.e. pre-catalytic) CoP_i states are observed, corresponding to a lower hole density. This contrasts to the multiply oxidised CoFe-PB states observed herein. This is consistent with the concept of enhanced performance following CoP_i deposition resulting from retarded recombination within $BiVO_4$ due to increased band bending, suggested to result from Schottky junction formation [11] (See **Scheme 1b**). A further difference is that in $BiVO_4/CoP_i$, hole transfer to the CoP_i was observed to be relatively slow and inefficient (occurring on order of seconds), despite similar apparent energy offsets for hole transfer (roughly 1 eV), and contributed little to the overall water oxidation flux.[11,12,13] One possible explanation for this is that the interface between CoFe-PB and the most thermodynamically favourable surface facets of $BiVO_4$ is either significantly more covalent or exhibits better epitaxy than $BiVO_4/CoP_i$ (Figure S7). This could favour charge transfer in the high surface area nanostructured $BiVO_4$ studied herein. An alternative hypothesis is that this difference could be related to the difference in morphology between the $BiVO_4$ studied, as in our previous study of $BiVO_4/CoP_i$ a flat (dense) $BiVO_4$ film with a planar junction to a thick (200 nm) CoP_i layer was used.[11] The $BiVO_4$ samples studied herein are highly textured and interface via a high surface area junction to an extremely thin CoFe-PB layer (20nm). Research is currently underway to further investigate the conclusions of this work - in particular, the effect of the semiconductor and co-catalyst morphology as well as the semiconductor/co-catalyst interface on the efficiency of hole transfer as well as the factors that control the kinetics of water oxidation – with the aim of constructing a set of simple and general design principles for assessing the compatibility of semiconductor/co-catalyst systems.

ASSOCIATED CONTENT

Supporting Information.

The Supporting Information is available free of charge.

Content: Material synthesis, description of the experimental set-ups, UV-Vis spectroscopy and additional SEC data, TA spectra at different voltages, fitting of PIAS decay, crystalline models of $BiVO_4$ and CoFe-PB surfaces and discussion of interface linkages.

AUTHOR INFORMATION

Corresponding Authors
*L. Francàs: l.francas@ic.ac.uk, J. Durrant: j.durrant@imperial.ac.uk, N. López: nlopez@iciq.es, J.R. Galán-Mascarós: jrgalan@iciq.

Author Contributions
‡These authors contributed equally to the manuscript. The manuscript was written through contributions of all authors. All authors have given approval to the final version of the manuscript.
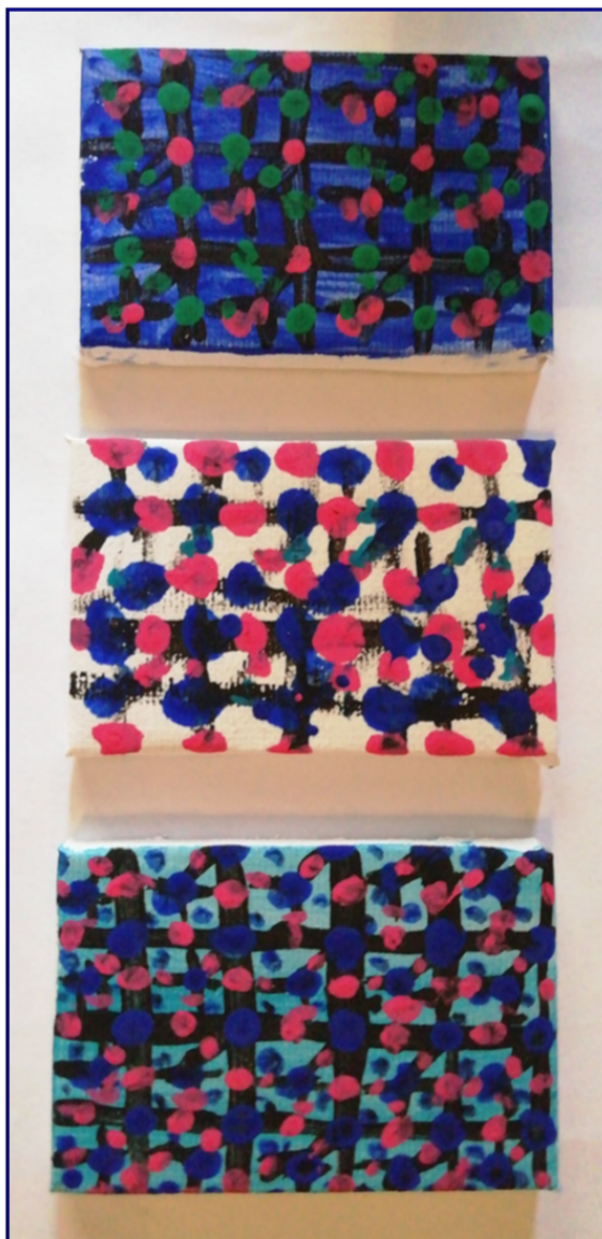
REFERENCES

[1] Fujishima, A.; Zhang, X.; Tryk, T.A. TiO$_2$ Photocatalysis and Related Surface Phenomena. *Surface Science Reports,* **2008**, *63*, 515–582.

[2] Hardee, K. L.; Bard, A. J. Semiconductor Electrodes V . The Application of Chemically Vapor Deposited Iron Oxide Films to Photosensitized Electrolysis. *Journal of the Electrochemical Society,* **1976**, *123*.

[3] Fàbrega, C.; Murcia-López, S.; Monllor-Satoca, D.; Prades, J. D.; Hernández-Alonso, M. D.; Penelas, G.; Morante, J.; Andreu, T. Efficient WO$_3$ Photoanodes Fabricated by Pulsed Laser Deposition for Photoelectrochemical Water Splitting with High Faradaic Efficiency. *Applied Catalysis B: Environmental,* **2016**, *189*.

[4] Park, J.; Donald, K.J.; Choi, K.-S. Progress in Bismuth Vanadate Photoanodes for Use in Solar Water Oxidation. *Chem. Soc. Rev.,* **2013**, *42*, 2321–2337.

[5] Peter, L. M.; Wijayantha, U. K. Photoelectrochemical Water Splitting at Semiconductor Electrodes: Fundamental Problems and New Perspectives. *ChemPhysChem,* **2014**, *15*, 1983–1995.

[6] Tamirat, A.; Rick, J.; Dubale, A.; Su, W.-N.; Hwang, B.-J. Using hematite for photoelectrochemical water splitting: a review of current progress and challenges. *Nanoscale Horizons,* **2016**, *1,* 243-267.

[7] Steinmiller, E. M., Choi, K.-S. Photochemical Deposition of Cobalt-Based Oxygen Evolving Catalyst on a Semiconductor Photoanode for Solar Oxygen Production. *Proceedings of the National Academy of Sciences,* **2009**, *106,* 20633-20636.

[8] Zhong, D. K.; Gamelin, D. R. Photoelectrochemical Water Oxidation by Cobalt Catalyst ("Co−Pi")/α-Fe$_2$O$_3$ Composite Photoanodes: Oxygen Evolution and Resolution of a Kinetic Bottleneck. *J. Am. Chem. Soc.,* **2010**, *132*, 4202–4207.

[9] Badia-Bou, L.; Mas-Marza, E.; Rodenas, P.; Barea, E. M.; Fabregat-Santiago, F.; Gimenez, S.; Peris, E.; Bisquert, J. Water Oxidation at Hematite Photoelectrodes with an Iridium-Based Catalyst. *J. Phys. Chem. C,* **2013**, *117*, 3826–3833.

[10] Kanan, M. W.; Nocera, D. G. In Situ Formation of an Oxygen-Evolving Catalyst in Neutral Water Containing Phosphate and Co^{2+}. *Science,* **2008**, *321*, 1072–1075.

[11] Ma, Y.; Le Formal, F.; Kafizas, A.; Pendlebury, S. R.; Durrant, J. R. Efficient suppression of back electron/hole recombination in cobalt phosphate surface-modified undoped bismuth vanadate photoanodes. *J. Mater. Chem. A,* **2015**, *3*, 20649–20657.

[12] Zachäus, C.; Abdi, F. F.; Peter, L. M.; van de Krol, R. Photocurrent of BiVO$_4$ is Limited by Surface Recombination, not Surface Satalysis. *Chem. Sci.,* **2017**, *8*, 3712–3719.

[13] Ma, Y.; Kafizas, A.; Pendlebury, S. R.; Le Formal, F.; Durrant, J. R. Photoinduced

Absorption Spectroscopy of CoPi on BiVO4: The Function of CoPi during Water Oxidation. *Adv. Funct. Mater.,* **2016**, *26*, 4951–4960.

[14] Ma, Y.; Mesa, C. A.; Pastor, E.; Kafizas, A.; Francàs, L.; Le Formal, F.; Pendlebury, S. R.; Durrant, J. R. Rate Law Analysis of Water Oxidation and Hole Scavenging on a BiVO4 Photoanode. *ACS Energy Lett.,* **2016**, *1*, 618–623.

[15] Ma, Y.; Pendlebury, S. R.; Reynal, A.; Le Formal, F.; Durrant, J. R. Dynamics of Photogenerated Holes in Undoped $BiVO_4$ Photoanodes for Solar Water Oxidation. *Chem. Sci.,* **2014**, *5*. 2964-2973.

[16] Surendranath, Y.; Kanan, M. W.; Nocera, D. G. Mechanistic Studies of the Oxygen Evolution Reaction by a Cobalt-Phosphate Catalyst at Neutral pH. *J. Am. Chem. Soc.,* **2010**, *132*, 16501–9.

[17] Hegner, F. S.; Herraiz-Cardona, I.; Cardenas-Morcoso, D.; Lopez, N.; Galan-Mascaros, J.-R.; Gimenez, S. Cobalt Hexacyanoferrate on BiVO4 Photoanodes for Robust Water Splitting. *ACS Appl. Mater. Interfaces,* **2017**, *9*, 37671–37681.

[18] Pintado, S.; Goberna-Ferrón, S.; Escudero-Adán, E. C.; Galán-Mascarós, J.-R. Fast and Persistent Electrocatalytic Water Oxidation by Co-Fe Prussian Blue Coordination Polymers. *J. Am. Chem. Soc.,* **2013**, *135*, 13270–13273.

[19] Goberna-Ferrón, S.; Hernández, W. Y.; Rodríguez-García, B.; Galán-Mascarós, J.-R. Light-Driven Water Oxidation with Metal Hexacyanometallate Heterogeneous Catalysts. *ACS Catal.,* **2014**, *4*, 1637–1641.

[20] Indra, A.; Paik, U.; Song, T. Boosting Electrochemical Water Oxidation with Metal Hydroxide Carbonate Templated Prussian Blue Analogues. *Angew. Chem. Int. Ed.,* **2018**, *57*, 1241–1245.

[21] Han, L.; Tang, P.; Reyes-Carmona, A.; Rodriguez-Garcia, B.; Torrens, M.; Morante, J.; Arbiol, J.; Galan-Mascaros, J.-R. Enhanced Activity and Acid pH Stability of Prussian Blue-type Oxygen Evolution Electrocatalysts Processed by Chemical Etching. *J. Am. Chem. Soc.,* **2016**, 16037-16045.

[22] Klahr, B.; Gimenez, S.; Fabregat-Santiago, F.; Bisquert, J.; Hamann, T. W. Photoelectrochemical and Impedance Spectroscopic Investigation of Water Oxidation with "Co–Pi"-Coated Hematite Electrodes. *J. Am. Chem. Soc.,* **2012**, *134*, 16693–16700.

[23] Hegner, F. S.; Cardenas-Morcoso, D.; Gimenez, S.; Lopez, N.; Galan-Mascaros, J.-R.. Level Alignment as Descriptor for Semiconductor/Catalyst Systems in Water Splitting: The Case of Hematite/Cobalt Hexacyanoferrate Photoanodes. *ChemSusChem,* **4552**, *10*, 4552–4560.

[24] R. O. Lezna, R. Romagnoli, N. R. de Tacconi, K. Rajeshwar, *J. Phys. Chem*., **2002**, *106*, 3612-3621.

[25] Kulesza, P. J.; Zamponi, S.; Malik, M. A.; Berrettoni, M.; Wolkiewicz, A.; Marassi, R. Spectroelectrochemical Characterization of Cobalt Hexacyanoferrate Films in Potassium Salt Electrolyte. *Electrochim. Acta,* **1998**, *43*, 919–923.

[26] Pastor, E.; Le Formal, F.; Mayer, M. T.; Tilley, D. S.; Francàs, L.; Mesa, C. A.; Grätzel, M.; Durrant, J. R. Spectroelectrochemical Analysis of the Mechanism of (Photo)Electrochemical Hydrogen Evolution at a Catalytic Interface. *Nat. Commun.,* **2017**, *8,* 14280.

UNIVERSITAT
ROVIRA i VIRGILI